

École doctorale n° XXX : Texte

**Doctorat ParisTech
(mémoire provisoire)
T H È S E**

pour obtenir le grade de docteur délivré par

I'École Nationale Supérieure d'Arts et Métiers

Spécialité “ Mécanique-matériaux (AM) ”

présentée et soutenue publiquement par

Adrien GOMAR

le 14 avril 2014

**Multi-Frequential Harmonic Balance Approach
for the Simulation of Contra-Rotating Open Rotors :
Application to Aeroelasticity**

Directeur de thèse : **Paola CINNELLA**
Co-encadrement de la thèse : **Frédéric SICOT**

Jury

M. Christophe CORRE , Professeur, ENSE3, Grenoble (France)	Rapporteur
M. Li HE , Professeur, University of Oxford, Oxford (Royaume-Uni)	Rapporteur
M. Jean-Camille CHASSAING , Maître de Conférences HDR, UPMC, Paris (France)	Examinateur
Mme Paola CINNELLA , Professeur, Università del Salento, Lecce (Italie)	Examinateur
M. Clément DEJEU , Ingénieur, Snecma (Safran), Villaroche (France)	Examinateur
M. Pascal FERRAND , Directeur de recherche CNRS, LMFA, Lyon (France)	Examinateur
M. Frédéric SICOT , Docteur, CERFACS, Toulouse (France)	Examinateur

T
H
È
S
E

*It's better to regret something you did
than something you didn't do*

Deep Kick – One Hot Minute
RED HOT CHILI PEPPERS

Contents

Introduction	ix
I General information	1
1 Contra-rotating open rotors	3
1.1 Generalities of propulsion	4
1.1.1 Thrust equation	4
1.1.2 Global propulsive efficiency	5
1.1.3 Toward propeller engines	6
1.2 Propellers	6
1.2.1 Geometry	6
1.2.2 Velocity triangle	7
1.2.3 Similarity coefficients	8
1.2.4 Main physical phenomena	8
1.3 Contra-rotating open rotors	9
1.3.1 Geometry	9
1.3.2 Velocity triangle	10
1.3.3 Similarity coefficients	11
1.4 Unsteadinesses	11
1.4.1 Unsteady effects	11
1.4.2 Main kinds of unsteadiness	11
1.5 Challenges	12
2 Introduction to aeroelasticity	17
2.1 What is aeroelasticity	18
2.2 Main aeroelastic phenomena in turbomachinery	18
2.2.1 Forced response	18
2.2.2 Flutter	18
2.3 Computational AeroElasticity (CAE)	20
2.3.1 Modal analysis	20
2.3.2 Structural dynamics of turbomachinery blade	21
2.3.3 Phase theorem	21
2.3.4 Weak-coupling approach	22
2.3.5 Stability curve	22

3 Fourier-based time methods	25
3.1 Introduction	26
3.2 The <u>Linearized Unsteady Reynolds-averaged Navier–Stokes</u> method (LUR)	26
3.2.1 Mono-frequential formulation	27
3.2.2 Extension to the Navier–Stokes equations	27
3.2.3 Numerical cost	27
3.3 The <u>Non-Linear Harmonic</u> method (NLH)	27
3.3.1 Mono-frequential formulation	28
3.3.2 Multi-frequential formulation	29
3.3.3 Extensions	31
3.3.4 Numerical cost	33
3.4 The <u>Non-Linear Frequency Domain</u> method (NLFD)	33
3.4.1 Mono-frequential formulation	33
3.4.2 Extensions	35
3.4.3 Numerical cost	36
3.5 The <u>Harmonic Balance</u> method (HB)	36
3.5.1 Mono-frequential formulation	36
3.5.2 Multi-frequential formulation	38
3.5.3 Extensions	39
3.5.4 Numerical cost	42
3.6 Convergence of the spectral operator	43
3.6.1 Theoretical results	43
3.6.2 Motivating example: numerical derivation of a smooth function	43
3.7 Periodic flows in turbomachinery	45
II Advantages and limitations of Fourier-based time methods	47
4 Preliminary validations of the harmonic balance approach	49
4.1 Linear advection of a periodic signal	50
4.1.1 Presentation of the test case	50
4.1.2 Numerical setup	50
4.1.3 Validation of the mono-frequential approach	51
4.1.4 Validation of the multi-frequential approach	54
4.2 Application to a non-linear system of equations	57
4.2.1 Presentation of the case	57
4.2.2 Numerical setup	57
4.2.3 Validation of the multi-frequential approach	58
5 Conditioning of multi-frequential harmonic balance methods	63
5.1 Condition number and contra-rotating open rotor aeroelasticity	64
5.2 Highlighting the problem	65
5.3 Proposed cure: automatic optimization of time instances	68
5.3.1 <u>Almost-Periodic Fourier Transform</u> algorithm (APFT)	68
5.3.2 Gradient-based <u>OPTimization</u> algorithm (OPT)	68
5.3.3 Assessment of the algorithms	70
5.3.4 Distribution of the time instances	72

6 Convergence of Fourier-based time methods for turbomachinery wake passing problems	75
6.1 Periodic problems with an infinite Fourier spectrum	76
6.2 Toward turbomachinery wakes	79
6.3 Application to a model turbomachinery configuration	83
6.3.1 Presentation of the case	83
6.3.2 Numerical Setup	84
6.3.3 Spectral convergence study	85
6.3.4 Comparison with the theoretical error measure	93
6.3.5 Toward an <i>a priori</i> error estimate	93
III Applications	97
7 11th standard aeroelastic configuration	99
7.1 Presentation of the case	100
7.2 Numerical setup	101
7.3 Subsonic case	103
7.4 Transonic case	105
8 Isolated low-speed CROR configuration	109
8.1 Presentation of the case	110
8.2 Numerical setup	111
8.3 Steady results	115
8.3.1 Convergence analysis	115
8.3.2 Similarity coefficients	115
8.3.3 One-dimensional results: radial profiles	116
8.3.4 Two dimensional results: radial and axial cuts	117
8.4 Spectral convergence of the harmonic balance computations	122
8.4.1 Using the prediction tool	122
8.4.2 Analyzing the similarity coefficients	123
8.4.3 Analyzing the blade response	123
8.4.4 Analyzing the radial cuts	125
8.5 Unsteady rigid-motion results	126
8.5.1 Similarity coefficients	126
8.5.2 Two-dimensional results: harmonic blade response	126
8.5.3 Two-dimensional results: axial cuts	127
8.5.4 Two-dimensional results: radial cut of harmonic pressure	128
8.6 Aeroelastic results	131
8.6.1 Stability curve	131
8.6.2 Local excitation	131
9 Isolated high-speed CROR configuration	135
9.1 Presentation of the case	136
9.2 Numerical setup	136
9.3 Steady results	138
9.3.1 Analysis of the convergence	138

9.3.2	Similarity coefficients	138
9.3.3	Radial profiles	140
9.3.4	Flow field around the blades	142
9.4	<i>A priori</i> estimate of the required number of harmonics	145
9.4.1	Using the prediction tool	145
9.4.2	Analyzing the radial cut	145
9.5	Unsteady rigid-motion results	146
9.5.1	Similarity coefficients	146
9.5.2	Two-dimensional results: harmonic blade response	146
9.5.3	Two-dimensional results: axial cuts	147
9.6	Aeroelastic results	149
9.6.1	Stability curve	149
9.6.2	Local excitation	149
9.6.3	Influence of the number of harmonics on the aeroelastic results	151
Conclusion		155
Appendices		163
A Detailed algorithm to compute the convergence criteria		163
A.1	Detailed algorithm to compute ε_1	163
A.2	Detailed algorithm to compute ε_2	164
A.3	Detailed algorithm to the tangential accumulated energy from a mixing plane computation	166

Introduction

Global warming may be one of the biggest challenges that human kind will have to face in the forthcoming decades if not years. According to the last scientific report of the Intergovernmental Panel on Climate Change (IPCC) [58] "The largest contribution to total radiative forcing¹ is caused by the increase in the atmospheric concentration of CO_2 since 1750".

A part of these CO_2 emissions and in general pollutants stems from the transport industry and in particular the aeronautical industry. Hopefully for the earth, the rarefaction of crude oil accelerates the decision making. In particular, in the seventies, the two oil crisis showed the aeronautical industries their dependence toward energy resources. To face this issue, the U.S. Senate directed NASA in 1975 to look for every potential fuel-saving concept for aircraft engines. The Advanced Turboprop project was born [44] and led to the concept of Contra-Rotating Open Rotor (CROR). It differentiates from the Contra-Rotating Propeller (CRP) engine, that has been studied by the United-Kingdom (at the beginning of the twenties century) and Russia (in the forties), by the Mach number for which it is designed: the CROR is meant to work on transonic inflow conditions, enabling its use for commercial aviation. This CROR concept showed a potential for large fuel savings but led to higher noise emissions due to the absence of a duct. The high noise emissions combined with the decrease of the price of the barrel in the late eighties, the contra-rotating open rotor never reached the commercial aviation.

Today, the cost of the barrel is almost at its maximum as shown in Figure 1. In parallel,

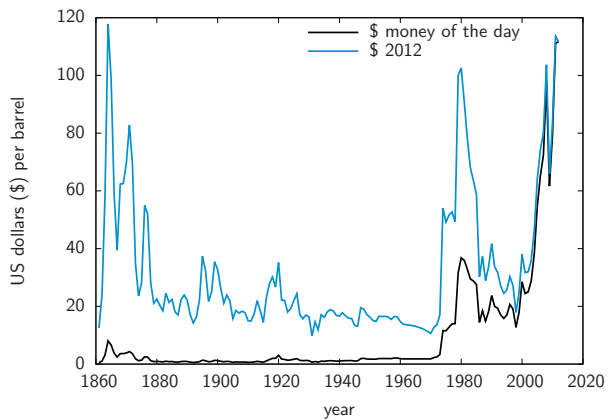


Figure 1: Evolution of the cost of a barrel from 1861 to 2012, from BP [1].

Airbus forecasts a doubled number of passengers in 2031 [3]. For that reason, the Euro-

¹namely global warming

pean commission has set, through the Advisory Council for Aeronautics Research in Europe (ACARE), demanding objectives to reduce these emissions by 2050: the noise, CO_2 and NO_x emissions should be reduced by 65%, 75% and 80%, respectively, with respect to the value of 2000. Therefore, to allow a sustainable air transportation, new concepts are needed for both the engines and the aircraft in general. Several have emerged, among which lightweight construction with advanced composite structure, airport collaborative decision making with continuous climb departure and less waiting in taxi, aerodynamically optimized wing geometries, *e.g.* laminar wings, and fuel efficient engines, to name but a few. For the latter, two main types of engine are currently studied: the Ultra-High Bypass Ratio (UHBR) engine that is based on a larger fan exhaust engine improving thus the propulsive efficiency, and the CROR engine that relies on two rows of contra-rotating rotors, that proved its viability during experiments within the framework of the Advanced Turboprop project of NASA [44]. In this work, the focus will be on the CROR engine.

The industrial design of turbomachinery, and by extension of contra-rotating open rotors, is usually based on steady flow analysis, for which the reference simulation tool is the three-dimensional Reynolds-Averaged Navier–Stokes (RANS) steady computation. However, this approach finds its limits when unsteady phenomena become dominant. This is the case of contra-rotating open rotors, where the interaction between the two rotors is of prior importance. In such a context, engineers need now tools to account for these effects as early as possible in the design cycle. With the growth of computational power, unsteady computations are entering industrial practice, but the associated restitution time remains an obstacle for daily basis applications. For this reason, efficient unsteady approaches are receiving a lot of attention.

At CERFACS, several unsteady approaches have been investigated to reduce the computational time associated with the unsteady simulation of CROR configurations. These are seldom carried on the whole circumference of the annulus due to the high computational cost. A first approach is therefore to assume cyclic periodicity, which allows to solve for only one blade passage and thus drastically reduce the computational domain. In the turbomachinery community, the phase-lag approach has shown to be a very efficient method to reduce the computational domain while maintaining a good capture of the unsteady flow physics. In this way, Burnazzi [9] evaluated the phase-lag approach by applying it to a 3D contra-rotating open rotor configuration. The author showed that the interactions between the two rotors can be retrieved, allowing thus a large computational time reduction. An additional gain can be expected by working on the temporal scheme used to solve the equations. To achieve this, Fourier-based time methods for periodic flows have undergone major developments in the last decade (see He [48] for a recent review). The basic idea is to decompose time-dependent flow variables into Fourier series, which are then injected into the equations of the problem. The time-domain problem is thus made equivalent to a frequency-domain problem, where the complex Fourier coefficients are the new unknowns. At this point, two strategies coexist to obtain the solution. The first one is to solve directly the Fourier coefficients, using a dedicated frequency-domain solver, as proposed by He and Ning [49]. The second strategy is to cast the problem back to the time domain using the inverse Fourier transform, as proposed by Hall et al. [47] with the Harmonic Balance (HB) method. The unsteady time-marching problem is thus transformed into a set of steady equations coupled by a source term. This term corresponds to a spectral approximation of the time-derivative in the exact equations. The main advantage of solving in the time domain is that it can be implemented into an existing

classical RANS solver, taking advantage of all classical convergence-accelerating techniques for steady-state problems. Sicot [87] implemented the HB method into the *elsA* [12] CFD code that is used at CERFACS. Applied to turbomachinery configurations, this method showed a computational gain of one to two orders of magnitude compared to classical time-marching approaches. Applied to CROR configurations, Yabili [110] showed that the computational time reduction was not conclusive. In fact, a large number of harmonics was needed to properly capture the unsteadinesses compared to turbomachinery configurations, lowering the computational gain. Therefore, François [33] deeply investigated the different unsteady approaches available for turbomachinery computations, among which the HB approach, and evaluated them on CROR simulations. The author confirmed that the harmonic balance method can retrieve unsteady flow features for a reduced cost at a gain that is relatively smaller compared to what was obtained on former turbomachinery applications. In parallel, Guédene [42] extended the harmonic balance approach to a multi-frequential framework. This method allows then to compute unsteadinesses whose frequencies are not harmonically related, which opens new perspectives.

Several challenges, such as aerodynamic, aeroacoustic and aeroelasticity are still open for contra-rotating open rotor to become a viable engine for the next generation aircraft. In this work, we assess the aeroelasticity of contra-rotating open rotor by using the multi-frequential harmonic balance approach developed and implemented by Guédene [42]. Actually, the main unsteadinesses of the flow field are known to be correlated with the so-called blade passing frequency. This frequency depends on the rotation speed of the current rotor and the number of blades of the opposite rotor. In contrast to that, the frequency that drives the aeroelasticity of CROR blades depends on their structural properties. As such, the frequencies of both the aerodynamic field and the aeroelasticity are not harmonically related, which justifies the use of the multi-frequential harmonic balance approach.

The aim of this study is to assess the multi-frequential harmonic balance to estimate the flutter properties of contra-rotating open rotor configurations. In this way, the dissertation is divided in three parts:

- *Part I* first presents general information on contra-rotating open rotors (*Chapter 1*). The basic equations governing the aeroelasticity of turbomachinery are presented and the chosen numerical approach is detailed (*Chapter 2*). Then, the mathematical framework that allows the derivation of Fourier-based time methods and their underlying properties are presented (*Chapter 3*), with focus on the multi-frequential harmonic balance approach.
- *Part II* presents the advantages and limitations of Fourier-based time methods. The chosen approach, namely the harmonic balance, is validated for linear and non-linear equations in *Chapter 4*. Both the mono-frequential and the multi-frequential formulations are shown to give spectral accuracy, which is a convergence property specific to Fourier-based time methods. It is emphasized that a large CPU gain can be expected in the case of contra-rotating open rotor aeroelasticity. However, high condition number can lead to divergence of the computations when using the multi-frequential harmonic balance approach (*Chapter 5*). This is first highlighted on two model problems and then cured using an original optimization algorithm. Finally, the convergence of the harmonic balance that was shown to be case dependent is assessed (*Chapter 6*). It is demonstrated

that the difference in convergence is linked to the thickness of the wakes observed behind turbomachinery blades, which extends to CROR blades. Based on this observation, a prediction tool is developed to estimate the number of harmonics needed to compute a given turbomachinery (and CROR) configuration using a mixing plane computation. The relative CPU gain to be expected can thus be estimated and help the decision making in choosing an unsteady approach over another one.

- Based on the work done in the second part, the proposed approach retained in this thesis, namely the multi-frequential harmonic balance method along with a weak aeroelastic coupling approach, is applied on different configurations in *Part III*. First, it is validated on a reference configuration against experimental results and other numerical approaches found in the literature (*Chapter 7*). This gives us confidence to apply the approach on an industrial isolated contra-rotating open rotor application at low-speed (*Chapter 8*) and high-speed (*Chapter 9*) flight conditions. The aeroelastic results are finally discussed based on the computed unsteady flow field.

Part I

General information

Contra-rotating open rotors

Abstract

In this chapter, we first recall the thrust and propulsive efficiency equations. Using them, the propeller engines are shown to be good candidates for efficient alternative engines, mainly due to a high bypass ratio. Geometry, general principles, similarity coefficients and main physical phenomena of such engines are described. In addition to that, it is shown that even if efficient, propeller engines suffer from a residual swirl motion. To tackle this problem, the contra-rotating open rotor technology is presented along with its main source of unsteadiness. The challenges associated to this engine are finally detailed and we show that aeroelasticity needs to be accounted for.

1.1 Generalities of propulsion

For an aircraft in steady flight conditions, lift balances weight and thrust balances drag. This explains why engineers try indefinitely to reduce weight while increasing thrust. A trade-off between both aspects is to work on the propulsive efficiency of the engine. In this section, general information on propulsion are given, that leads to the concepts of propeller and contra-rotating open rotor.

1.1.1 Thrust equation

The force applied on an engine, namely the thrust, comes from the static pressure distribution and the viscosity of the wetted areas. To compute it, we assume for simplicity that:

- the engine is schematically represented by a tube, as shown in Figure 1.1,
- the flow is steady (steady-state hypothesis),
- the viscosity effects are negligible compared to the pressure effects,
- the pressure surrounding the engine p_∞ is constant,
- the inlet pressure p_0 , the outlet pressure p_1 and the pressure surrounding the engine p_∞ are equal, meaning that the nozzle is adapted.

The problem parametrization is schematically represented in Figure 1.1. With the given hy-

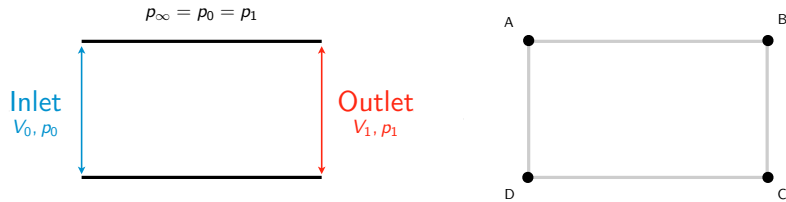


Figure 1.1: Engine parametrization for the computation of the thrust.

pothesis, the thrust, which is the resultant force projected onto the x-axis, is defined as

$$F_x = \iint_{BC+DA} p_{int} d\vec{S} - \iint_{BC+DA} p_\infty d\vec{S}, \quad (1.1)$$

where p_{int} is the internal static pressure distribution. The integral on $AB + CD$ is zero due to the projection on the x-axis. Moreover, as the surrounding pressure is constant

$$\iint_{BC+DA} p_\infty d\vec{S} = p_\infty \iint_{BC+DA} d\vec{S} = p_\infty (S_1 - S_0). \quad (1.2)$$

The distribution of internal pressure is difficult to estimate. To alleviate this, we make use of the Euler's momentum equation applied to the internal fluid

$$\iint_S (\rho \vec{V} \cdot d\vec{S}) V = \iint_S p d\vec{S} \quad (1.3)$$

The velocity being zero at walls, the left-hand side of the Eq. (1.3) simplifies to

$$\iint_S \left(\rho \vec{V} \cdot d\vec{S} \right) V = -\rho_0 V_0 S_0 V_0 + \rho_1 V_1 S_1 V_1 = \dot{m} (V_1 - V_0), \quad (1.4)$$

where \dot{m} is the mass-flow rate going through the engine. The right-hand side of Eq. (1.3), projected onto the x-axis, is equal to

$$\iint_S p d\vec{S} = \iint_{BC+DA} p d\vec{S} = p_\infty \iint_{BC+DA} d\vec{S} = p_\infty (S_1 - S_0), \quad (1.5)$$

since we consider that $p_0 = p_1 = p_\infty$. Finally the thrust F_x simplifies to

$$F_x = \dot{m}(V_1 - V_0) \quad (1.6)$$

From this simple equation, one can see that to increase the thrust F_x , there are two parameters: the mass-flow and the axial velocity increment.

1.1.2 Global propulsive efficiency

The global propulsive efficiency η measures the success in converting a mechanical power into a propulsive power. It results from the combination of the kinetic efficiency η_K and the propulsive efficiency η_{PR}

$$\eta = \eta_K \times \eta_{PR}. \quad (1.7)$$

This is schematically represented in Figure 1.2.

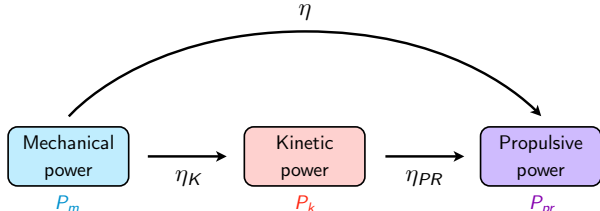


Figure 1.2: Efficiency relations from mechanical power to propulsive power.

Kinetic efficiency The kinetic efficiency measures the success in converting the mechanical power P_m into a kinetic power P_k

$$\eta_K = \frac{P_k}{P_m}. \quad (1.8)$$

The mechanical power delivered as input can be computed through the first thermodynamic principle. In fact, in absence of heat exchange, the mechanical power P_m can be estimated as

$$P_m = \dot{m}(h_{i_1} - h_{i_0}), \quad (1.9)$$

where h_i is the total enthalpy and subscript 0 and 1 are the input and output of the propulsion system, respectively, as represented in Figure 1.1. The kinetic power P_k is given by

$$P_k = \dot{m} \left(\frac{1}{2} V_1^2 - \frac{1}{2} V_0^2 \right). \quad (1.10)$$

This leads to a kinetic efficiency that can be expressed as

$$\eta_K = \frac{V_1^2 - V_0^2}{2(h_{i_1} - h_{i_0})}. \quad (1.11)$$

Propulsive efficiency The propulsive efficiency η_{PR} measures the success in creating a propulsive power P_{pr} from a kinetic power P_k

$$\eta_{PR} = \frac{P_{pr}}{P_k}. \quad (1.12)$$

The propulsive power is computed using the thrust F_x

$$P_{pr} = F_x \times V_\infty, \quad (1.13)$$

where V_∞ is the free-stream velocity. Finally, if the free-stream velocity is the inlet velocity V_0 and the inlet and outlet velocities are purely axial

$$\eta_{PR} = \frac{1}{1 + \frac{V_1 - V_0}{2V_0}}$$

(1.14)

This formula means that the most efficient engine produces a very small velocity increment.

1.1.3 Toward propeller engines

One way to improve the environmental footprint of airplanes engines is to increase the propulsive efficiency by reducing the kinetic power needed to drive the engine. According to the propulsive efficiency formula, doing so while maintaining the thrust can be achieved through a higher mass-flow rate. Two new concepts are thus derived from this simple statement: the Ultra-High Bypass Ratio (UHBR) which is basically a turbofan with a larger fan exhaust, and the propeller, the mass-flow rate of which is not limited by the architecture, as the blades are not within a nacelle. In the following section, the propeller engine will be detailed and the drawbacks of such an architecture will be highlighted to motivate the use of a second propeller row, yielding the contra-rotating open rotor architecture.

1.2 Propellers

1.2.1 Geometry

A propeller is composed of a hub and a rotating set of B blades as schematically represented in Figure 1.3. The hub is the part on which the blades are mounted. We set the diameter of these blades being D and their rotation speed being Ω . In front of the propeller, there is a spinner which is a conic element that conducts the inflow to the propeller blades. The propeller can be seen as a turbofan whose fan is not within a nacelle. This absence implies that theoretically, the mass-flow can be infinite. To quantify this, it is common for engines to consider the bypass ratio. It is defined as the ratio of the cold air (the fan exhaust) divided by the hot air (the air that goes through the engine core). To give an idea, one of the highest bypass ratio engine on today's aircraft is obtained by the Pratt & Whitney PW1000G with a 12 bypass ratio. This

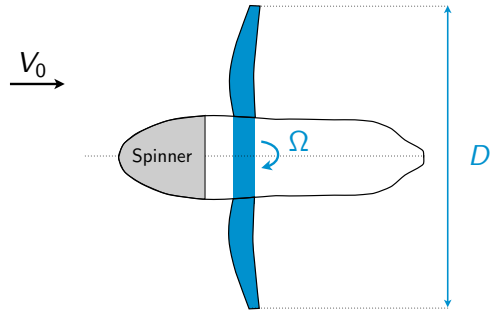


Figure 1.3: Geometry of a propeller.

number is representative of the mass-flow rate generated by the engine. However, we have seen that mass-flow and the velocity difference are the two parameters that can be used to increase the thrust. Assuming that in a classical ducted turbofan, the bypass ratio is limited to 12, the only way to further increase the thrust is to increase the velocity which deteriorates the propulsive efficiency. For the sake of comparison, propellers are estimated to have a bypass ratio of 50. This explains why this architecture has regained interest.

1.2.2 Velocity triangle

The velocity triangle applied to a propeller configuration is shown in Figure 1.4. The aim of a propeller is to create thrust through an increase of the axial velocity noted ΔV_x in the diagram. To do so, the relative flow field is straighten up. This gives both an increase in axial velocity but also in tangential velocity. In fact, the inflow that was purely axial retrieves a tangential component at the outlet. This is called the swirl and is a lost energy as it cannot be used to produce thrust. Moreover, the relative velocity W should be kept subsonic otherwise the

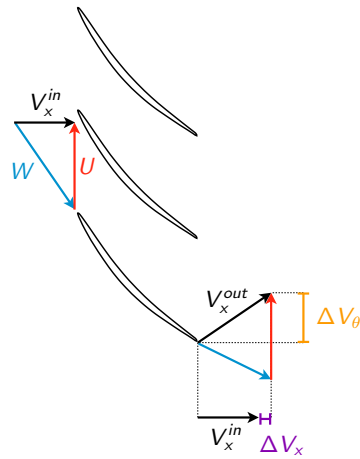


Figure 1.4: Velocity triangle applied to a propeller.

propulsive efficiency is reduced. This limits the free-stream velocity V_0 of the aircraft and the size of the propeller as the rotation speed velocity depends on the radius of the blades. This explains why propellers have been limited so far to low-speed inflow conditions.

1.2.3 Similarity coefficients

To evaluate the performance of the propeller, four similarity coefficients are commonly used: the advance ratio J that represents the operating point of the propeller, the thrust C_T and power C_P coefficients and finally the efficiency η

$$J = \frac{V_0}{nD}, \quad C_T = \frac{F_x}{\rho n^2 D^4}, \quad C_P = \frac{M_x \Omega}{\rho n^3 D^5}, \quad \eta = J \frac{C_T}{C_P}, \quad (1.15)$$

where V_0 is the free-stream velocity as shown in Figure 1.3, ρ the free-stream density, n the rotation frequency ($n = \Omega/2\pi$), F_x the thrust and M_x the axial torque. The efficiency defined here is actually the global propulsive efficiency as it gives the ratio of the propulsive power over the mechanical power.

An estimation of the variation of the advance ratio J and the efficiency η depending on the flight conditions is given by Bousquet [7]

$$(\text{cruise}) \quad 0.8 < \eta < 0.95, \quad 1 < J < 3.5 \quad (1.16)$$

$$(\text{take-off and landing}) \quad 0.5 < \eta < 0.8, \quad J < 1. \quad (1.17)$$

1.2.4 Main physical phenomena

The main physical phenomena that can be seen in a propeller are schematically represented in Figure 1.5. Firstly, due to the presence of a boundary layer on the pressure and suction

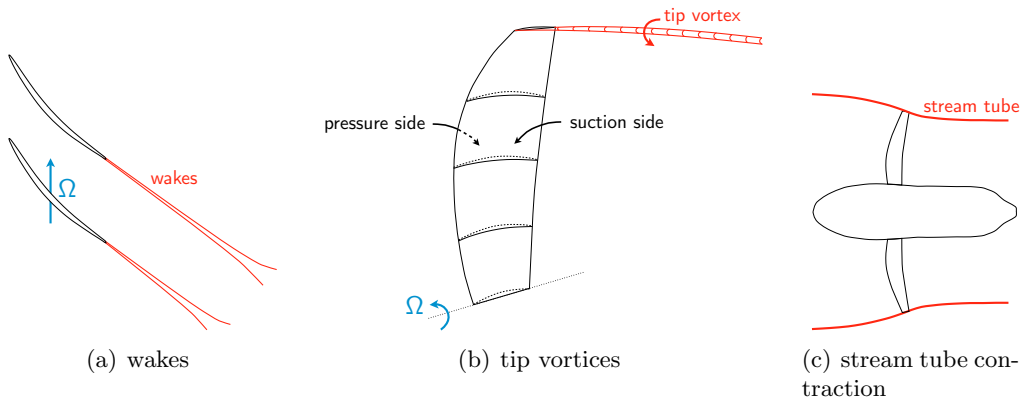


Figure 1.5: Main physical phenomena seen in a propeller.

sides of the blades, a wake is shed behind each blade, which involves a momentum deficit (Figure 1.5(a)). It is mostly a two-dimensional phenomenon seen at each radius. Secondly, in the tip region of the blade, the pressure difference between each side of the blade induces a vortex that is counter-rotating with respect to the rotation speed (Figure 1.5(b)). They are advected by the local relative velocity giving them an helical path propagating downstream. To reduce this phenomenon, one way is to modify the geometry of the tip of the blades. Finally, the propeller generates thrust through an acceleration of the fluid. Thus, the stream tube is contracted (Figure 1.5(c)). All of these phenomena are stationary in their relative frame of reference.

1.3 Contra-rotating open rotors

As shown above in a single rotor propeller, the outlet velocity is not axial yielding a residual tangential velocity ΔV_θ , which forms the swirl. This is a lost energy that deteriorates the propulsive efficiency. To recover it, a second contra-rotating rotor can be used [44]. We will see in this section through a simple velocity triangle exercise that the swirl is annulled by the second rotor. This allows to create more thrust with the same inflow conditions. The loading of the blades can thus be reduced compared to propeller blades, for a given level of thrust. This increases the propulsive efficiency for transonic flight conditions as shown by Hughes and Gazzaniga [57] and reported in Figure 1.6.

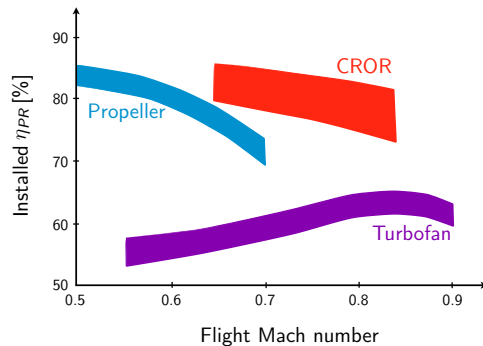


Figure 1.6: Benefit of using a contra-rotating open rotor, from Hughes and Gazzaniga [57].

1.3.1 Geometry

Figure 1.7 depicts the main geometrical parameters of a CROR. It is composed of two rotors, the first one is called the front rotor and the second one is called the rear or aft rotor. Generally, they do not have the same diameter and rotation speed. Thus, subscript f and r denotes respectively, the front and the rear parameters. The difference of diameter is called the clipping or cropping of the blades and is evaluated through the non-dimensional parameter κ

$$\kappa = \frac{D_f - D_r}{D_f}. \quad (1.18)$$

By clipping the rear rotor blades, tip vortices shed by the front rotor are not likely to hit the rear rotor. Finally, the spacing between the rotors is evaluated as the difference between the axial minimum of the rear blade minus the axial maximum of the front blade. The spacing is one of the adjustment parameters used to minimize the unsteady interaction between the rotors to reduce noise. In fact, heterogeneities are lessened along with the convection of the flow field. These heterogeneities are responsible for the unsteady interactions and, by extrapolating, for noise generation.

Two types of contra-rotating open rotors have emerged. The first type is the puller configuration, whose blades are near the front of the spinner as shown in Figure 1.8. As the name indicates, this configuration is mounted in front of the wing. It is particularly interesting as the blades will see a uniform flow. However, these all suffer from the same incidence as that of the wing. This can give large in-plane forces (forces normal to the rotation axis [33]) compared to pusher configurations. In opposite, the deflection of the flow due to the wing provides

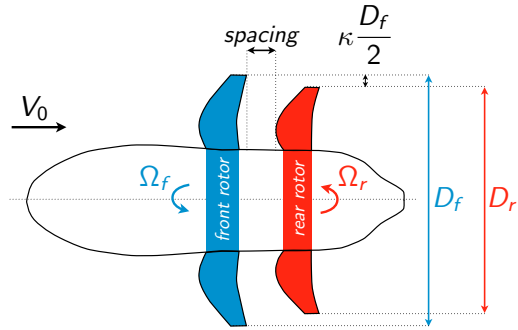


Figure 1.7: Geometry of a contra-rotating open rotor.

a smaller incidence. Moreover, the distortion generated by the CROR will disturb the flow around the wing. As one way to reduce consumption of airplanes is to have laminar wings, this configuration is less studied. The second type is the pusher configuration. It is designed to be mounted on a pylon which will thus interact with the CROR, but laminar wings might be considered with this configuration. In this work, we will deal with a pusher configuration in Chapters 8 and 9.

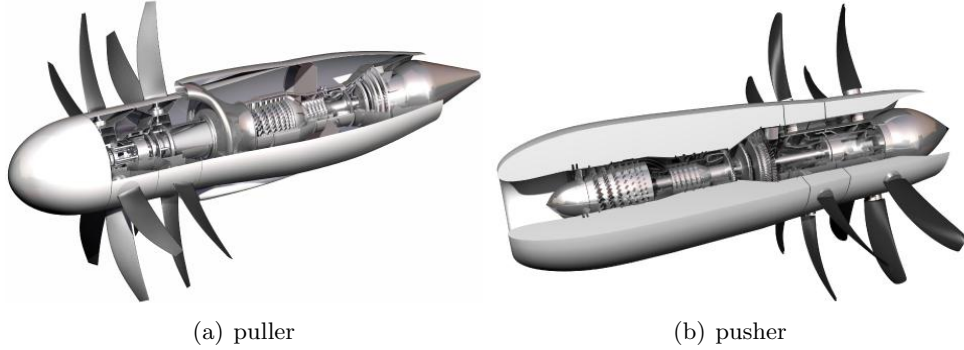


Figure 1.8: Types of contra-rotating open rotor, courtesy Rolls-Royce.

1.3.2 Velocity triangle

Figure 1.9 shows the application of the velocity triangle to a CROR configuration. The swirl energy that was lost by the propeller is now used to produce more thrust. Therefore, a CROR will finally have a better propulsive efficiency than a propeller, which explains its study as a greener engine. In the eighties, Strack et al. [95] and Hager and Vrabel [44] showed that using a contra-rotating open rotor technology over a single propeller gave an increase of 6 – 8% in propulsive efficiency, explaining its regain of interest. Today, high-speed propellers blades might lead to higher increase in efficiency while keeping a flight Mach number close to 0.8, enabling its use for commercial aviation.

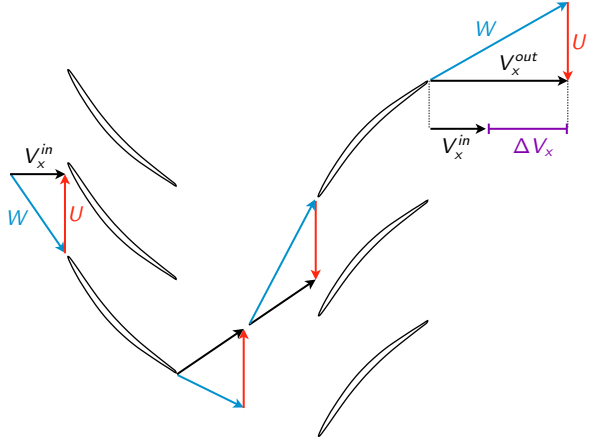


Figure 1.9: Velocity triangle applied to a contra-rotating open rotor.

1.3.3 Similarity coefficients

In the case of a CROR configuration, the front and the rear rotors have to be considered. Two main ways exist to evaluate the global value of the similarity coefficients. The first one, chosen by Béchet et al. [5] among others, is to consider that the non-dimensional parameter D , n and J are those of the front rotor for both rotors

$$J_f = J_r = \frac{V_0}{n_f D_f}, \quad C_T = \frac{F_{x_f} + F_{x_r}}{\rho_f n_f^2 D_f^4}, \quad C_P = \Omega_f \frac{M_{x_f} + M_{x_r}}{\rho_f n_f^3 D_f^5}, \quad \eta = J_f \frac{C_T}{C_P}. \quad (1.19)$$

The second one uses the non-dimensional parameter of the current rotor, as done by Stuermer [96] and Zachariadis and Hall [111]. The first approach is retained for the current work as it allows to simplify the comparison of the similarity coefficient with equivalent propellers.

1.4 Unsteadinesses

1.4.1 Unsteady effects

The flow field generated behind the front rotor is steady in its frame of reference. Nevertheless, due to the relative speed difference between the front and the rear rotors, these steady flow distortions are seen as unsteady features by the rear rotor. These unsteadinesses are correlated with the Blade Passing Frequency (BPF)

$$f_{BPF} = \frac{\Omega_{rel} B_{opp}}{2\pi}, \quad (1.20)$$

where Ω_{rel} is the relative speed difference between the current and the opposite row and B_{opp} the number of blades in the opposite row.

1.4.2 Main kinds of unsteadiness

Wakes and potential effects Compared to an isolated rotor, as for the case of a propeller, the presence of the rear rotor gives rise to an unsteady interaction by means of potential effects. In addition, wakes generated behind the front rotor interact with the rear rotor. This

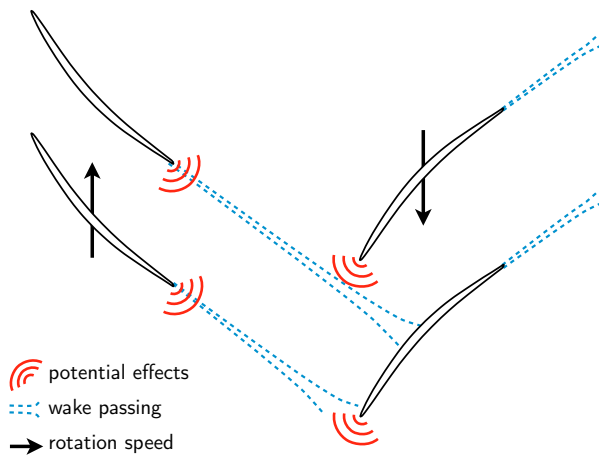


Figure 1.10: Wakes and potential effects in a contra-rotating open rotor.

is schematically represented in Figure 1.10. These two phenomena are correlated with the blade passing frequency. In addition to this, vortex shedding phenomena may occur behind the blades, the frequency of which is not known *a priori*. This phenomenon is more likely to appear behind blades with a bluff trailing edge. However, this is not a common design for industrial compressor configurations as bluff trailing edges give larger drag. Therefore, we can consider here that wake and potential effects are the main unsteady phenomena, and these are correlated with the blade passing frequency.

Non-uniform inflow and installation effects In maneuver, the CROR is in incidence with respect to the incoming flow which results in a non-uniform velocity triangle on the blades. This leads to in-plane forces, which represents an unsteady phenomenon whose frequency is correlated with the rotation frequency $\Omega/2\pi$. The presence of a pylon (installation effect) gives rise to an unsteady frequency also correlated with the rotation frequency when a pusher CROR is considered. It is important as it changes both performance and flow behavior around the CROR.

1.5 Challenges

Several challenges are still open for CROR to become a viable engine for the next generation aircraft. In this way, we classify and describe each of them in the following sections.

Classification Figure 1.11 depicts current challenges associated with CROR configurations. Three main fields are involved: Aerodynamics, Aeroacoustics and Aeroelasticity.

Aerodynamics Theoretically, the CROR is meant to have a better propulsive efficiency than a turbofan or a propeller. However, as it is a new architecture, studies need to be conducted to better understand the inherent flow physics. In particular, aerodynamic interactions between the two rotors need to be better understood.

Research on the Aerodynamics of CROR is divided in two main axes: the first axis deals with the design of CROR while the second one analyzes the unsteady flow physics that develop

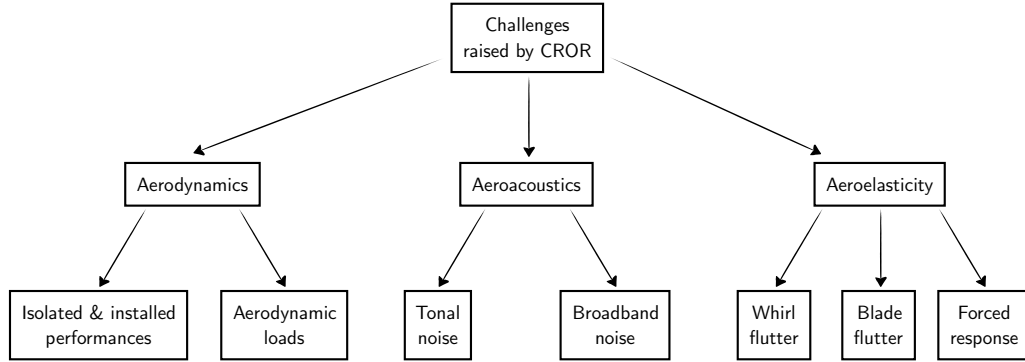


Figure 1.11: Challenges raised by contra-rotating open rotors.

on a given design.

Concerning the first axis, Hendricks [51] developed an open-rotor cycle model based on experimental performance characteristics made at NASA. This is an empiric approach that suffers from the impossibility to build new designs. Peters and Spakovszky [81] developed a similar code to design their CROR. The aeroacoustic characteristics of the final design is assessed by a full annulus unsteady simulation even though the design is based on experimental correlations. To improve the approach to design new CROR, Béchet et al. [5] used a lifting-line code to initialize a gradient optimization procedure based on mixing-plane computations. This led to a gain of almost a half point in CROR efficiency. This is more general than an empiric strategy if the mixing-plane computations are reliable to assess the performance parameters of CROR.

Concerning the second axis, Zachariadis and Hall [111] compared the performance prediction of mixing plane computations to experimental data made on an open-rotor test case. They found a fair agreement for the thrust and power coefficients, however small discrepancies on the coefficients led to significant errors on their ratio, *i.e.* the efficiency. Vion et al. [107] and Stuermer [96] used unsteady CFD computations to assess the unsteady performance and flow features. Stuermer [96] and François et al. [34] demonstrated through a code to code comparison that CFD was mature enough to estimate in-plane forces.

Aeroacoustics Lot of research efforts are put on the second challenge which is Aeroacoustics since the absence of a duct allows noise generated by CROR to propagate far away. In the late eighties, Hager and Vrabel [44] conducted at NASA a large project on innovative propulsion systems for the next generation aircrafts. The potential of the CROR configuration was identified but the noise emitted was so high that the only way thought to use such an engine was to put noise liners in the fuselage. This resulted in increased weight. This is why, today, a lot of research effort is put on the understanding and mastering of noise sources in CROR. Two main types of noise have been identified: tonal noise which comes from the interaction of both rotors and is mainly present at low-speed flight conditions (namely take-off and landing) and broadband noise which comes from turbulence and is predominant at high-speed flight conditions (namely cruise). Several CFD studies have been performed in the literature. Peters and Spakovszky [81] showed that unsteady CFD simulation is able to reproduce the aeroacoustic footprint of a CROR. They then optimized their CROR and showed that this optimized CROR design may be mature enough for noise certification. Hoffer et al. [53] and Ferrante et al. [32]

developed an efficient CFD approach to simulate the aeroacoustics of CROR. It is based on a Fourier-based time method. The approach is able to account for incidence effects which is particularly interesting considering that the noise of installed configuration is drastically different from the isolated one (see Hager and Vrabel [44]).

Aeroelasticity The third challenge is less studied in the numerical literature. Three main aeroelastic phenomena have been identified during preliminary studies during the eighties by Hager and Vrabel [44]: whirl flutter, *i.e.* the self-excited movement of the whole nacelle, blade flutter, *i.e.* the vibration of the blades, and forced response, *i.e.* the excitation of blades modes by the distortions shed by the rotors or the pylon. For a turbofan engine to achieve certification, it must be demonstrated that one released fan blade can be safely contained within the engine's fan case as written in the Certification Specifications for Engines (CSE) of the EASA:

”It must be demonstrated that any single compressor or turbine blade will be contained after Failure and that no Hazardous Engine Effect can arise as a result of other Engine damage likely to occur before Engine shut down following a blade Failure”

In the case of propellers and contra-rotating open rotors, due to the absence of a nacelle, this can not be done. To achieve certification, it must be demonstrated that the probability of a blade failure (or any failure) should not exceed 10^{-8} per propeller flight hour as written in the Certification Specifications for Propellers (CSP) of the EASA:

”It must be shown that Hazardous Propeller Effects will not occur at a rate in excess of that defined as Extremely Remote. The estimated probability for individual failures may be insufficiently precise to enable the total rate for Hazardous Propeller Effects to be assessed. For Propeller certification, it is acceptable to consider that the intent of this paragraph is achieved if the probability of a Hazardous Propeller Effect arising from an individual failure can be predicted to be not greater than 10^{-8} per Propeller flight hour. It will also be accepted that, in dealing with probabilities of this low order of magnitude, absolute proof is not possible and reliance must be placed on engineering judgment and previous experience combined with sound design and test philosophies”

This explains why aeroelasticity of contra-rotating open rotors should be assessed. Whirl flutter and forced response have been investigated in the CROR literature. The former has been assessed by Sicot and Dugeai [88] and Verley and Dugeai [103] but these studies mainly discuss the simulation tools needed to compute such a phenomenon as no experimental data are available. The latter has been investigated by Ruiz-Calavera and Perdones-Diaz [83] on installed puller propellers and by Laban et al. [63] on CROR using a strong-coupling approach.

Summary

The concept of contra-rotating open rotor has been presented along with the basic flow phenomena that develop within it. These unsteady phenomena are mostly correlated with the blade passing frequency, except for the installation effects and the non-uniform inflow. The challenges associated with this type of engine are recalled and it is highlighted that aeroelasticity of such systems remain to be accounted

for. This is why the present work will focus on aeroelasticity, which is introduced in the following chapter.

Introduction to aeroelasticity

Abstract

In this chapter, the basic elements to understand aeroelasticity in turbomachinery and by extension in contra-rotating open rotors are detailed. Firstly, the definition and the basic equations governing dynamic aeroelasticity are presented. The two main aeroelastic phenomena that develop in turbomachinery, namely forced response and flutter, are then presented. The latter is investigated in this work and the computational approach retained to simulate it, namely the weak-coupling approach, is presented. The variables that are used to quantify the flutter boundary are finally presented.

2.1 What is aeroelasticity

The study of aeroelasticity in turbomachineries takes its origin in the first engines failure during the sixties [25]. Also called dynamic aeroelasticity, it is the interaction between three forces: the aerodynamic (\mathcal{A}), the elastic (\mathcal{E}) and the inertial forces (\mathcal{I}) as shown by the Collar [20] triangle represented in Figure 2.1.

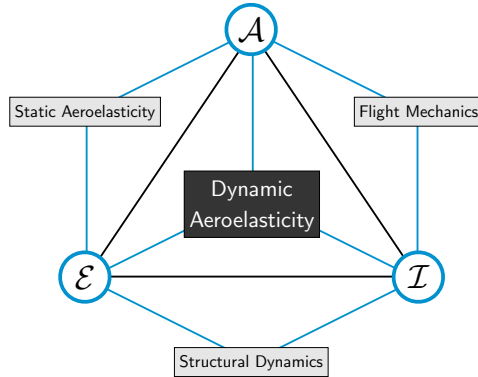


Figure 2.1: Collar triangle for dynamic aeroelasticity.

From a structural point of view, the dynamic aeroelasticity is governed by

$$M\ddot{x}(t) + D\dot{x}(t) + Kx(t) = f(t) \quad (2.1)$$

where M , D and K are the structural mass, damping and stiffness matrices, respectively. $x(t)$ and $f(t)$ denote the displacement and aerodynamic force vectors, respectively. The displacement vector is defined relatively to the steady-state position of the system. In turbomachinery and by extension in CROR, it is the steady-state position in rotation.

2.2 Main aeroelastic phenomena in turbomachinery

2.2.1 Forced response

As shown previously in Sec. 1.4, wakes and potentials effects give rise to unsteady fluctuations in CROR configurations. These fluctuations can generate large vibration levels on the blades. When the structural modes are excited by the rotation speed or its multiples, resonance can occur, hence the term forced response. The frequency associated to the rotation speed or its multiples is called Engine Order (EO). At the design phase, one step to minimize forced response is to use the Campbell diagram shown in Figure 2.2 which schematically represents such resonance. Blue points show the crossing of engine order with the blade eigenfrequencies within the operating range. The Campbell diagram does not give any information about the absolute level of vibration. Therefore, it is mostly used to rank potential designs [68]. This phenomenon will not be studied in this thesis.

2.2.2 Flutter

Flutter is defined as a self-excited, unstable self-sustained vibration. In turbomachinery, this is more likely to appear on blades. One of the most impressive manifestation of flutter occurred on

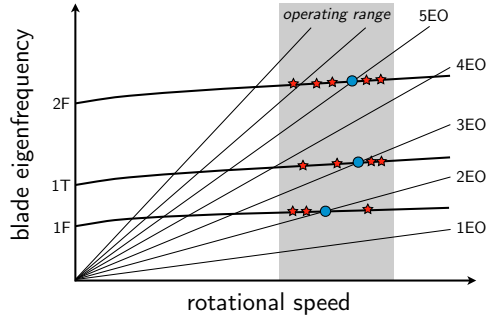
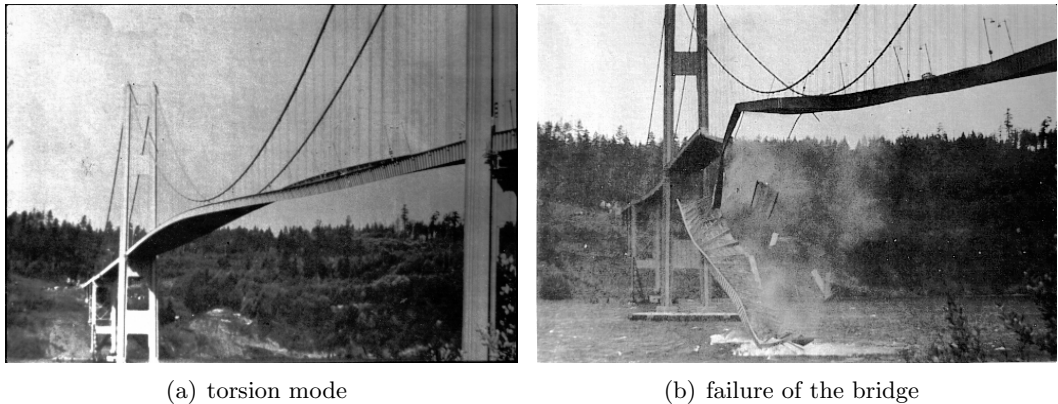


Figure 2.2: Campbell diagram with forced response (blue circles) and flutter behavior (red stars).

the Tacoma Narrows bridge in November 7th, 1940. Four months after being built, the bridge experienced torsional flutter excited by a 64 km.h^{-1} wind. The first and second torsional modes were observed. A few hours later, the bridge fell down as seen in Figure 2.3. Hopefully, no human was injured, but this event showed the importance of taking into account the flutter phenomenon as it is a very energetic event, that can lead to the failure of the system.



(a) torsion mode (b) failure of the bridge

Figure 2.3: Tacoma Narrows bridge flutter, from Smith [93].

Three vibration scenarios can appear, one leading to flutter. The first scenario is the damped (or positively damped) vibration meaning that the amplitude of the displacement decreases with respect to time, as shown in Figure 2.4(a). This is the most wanted behavior as the system tends to a stable point. In this case, the blade is said to be flutter-free for the studied mode. The second scenario is the amplified (or negatively damped) vibration, namely flutter, shown in Figure 2.4(b). This was the scenario that occurred on the Tacoma bridge. This scenario ultimately leads to failure, which is not acceptable. This is particularly critical on CROR configurations, as a blade failure might lead to the crash of the airplane as detailed in Sec. 1.5. The last scenario is the Limit Cycle Oscillation (LCO) vibration. In this scenario, the deformation increases until a certain amplitude and then stays constant. This scenario is not destructive by essence compared to the amplified scenario. However, if the blade is repetitively excited by LCO, the blade can fail because of structure fatigue.

The development of one scenario over another one is linked to the fluid response to the

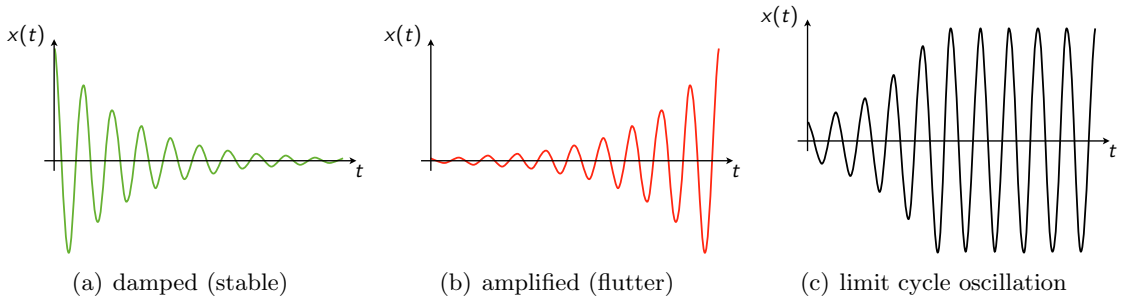


Figure 2.4: Different vibration scenarios for the flutter phenomenon.

vibration of the blade. In fact, if the aerodynamic loads projected on the direction of the displacement is positive, this means that the vibration will be amplified. In opposite, if the force is in opposed direction, the vibration will be damped. Therefore, the out-of-phase component of the aerodynamic force compared to the displacement vector will give the sign of the aerodynamic damping. The amplitude will give its strength.

In this thesis, only the flutter boundary is assessed and a weak-coupling approach is chosen as detailed in the following Section.

2.3 Computational AeroElasticity (CAE)

Solving Eq. (2.1) analytically is generally not feasible. In fact, in turbomachinery, the flow exhibits non-linear features such as turbulence, shock and boundary-layer interaction, to name but a few, that are out of reach for analytical methods.

Two main strategies exist then for solving Eq. (2.1): the strong-coupling and the weak-coupling strategies. The strong-coupling approach either solves the equation directly or two solvers are coupled to compute the aerodynamic and the structural response of the system. The strong-coupling remains computationally expensive [4] and numerically stiff [21]. This approach has been used to assess the aeroelasticity of propellers [83] and CROR [63]. However, the strong-coupling remains computationally expensive [4]. It is therefore not used in this thesis.

Conversely, the weak-coupling approach has been widely used in the turbomachinery aeroelasticity community [68]. This method uses a modal approach to identify the structural modes. These modes are then prescribed with a harmonic motion in the aerodynamic flow solver. The aerodynamic force is finally post-processed to analyze if it amplifies the motion of the blade or damps it.

2.3.1 Modal analysis

To identify the structural modes, the aerodynamic force $f(t)$ and the structural damping matrix D are considered to be zero and Eq. (2.1) becomes

$$M\ddot{x}(t) + Kx(t) = 0. \quad (2.2)$$

Considering now that the displacement vector $x(t)$ is harmonic yields the eigen-value problem

$$\det(K - \omega^2 M) = 0. \quad (2.3)$$

The solution of this equation are the modes ψ_r and their associated angular frequencies ω_r , verifying

$$(K - \omega_r^2 M) \psi_r = 0. \quad (2.4)$$

The modes define a modal basis $\Psi = [\psi_0 \psi_1 \dots \psi_n]$. Once it is identified, either by mean of a Finite Element model or an experimental identification, Equation (2.1) becomes

$$M_m \ddot{q}(t) + D_m \dot{q}(t) + K_m q(t) - \Psi^\top f(t) = 0, \quad x(t) = \Psi q(t). \quad (2.5)$$

M_m , D_m and K_m are the modal mass, damping and stiffness, respectively expressed as

$$M_m = \Psi^{-1} M, \quad D_m = \Psi^{-1} D, \quad K_m = \Psi^{-1} K, \quad \Psi^{-1} = \Psi^\top. \quad (2.6)$$

As the modes are orthogonal by definition, M_m , D_m and K_m are diagonal matrices and Equation (2.5) is a system of completely decoupled equations.

2.3.2 Structural dynamics of turbomachinery blade

The modes are classified by their global shape, among which bending/flection (noted F) and torsion (noted T) modes are the main ones. Then they are classified depending on the number of deflection lines that they include. If one deflection line is present in a flection mode, it is called 1F and 2F if two deflection lines are seen, as shown in Figure 2.5.

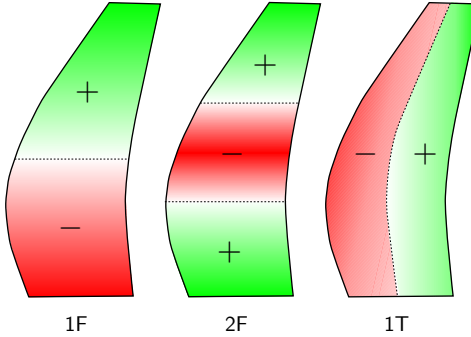


Figure 2.5: Blade mode shape nomenclature.

2.3.3 Phase theorem

In 1956, Lane [65] demonstrated for the case of small vibration amplitude, that each blade in a perfect turbomachine (no mistuning) vibrates with identical modal amplitudes with a constant Inter-Blade Phase Angle (IBPA) sometimes noted σ . According to Lane [65], the possible values for a rotor mode of B blades are

$$\boxed{\text{IBPA}[\circ] = \frac{360 \times n_d}{B}} \quad n_d \in [0, B - 1] \quad (2.7)$$

where n_d is the nodal diameter. A zero degree value IBPA means that the blades are vibrating in phase, a 180° or -180° IBPA means that the blades vibrates in phase opposition.

2.3.4 Weak-coupling approach

The modes being identified, these are prescribed with a small vibration amplitude and a harmonic motion. Due to the phase theorem, the easiest way to express the mode is to use a complex notation. The displacement vector projected on the modal basis becomes

$$\hat{x}(t) = (h_r + ih_i)e^{i\omega t}, \quad (2.8)$$

where h_r and h_i are the real and imaginary displacement modes, respectively, and ω the angular frequency. As the motion is harmonic, the fluid response is supposed to be harmonic too. In particular, the unsteady aerodynamic force $f(t)$ exerted by the fluid is due to the static pressure and can be expressed as

$$\hat{f}(t) = (p_r + ip_i)Se^{i\omega t}. \quad (2.9)$$

The damping can then be computed by considering the work per cycle W_c defined as

$$W_c = \int_0^T \dot{x}(t) \cdot f(t) dt, \quad T = \frac{2\pi}{\omega}. \quad (2.10)$$

Using the complex approach

$$W_c = \int_0^T \Re(\dot{\hat{x}}(t)) \cdot \Re(\hat{f}(t)) dt. \quad (2.11)$$

The development of this equation leads to

$$W_c = \pi S [h_r p_i - h_i p_r]. \quad (2.12)$$

According to Carta [15], the aerodynamic damping can be expressed using the work per cycle W_c , which gives

$$\text{Damping } [-] = -\frac{\pi S [h_r p_i - h_i p_r]}{2M_m \omega^2} \quad (2.13)$$

The mechanical damping D_m is difficult to estimate but is negligible compared to the aerodynamic damping [75]. Therefore, estimating only the aerodynamic damping is the discriminant test case.

2.3.5 Stability curve

The damping as a function of the IBPA, sometimes referred to as the stability or S-curve, is used to display the aeroelastic results. It is shown in Figure 2.6. The shape of this curve is known to display an S for most of the turbomachinery configurations. In our simulations, we will check that this empirical statement is observed. The negatively damped modes are said to be unstable and can be subject to flutter. The least stable modes are usually found at low IBPA.

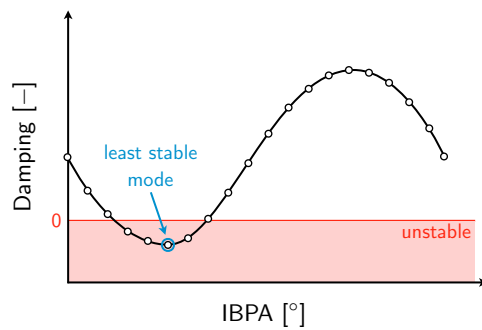


Figure 2.6: Stability curve.

Summary

Contra-rotating open rotors are made of thin rotor blades that see unsteadinesses coming from the opposite rotor. The study of the coupling between the structural displacement and the unsteady flow field is called dynamic aeroelasticity. Two approaches exist to simulate such a phenomenon: the strong-coupling and the weak-coupling. Even though strong-coupling remains more accurate, the cost of such an approach prevents its use in the industry. Therefore, the weak-coupling approach is the method that will be used in this work to assess the flutter of contra-rotating open rotors. It has been described in this chapter. The formula to compute the damping within the weak-coupling approach has been given. In the next chapter, Fourier-based time methods will be presented as they are good candidates to efficiently simulate the aeroelasticity of contra-rotating open rotors within the weak-coupling approach.

Fourier-based time methods

Abstract

The main Fourier-based time methods are presented in this chapter: the Linearized Unsteady Reynolds-averaged Navier–Stokes (LUR), the Non-Linear Harmonic (NLH), the Non-Linear Frequency Domain (NLFD) and the Harmonic Balance (HB) methods. The LUR method comes from a linearization of the governing equations while the three others are built to take into account the non-linearities. The NLH, NLFD and HB methods rely on a decomposition of the variable of interest in Fourier series. By truncating these at order N , $2N+1$ steady equations coupled by a source term are obtained. Emphasis is put on the development of the multi-frequential formulation and its mathematical background to allow multi-frequential applications. This is the case, for instance, of a pylon/rotor/rotor configuration (namely an installed pusher CROR) or a CROR with vibrating blades, which is the purpose of the current work. The applicability of these methods is demonstrated in the literature through simple test cases for which an analytical solution is known, 2D/3D academic turbomachinery configurations, industrial subsonic/transonic multi-stage applications, aeroelastic configurations and even unsteady optimization problems, proving their maturity. The cost of the methods is about $2N+1$ times the cost of a steady computation with N being the number of computed harmonics. The current study relies on the former work of Sicot [87], who initially implemented the harmonic balance method into the *elsA* code at CERFACS, and on the work of Guédene [42], who extended it to the multi-frequential framework.

3.1 Introduction

There is a large variety of Fourier-based time methods in the literature. The most used ones in the turbomachinery community will be presented in this section. In total, four Fourier-based methods are presented: the Linearized Unsteady Reynolds-averaged Navier–Stokes method (LUR), the Non-Linear Harmonic method (NLH), the Non-Linear Frequency Domain method (NLFD) and the Harmonic Balance method (HB). These names are chosen here for clarity but alternative appellations may be found sometimes. When this is the case, an effort will be made to synthesize these appellations to give a good overview of the types of Fourier-based time methods existing in the literature and their differences. Originally, these approaches have been developed to efficiently simulate unsteady periodic phenomena.

For simplicity, the key features of the methods are described for a simple non-linear partial differential equation, namely the inviscid Burger's equation written in conservative form as

$$\frac{\partial u}{\partial t} + \frac{1}{2} \frac{\partial u^2}{\partial x} = 0. \quad (3.1)$$

3.2 The Linearized Unsteady Reynolds-averaged Navier–Stokes method (LUR)

Verdon and Caspar [102] originally developed the unsteady linearized method in the framework of potential flows. Later on, Hall and Crawley [46] extended it to the Euler equations and Clark and Hall [19] applied it to the Reynolds-Averaged Navier–Stokes equations, yielding the LUR method. This method relies on a decomposition of the variables into a base part (generally the steady-state) and a small-disturbance unsteady component

$$u = \bar{u} + u', \quad (3.2)$$

where u' is considered to be a small unsteady perturbation. In his PhD thesis, Hall [45] defines small to be less than 10% of the steady flow. Injecting Eq. (3.2) into Eq. (3.1) yields

$$\frac{\partial u'}{\partial t} + \frac{1}{2} \frac{\partial}{\partial x} [\bar{u}^2 + 2\bar{u}u' + u'u'] = 0. \quad (3.3)$$

By means of linearization, *i.e.* collecting terms of equal order (equivalently $\bar{u}' = 0$) and neglecting terms of order greater than one, Eq. (3.3) can be split into a steady equation

$$\frac{1}{2} \frac{\partial \bar{u}^2}{\partial x} = 0, \quad (3.4)$$

and an unsteady first-order perturbation equation

$$\frac{\partial u'}{\partial t} + \frac{\partial}{\partial x} [\bar{u}u'] = 0. \quad (3.5)$$

There is a one-way coupling between the two equations: the steady field is first computed using Eq. (3.4) and is secondly given as an input to the perturbation equation to compute the corresponding unsteady disturbance (Eq. (3.5)). However, the computed perturbation is not used to update the steady solution. Hence the one-way coupling.

3.2.1 Mono-frequential formulation

As mentioned before, Fourier-based time methods have been developed to efficiently capture periodic phenomena. Hence, assuming that the velocity perturbation is harmonic with angular frequency ω , one can write

$$u' = \hat{u}_1 e^{i\omega t} + \hat{u}_{-1} e^{-i\omega t}, \quad (3.6)$$

with \hat{u}_1 and \hat{u}_{-1} being complex conjugates giving a real value for the perturbation. Injecting this definition into Eq. (3.5) and using the orthogonality property of the complex exponentials leads to

$$\begin{cases} i\omega \hat{u}_1 + \frac{\partial}{\partial x} [\bar{u}\hat{u}_1] &= 0, \\ -i\omega \hat{u}_{-1} + \frac{\partial}{\partial x} [\bar{u}\hat{u}_{-1}] &= 0. \end{cases} \quad (3.7)$$

Finally a pseudo-time τ is added to time-march Eq. (3.4) and Eq. (3.7) to the steady-state, giving three equations in total

$$\boxed{\begin{cases} \frac{\partial \bar{u}}{\partial \tau} + \frac{\partial \bar{u}^2}{\partial x} &= 0, \\ \frac{\partial \hat{u}_1}{\partial \tau} + i\omega \hat{u}_1 + \frac{\partial}{\partial x} [\bar{u}\hat{u}_1] &= 0, \\ \frac{\partial \hat{u}_{-1}}{\partial \tau} - i\omega \hat{u}_{-1} + \frac{\partial}{\partial x} [\bar{u}\hat{u}_{-1}] &= 0 \end{cases}} \quad (3.8)$$

3.2.2 Extension to the Navier–Stokes equations

To extend the LUR method to the Reynolds-Averaged Navier–Stokes equations, one has to consider their linearized counterpart. The reader is referred to the paper of Clark and Hall [19] for a detailed development of the LUR method for the Navier–Stokes equations.

3.2.3 Numerical cost

As the method is based on three equations in total, one steady equation (namely a classical RANS equation) and two perturbation equations, if $\$_{RANS}$ denotes the CPU and memory cost of one steady computation, then the cost of the LUR method can be estimated as

$$\$_{LUR} = 3 \times \$_{RANS}. \quad (3.9)$$

In practice, only two computations are performed since the steady computation is usually available beforehand.

3.3 The Non-Linear Harmonic method (NLH)

Originally developed by He and Ning [49] and Ning and He [79], the NLH method relies on a decomposition of the conservative variables into a time-averaged part plus an unsteady perturbation

$$u = \bar{u} + u', \quad (3.10)$$

where $\bar{\cdot}$ denotes the time-averaging operator and \cdot' its unsteady perturbation counterpart. By injecting Eq. (3.10) into Eq. (3.1), one gets

$$\frac{\partial u'}{\partial t} + \frac{1}{2} \frac{\partial}{\partial x} [\bar{u}^2 + 2\bar{u}u' + u'u'] = 0. \quad (3.11)$$

The equation for the time-averaged part can be obtained by time-averaging Equation (3.11)

$$\frac{\partial}{\partial x} [\bar{u}^2 + \bar{u}'u'] = 0, \quad (3.12)$$

The term $\bar{u}'u'$ accounts for the non-linearities of the considered equations. This term reflects the influence of the unsteady contribution to the time-average, which was neglected in the LUR approach. It is called the non-linear (or the deterministic) stress terms, by analogy with the Reynolds stress terms. The equation for the unsteady perturbation is then obtained by keeping the first-order terms of the unsteady Eq. (3.11). This means that the term $u'u'$ is neglected, yielding

$$\frac{\partial u'}{\partial t} + \frac{\partial}{\partial x} [\bar{u}u'] = 0. \quad (3.13)$$

Note that neglecting the high-order terms (namely $u'u'$ for the Burger's equation) is almost similar to linearizing the equation. However, in the NLH approach, the time-averaged $\bar{u}'u'$ of $u'u'$ is kept in Equation (3.12) which accounts for a part of the non-linearities. Thus, the method is not linear. Equations (3.12) and (3.13) are simultaneously solved, leading to a two-way coupling.

3.3.1 Mono-frequential formulation

Up to now, no assumption has been made neither on the velocity u , nor on its time-averaged part or unsteady perturbation part. Assuming now that the velocity perturbation is periodic in time with period $T = 2\pi/\omega$, the unsteady perturbation can be decomposed into a Fourier series

$$u' = \sum_{\substack{k=-\infty \\ k \neq 0}}^{\infty} \hat{u}_k e^{i\omega kt}, \quad (3.14)$$

where the $k = 0$ term is omitted as it is accounted for in the \bar{u} part. The complex exponentials family forming an orthogonal basis, we retrieve for all harmonics $-\infty \leq k \leq \infty$, $k \neq 0$

$$i\omega k \hat{u}_k + \frac{\partial}{\partial x} [\bar{u} \hat{u}_k] = 0, \forall k. \quad (3.15)$$

Each one of harmonic Eq. (3.15) represents now a steady-flow-like equation as no temporal derivative is present anymore.

The term $\bar{u}'u'$ remains in the time-averaged Equation (3.12) and needs to be computed. It can be directly worked out when the harmonics are known from Eq. (3.15)

$$\begin{aligned} u'u' &= \left[\sum_{\substack{k=-\infty \\ k \neq 0}}^{\infty} \hat{u}_k e^{i\omega kt} \right] \left[\sum_{\substack{k=-\infty \\ k \neq 0}}^{\infty} \hat{u}_k e^{i\omega kt} \right] \\ &= \sum_{\substack{k=-\infty \\ k \neq 0}}^{\infty} (\hat{u}_k)^2 e^{i2\omega kt} + 2 \sum_{\substack{k,j=-\infty \\ k \neq j \neq 0}}^{\infty} \hat{u}_k \hat{u}_j e^{i\omega(k+j)t}. \end{aligned} \quad (3.16)$$

Thus, the time-average becomes

$$\begin{aligned}\overline{u'u'} &= \frac{1}{T} \int_{t=0}^T \left[\sum_{\substack{k=-\infty \\ k \neq 0}}^{\infty} (\hat{u}_k)^2 e^{i2\omega kt} + 2 \sum_{\substack{k,j=-\infty \\ k \neq j \neq 0}}^{\infty} \hat{u}_k \hat{u}_j e^{i\omega(k+j)t} \right] dt \\ &= \frac{2}{T} \int_{t=0}^T \sum_{\substack{k,j=-\infty \\ k \neq j \neq 0}}^{\infty} \hat{u}_k \hat{u}_j e^{i\omega(k+j)t} dt,\end{aligned}\tag{3.17}$$

as the first term is periodic with a zero mean value. Moreover, this holds true for the terms $j \neq -k$. Therefore, Equation (3.17) becomes

$$\overline{u'u'} = \frac{2}{T} \int_{t=0}^T \sum_{\substack{k=-\infty \\ k \neq 0}}^{\infty} \hat{u}_k \hat{u}_{-k} dt.\tag{3.18}$$

As \hat{u}_k and \hat{u}_{-k} are complex conjugates, $\overline{u'u'}$ is finally equal to

$$\overline{u'u'} = 2 \sum_{\substack{k=-\infty \\ k \neq 0}}^{\infty} |\hat{u}_k|^2.\tag{3.19}$$

This last equation depends only on the computed harmonics, meaning that no term is modeled. Moreover, this term couples the time-average solution with the unsteady perturbation and takes into account a part of the non-linearities of the considered equation, which makes a great difference with the LUR approach presented in Sec. 3.2.

Finally, as computing an infinite number of harmonics is numerically not feasible, it is truncated at order N . This is a fair assumption as, for most of the physical flows, the energy is concentrated on a finite number of frequencies. Moreover, the goal of Fourier-based time methods is to have a compact representation of the unsteady time signals. As for a mesh grid convergence, the number of harmonics N will directly impact the accuracy of the unsteady representation of the signal. The discussion on the convergence of Fourier-based time methods will be introduced mathematically in Sec. 3.6 and discussed later on in this work in Chap. 6.

To summarize, the NLH method applied to Eq. (3.1) gives $2N$ perturbation equations and one time-averaged equation making $2N+1$ equations in total. A pseudo-time (τ) derivative is added to march the equations in pseudo-time to the steady-state solution of all the harmonics

$$\begin{cases} \frac{\partial \bar{u}}{\partial \tau} + \frac{\partial}{\partial x} [\bar{u}^2 + \overline{u'u'}] = 0, \\ \frac{\partial \hat{u}_k}{\partial \tau} + i\omega k \hat{u}_k + \frac{\partial}{\partial x} [\bar{u} \hat{u}_k] = 0, \quad k \in [-N, N], \quad k \neq 0 \end{cases}\tag{3.20}$$

The equations are coupled by the deterministic stress term $\overline{u'u'}$ defined in Eq. (3.19). The term $u'u'$ is neglected in this formulation.

3.3.2 Multi-frequential formulation

He et al. [50] extended the method to a multi-frequential formulation. Instead of writing the perturbation using a Fourier series as defined in Eq. (3.14), it is written using a sum of

harmonics each of which having an angular frequency ω_k

$$u' = \sum_{\substack{k=-N \\ k \neq 0}}^N \widehat{u}_k e^{i\omega_k t}. \quad (3.21)$$

Note that the term $k\omega$ in Eq. (3.14) is now replaced by ω_k meaning that the frequencies can be chosen arbitrarily. The derivation of the equations is kept the same and the following $2N + 1$ subset of equations is finally obtained

$$\begin{cases} \frac{\partial \bar{u}}{\partial \tau} + \frac{\partial}{\partial x} [\bar{u}^2 + \bar{u}' u'] = 0, \\ \frac{\partial \widehat{u}_k}{\partial \tau} + i\omega_k \widehat{u}_k + \frac{\partial}{\partial x} [\bar{u} \widehat{u}_k] = 0, \quad k \in [-N, N], \quad k \neq 0 \end{cases} \quad (3.22)$$

However, as the complex exponentials ($e^{i\omega_k t}$) do not form an orthogonal basis, writing Eq. (3.22) for each harmonic $k \in [-N, N]$, $k \neq 0$ is mathematically not true. He et al. [50] argued that the terms are collected for each harmonic. The same development is made by Vilmin et al. [104].

The coupling deterministic stress term is evaluated using the same equation as for the mono-frequential formulation

$$\overline{u' u'} = 2 \sum_{\substack{k=-\infty \\ k \neq 0}}^{\infty} |\widehat{u}_k|^2. \quad (3.23)$$

To give a mathematical framework to prove this assertion, let us consider the specific example of u' taken as

$$u' = (\widehat{u}_{-1} e^{-it} + \widehat{u}_1 e^{it}) + (\widehat{u}_{-2} e^{-i\pi t} + \widehat{u}_2 e^{i\pi t}), \quad (3.24)$$

namely, we consider Eq. (3.21) with the specific angular frequencies: $\omega_1 = 1$ and $\omega_2 = \pi$. The cross-term $u' u'$ is then equal to

$$\begin{aligned} u' u' &= (\widehat{u}_{-1})^2 e^{-2it} + (\widehat{u}_1)^2 e^{2it} + (\widehat{u}_{-2})^2 e^{-2\pi t} + (\widehat{u}_2)^2 e^{2\pi t} \\ &\quad + 2 \left[\widehat{u}_{-1} \widehat{u}_{-2} e^{i(-1-\pi)t} + \widehat{u}_{-1} \widehat{u}_2 e^{i(-1+\pi)t} + \widehat{u}_1 \widehat{u}_{-2} e^{i(1-\pi)t} + \widehat{u}_1 \widehat{u}_2 e^{i(1+\pi)t} \right] \\ &\quad + 2\widehat{u}_{-1} \widehat{u}_1 + 2\widehat{u}_{-2} \widehat{u}_2. \end{aligned} \quad (3.25)$$

In the mono-frequential framework, the frequencies are harmonically related and a common period T exists. This logically leads to the definition of the mean value \bar{f} of such a time-varying function $f(t)$ as

$$\bar{f} = \frac{1}{T} \int_0^T f(t) dt. \quad (3.26)$$

In the current multi-frequential example, π and 1 are not integer multiples of a common fundamental frequency. For this specific example, a common period T does not exist. Besicovitch [6] defines a mathematical framework for such functions, called almost-periodic functions. In this framework the temporal mean value is shown to exists. It is defined as

$$\bar{f} = \lim_{X \rightarrow \infty} \frac{1}{X} \int_0^X f(t) dt. \quad (3.27)$$

Applying the time-averaged operator to Eq. (3.25) yields

$$\overline{u' u'} = 2(\widehat{u}_{-1}\widehat{u}_1 + \widehat{u}_{-2}\widehat{u}_2) = 2(|\widehat{u}_1|^2 + |\widehat{u}_2|^2), \quad (3.28)$$

as the mean value of purely harmonic functions is zero. Extending this demonstration to the arbitrary case of a multi-frequential perturbation (Eq. (3.21)) leads to the general expression given in Eq. (3.23).

3.3.3 Extensions

Navier–Stokes equations As shown above, since the development of the NLH method is made in the frequency domain, applying the method to complex equations can be difficult. For the Navier–Stokes equations, this step is tedious due to the number of equations to treat. Nevertheless, Chen et al. [17], He and Ning [49], He et al. [50] and Vilmin et al. [104] have done this and the reader is referred to these papers for a detailed description. Note that in all those publications, turbulence is modeled using only the time-averaged quantities. This is another assumption as the turbulent field, in a wake for instance, is seen unsteady in the opposite row frame of reference [64]. Thus, this unsteadiness is not taken into account by the NLH method.

Turbomachinery computations Originally, the NLH method has been developed for turbomachinery applications. He and Ning [49] and Ning and He [79] computed isolated turbomachinery configurations. To reduce the domain to a single blade-to-blade passage, they consider a periodic boundary condition for the time-averaged part and a phase-lagged boundary condition for the perturbation part on the azimuthal boundaries

$$\begin{aligned} \bar{u}_U &= \bar{u}_L, \\ u'_U &= u'_L e^{i\sigma}, \end{aligned} \quad (3.29)$$

where subscripts U and L denote the upper and the lower boundaries, respectively, and σ is the inter-blade phase angle. This allows to compute isolated vibrating configurations thanks to the phase theorem of Lane [65] (see Sec. 2.3.3).

Chen et al. [17] added a rotor/stator treatment to allow the computation of stage configurations. To do so, the perturbation u' is exchanged at the interface using an azimuthal Fourier transform, whereas the time-average field \bar{u} and the deterministic stresses $\overline{u' u'}$ are azimuthally flux-averaged. To this aim, the azimuthal variations of the perturbation $\widehat{u}(\theta_i)$ are spatially Fourier transformed (\widetilde{u}_i) and exchanged at the interface ($\widetilde{u}_i = \widetilde{u}_j$). Subscript i and j denotes, respectively, the upstream and the downstream rows. This is schematically represented in Figure 3.1. Still the method is restricted to mono-frequential problems, since only one stage

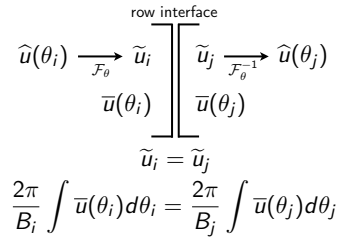


Figure 3.1: Exchange of the variables at rows interface as described by Chen et al. [17].

is considered, each row seeing the opposite blade passing frequency. Considering the time-averaged field to be constant in the azimuthal direction at the interface seems fair (in case without clocking effects), but there is no reason for $\overline{u'u'}$ to be so.

He et al. [50] extended the method to take into account multi-stage configurations through the development of a multi-frequential formulation. In fact, in such applications, a sandwiched row will see unsteadinesses coming from the upstream row (mainly wake effects) and potential effects from the downstream rows. In the general case where the surrounding rows do not have the same blade passing frequencies, multiple frequencies can be present in the current row. The same treatment is used at the rows interfaces meaning that the time-averaged quantities are flux-averaged and the fluctuations are exchanged through their azimuthal Fourier transform.

Vilmin et al. [104] extended the rotor/stator interface to a non-matching join sliding mesh interface which leads to the continuity of the unsteady flow field at the interface. The main difference with the previous treatment is that \bar{u} and $\overline{u'u'}$ are not flux-averaged but rather spatially Fourier transformed, which leads to the continuity of u at the interface, when the number of harmonics is sufficient.

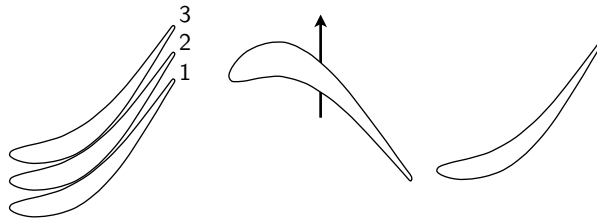


Figure 3.2: Different clocking positions for a stator/rotor/stator configuration.

Clocking effect Figure 3.2 shows three different clocking positions (sometimes also referred to as the indexing positions) of the first stator in a stator/rotor/stator configuration. In this figure, the first clocking position is aligned with the second stator. The second and the third clocking positions are not aligned with the second stator, which may give different level of perceived unsteadiness by the second stator. At a design phase, the engineer can choose any relative position of the rows and thus any clocking position. The relative position of both stator is of prior interest to choose the best clocking position. In fact, the wakes that are shed behind the first stator are cut by the rotor blades and transmitted to the second stator row. The stators being fixed, the wake of the first stator is seen as a stationary wave in the second stator. Hence, the importance of their relative position. For instance, Huber et al. [56] showed that on their 1.5 stage turbine, the variation of efficiency due to clocking position was equal to 0.8% of efficiency points, showing the importance of the clocking effect.

The brute force approach to compute the clocking effect on a configuration is to consider all the relative positions. This means that the geometry of the stator should be rotated for each new clocking position and hence a new unsteady computation should be run. The innovative procedure proposed by He et al. [50] is to consider the clocking effect as a steady wave. In fact, as both stator are fixed, a steady perturbation shed behind the first stator is still steady in the second stator. In terms of frequencies, a steady perturbation can be assimilated to a zero frequency mode. In He et al. [50] and Vilmin et al. [105], a perturbation with a zero frequency is thus additionally computed. The clocking effect can then be evaluated by post-processing the Fourier coefficient of the zeroth frequency mode. Recently, the computation of clocking

effects on arbitrary configurations has been made possible by Vilmin et al. [106]. This allows its use for pylon/rotor/rotor applications for instance, which is the configuration encountered in an installed CROR.

3.3.4 Numerical cost

Compared to the LUR method, the number of equations to solve is not constant here. In fact, if N denotes the number of harmonics computed in total (sum of the number of computed harmonics per perturbations) and if $\$_{\text{RANS}}$ denotes the CPU and memory cost associated to one steady computation, $2N$ harmonic equations and one time-average equation are solved, thus

$$\$_{\text{NLH}} = (2N + 1) \times \$_{\text{RANS}}. \quad (3.30)$$

However, Vilmin et al. [104] do not apply the NLH formulation to the turbulent equation (in their case, the one equation of Spalart and Allmaras [94]). Therefore, as only five equations are solved using the NLH approach, the turbulent equation being solved as a steady one, the cost becomes

$$\$_{\text{NLH}} = \frac{5 \times (2N + 1) + 1}{6} \times \$_{\text{RANS}}. \quad (3.31)$$

3.4 The Non-Linear Frequency Domain method (NLFD)

Originally proposed by McMullen et al. [71], the NLFD method relies on a simple observation: to develop Fourier-based time methods, and in particular the NLH method, one has made use of the Fourier series to efficiently represent an unsteady signal. This representation has then been used to develop the unsteady equation into $2N + 1$ steady equations: one time-averaged equation and $2N$ perturbation equations, where N denotes the number of harmonic kept to compute the solution. The problem is that the equations need to be resolved in the frequency domain meaning that all the numerical techniques should be adapted: the numerical schemes, the turbulent models and so on. The original idea proposed by McMullen et al. [71] is to make use of the fast Fourier Transform and its inverse to allow an easy implementation of the method into a classical time-domain solver.

3.4.1 Mono-frequential formulation

To explain the development of this method, let us first write Eq. (3.1) in the more general form

$$\frac{\partial u}{\partial t} + R = 0, \quad (3.32)$$

with

$$R = \frac{1}{2} \frac{\partial u^2}{\partial x}. \quad (3.33)$$

Consider now that both u and R are periodic in time with respect to period $T = 2\pi/\omega$ and can be written using Fourier series

$$\begin{aligned} u(t) &= \sum_{k=-\infty}^{\infty} \hat{u}_k e^{ik\omega t}, \\ R(t) &= \sum_{k=-\infty}^{\infty} \hat{R}_k e^{ik\omega t}. \end{aligned} \quad (3.34)$$

Note that decomposing $R(t)$ into a Fourier series is equivalent to use the Fourier decomposition of $u(t)$ and express $R(t)$ using the Fourier coefficients \hat{u}_k of u since the cross-terms that may arise are also expressed using the same complex exponentials. This comes from the fact that multiplying a complex exponential with another complex exponential just forms a new one at the power of the sum of the two. Injecting these decompositions into Eq. (3.32) and taking into account the orthogonality of the complex exponentials yields

$$ik\omega \hat{u}_k + \hat{R}_k = 0, \quad k \in [-\infty, \infty]. \quad (3.35)$$

As previously, only a small number of harmonics N is kept and a pseudo-time (τ) derivative is added to march the equations in pseudo-time to the steady-state solutions of all the harmonics

$$\frac{\partial \hat{u}_k}{\partial \tau} + ik\omega \hat{u}_k + \hat{R}_k = 0, \quad k \in [-N, N]$$

(3.36)

The fact that $R(t)$ is expressed using its own Fourier series makes it simpler to implement as it avoids developing its expression using the complex coefficients \hat{u}_k . However, \hat{R}_k must be evaluated. To do so, McMullen et al. [71] propose to use an Inverse Fast-Fourier Transform (IFFT) to get $u(t)$ from \hat{u}_k , as depicted in Figure 3.3. Then the considered governing equations are used to evaluate $R(t)$ which leads to \hat{R}_k through a Fast-Fourier Transform (FFT). Finally, the next iteration value \hat{u}_k is evaluated by adding \hat{R}_k and the corresponding temporal derivative $ik\omega \hat{u}_k$. All harmonics are coupled through the IFFT and FFT operations that needs all of the former to compute the counterpart temporal signal, hence the coupling. Moreover, in the non-viscous Burger's equation framework, the term $u'u'$ is no-longer neglected compared to the NLH approach and the computation of the deterministic stress terms is encompassed by the FFT and IFFT operations.

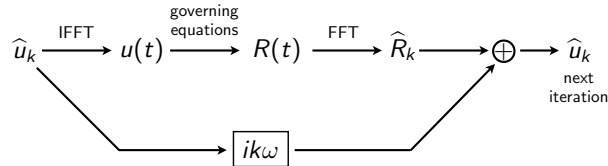


Figure 3.3: Simplified diagram of the computation of \hat{R}_k from \hat{u}_k for the non-linear frequency domain method.

3.4.2 Extensions

Navier–Stokes equations The Navier–Stokes equations can be written in finite-volume, semi-discrete form as

$$V \frac{dW}{dt} + R(W) = 0, \quad (3.37)$$

where V is the volume of the cell and W the vector of the average conservative variables over the control volume. This formulation is similar to Eq. (3.32) meaning that nothing particular has to be made to derive this approach for the Navier–Stokes equations. This is indeed attractive as the method can be applied almost directly, except for the FFT and IFFT step that should be added into the pseudo-time loop.

Aeroelastic computations Since both the structural and the aerodynamic equations are prone to time-periodic unsteadinesses, Kachra and Nadarajah [60] extended the NLFD approach to the strong-coupling of aeroelasticity within the two-dimensional Euler equations framework. Both the fluid dynamics and the structural equations are solved using the NLFD approach. They are coupled together every 15 multigrid cycles. A 2D plunging and pitching airfoil is considered. They demonstrate that with a one-harmonic NLFD computation, the flutter boundary of a NACA64A010 airfoil is correctly predicted. This leads to a gain of one order of magnitude compared to a classical time-marching procedure.

Gradient-based method to determine the frequency McMullen et al. [71] applied the NLFD to a cylinder vortex shedding. This could be done as the frequency of the vortex shedding was known *a priori* from experimental and numerical data. Note that this supposes that the numerical and the experimental vortex shedding frequencies are equal, which is generally not true [61]. However, for a given cylinder, it is generally not possible to know this frequency *a priori*. This is why McMullen et al. [72, 73] proposed a gradient based method for determining the frequency of a periodic phenomena where the frequency is unknown *a priori*. They argue that the frequency domain formulation helps forming a gradient operator to find the period T based on the minimization of the residuals of the unsteady equations. They applied their algorithm to find the frequency of the vortex shedding around a cylinder, and found it with a 3.5% accuracy compared to experimental data. Nevertheless, as a gradient method is used, a good initial guess is needed for the algorithm to converge. This limits the method to well-known unsteady problems. Moreover, the prior interest of the NLFD method is to reduce the cost compared to a classical time-marching scheme to solve the unsteady periodic problem. One may ask if applying the NLFD with a gradient based method is not finally more costly than a classical time-marching scheme.

Optimum shape design Nadarajah et al. [78] compared an optimum shape design strategy for pitching airfoils using both a classical time-marching scheme and the NLFD scheme within the Euler equations framework. It is shown that the NLFD method gives the same accuracy for the gradient and the optimum with only three time instants (namely $N = 1$) compared to 23 time instants needed for the time-marching approach. Nadarajah and Jameson [77] extended it to the three-dimensional Navier–Stokes equations. A wing undergoing a change in angle of attack as a function of time is computed and it is demonstrated that five instants (namely $N = 2$) are sufficient to provide accurate results. Tatossian et al. [97] applied it to

the aerodynamic shape optimization of hovering rotor blades in the Euler framework. The capability of their shape optimization process to redesign the Caradonna–Tung experimental blade is assessed and gives a proof of concept.

Adaptive method The problem of Fourier-based time methods is that the higher the number of computed harmonics, the higher the corresponding CPU and memory cost. There is thus a need to optimize the chosen number of harmonics. Mosahebi and Nadarajah [76] implemented an adaptive NLFD approach named the p-NLFD. Based on the energy of the last mode compared to the whole spectrum, the number of harmonics is increased if a fixed threshold is not reached. The novelty of the approach is that the number of harmonics can also decrease. This gives a speed-up of 2 in terms of CPU cost and memory reduction for the case of a vortex-shedding behind a cylinder, the frequency of which being known *a priori*.

3.4.3 Numerical cost

The NLFD method is close to the NLH approach in terms of number of equations solved. However, at each time-step, a fast Fourier transform is performed to cast back the harmonics into the time-domain in order to compute the residual $R(t)$. McMullen and Jameson [70] argue that the cost of the fast Fourier transform is less than the cost of the spatial derivatives. Kachra and Nadarajah [60] quantitatively estimate it to be approximately 2% of the cost of one iteration, which is negligible. Based on this affirmation, one can say that if $\$_{RANS}$ denotes the CPU and memory cost of one steady computation, the cost of the NLFD method can be approximated by

$$\$_{NLFD} = (2N + 1) \times \$_{RANS}. \quad (3.38)$$

This evaluation of the cost is confirmed using numerical simulations by McMullen et al. [72].

3.5 The Harmonic Balance method (HB)

The HB method has been originally proposed by Hall et al. [47], at that time named Harmonic Balance Technique (HBT). It can be considered as an improvement of the NLFD approach. In fact, instead of using the fast Fourier transform to cast back the equations to the time domain at each pseudo-iteration step, the equations are mathematically derived to be directly computed into the time-domain. To explain the method, we will again use the general form of the non-viscous Burger's equation as defined in Eq. (3.32). This study relies on the former work of Sicot [87] who implemented the harmonic balance method into the *elsA* [12] CFD code at CERFACS. Recently Guédene [42] extended it to the multi-frequential formulation, allowing contra-rotating open rotor aeroelastic computations. This is why this approach will be used in the current work.

3.5.1 Mono-frequential formulation

Following the same approach as the non-linear frequency domain one, it is considered that both u and R are periodic in time with respect to period $T = 2\pi/\omega$ and can be written using

Fourier series

$$\begin{aligned} u(t) &= \sum_{k=-\infty}^{\infty} \hat{u}_k e^{ik\omega t}, \\ R(t) &= \sum_{k=-\infty}^{\infty} \hat{R}_k e^{ik\omega t}. \end{aligned} \quad (3.39)$$

Injecting Eq. (3.39) into Eq. (3.32), and considering the orthogonality of the complex exponentials

$$ik\omega \hat{u}_k + \hat{R}_k = 0, \quad k \in [-N, N]. \quad (3.40)$$

In the same way as one uses Fourier coefficients to evaluate the temporal signal, one can reconstruct the Fourier coefficients using temporal evaluations. These are taken at evenly-spaced time instances sampling the period $T = 2\pi/\omega$. Moreover, according to the Nyquist-Shannon [86] sampling theorem, at least $2N$ time instances are needed to capture N frequencies. Actually $2N + 1$ time instances are used to prevent odd-even decoupling as demonstrated by van der Weide et al. [101]. \hat{u}_k can thus be expressed as a function of $u(t)$, using the inverse Fourier transform

$$\hat{u}_k = \frac{1}{2N+1} \sum_{n=0}^{2N} u(t_n) e^{-ik\omega t_n}. \quad (3.41)$$

If E denotes the matrix composed of the elements $(E)_{k,n} = e^{-i(k-N)\omega t_n}/2N+1$, one can write \hat{u}_k and \hat{R}_k as

$$\begin{aligned} \hat{u}_k &= Eu^*, \\ \hat{R}_k &= ER^*, \end{aligned} \quad (3.42)$$

where u^* and R^* denote the vectors formed of all the evaluations of u and R , respectively, made at $2N + 1$ time instances uniformly sampling the period of interest

$$\begin{aligned} u^* &= [u(t_0) \cdots u(t_{2N})], \\ R^* &= [R(t_0) \cdots R(t_{2N})]. \end{aligned} \quad (3.43)$$

E can thus be named the Fourier matrix. Note that conversely, using the inverse Fourier matrix E^{-1}

$$\begin{aligned} u^* &= E^{-1} \hat{u}_k \\ R^* &= E^{-1} \hat{R}_k. \end{aligned} \quad (3.44)$$

Injecting the matrix formulation of Eq. (3.42) in Eq. (3.40) gives

$$i\omega K E u^* + E R^* = 0, \quad (3.45)$$

where K is a diagonal matrix formed of all the $k \in [-N, N]$. Note that first, the matrix formulation encompass all harmonics $k \in [-N, N]$ and second, it does not require the orthogonality

of the complex exponentials. Now multiplying the equation by the inverse Fourier matrix E^{-1}

$$i\omega E^{-1}KEu^* + R^* = 0, \quad (3.46)$$

where R^* can now be substituted

$$i\omega E^{-1}KEu^* + \frac{\partial}{\partial x} \frac{(u^*)^2}{2} = 0. \quad (3.47)$$

What happened here is that instead of developing $R(t)$ in the frequency domain as made with the NLH approach, which is tedious, this term is kept in this form through all the development process. Since $R(t)$ only includes spatial derivatives, no temporal non-linear terms arise by using the Fourier decomposition. Thus, multiplying it by the inverse Fourier matrix leads to the unity matrix. $R(t)$ is then simply evaluated at $2N + 1$ time instances.

This approach is really close to the NLFD method. The higher order perturbation terms are taken into account in the equations. However, as the development is on the equations and not during the time loop, we get $2N + 1$ steady equations, by definition in the time domain, that are coupled by a source term. The source term appears as a spectral operator defined as

$$D_t = i\omega E^{-1}KE. \quad (3.48)$$

To compute D_t , Hall et al. [47] inverse the Fourier matrix E . In an easier way, Gopinath and Jameson [39] provided an analytical formulation of the source term defined in Eq. (3.48) and renamed the HB approach the Time Spectral Method (TSM). It is a matrix operator whose elements are defined as

$$(D_t)_{k,n} = \begin{cases} \frac{\pi}{T}(-1)^{k-n} \csc\left(\frac{\pi(k-n)}{2N+1}\right) & , k \neq n, \\ 0 & , k = n. \end{cases} \quad (3.49)$$

The main difference with the NLFD approach is that the source term matrix D_t is known at the first iteration and does not change, meaning that we do not spend time computing a fast Fourier transform and its inverse at each time-step, even though the source term $D_t(u^*)$ needs to be evaluated.

Finally, adding a pseudo-time (τ) derivative to time march the equations to the steady-state, the mono-frequential formulation of Eq. (3.1) in the harmonic balance framework is given by

$$\frac{\partial u^*}{\partial \tau} + D_t(u^*) + \frac{\partial}{\partial x} \frac{(u^*)^2}{2} = 0$$

(3.50)

with D_t defined using Eq. (3.49). As for the NLFD method, the term $u'u'$ is not neglected in the current approach.

3.5.2 Multi-frequential formulation

In the framework of almost-periodic functions [6], a function $f(t)$ composed of multiple frequencies non necessarily harmonically related can be approximated by an almost-periodic discrete Fourier transform

$$f(t) \approx \sum_{k=-N}^N \hat{f}_k e^{i\omega_k t}. \quad (3.51)$$

In this framework, Gopinath et al. [41] and Ekici and Hall [28] extended the harmonic balance approach to a multi-frequential formulation. To do so, they considered a Fourier matrix defined as

$$(E)_{k,n} = \frac{1}{2N+1} e^{-i\omega_{k-N} t_n}, \quad (3.52)$$

where N is the chosen number of frequencies. Note that replacing ω_{k-N} by $(k-N)\omega$ gives the mono-frequential inverse Fourier matrix back. However, in the multi-frequential case, the inverse Fourier matrix E^{-1} has to be numerically computed from E . Actually, as demonstrated by Gopinath et al. [41], it is easier to express E^{-1} analytically, compute its temporal derivative (that is hence analytical too) and inverse it numerically to obtain E . In fact, the source term can be written as $D_t = \frac{\partial E^{-1}}{\partial t} E$ which ease its computation.

Using the same process as for the mono-frequential formulation, Eq. (3.32) becomes

$$iE^{-1}PEu^* + R^* = 0, \quad (3.53)$$

where P is a diagonal matrix formed of all the angular frequencies ω_k . Note that the exponentials do not need to form an orthogonal family here. The only need is to have the multi-frequential Fourier matrix E to be invertible which is the case [28]. This is really close to the mono-frequential formulation given in Eq. (3.46). Finally, adding a pseudo-time (τ) derivative to time-march the equations to the steady-state, the multi-frequential formulation of Eq. (3.1) in the harmonic balance framework reads

$$\frac{\partial u^*}{\partial \tau} + D_t(u^*) + \frac{\partial}{\partial x} \frac{(u^*)^2}{2} = 0$$

(3.54)

with D_t defined as

$$D_t = iE^{-1}PE, \quad (3.55)$$

and again $u^* = [u(t_0) \cdots u(t_{2N})]$ and $R^* = [R(t_0) \cdots R(t_{2N})]$.

3.5.3 Extensions

Navier–Stokes equations As for the NLFD approach, since the Navier–Stokes equations can be written in finite-volume, semi-discrete form as

$$V \frac{dW}{dt} + R(W) = 0, \quad (3.56)$$

nothing particular has to be made to derive this approach for the Navier–Stokes equations, except adding the source term computation in the time-loop. This shows its advantage over the NLFD and particularly over the NLH method.

Turbomachinery computations Originally, the HB method has been developed for turbomachinery applications. Hall et al. [47] applied the method to the computation of the flutter boundary of the front stage rotor of a modern high-pressure transonic compressor. To reduce the computational domain to a single blade passage, a phase-lagged boundary condition is used at the azimuthal interfaces

$$\hat{u}_{k,U} = \hat{u}_{k,L} e^{i\sigma k}, \quad (3.57)$$

for $k \in [-N, N]$, where subscript U and L denote respectively the upper and lower azimuthal boundaries, and σ denotes the inter-blade phase angle. This boundary condition allows to compute isolated aeroelastic configurations using only one blade-passage.

van der Weide et al. [101] extended the approach to take into account the periodic boundary conditions when the equations are solved in the cartesian coordinate system. The efficiency of the method was demonstrated with the NASA-Stage 35 compressor. In that case, engineering accuracy is obtained with only $N = 5$ harmonics. Nothing is said on the strategy used at the rows interface.

Ekici and Hall [28] and Gopinath et al. [41] extended the method to a multi-frequential formulation. As such, it can then be applied to multi-stage configurations. Both of them demonstrated the applicability of the method on a two-dimensional multi-stage compressor called configuration D. The strategy used by Ekici and Hall [28] to exchange the variables at the rows interface is schematically represented in Figure 3.4. The temporal and azimuthal

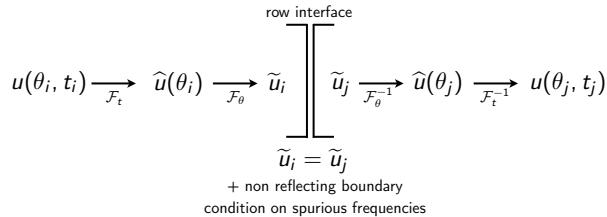


Figure 3.4: Exchange of the variable at rows interface as described by Ekici and Hall [28].

variations of the field (here represented as $u(\theta_i, t_i)$) in row i are Fourier transformed first with respect to time giving $\hat{u}(\theta_i)$, and then to space to obtain the spatio-temporal modes \tilde{u}_i . At the interface, these modes are transmitted using a non-reflecting boundary condition filtering the spurious modes. In fact, as only some temporal modes are computed using the HB approach, only those will be kept when transmitted to the opposite row. Finally, the inverse operations are carried out in the opposite row: first an inverse azimuthal Fourier transform is performed and second an inverse temporal Fourier transform is done which gives $u(\theta_j, t_j)$ in row j . Gopinath et al. [41] used a different approach to transfer the information at the interface as shown in Figure 3.5. In most time-domain solver, a sliding mesh treatment exists

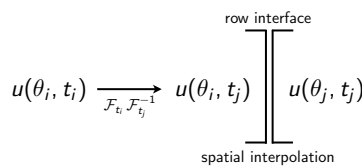


Figure 3.5: Exchange of the variable at rows interface as described by Gopinath et al. [41].

to interpolate azimuthal variations between consecutive rows. Therefore, Gopinath et al. [41] interpolates temporally the field on the time instances used for the HB computation in the opposite row. To do so, they used a temporal Fourier transform combined with an inversed one using the time instances of the opposite row. Then, they applied the sliding mesh treatment to spatially transfer the information. As spurious effects can appear, the time interpolation is done, not on the $2N + 1$ samples of the opposite row, but rather on $2 \times (2N + 1)$ samples. This over-sampling helps isolating the spurious effects on the higher harmonics to suppress them.

Ekici and Hall [29] applied the multi-frequential method to the effect of wake passing on the vibration of a turbine blade. Note that the stator is modeled by an unsteady wake injection but not computed. Two frequencies are involved: the blade passing frequency of the opposite row, here the stator row that is modeled through an unsteady wake injection, and the aeroelastic frequency, justifying the use of the multi-frequential formulation.

At CERFACS, Sicot et al. [90] implemented the harmonic balance into the *elsA* [12] CFD code and analyzed the rotor/stator interaction in a subsonic compressor. To reduce the computational domain, phase-lag boundary conditions are implemented using the general expression of the phase-lag due to different number of blades in the different rows provided by Gerolymos and Chapin [36]

$$\sigma = -2\pi \operatorname{sign}(\Omega_{cur} - \Omega_{opp}) \left(1 - \frac{B_{opp}}{B_{cur}} \right), \quad (3.58)$$

where Ω denotes the rotation speed, B the number of blade and subscript *opp* and *cur*, respectively, the opposite and the current row. The same treatment as Gopinath et al. [41] is used at the interface. Guédene [42] extended this to the multi-frequential framework. The author showed that unsteadinesses coming from upstream and downstream rows can be retrieved with a good accuracy using only a limited number of harmonics.

Choice of the frequencies for the multi-frequential formulation Due to the non-linearity of the considered equations, the presence of two or more base frequencies can lead to the emergence of combinations of them. This leads to a set of possible frequencies that is two-dimensional or more. As an infinite number of frequencies can not be computed, this set has to be truncated. In the electronic literature, Kundert et al. [62] propose two types of truncation: the "square grid" and the "diamond grid" truncations. These are schematically represented in Figure 3.6. Dots represent frequencies that are computed by the multi-frequential harmonic balance approach. In the turbomachinery literature, Gopinath et al. [41] follows the diamond

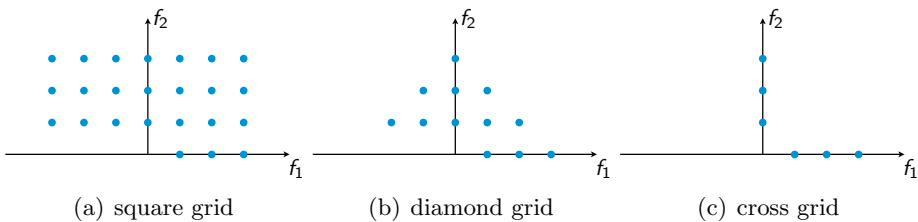


Figure 3.6: Truncation grids for reducing the input set of frequencies of multi-frequential harmonic balance computations.

grid pattern while Ekici and Hall [28] seems to choose a square grid pattern. In his PhD thesis, Guédene [42] first choose the frequencies by knowing which one emerge based on a reference classical time-marching computation. Of course, this approach can only be done *a posteriori* which limits the predictability of the method. He also made computations with a "cross grid" truncation (shown in Figure 3.6), this new type of truncation scheme only considers the harmonics of the base frequencies. Guédene [42] showed that this truncation pattern gives similar if not better results than the "diamond grid" truncation pattern. This "cross grid" truncation pattern will be used in the current work when using the multi-frequential approach.

Aeroelastic simulations Thomas et al. [98] used the method to determine the Limit-Cycle Oscillation (LCO) solution of a transonic airfoil configuration using the Euler equations and Thomas et al. [99] extended it to the viscous Navier-Stokes equations. For external-flow aeroelasticity, the HB approach has been thoroughly validated by Dufour et al. [23], Gopinath and Jameson [39], Sicot et al. [89], Woodgate and Badcock [109], mostly for the AGARD test cases of Davis [22]. Dufour et al. [23] highlighted the benefits of using a non-linear approach for oscillating-flap simulations compared to linearized approaches. A one-harmonic HB simulation gives results comparable to an expensive time-marching simulation. Huang and Ekici [54] applied the mono-frequential HB method to the flutter prediction of the 11th standard configuration for aeroelasticity [35]. They show that with only one harmonic, the local harmonic response of the fluid is superimposed with the results of a time-marching simulation. The same study has been performed in this work as detailed in Chap. 7 and the same conclusions are drawn. These results have been published in Sicot et al. [90]. In the context of the current thesis, Sicot et al. [91] applied the multi-frequential method to the aeroelasticity of a contra-rotating fan, proving the maturity of the approach.

Transient problems Mavriplis et al. [69] extended the method to an hybrid polynomial-harmonic balance approach. It allows to use the method for maneuver simulations, where a part of the simulation exhibits a physical transient.

Gradient-based method to determine the frequency With the same approach as McMullen et al. [72], Gopinath and Jameson [40] developed a gradient-based method to estimate the frequency of the vortex shedding behind a cylinder and of a NACA0012 airfoil at high angle of attack using the harmonic balance approach. The results are superimposed with a classical time-marching approach ones.

Optimum shape design Thomas et al. [100] used an automatic differentiation compiler to derive an adjoint code from their harmonic balance code. This adjoint code is then evaluated on the NLR 7301 supercritical airfoil section. The computation of the sensibilities is finally classically compared to a finite-difference and shows to be in good agreement with these, validating the given approach.

Adaptive method Maple et al. [67] presented an adaptive harmonic balance approach. To do so, the number of harmonics is increased if the energy of the last harmonic divided by the cumulative sum of the energy of each harmonic is larger than a given threshold. During the first iterations, only a low number of harmonics is kept. Then, when the flow is almost converged, the adaptive harmonic balance approach is used. This ensures that higher order harmonics are not injected at the first iterations, when the flow is not physical. A 86% reduction in time (and in memory footprint) is seen compared to a resolved (converged in terms of harmonics N) harmonic balance computation. This has to be compared to the 2 factor speed-up observed by Mosahebi and Nadarajah [76] with an adaptive NLFD approach.

3.5.4 Numerical cost

As mentioned before, the cost of the method is linked to the number of simulated time instances. In fact, each new time instance corresponds to an additional steady computation. Thus, if

$2N + 1$ time instances are considered and if $\$_{\text{RANS}}$ denotes the CPU and memory cost of one steady computation, the cost of the HB method can be approximated by

$$\$_{\text{HB}} = (2N + 1) \times \$_{\text{RANS}}. \quad (3.59)$$

Note that Ekici and Hall [28, 29] use $3N + 1$ time instances or more to prevent the bad conditioning of the source term when using the multi-frequential formulation. This will be detailed later on this thesis in Chapter 5 and an innovative solution will be proposed. In that case, the cost is bigger and scales with the chosen number of time instances.

3.6 Convergence of the spectral operator

This section provides theoretical results on the convergence of Fourier-based time methods as well as an example motivating the use of such an approach for the current work.

3.6.1 Theoretical results

The convergence of the spectral operator depends on the regularity of the approximated function. Consider a function $u(t)$ that is continuous, periodic and bounded in $[0, T]$ and let $P_N(u(t))$ denote its truncated Fourier series

$$P_N(u(t)) = \sum_{k=-N}^N \hat{u}_k e^{ik\omega t}. \quad (3.60)$$

The \mathcal{L}_2 -norm of the error writes

$$\|u\|_2 = \left(\int_0^T |u(t) - P_N(u(t))|^2 dt \right)^{1/2}. \quad (3.61)$$

If $u(t)$ is m -times continuously differentiable in $[0, T]$ ($m \geq 1$) and its j -th derivative is periodic on $[0, T]$ for all $j \leq m - 2$ then, it exists $k_0 \in [1, N]$ such that

$$\hat{u}_k = \mathcal{O}(k^{-m}), \text{ for } k > k_0, \quad (3.62)$$

where \hat{u}_k is the k -th Fourier coefficient of $u(t)$. This equation means that, the more regular the function is, the faster the convergence rate of the Fourier coefficients. The property of the error to decay exponentially as soon as the function is approximated by a number of harmonics greater than k_0 , is called spectral accuracy [14]. Note that k_0 is not known but is rather essential for the analysis. For k below k_0 , approximating the function $u(t)$ with its Fourier series yields unacceptably high errors.

3.6.2 Motivating example: numerical derivation of a smooth function

To assess the capability of the HB operator, used in the present work, to provide accurate approximations of the time-derivative, we consider the simple example of a pure five-harmonic signal of the form

$$u(t) = \cos(\omega t) + \sin(2\omega t) + \cos(3\omega t) + \sin(4\omega t) + \cos(5\omega t), \quad (3.63)$$

where $\omega = 2\pi f$ and f is the temporal frequency of the considered phenomenon. The analytical derivative is then

$$\frac{du}{dt} = \omega [-\sin(\omega t) + 2 \cos(2\omega t) - 3 \sin(3\omega t) + 4 \cos(4\omega t) - 5 \sin(5\omega t)]. \quad (3.64)$$

The exact derivative is compared to the approximated one obtained by applying the HB operator defined in Eq. (3.48). Two Finite-Difference (FD) schemes are used for comparison: a second-order centered scheme

$$\frac{du}{dt}(t = t_q) = \frac{u_{q+1} - u_{q-1}}{2\Delta t} + \mathcal{O}(\Delta x^2), \quad (3.65)$$

where $u_q = u(t_q)$ and $u_{q+1} = u(t_{q+1})$ and so on, and a fourth-order centered scheme

$$\frac{du}{dt}(t = t_q) = \frac{-u_{q+2} + 8u_{q+1} - 8u_{q-1} + u_{q-2}}{12\Delta t} + \mathcal{O}(\Delta x^4), \quad (3.66)$$

are also used for comparison. For finite-difference schemes, we assume that the time line is discretized by a regular mesh of step Δt , such that $t_q = q\Delta t$.

Figure 3.7 shows the resulting approximations of the derivative over one period. Four

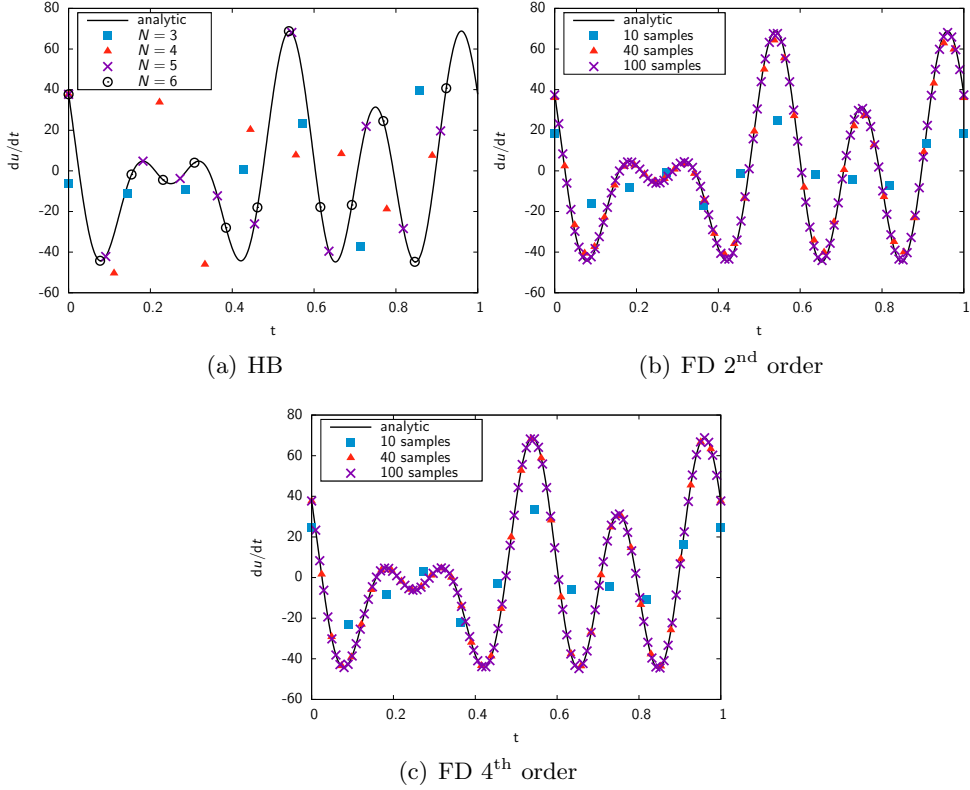


Figure 3.7: Time-derivative estimation by the harmonic balance operator, the 2nd order and 4th finite-difference schemes.

sampling levels are tested for the HB operator: 7, 9, 11 and 13 time instances per period corresponding to $N = 3, 4, 5$ and 6, respectively. For the FD schemes, the periodicity time

interval is sampled by 10, 40 and 100 points. For 40 samples, the 4th order FD scheme almost fits the analytical solution. On the other-hand, the HB operator prediction is superimposed with the analytical solution by using 11 samples, *i.e.* $N = 5$. Beyond that, further increasing the number of harmonics (or samples) does not improve the solution.

To quantitatively analyze the results, the \mathcal{L}_2 -norm of the absolute error with respect to the analytical derivative is computed for the different schemes and sampling levels (see Figure 3.8). As expected, the error of the 4th order FD decreases faster than the 2nd order for a given

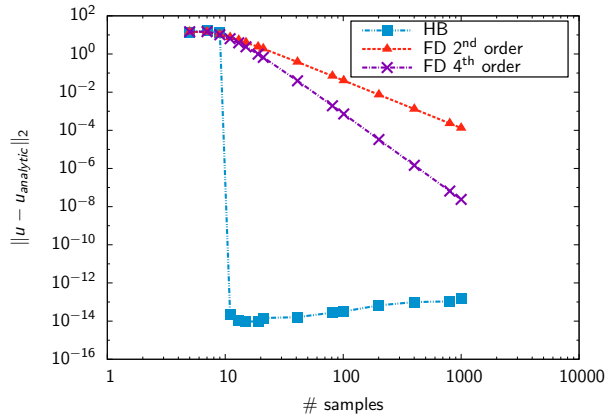


Figure 3.8: \mathcal{L}_2 -norm of the error for each time-derivative schemes.

sampling level. When the number of harmonics is low (*i.e.* $N < 5$), the error is high for the HB operator. But as soon as $N \geq 5$, the error drastically decreases to machine precision. This illustrates the spectral accuracy as explained in Sec. 3.6.1. In fact, the function defined in Eq. (3.64) approximated by the spectral operator is infinitely differentiable and periodic in $[0, T]$. Thus, using the properties established in Sec. 3.6.1, the convergence rate of the spectral operator is $\mathcal{O}(k^{-\infty})$ for $k > k_0$, here $k_0 = 5$. In this case, k_0 reflects the frequency content of the signal (namely 5 harmonics).

The study of the convergence applied to the resolution of turbomachinery harmonic balance computations will be detailed in Chap. 6.

3.7 Periodic flows in turbomachinery

In this thesis, the final application is contra-rotating open rotor configurations. To bound Fourier-based time methods for such applications, we propose a classification of the unsteady phenomena that can be computed using such approaches.

Inspired by Hodson [52], a diagram presenting the unsteadinesses seen in a CROR is shown in Figure 3.9. A distinction is made between unsteadinesses whose frequencies are known or not. From the bibliography presented previously, almost all unsteady flows can be computed using Fourier-based time methods. The current implementation of the HB method available for this thesis is able to compute all the unsteady effects highlighted by a bold text. In the literature, the presented work of Mavriplis et al. [69] allows to compute transient unsteady flows resulting from a change of operating point and/or a maneuver and the work of McMullen et al. [72] and Gopinath and Jameson [40] allows to capture periodic flows whose frequency is unknown. These two kinds of unsteadiness are added to the current panel of applications that

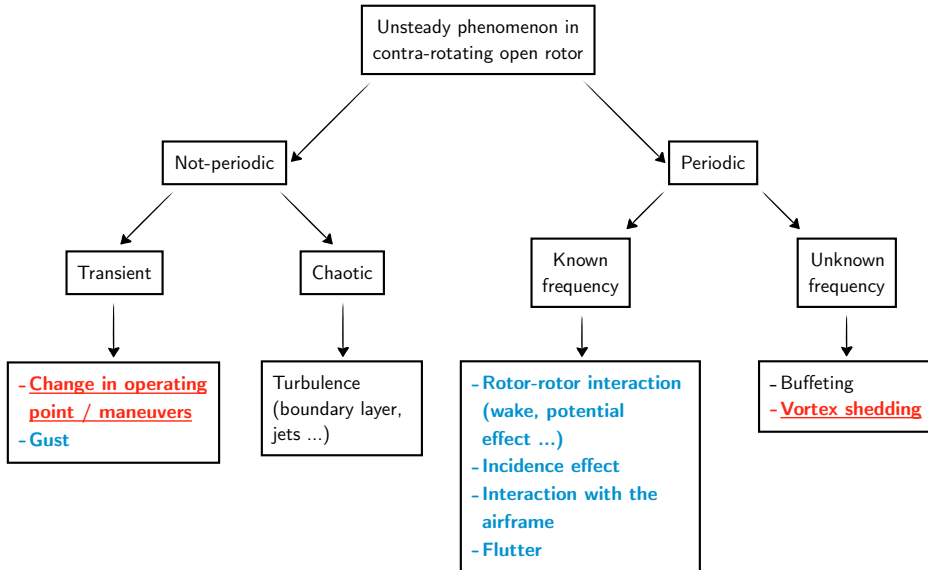


Figure 3.9: Main unsteady phenomena seen by contra-rotating open rotors. Bold blue text highlights applications that can be treated with the harmonic balance implementation available in the current work and underlined red text shows additional applications made possible by extensions available in the literature.

can be treated by Fourier-based time methods and are highlighted by an underlined text. Note that the gradient algorithm presented by McMullen et al. [72] and Gopinath and Jameson [40] is only able to converge when a good approximate of the solution is given, meaning that this strategy fails when one has no estimate of the value of the frequency for the considered phenomenon. It can also be inferred that using such an optimization algorithm coupled with a Fourier-based time method might require more computational time than a classical time-marching scheme, which limits its applicability to academic configurations.

Summary

Four Fourier-based time methods have been presented in this chapter. The main mathematical developments have been discussed and the underlying hypotheses/weaknesses of each method have been highlighted. The harmonic balance method, that will be used in the current work, has been selected because of its ability to tackle both mono- and multi-frequential applications. To do so, the unsteady equation is transformed into a subset of $2N + 1$ steady-state equations coupled by a source term which is analytical in the mono-frequential formulation and of matrix form in the multi-frequential framework. The vast literature available on these methods shows that they are ready for industrial, numerically demanding unsteady applications. Moreover, the method is shown to be suitable for the computation of aeroelastic phenomena on contra-rotating configurations investigated in the present work. Nevertheless, some numerical issues may arise in specific configurations. Before applying the harmonic balance method to CROR, we investigate these aspects in the following chapters and suggest possible solutions.

Part II

Advantages and limitations of Fourier-based time methods

Preliminary validations of the harmonic balance approach

Abstract

In this chapter the mono- and multi-frequential harmonic balance approaches are validated. In this aim, two model problems are used. Firstly, the harmonic balance method is applied to the linear advection equation supplemented with unsteady boundary conditions of different frequency content. Mono- and multi-frequential unsteady signals are injected and compared to exact solutions. The spectral accuracy of the method is verified. Moreover, the ability of the multi-frequential approach to capture signal composed of segregated frequencies is underlined. Based on these results, the aeroelasticity of contra-rotating open rotors is put into perspectives. Secondly, the multi-frequential approach is assessed for a channel flow problem solved using the *elsA* [12] CFD code within the Navier–Stokes equations framework. The results are shown to be superimposed with a classical time-marching solution.

4.1 Linear advection of a periodic signal

4.1.1 Presentation of the test case

To validate the harmonic balance approach within a linear framework, the resolution of the advection equation is considered. It is defined as

$$\frac{\partial u}{\partial t} + c \frac{\partial u}{\partial x} = 0, \quad (4.1)$$

with the constant advection speed c assumed as positive. The equation is solved in the domain $x \in [0, L_x]$. Periodic perturbations of different shapes are imposed at the left boundary

$$u(0, t) = u_l(t), \quad (4.2)$$

where u_l is a periodic function of period $T = L_x/c$. These perturbations are advected across the computational domain and leave from the right boundary. After a transient of time length $T_{trans} = L_x/c$, the solution at any point x in the space domain achieves a periodic state. The exact solution for this periodic state is a periodic function of the form

$$u_{ex}(x, t) = u_l(x/c + t). \quad (4.3)$$

For simplicity, L_x and c are taken as unity.

4.1.2 Numerical setup

The space derivative is discretized by means of a centered fourth-order finite-difference scheme on a uniform Cartesian mesh

$$\frac{\partial u}{\partial x}(x = x^i, t = t_q) = \frac{-u_q^{i+2} + 8u_q^{i+1} - 8u_q^{i-1} + u_q^{i-2}}{12\Delta x} + \mathcal{O}(\Delta x^4), \quad (4.4)$$

A very fine space step is used ($\Delta x = 5 \times 10^{-4}$) in order to rule out spatial approximation errors. This corresponds to 2,000 grid points in the domain. The solution at the last mesh point on the right of the domain is extrapolated from the inside. To this aim, a standard second-order and a first-order upwind discretization schemes are used to approximate the space derivative at the last two mesh points on the right, respectively

$$\begin{aligned} \frac{\partial u}{\partial x}(x = x^{m-1}, t = t_q) &= \frac{3u_q^{m-1} - 4u_q^{m-2} + u_q^{m-3}}{2\Delta x} + \mathcal{O}(\Delta x^2), \\ \frac{\partial u}{\partial x}(x = x^m, t = t_q) &= \frac{u_q^m - u_q^{m-1}}{\Delta x} + \mathcal{O}(\Delta x), \end{aligned} \quad (4.5)$$

where m is the total number of grid points.

Time-discretization is achieved through the HB method (described in Sec. 3.5) with a standard four-step Runge-Kutta method [59] used to pseudo-time march the HB equations to the steady-state. The k^{th} step is evaluated by

$$u_k = u_q - \alpha_k \Delta t \left[c \frac{\partial u_{k-1}}{\partial x}(t = t_q + \alpha_{k-1} \Delta t) + D_t(u_k) \right], \quad (4.6)$$

where $\alpha_0 = 0$, $\alpha_1 = 1/4$, $\alpha_2 = 1/3$, $\alpha_3 = 1/2$, $\alpha_4 = 1$. The HB source term $D_t(u_k)$ is computed using Eq. (3.55). The CFL number in pseudo-time is set to 1 to ensure stability of the explicit time-marching scheme.

4.1.3 Validation of the mono-frequential approach

A perturbation in the form of a finite sum of sine functions, similar to the one used in Sec. 3.6.2, is applied at the left boundary

$$u_l(t) = \cos(\omega t) + \sin(2\omega t) + \cos(3\omega t) + \sin(4\omega t) + \cos(5\omega t). \quad (4.7)$$

Harmonic balance computations are run with 1 to 10 harmonics. For each computation, we show spatial distributions of the solution at three time instances, namely $t = 0$, $t = T/3$ and $t = 2T/3$. Since these instances are not necessarily used in the HB discretization, a temporal interpolation is performed. To do so, the frequency content of the HB solution is used together with an inverse Fourier transform on the time-vector $[0, T/3, 2T/3]$. Figure 4.1 depicts the results of HB computations using 1 to 6 harmonics. The analytical solution is also reported for comparison.

The accuracy of the solution improves with the number of harmonics, until it reaches the frequency content of the injected signal, *i.e.* 5 harmonics. For higher sampling levels, the results of HB computations are superimposed with the analytical solution, validating the current approach.

The \mathcal{L}_2 -norm of the error in time is computed over all the time instances at each grid point over the domain. Then, the average in space is computed. The error is shown as a function of the number of harmonics in Figure 4.2. Two results are displayed: one for the reference mesh (2,000 grid points) and one for a refined mesh (4,000 grid points). The convergence of the HB computations is slow for $N \leq 4$. However, when the number of harmonics composing the injected function is reached ($N = 5$), the error is minimum and computing more harmonics does not change the error. As introduced in Sec. 3.6, the convergence rate of Fourier-based time methods is inherently linked to the spectrum of the temporal phenomenon that one wants to capture. This property is still seen when solving the linear advection equation. Here a finite discrete spectrum composed of only five harmonics is imposed. The value of the plateau obtained after $N = 5$ is representative of the error introduced by the different discretizations. In fact, refining the mesh changes this value without modifying the error levels of the lower harmonics points as indicated by Figure 4.2.

The temporal discrete Fourier transform of the computational results is compared to the analytical results in Figure 4.3. When the number of harmonics grows in the spectral computations, the Fourier transform gets closer to the analytical solution. When the whole frequency content of the injected function is contained in the HB solution, the numerical results are superimposed with the analytical ones. For intermediate sampling frequencies, as for instance the three-harmonics HB computation, the resolved harmonics have higher amplitudes than the exact one, since they compensate for harmonics that are not resolved.

When the number of harmonics composing the spectrum of the computed signal is reached, the computational results are superposed with the analytical ones, namely we obtain spectral accuracy. This is the main advantage of Fourier-based time methods: when the signal has a narrow spectrum, as it is the case for the sum of sine function used here, the convergence can be very fast compared to a classical time-marching scheme as only a few number of time instances is necessary to retrieve the unsteadiness.

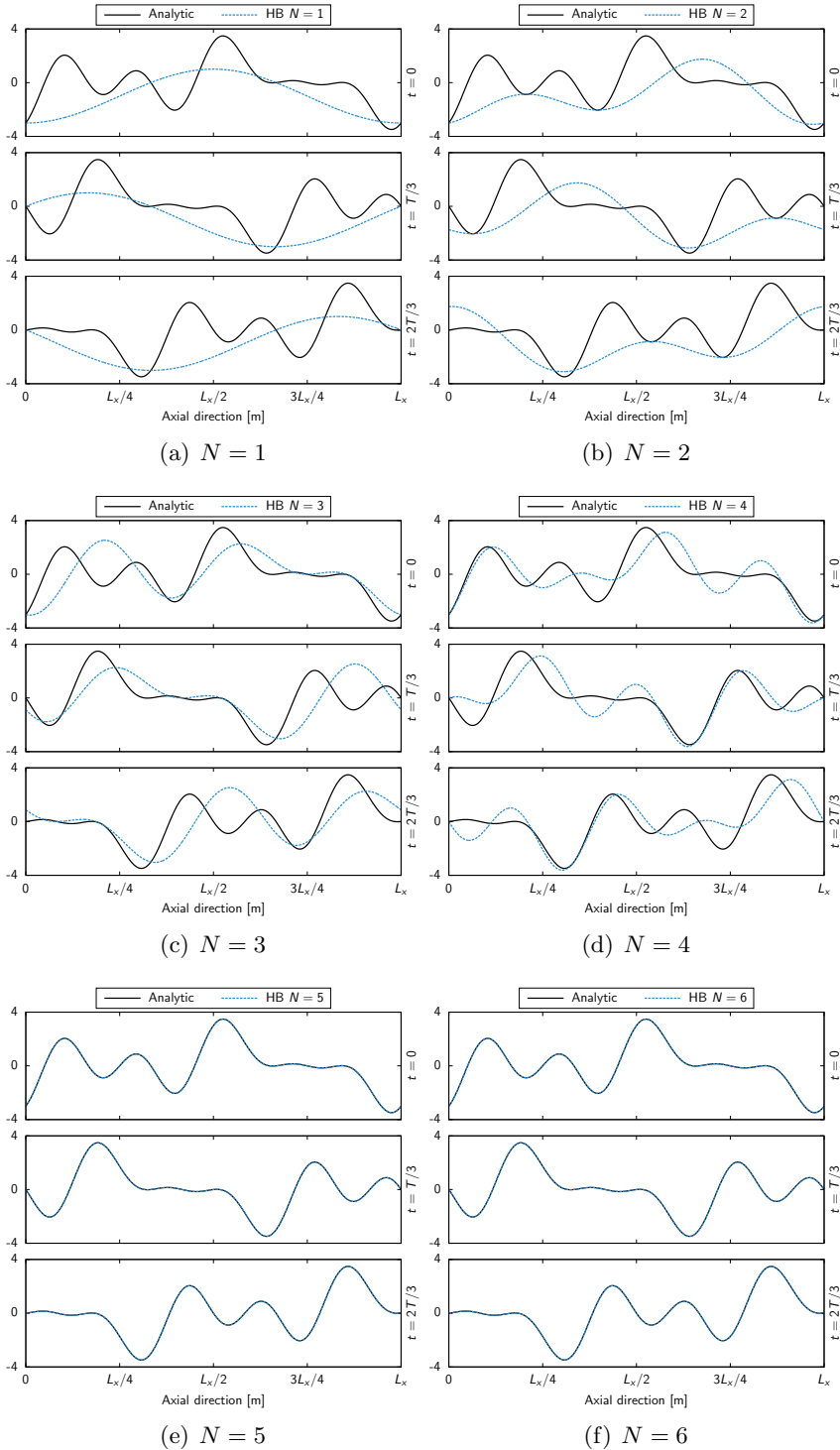


Figure 4.1: Linear advection of a sum of sine functions: numerical solutions at different time instances for different numbers of harmonics.

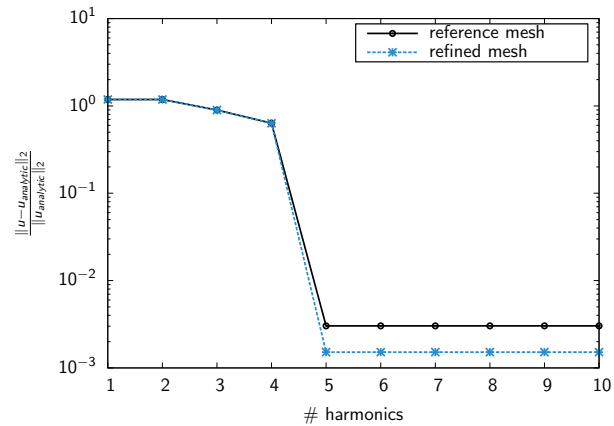


Figure 4.2: Linear advection of a sum of sine functions: convergence of the HB method error.

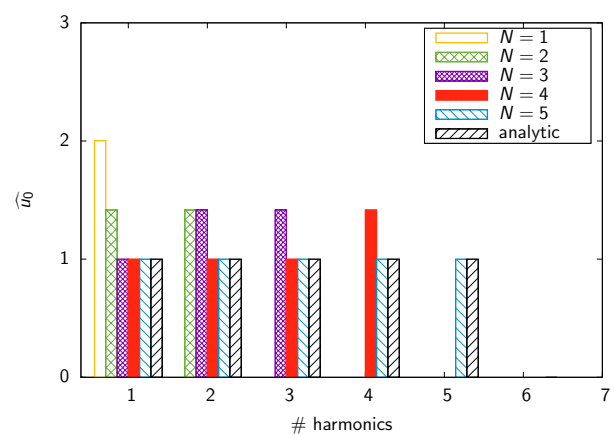


Figure 4.3: Linear advection of a sum of sine functions: discrete Fourier transform.

4.1.4 Validation of the multi-frequential approach

In Section 3.5.2, the multi-frequential harmonic balance approach has been presented. In this method, the frequencies can be chosen arbitrarily. This becomes particularly interesting when dealing with signal/flow field composed of segregated frequencies. To emphasize that, let us consider the linear advection problem with a perturbation in the form of a sum of two sine functions, applied at the left boundary

$$u_l(t) = \sin(\omega t) + \sin(22\omega t). \quad (4.8)$$

Using a mono-frequential approach

Obviously, computing the advection of such a perturbation using a classical time-marching scheme would require to discretize the smaller period. The largest frequency (here $f_2 = 22$ Hz) acts as a bottleneck as the time-step will be chosen according to this frequency. The cost scales thus with the ratio of f_2/f_1 .

This holds true when computing the solution using the mono-frequential harmonic balance approach. In fact, the frequencies can not be chosen arbitrarily. Therefore, to compute such a configuration, a $N = 22$ harmonic computation will be needed to be spectral accurate. To emphasize that, mono-frequential HB computations are run with 1 to 25 harmonics. As made previously, for 6 chosen computations of the 25 computations, we show spatial distributions of the solution at three time instances, namely, $t = 0$, $t = T/3$ and $t = 2T/3$. It is shown in Figure 4.4. Again, the accuracy in capturing the injected function improves with the number of harmonics, until it reaches the frequency content of the injected signal, *i.e.* 22 harmonics. After that, the results of the HB computations are superimposed with the analytical solution. The problem, with such a segregation of frequencies, is that the mono-frequential version suffers from the same problems as a classical time-marching scheme in terms of computational cost.

To quantitatively analyze the results, the discrete \mathcal{L}_2 -norm of the error is shown in Figure 4.5 for the mono-frequential HB computations ranging from 1 to 25 harmonics. When the number of harmonics used to compute the solution is higher than the content of the spectrum, the error decreases drastically. The spectral accuracy is retrieved but only starting at $N = 22$. In fact, similar as in Sec. 4.1.3, the injected function is indefinitely differential and periodic yielding an infinite convergence slope. We can observe a slight local convergence for the $N = 5$ harmonics HB computation. This is due to the fortunate capture of the low-frequency pattern of the injected function as shown in Figure 4.4(b).

Using a multi-frequential approach

One of the advantage of the multi-frequential HB method, introduced in Sec. 3.5.2 and used in this work, is that it can take arbitrary frequencies into account. In the case of an injected signal with a large frequency segregation, the benefit might be tremendous. Let us consider again the signal defined in Eq. (4.8) and compute one HB simulation using $f_1 = 1$ Hz and $f_2 = 22$ Hz as input frequencies. This gives a computation of two coupled calculation that is nine times faster than the $N = 22$ converged mono-frequential HB computation. Again we show spatial distributions of the solution at three time instances, namely $t = 0$, $t = T/3$ and $t = 2T/3$ in Figure 4.6. With only two input frequencies, the multi-frequential HB solution is superimposed with the analytical solution. Moreover, the $\mathcal{L}2$ -norm of the error is exactly the same as the one of the $N = 22$ mono-frequential approach.

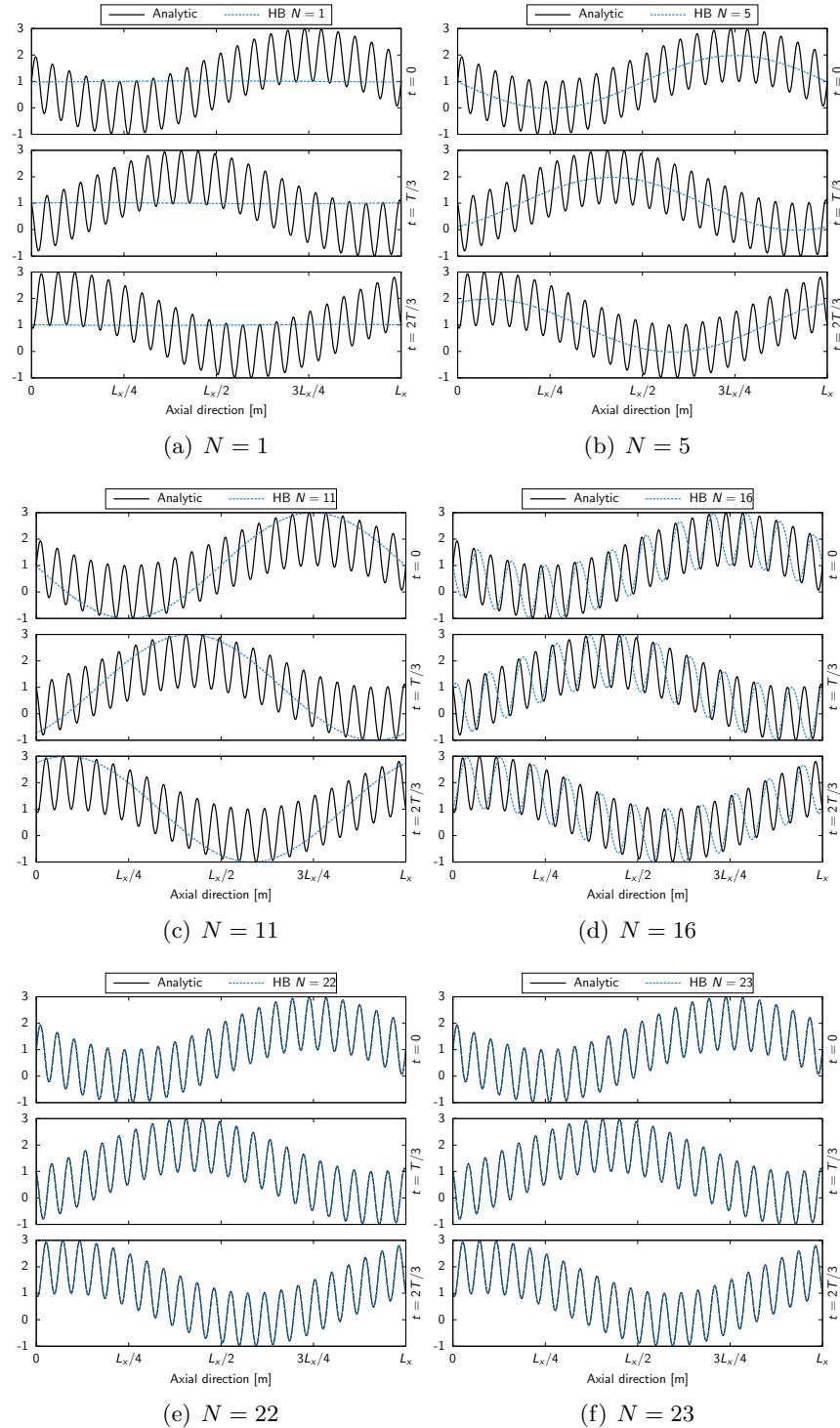


Figure 4.4: Linear advection of a sum of two segregated sine functions: numerical solutions at different time instances for different numbers of harmonics.

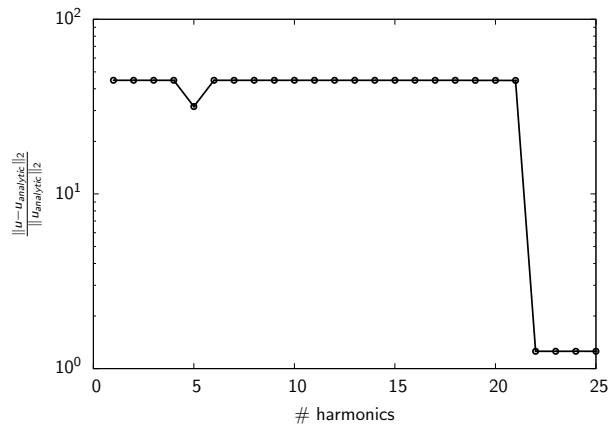


Figure 4.5: Linear advection of a sum of two segregated sine functions: convergence of the mono-frequential HB method error.

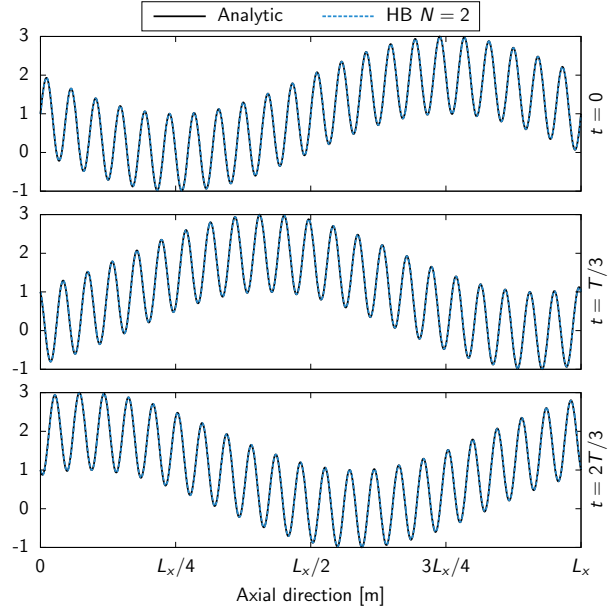


Figure 4.6: Linear advection of a sum of two segregated sine functions: numerical solutions at different time instances for different numbers of harmonics using the multi-frequential harmonic balance method.

This validates the multi-frequential approach used along with segregated frequencies which is the case of contra-rotating open rotor aeroelasticity.

4.2 Application to a non-linear system of equations

Both the mono- and multi-frequential harmonic balance approaches have been validated on a linear equation. In this section, the multi-frequential harmonic balance developed and implemented by Guédene [42] into the *elsA* [12] CFD code is assessed within a non-linear framework, namely the Navier–Stokes equations.

4.2.1 Presentation of the case

The second case consists of a 2D channel with a constant left injection at a transonic Mach number ($M_0 = 0.7$) supplemented with a time-varying unsteady back pressure. As the pressure is oscillating at the outlet, the imposed unsteady pressure fluctuations travel within the flow at the velocity $u + c$ and $u - c$, where u denotes the local flow velocity and c the speed of sound. Since the pressure waves are generated at the outlet, only the $u - c$ waves are seen, resulting in pressure waves propagating upstream of the channel. The axial length of the channel is $L_x = 100$ m and the transversal one is $L_y = 1$ m. Figure 4.7 shows a sketch of the considered channel flow problem.

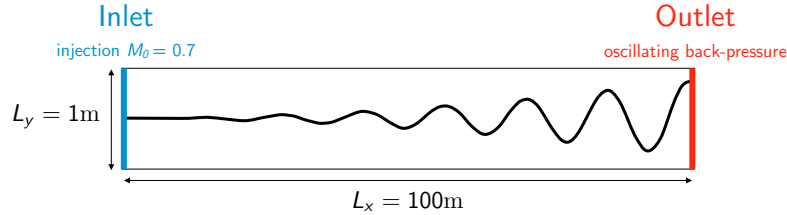


Figure 4.7: Sketch of the channel flow problem.

Merkle and Athavale [74] give an analytical solution for incompressible flows with small pressure fluctuations, assuming thus a linear unsteady flow. However, this channel flow problem is set up to highlight the properties of the harmonic balance in a non-linear framework which is not the hypothesis of Merkle and Athavale [74]. This is why, to get confidence into our forthcoming results for this model problem, this last will be validated below against a classical time-marching scheme in Sec. 4.2.3.

4.2.2 Numerical setup

The mesh consists of 997 points along the axial direction and 9 in the transverse one, which corresponds to equal spacings in both directions.

The boundary conditions are: (i) a constant injection condition for the inlet where the total pressure p_{i0} and enthalpy h_{i0} are set, (ii) symmetric conditions for the upper and lower bounds as the flow is assumed to be symmetric in the transverse direction, and (iii) a fluctuating static pressure imposed at the outlet

$$p_{s1}(t) = \bar{p}_{s1} [1 + a_1 \sin(2\pi f_1 t) + a_2 \sin(2\pi f_2 t)], \quad (4.9)$$

where \bar{p}_{s_1} is the temporal average static pressure, a_n the amplitude of the n^{th} mode and f_n its frequency. Only two modes (f_1, f_2) are injected but due to the non-linearity of the Navier–Stokes equations, new frequency combinations rise. The mean velocity of the flow is imposed through a static pressure condition \bar{p}_{s_1} at the outlet

$$\bar{p}_{s_1} = \frac{p_{i0}}{\left(1 + \frac{\gamma-1}{2} M_0^2\right)^{\frac{\gamma}{\gamma-1}}}, \quad (4.10)$$

the mean velocity is thus set by imposing the inlet target mean Mach number value M_0 . We assume here that the flow is isentropic as no geometrical object disturbs the flow field.

The *elsA* [12] CFD code developed by ONERA is used to solve this channel flow problem. In fact, the aim of this model problem is to use the same solver as the one used in the application part of this work so that the results shown here can be directly transposed later on. This code solves the RANS equations using a cell-centered approach on multi-blocks structured meshes. Several time-integration schemes are available, in particular the Dual Time-Stepping [59] (DTS) as well as the time-domain harmonic balance method implemented by Sicot et al. [89] for the mono-frequent formulation and extended by Guédene et al. [43] to multi-frequent flows.

The present configuration is turbulent as the Reynolds number based on the inlet flow velocity and the axial length of the channel is about $R_e \approx 2.0 \times 10^9$. To this aim, turbulence is modeled using the one-equation model of Spalart and Allmaras [94]. Roe's scheme [82] along with a third-order MUSCL extrapolation is used for the spatial discretization of the convective fluxes. An implicit backward Euler scheme is used to march the HB equations in pseudo-time.

4.2.3 Validation of the multi-frequent approach

We propose now to validate the channel flow problem within the multi-frequent harmonic balance framework in order to have confidence in the forthcoming results that will use this approach. To do so, two non-harmonically related frequencies are chosen as input for the outlet boundary condition: $f_1 = 3$ Hz and $f_2 = 17$ Hz.

The classical DTS time-marching scheme is taken for comparison. Convergence in time discretization is obtained after 20 periods using 160 instants per almost-period. Since the frequencies are integers and coprime, the period is $T = 1$ s. Iterative convergence for the inner loop is considered achieved when the normalized residuals drop by 10^{-2} within a maximum of 50 sub-iterations.

The results obtained with the DTS scheme are compared to the HB results for pressure waves amplitudes of $a = a_1 = a_2 = 0.001$ (see Eq. (4.9)). The transient of the DTS computation is shown in Figure 4.8, illustrating the propagation of the waves with a slight attenuation of the high-frequency ones.

Due to the non-linearity of the Navier–Stokes equations, the two frequencies f_1 and f_2 give rise to linear combinations of them. Therefore, the results are analyzed for frequencies $1 < f < 40$ Hz and the dominant frequencies (the one that have the highest amplitudes) are set for the HB computation. To do so, pressure signals are probed upstream, in the middle and downstream of the channel at $y = 0.5$ m and $x = [25 \text{ m}, 50 \text{ m}, 75 \text{ m}]$, respectively. The spectra of the aforementioned unsteady pressure signals, obtained with a Fourier Transform, are plotted in Figure 4.9. The labeled frequencies are the dominant ones, as for each probe, these have a high amplitude. Those nine frequencies are thus selected as input frequencies

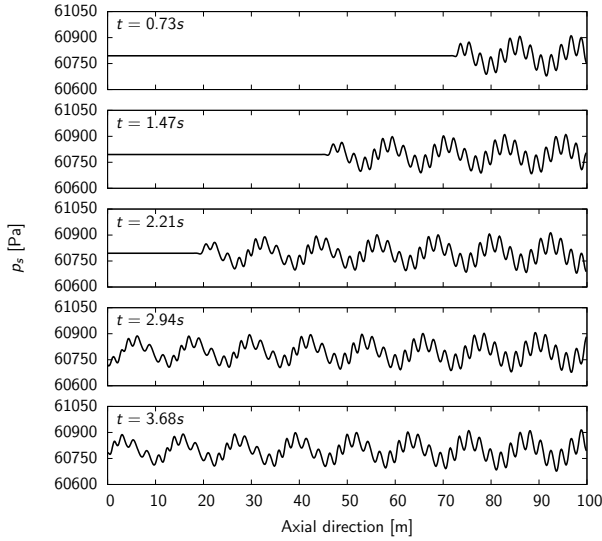


Figure 4.8: DTS computation: transient propagation of the pressure waves.

for the HB computation. Actually, this corresponds to a rectangular grid truncation (see Sec. 3.5.3).

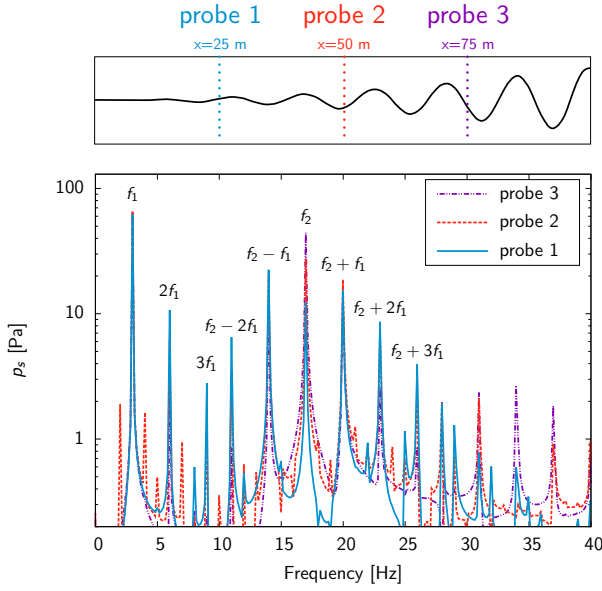


Figure 4.9: Spectra of the pressure signals.

The HB computation using the previously mentioned frequencies is run and a discrete Fourier transform is computed at several axis positions in the middle of the channel ($y = 0.5$ m). This is the same post-processing as the one done previously to retrieve Figure 4.9, but for all axial grid points. Figure 4.10 shows the results for the frequencies that have been set for the multi-frequential HB computation. The overall agreement between the DTS and the HB is fair. Some local discrepancies can be observed upstream for frequencies $f_2 + 3f_1$, $f_2 - f_1$ and $f_2 - 2f_1$. These are caused by aliasing but they are minimal regarding the temporal evolution,

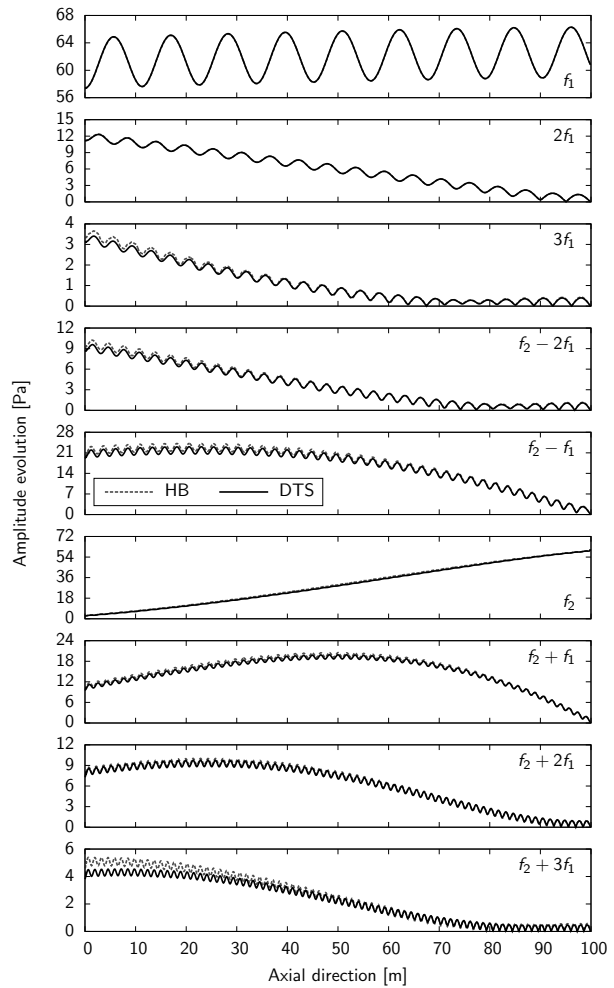


Figure 4.10: Spatial evolution of the amplitude of the dominant frequencies in the channel flow configuration, for $f_1 = 3$ Hz and $f_2 = 17$ Hz.

as shown in Figure 4.11, where the time evolution of pressure signals is extracted at all probes. The difference between the HB and the DTS method is negligible proving that the present multi-frequential harmonic balance approach is able to accurately capture multi-frequential unsteady signals.

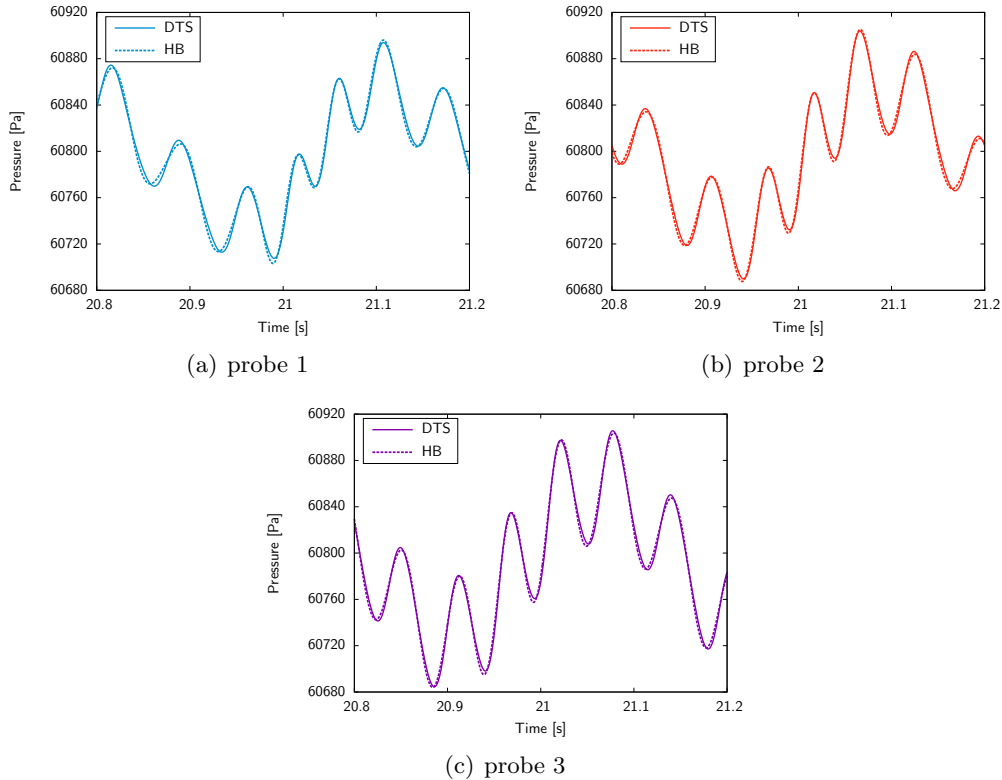


Figure 4.11: Unsteady pressure signals at different axial positions.

Summary

The mono- and multi-frequential harmonic balance approaches have been validated in this chapter against selected test problems. If the provided number of harmonics is greater than a threshold value depending on the specif configuration, the solution is superimposed with the exact/reference solution for both linear and non-linear test cases. This property is called spectral accuracy. In addition to that, it is shown that the multi-frequential harmonic balance approach is a good candidate for the simulation of problems involving segregated frequencies. Actually, this is the case of contra-rotating open rotor aeroelasticity. In the following chapter, we will see that an issue rises when considering segregated frequencies with the multi-frequential harmonic balance approach. As this is likely to be the case for contra-rotating open rotor aeroelasticity, an original approach is proposed to alleviate this problem.

Conditioning of multi-frequentia harmonic balance methods

Abstract

Problems characterized by multiple frequencies, as for instance the aeroelasticity of contra-rotating open rotors, require multi-frequentia harmonic balance discretization operators. These can be ill-conditioned for some combinations of the discrete frequencies. In this chapter, we investigate the sensitivity of harmonic balance solutions to the condition number of the discrete Fourier transform matrix for a linear advection problem and a non-linear channel flow problem. Highlighted is the fact that when the condition number is greater than one, the unsteadiness can be badly reproduced preventing the use of such an approach. To improve the condition number, we consider a non-uniform distribution of the times instances (Guédene [42]), along with an optimization algorithm minimizing the condition number of the discrete Fourier transform matrix. The optimization algorithm developed in the present work gives very good results for any input frequencies, enabling the use of the multi-frequentia harmonic balance for the simulation of contra-rotating open rotor aeroelasticity. This work has been published in

T. Guédene, A. Gomar, F. Gallard, F. Sicot, G. Dufour, and G. Puigt. Non-Uniform Time Sampling for Multiple-Frequency Harmonic Balance Computations. *Journal of Computational Physics*, 236:317–345, March 2013

5.1 Condition number and contra-rotating open rotor aeroelasticity

As shown previously in Sec. 1.4, the main unsteady phenomena encountered in CROR can be correlated with the blade passing frequency. In addition to that, the aeroelastic phenomenon studied here, namely blade flutter sensibility, has a vibration frequency that is imposed (weak-coupling approach) which depends on the proper modes of the structure (see Sec. 2.2.2). In general, these are not harmonically related nor of the same order of magnitude. Hence the use of the multi-frequential formulation of the HB approach.

The condition number κ of a matrix A is defined as

$$\kappa(A) = \kappa(A^{-1}) = \|A\| \cdot \|A^{-1}\|, \quad \kappa(A) \geq 1, \quad (5.1)$$

where $\|\cdot\|$ denotes a matrix norm. Considering the resolution of the system of equations $Ax = b$, if A is invertible and if δA , δx and δb are the numerical errors associated with the computation of A , x and b , respectively, then

$$(A + \delta A)(x + \delta x) = b + \delta b. \quad (5.2)$$

By definition, the condition number sets an upper bound for the error made on x

$$\frac{\|\delta x\|}{\|x\|} \leq \kappa(A) \left[\frac{\|\delta A\|}{\|A\|} + \frac{\|\delta b\|}{\|b\|} \right]. \quad (5.3)$$

By transposing this to our problem, namely A is the residual, b the source terms and x the conservative variables, one can say that the error on the iterative resolution of the governing equations can therefore be amplified by the harmonic balance source term. Using the definition given in Eq. (5.3), this amplification is led by the condition number of the source term which is driven by the DFT matrix E .

In the mono-frequential formulation, the logical sampling is the uniform one which has the good property of providing a well conditioned DFT matrix E . In fact, in this framework, E is orthogonal giving the smallest condition number $\kappa(E) = 1$. In the multi-frequential framework, the condition number of the DFT matrix E is not always unity and varies under frequencies and time instances change [62]. The frequencies being imposed by the problem that is simulated, the only degrees of freedom left to control the condition number are the time instances. Moreover, the amplitude of the unsteadinesses, represented by δx , can not be *a priori* controlled as it is ruled by the flow physics.

All variations of the HB approach proposed in the literature rely on a uniform time sampling of the longest period of interest (though the number of samples can differ). This uniform time sampling can raise stability issues. To emphasize this, let us consider two independent frequencies f_1 and f_2 playing the role of the blade passing frequency and the vibration frequency, respectively. The two frequencies are arbitrarily chosen between 1 and 10,000 Hz and the corresponding condition number of the DFT matrix E is computed. 100 points are used to discretize each frequency interval giving a frequency step of 100 Hz. The results using a uniform time sampling are reported in Figure 5.1. The problem being symmetric in (f_1, f_2) , so are the results. Moreover, only the ratio of f_2 over f_1 is important as the shape of the solution is constant under a translation of vector $(1, f_1/f_2)$.

Almost half of the set of frequencies have a DFT matrix E with a condition number greater than ten. The minimum values are obtained with harmonically related couples of frequencies.

In fact, the white zones in Figure 5.1 are the regions where $f_2 = nf_1$ with $n \in \mathbb{N}$ or $1/n \in \mathbb{N}$. Elsewhere, the condition number is large and grows exponentially. To highlight this, the

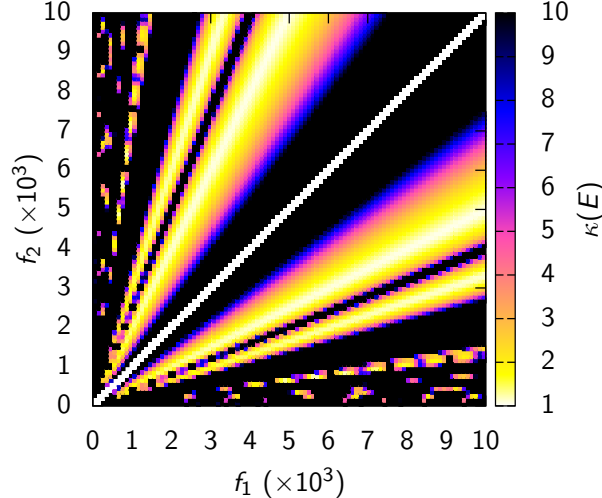


Figure 5.1: Condition number of the discrete Fourier transform matrix E using two independent frequencies and evenly-spaced time instances.

minimum (min), maximum (max), mean and standard deviation (std) values of the previous example are summarized in Tab. 5.1. The values of the maximum, mean and standard deviation

min	max	mean	std
1.0	9.4×10^{16}	1.5×10^{14}	2.8×10^{15}

Table 5.1: Condition number of the discrete Fourier transform matrix E : statistics for two independent frequencies using evenly-spaced time instances.

are tremendous. Moreover, this last is greater than the mean ($\text{std} > \text{mean}$) preventing the blindly use of such a sampling strategy for multi-frequential HB computations. In numerical methods, it is common to deal with ill-conditioned problems. However, we will show below that HB results are very sensitive to the condition number of the DFT matrix E . To do so, the linear advection problem presented in Sec. 4.1.1 and the channel flow problem presented in Sec. 4.2.1 are used with varying condition number and input unsteady signals.

5.2 Highlighting the problem

Linear advection problem A pure harmonic signal is imposed at the left boundary condition of the linear advection equation problem presented in Sec. 4.1.1

$$u_l(t) = 1 + \sin(2\pi ft). \quad (5.4)$$

The minimal condition number ($\kappa(E) = 1$) is obtained with evenly-spaced time instances. In fact, as the injected function is mono-frequential, the theoretical lower bound of the condition

number is obtained by using evenly-spaced time instances. The time instances of the harmonic balance computations are chosen to reach varying condition numbers such that $1 \leq \kappa(E) \leq 10$.

As shown in the previous section, configuration with high condition number amplify the errors due to the iterative resolution of the linear advection equation. This is illustrated in Figure 5.2 which shows the evolution of the results with a varying condition number. The amplitude of the sinusoidal function is either under or over-estimated when $\kappa(E) \neq 1$. However, the higher the condition number, the worse the accuracy in capturing the amplitude of the injected function. Moreover, when $\kappa(E) \geq 6$, the shape of the solution is even inverted which would lead to bad conclusions if analyzed as it.

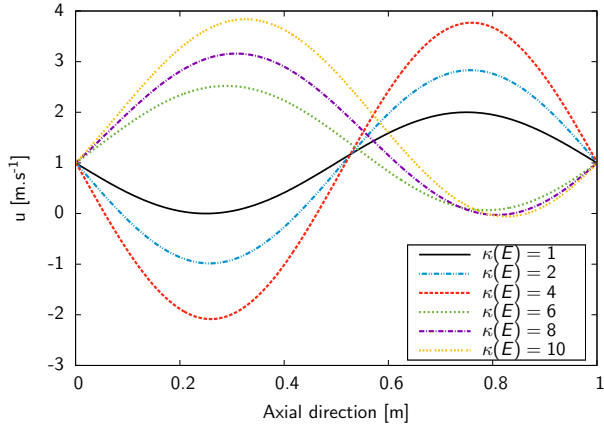


Figure 5.2: Linear advection of a sinusoidal function: numerical steady-state solutions at $t = 0$ for varying condition number.

Channel flow problem The previous example shows that the harmonic balance solutions are very sensitive to the condition number. To further analyze the condition number issue, we consider the unsteady channel flow with oscillating back-pressure as described in Sec. 4.2.1. It is computed with a single frequency oscillating back-pressure at the outlet: $f_1 = 3$ Hz, the second frequency having a zero amplitude ($a_2 = 0$)

$$p_{s_1}(t) = \bar{p}_{s_1} [1 + a_1 \sin(2\pi f_1 t)]. \quad (5.5)$$

This helps understanding the behavior of the HB source term within the Navier–Stokes equations framework.

As the oscillating back-pressure is composed of only one frequency, it is mono-frequential. Thus, by using evenly-spaced time instances, the condition number of the source term is $\kappa(E) = 1$. To highlight the issue related to the condition number, the time instances are chosen to reach varying condition numbers such that $1 \leq \kappa(E) \leq 3.43$. Two frequencies are specified for the HB computation: f_1 and its first harmonic $2f_1$.

The results in Figure 5.3 show that for a condition number $\kappa(E) \geq 2.24$ and wave input amplitude $a_1 = 0.05$, the computation diverges. However, the computations with the same condition numbers but with a smaller input amplitude $a_1 = 0.01$ converge. In fact, the condition number amplifies the errors made during the iterative process. When the input waves have a smaller amplitude, the iterative errors are lower by essence, hence the convergence.

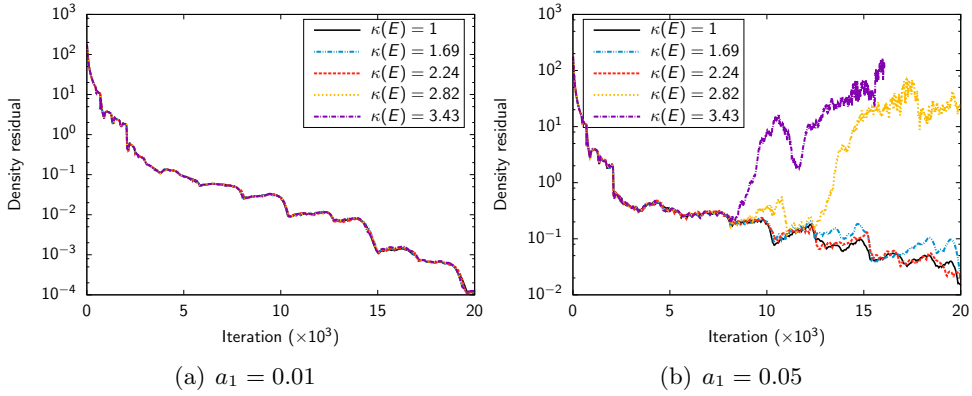


Figure 5.3: Relation between the condition number $\kappa(E)$ and the convergence of the solution.

The problem is that for a given configuration, the amplitude of the computed unsteady phenomena can not be *a priori* known.

Varying condition number values have been found in the literature. Precisely, Gopinath et al. [41] and Ekici and Hall [28] assessed their implementation of the multi-frequential HB method on a 2D multi-stage compressor. It is composed of a rotor sandwiched by two stators having 32, 40 and 50 blades, respectively. Various combinations of the stators blade passing frequencies are considered, but always with evenly-spaced time instances sampling the largest period. While Gopinath et al. [41] use $2N + 1$ samples (noted EVE $2N + 1$), Ekici and Hall [28] over-sample this period with $3N + 1$ time instances (noted EVE $3N + 1$). This leads to a rectangular $(2N + 1) \times (3N + 1)$ almost-periodic Fourier matrix that gives thus HB computations that are more CPU and memory demanding (see Sec. 3.5.4). The chosen frequencies and the *a posteriori* associated condition numbers of the above references are given in Tab. 5.2. In bold text is highlighted the condition number used in the original computations. The values vary between 2.07 and 16.66 which can lead to divergence with some high amplitude unsteadinesses. For $N = 4$, the oversampling approach of Ekici and Hall [28], using $3N + 1$ time instances, efficiently reduces the condition number. But for this case, the use of evenly-spaced time instances is sufficient as the condition number seems to be small enough for the considered magnitude of unsteadiness. However, such an approach fails when dealing with configurations

Reference and # harmonics	$\kappa(E)$
EVE ($2N + 1$)	EVE ($3N + 1$)
Gopinath et al. [41] ($N = 2$)	3.79
Ekici and Hall [28] ($N = 3$)	5.40
Gopinath et al. [41] ($N = 4$)	11.25
Gopinath et al. [41] ($N = 7$)	16.66

Table 5.2: Literature review of the condition number used in multi-frequential harmonic balance computations.

where:

- the amplitude of unsteadinesses is large as for instance large oscillations of a blade,
- the frequencies are widely segregated. In fact, as shown previously in Sec. 5.1, the more segregated the frequencies, the higher the condition number using a uniform time sampling. This condition number can be tremendous ($\kappa(E) \gg 100$) preventing the use of such an approach for given configurations.

Moreover, as the amplitude of unsteadinesses plays a crucial role in the amplification done by the condition number, the only way to ensure that a simulation will converge is to minimize the condition number. Therefore, the section below will be dedicated to the development of algorithms to achieve this goal.

5.3 Proposed cure: automatic optimization of time instances

Two algorithms that automatically choose the time instances in order to minimize the condition number are presented: first, the Almost Periodic Fourier Transform (APFT) algorithm, initially proposed in the literature for electronics problems and implemented by Guédene [42] in his PhD thesis, is described, then a gradient-based OPTimization algorithm over the condition number (OPT), developed in the current work, is presented.

5.3.1 Almost-Periodic Fourier Transform algorithm (APFT)

Based on the work of Kundert et al. [62] in electronics, the APFT algorithm has been implemented by Guédene [42] during his PhD thesis. The algorithm is designed to maximize the orthogonality of the multi-frequential IDFT matrix in order to minimize its condition number. To do so, a Gram-Schmidt orthogonalization procedure is conducted. First, the period associated with the smallest frequency ($2\pi/\omega_{min}$) is oversampled with M evenly-spaced time instances, $M \gg 2N + 1$ being specified by the user with N the number of frequencies. Considering these time instances, a rectangular multi-frequential IDFT matrix is built. This rectangular matrix can be seen as a set of M vectors of length $2N + 1$. The first vector noted V_0 (corresponding to $t = 0$) is arbitrarily chosen as the first time instance and any component in the direction of V_0 is removed from the following vectors using the Gram-Schmidt formula

$$V_s = V_s - \frac{V_0^\top V_s}{V_0^\top V_0} V_0, \quad s = 1 \cdots M - 1. \quad (5.6)$$

The remaining vectors are now orthogonal to V_0 . Initially, the vectors had the same Euclidean norm. Therefore, the vector that has now the largest norm is the most orthogonal to V_0 . It is thus assigned to V_1 . The previous operations are then performed on the $M - 2$ remaining vectors using V_1 as starting point. This process is repeated until the required $2N + 1$ vectors are defined. As a time instance corresponds to a vector, $2N + 1$ time instances are obtained, which enables the construction of the multi-frequential IDFT matrix. This algorithm is summarized in Algo. 1.

5.3.2 Gradient-based OPTimization algorithm (OPT)

A more direct approach is to seek directly a set of time instances that minimize the condition number of the associated multi-frequential IDFT matrix. This minimization problem can be solved numerically by an optimization algorithm.

Algorithm 1 The Almost Periodic Fourier Transform Algorithm (APFT)

```

 $\omega_{min} \leftarrow \min(|\omega_k|, 1 \leq k \leq N)$ 
for  $m \leftarrow 0 \dots M - 1$  do
     $t_m \leftarrow \frac{2\pi}{\omega_{min}} \frac{m}{M}$ 
end for
for  $n \leftarrow 1 \dots 2N$  do
    for  $m \leftarrow n + 1 \dots M$  do
         $V_m \leftarrow V_m - \frac{V_n^\top \cdot V_m}{V_n^\top \cdot V_n} V_n$ 
    end for
    argmax() returns the index of the largest member of a set
     $k = \text{argmax}(\|V_s^n\|, n + 1 \leq s \leq M)$ 
    swap( $V_{n+1}, V_k$ )
    swap( $t_{n+1}, t_k$ )
end for
 $\mathbb{T}_{optimized} \leftarrow [t_0 \dots t_{2N}]$ 

```

The limited memory optimization method of Byrd et al. [10] (noted L-BFGS-B) is used to look for a minimum of the condition number of the multi-frequential IDFT matrix $\kappa(E^{-1}[\mathbb{T}])$ as function of the time instances vector \mathbb{T} . This quasi-Newton algorithm approximates the inverse Hessian matrix $H(\kappa(E^{-1}[\mathbb{T}]))^{-1}$ with the BFGS formula in order to decrease the objective $\kappa(E^{-1}[\mathbb{T}])$ in the direction $-H(\kappa(E^{-1}[\mathbb{T}]))^{-1}\nabla\kappa(E^{-1}[\mathbb{T}])$. In the present case, the derivative $\nabla\kappa(E^{-1}[\mathbb{T}])$ of the objective with respect to the time instances is approximated by a first-order finite-differences. The descent direction is associated with the search for a zero of the gradient, which is a necessary condition for an extrema, in a second-order Taylor series. Finally, a line search on α is performed to minimize $\kappa(E^{-1}[\mathbb{T} - \alpha H(\kappa(E^{-1}[\mathbb{T}]))^{-1}\nabla\kappa(E^{-1}[\mathbb{T}])])$. An open-source implementation of this broadly-used algorithm is employed [80].

Gradient descent methods being local, the L-BFGS-B method converges to a local minimum of the condition number. This minimum is unsatisfying if the starting time instances vector \mathbb{T} is not well chosen, therefore a strategy to find an appropriate initial point is required. To this aim, the smallest angular frequency ω_{min} is used as a base angular frequency to create a set Ω

$$\Omega = [\frac{1}{M}\omega_{min} \dots \frac{m+1}{M}\omega_{min} \dots \omega_{min}], \quad (5.7)$$

where M denotes the desired number of initial guesses. This gives a set of periods. Each of them are then evenly sampled to obtain a set of time instances \mathbb{T}_m

$$\mathbb{T}_m = \left[0, \frac{2\pi M}{(2N+1)(m+1)\omega_{min}} \dots \frac{2N\pi M}{(2N+1)(m+1)\omega_{min}} \right] \quad (5.8)$$

These time instances sets are finally used as initial guesses for the L-BFGS-B algorithm.

The multi-frequential IDFT matrix is then built for each one of these time instances and the corresponding condition numbers are computed. A large number M , typically thousands, of fractions of the greatest period gives a large set of potential time instances vectors. This is acceptable given the very low cost of the computation of the condition number on such small

matrices of size $(2N + 1) \times (2N + 1)$. From this set, the time instances vector associated with the multi-frequential IDFT matrix having the smallest condition number is taken as a starting point. The optimization algorithm actually achieves a local adjustment of the time instances.

In this way, the exploitation capability of the gradient-based optimizer is well combined with the exploration capacity of the sampling. The OPT algorithm is summarized in Algo. 2.

Algorithm 2 The gradient-based OPTimization algorithm (OPT)

```

 $\omega_{min} \leftarrow \min(|\omega_k|, 1 \leq k \leq N)$ 
for  $m \leftarrow 0 \dots M - 1$  do
     $\omega_m \leftarrow \frac{m+1}{M} \cdot \omega_{min}$ 
    for  $i \leftarrow 0 \dots 2N$  do
         $t_i \leftarrow \frac{i \cdot 2\pi}{\omega_m \cdot (2N + 1)}$ 
    end for
     $\mathbb{T}_m \leftarrow [t_0 \dots t_i \dots t_{2N}]$ 
     $C_m \leftarrow \kappa(E^{-1}[\mathbb{T}_m])$ 
end for
argmin() returns the index of the smallest member of a set
 $k \leftarrow \text{argmin}(C_m, 0 \leq m \leq M - 1)$ 
min_l-bfgs-b ( $\kappa(E^{-1}[\mathbb{T}]), \mathbb{T}_{ini}$ ) returns the optimal time instances vector  $\mathbb{T}$  using the condition number  $\kappa(E^{-1}[\mathbb{T}])$  as objective function for the L-BFGS-B algorithm and  $\mathbb{T}_{ini}$  as starting point.
 $\mathbb{T}_{optimized} \leftarrow \text{min_l-bfgs-b}(\kappa(E^{-1}[\mathbb{T}]), \mathbb{T}_{ini} = \mathbb{T}_k)$ 

```

5.3.3 Assessment of the algorithms

Taking the same independent couples of frequencies (f_1, f_2) as the one used in Sec. 5.1, the condition number of the multi-frequential DFT matrix $\kappa(E)$ is computed, highlighting the ability of the different algorithms to choose the time instances that minimize the condition number, for any input frequencies. This assessment is only made for two frequencies, but the results are similar when increasing the number of frequencies. As two frequencies are involved, five time instances are required. The results for the three algorithms are depicted in Figure 5.4: (i) APFT: the Almost Periodic Fourier Transform algorithm, (ii) OPT: the gradient-based OPTimization algorithm and (iii) EVE: EVEnly spaced time instances oversampling the largest period as done in Gopinath et al. [41] using $2N + 1$ time instances and in Ekici and Hall [28] and Ekici et al. [30] using $3N + 1$ time instances. Table 5.3 gives some statistics about the results obtained with each algorithm to give the reader a quantitative overview of the efficiency of the different algorithms.

The EVE algorithms give fair results ($\kappa(E) \leq 2$) only at discrete couples of frequencies, corresponding to the particular cases where f_2 is a multiple of f_1 , as shown in Sec. 5.1. This is not promising as these cases can be computed using the mono-frequential formulation and thus does not need non-uniform time instances. Oversampling improves the results. In fact, the mean condition number obtained with $3N + 1$ samples indicates that the higher the number of time instances the better the condition number. However the multi-frequential DFT matrix becomes rectangular. The memory and CPU cost being proportional to the number of time instances (see Sec. 3.5.4), such a strategy can not be used in an industrial context. The APFT

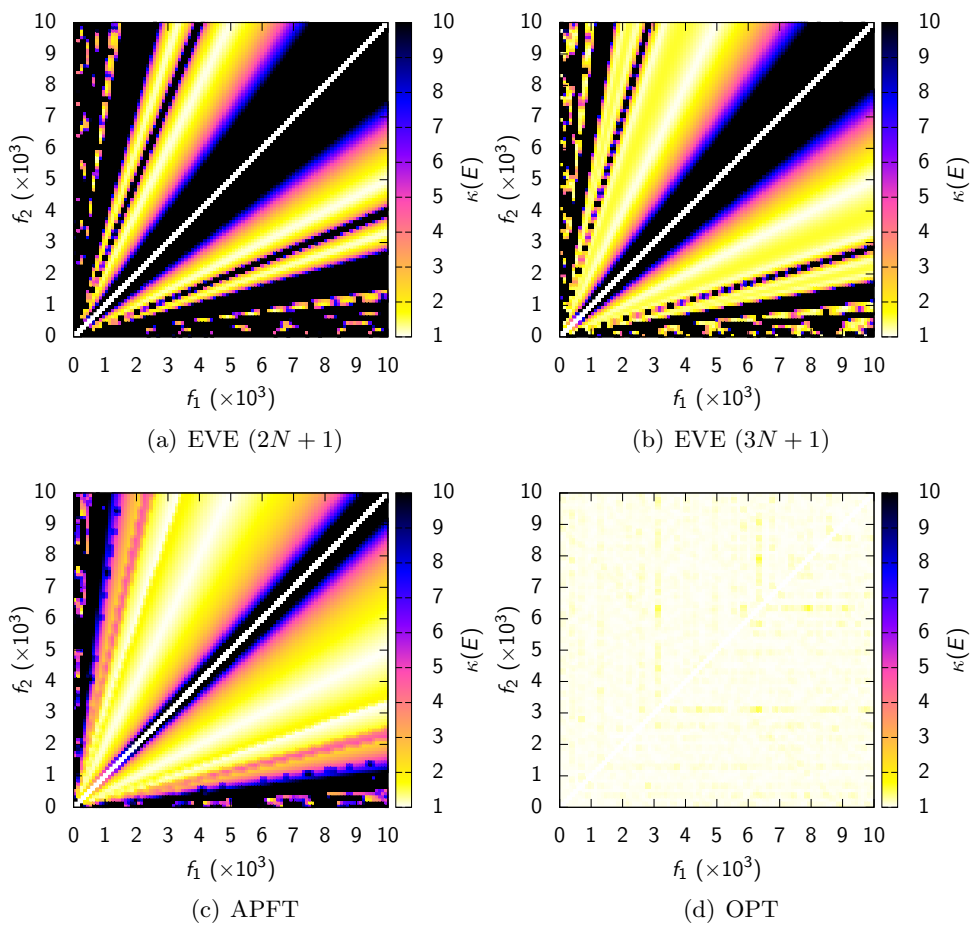


Figure 5.4: Condition number of the discrete Fourier transform matrix E using two independent frequencies and four different algorithms to choose the time instances.

algorithm improves the results, as it gives $\kappa(E) \leq 2$ for a large interval but fails when the frequencies are too close from one another ($f_1 \approx f_2$) or when they are significantly different ($f_1 \ll f_2$ or $f_1 \gg f_2$). Finally, the OPT algorithm gives a condition number close to unity for all couple of frequencies (f_1, f_2) . Moreover, as shown in Tab. 5.3, the OPT algorithm is the only one to give a standard deviation that is smaller than the mean, proving its robustness.

	min	max	mean	std
EVE (2N + 1)	1.0	9.4×10^{16}	1.5×10^{14}	2.8×10^{15}
EVE (3N + 1)	1.0	3.7×10^{16}	4.7×10^{13}	9.5×10^{14}
APFT	1.0	81.2	5.9	9.0
OPT	1.0	2.6	1.1	7.7×10^{-2}

Table 5.3: Condition number of the discrete Fourier transform matrix E statistics for two independent frequencies using four different algorithms to choose the time instances.

The configurations encountered in the turbomachinery literature are taken again to demonstrate the capability of the presented algorithms to minimize the condition number regardless of the input frequencies. The results are shown in Tab. 5.4. The APFT algorithm improves the condition number compared to the EVE (2N + 1) but can give relatively large condition numbers, here 12.95. In opposite, the OPT algorithm developed in the present contribution gives results close to one for the four configurations.

Reference and # harmonics	$\kappa(E)$			
	EVE (2N + 1)	EVE (3N + 1)	APFT	OPT
Gopinath et al. [41] ($N = 2$)	3.79	3.00	1.72	1.08
Ekici and Hall [28] ($N = 3$)	5.40	3.84	1.71	1.00
Gopinath et al. [41] ($N = 4$)	11.25	2.07	3.46	1.13
Gopinath et al. [41] ($N = 7$)	16.66	14.61	12.95	1.00

Table 5.4: Literature review of the condition number used in multi-frequential harmonic balance computations compared to the presented algorithms.

Thus, the non-uniform time sampling proposed by Guédeney [42] used together with the OPT algorithm developed in the present contribution enables to tackle problems with large frequency separation and/or large unsteadinesses, namely CROR aeroelasticity.

5.3.4 Distribution of the time instances

For harmonically-related frequencies, the set of time instances that minimize the condition number is provided by a uniform sampling of the fundamental frequency period as it gives the theoretical lower bound $\kappa(E) = 1$. Since the frequencies are harmonically related, the distribution of the time instances on the other frequencies is also uniform. In fact, considering

the frequency vector $F = [f_1 \cdots f_k = kf_1 \cdots Nf_1]$ and the time instances vector \mathbb{T} uniformly sampling the smallest frequency

$$\mathbb{T} = \left[0, \frac{1}{f_1(2N+1)} \cdots \frac{2N}{f_1(2N+1)} \right], \quad (5.9)$$

then the product of the i^{th} term of \mathbb{T} to its associated frequency is

$$f_1 \frac{i}{f_1(2N+1)} = k f_1 \frac{i}{k f_1(2N+1)} = f_k \frac{i}{f_k(2N+1)}. \quad (5.10)$$

Equation (5.10) means that evenly-spaced time instances for the fundamental frequency are still seen as evenly spaced by the k^{th} harmonic. This is an explanation why the condition number of the multi-frequential IDFT matrix E^{-1} will be unity as each frequency is sampled by evenly-spaced time instances [8].

Now, considering non-harmonically related frequencies, there is mathematically no reason for evenly-spaced time instances over the smallest frequency to be seen as evenly spaced by the other frequencies in general.

Figure 5.5 shows the distribution of the time instances, relative to each frequency period, obtained by the presented algorithms for the frequencies $f_1 = 3$ Hz and $f_2 = 17$ Hz. To do so, the chosen time instances are redistributed on the considered frequency period by applying a modulo to it

$$\mathbb{T}_j^{[f_k]} = \mathbb{T}_j \text{ modulo } 1/f_k \quad (5.11)$$

Then, they are divided by the latter, so that the results are dimensionless. In light gray line is depicted the $y = x$ function representing the evenly-spaced solution on the considered period. Baring in mind that if each frequency sees evenly-spaced time instances, then the condition number is the smallest, the optimal solution would be to have relative time instances on $y = x$ for each period. Running the EVE (2N+1), APFT and OPT algorithms leads to a condition number of 33.1, 3.8 and 1.1, respectively. The EVE algorithm gives a perfect distribution of the time instances with respect to period $1/f_1$ as the time instances are sampled on the period $1/f_1$. However, it gives results that are far from the evenly-spaced time instances within period $1/f_2$. The APFT algorithm is nowhere near the evenly-spaced solution for both the considered periods, but closer than EVE regarding period $1/f_2$. Finally, the OPT algorithm is the only one to be close to the evenly-spaced solution for each period considered. This explains the very good condition numbers obtained with the OPT algorithm.

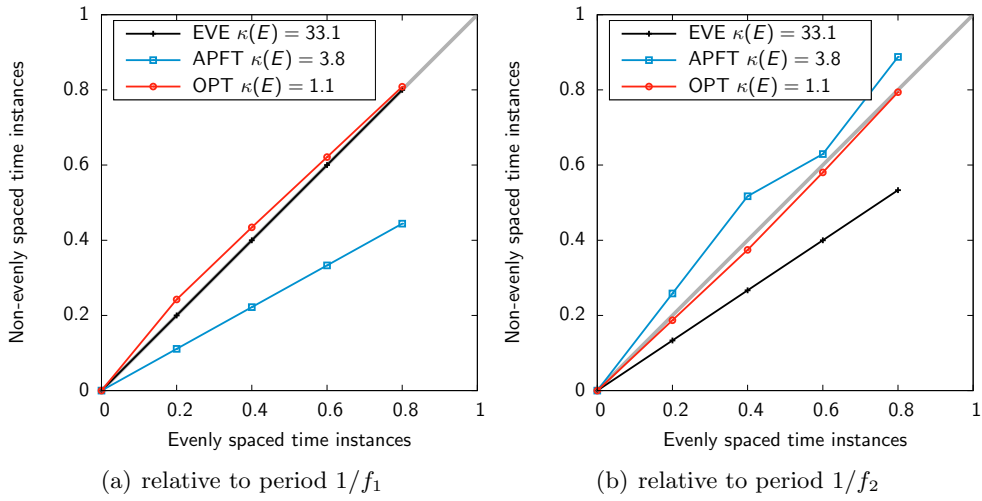


Figure 5.5: Distribution of the time instances on each frequency periods.

Summary

In this chapter, we demonstrated that the time sampling has a major effect on the stability of the multi-frequential harmonic balance approach, due to the condition number of the discrete Fourier transform matrix. One way to tackle this issue, is to consider a non-uniform time sampling along with an algorithm to properly choose the time instances as proposed by Guédeney [42]. The Almost-Periodic Fourier Transform algorithm (APFT) algorithm, originally developed by Kundert et al. [62] and implemented by Guédeney [42], is shown to improve the discrete Fourier transform matrix condition number. However, for segregated frequencies, this condition number is shown to remain too large to be used within an industrial context. As the aeroelasticity of contra-rotating open rotors is by essence composed of segregated frequencies, new algorithms are needed. This is why, a gradient-based OPTimization algorithm (OPT) has been developed in the current work. It directly minimizes the condition number thanks to a gradient-based optimization method. This last has proved to give a condition number that is almost unity (*i.e.* the theoretical lower bound) for any input frequencies, thus alleviating the stability issues encountered for arbitrary multi-frequential HB computations.

Convergence of Fourier-based time methods for turbomachinery wake passing problems

Abstract

Efficiency of Fourier-based time methods results from a trade-off between accuracy and costs requirements. On one hand, the accuracy depends on the number of harmonics used to represent the frequency content of the time signal; on the other hand, computational costs and memory consumption of the computations also scale with the number of harmonics. The problem is that this number is configuration-dependent. Studies on the convergence of Fourier-based time methods for turbomachinery simulations have been previously reported in the literature, but with scattered results. For instance, using a frequency-domain approach, Vilmin et al. [104] obtain accurate solutions using 5 harmonics for a compressor stage and 3 harmonics for a centripetal turbine stage. For a transonic compressor stage with forced blade vibration, Ekici [27] use up to 7 harmonics with a time-domain harmonic balance approach. Finally, for a subsonic compressor stage, Sicot et al. [90] report that 4 harmonics is the minimal requirement to properly capture wake interactions. Moreover, a high number of harmonics ($\gg 10$) can prevent the use of such an approach, as it might be more expensive than a classical time-marching approach. This is particularly true on CROR configurations where the number of harmonics needed to reach convergence has been shown to be greater than ten on some configurations, as shown by François [33]. In this chapter, the accuracy and convergence properties of Fourier-based time methods are investigated. It is highlighted that the convergence rate of these methods, in terms of harmonics required to describe the solution with a given level of accuracy, depends on the spectral content of the solution itself: Fourier-based time methods are particularly efficient for flow problems characterized by a narrow Fourier spectrum. Based on the similarity law of Lakshminarayana and Davino [64], the specific case of turbomachinery wake passing is considered and an analytical truncation error is defined. Then, a model turbomachinery problem is set up, which shows that the analytical truncation error can be *a priori* estimated using a mixing-plane steady computation. This work has been submitted in

A. Gomar, Q. Bouvy, F. Sicot, G. Dufour, P. Cinnella, and B. François. Convergence of Fourier-based time methods for turbomachinery wake passing problems. *Journal of Computational Physics*, submitted in December 2013

6.1 Periodic problems with an infinite Fourier spectrum

In fluid dynamics, the simplest model representative of a shock wave is the step function. It is a discontinuous function that may be difficult to capture for Fourier-based time methods. The periodic step function over the period $T = L_x/c$ is defined as

$$u_l(t) = \begin{cases} 0, & \text{if } 0 \leq t < \frac{T}{2}, \\ 1, & \text{if } \frac{T}{2} \leq t < T. \end{cases} \quad (6.1)$$

The linear advection model problem defined in Sec. 4.1.1 is used here to assess the capability of the harmonic balance approach to capture discontinuous unsteadinesses.

Figure 6.1 depicts the results of HB computations using one to six harmonics at different time instances. The convergence rate is slow, and for the six-harmonics HB computation the shape of the rectangular function is still barely captured. The well-known Gibbs [37] phenomenon is observed, which is a typical drawback of Fourier-based methods applied to discontinuous problems, see *e.g.* Canuto et al. [14].

The \mathcal{L}_2 -norm of the error is depicted in Figure 6.2. The convergence of the sum of sine functions, that has been studied in Sec. 4.1.3, is added for comparison. The convergence rate is different from the previous one: the error decreases slowly when more harmonics are introduced, but the exact solution is never reached, unless an infinite number of harmonics is considered.

The discrete Fourier transform of the results is computed and compared to the analytical result in Figure 6.3. For this case, the spectrum is not finite and cannot be captured accurately with a finite number of samples. Adding more harmonics improves the results but the analytical solution is out of reach of the harmonic balance approach.

To summarize, Fourier-based time methods are unadapted for unsteady signals for which the Fourier spectrum is wide. In the next section, wake passing is modeled by an analytical function. This allows to assess the convergence of Fourier-based time methods for such problems.

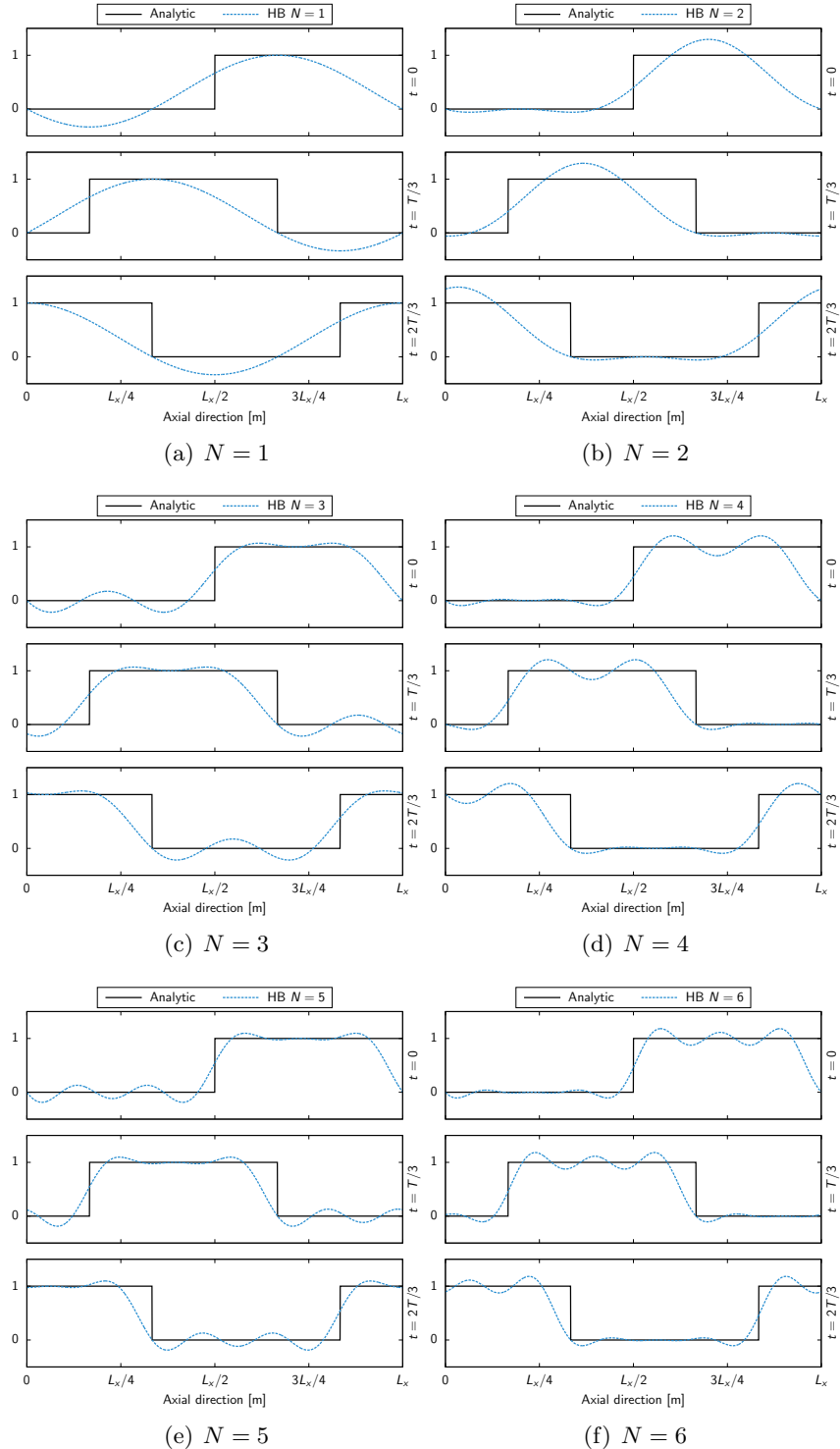


Figure 6.1: Linear advection of a rectangular function: numerical solutions at different time instances for different numbers of harmonics.

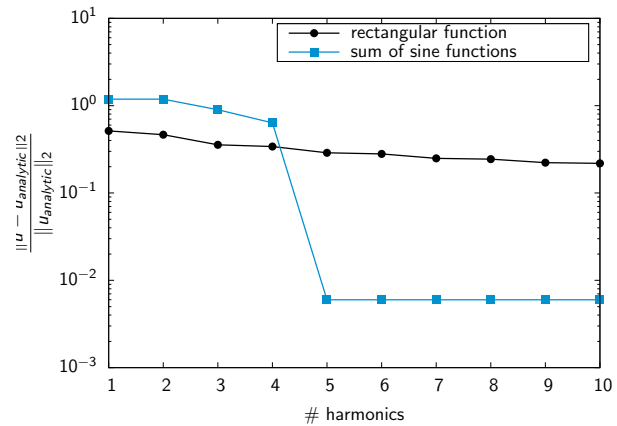


Figure 6.2: Linear advection of a rectangular function: convergence of the HB method error.

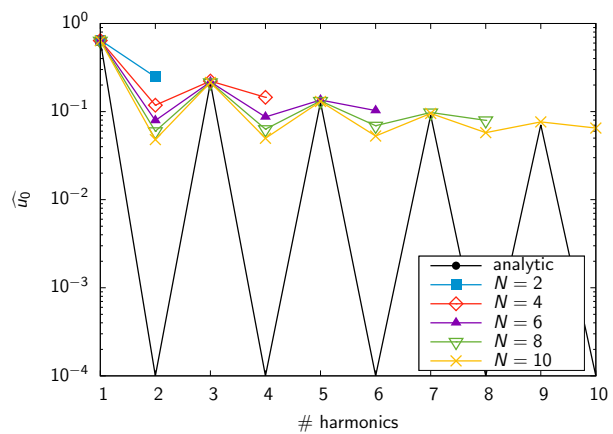


Figure 6.3: Linear advection of a rectangular function: discrete Fourier transform.

6.2 Toward turbomachinery wakes

Consider for simplicity a turbomachinery stage composed of two rotors, as for instance a CROR configuration. A wake is shed behind the upstream rotor. It is stationary in the frame of reference attached to the upstream rotor. However, when it crosses the rotor/rotor interface,

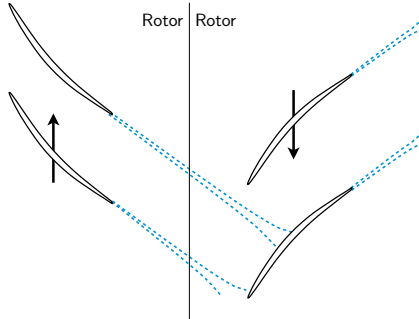


Figure 6.4: Characteristic wakes in a CROR configuration.

the wake becomes unsteady in the frame of reference of the second wheel. Thus, an upstream steady spatial distortion becomes unsteady in the downstream row.

Lakshminarayana and Davino [64] showed that the wake behind turbomachinery blades follows a similarity law for the velocity. It can be empirically approximated by a Gaussian function:

$$u_l(t) = u_m \left[1 - \Delta u \cdot e^{-0.693(2\frac{\theta}{L})^2} \right], \quad (6.2)$$

where u_m denotes the free-stream velocity, Δu the axial wake velocity deficit, and L the wake width, defined as the full width at half maximum. The azimuthal coordinate θ is here assimilated as ct/L_x .

Therefore, in the downstream frame of reference, wakes coming from the upstream wheel can be represented, to a first approximation, as the periodic advection of a Gaussian function from the inter-wheel interface.

To study the convergence properties of such a function, we consider again the linear advection problem defined in Sec. 4.1, with u_l now taken equal to a Gaussian function. The full width at half maximum L of the wake is set to 10% of the domain size, u_m is set to c and Δu to 10% of u_m .

Figure 6.5 depicts the HB computations for one to six harmonics. The numerical solution start to converge toward the Gaussian function starting from $N = 6$ harmonics. When the number of harmonics is too small, the width and the depth of the wake are badly approximated by the method, and the solution exhibits some spurious oscillations.

Figure 6.6 shows the quantitative convergence of the \mathcal{L}_2 error. The convergence curves for the two functions studied in the previous sections are also reported for comparison. The error follows now a nearly exponential convergence. The discrete Fourier transform of the results is depicted against the analytical result in Figure 6.7. The $N = 2$ and $N = 4$ computations badly capture the amplitudes of the resolved harmonics. Starting from $N = 6$, some of the lower frequencies are correctly captured, whereas high frequencies are always under-estimated. The capture of the amplitudes improves when further harmonics are added to the computation.

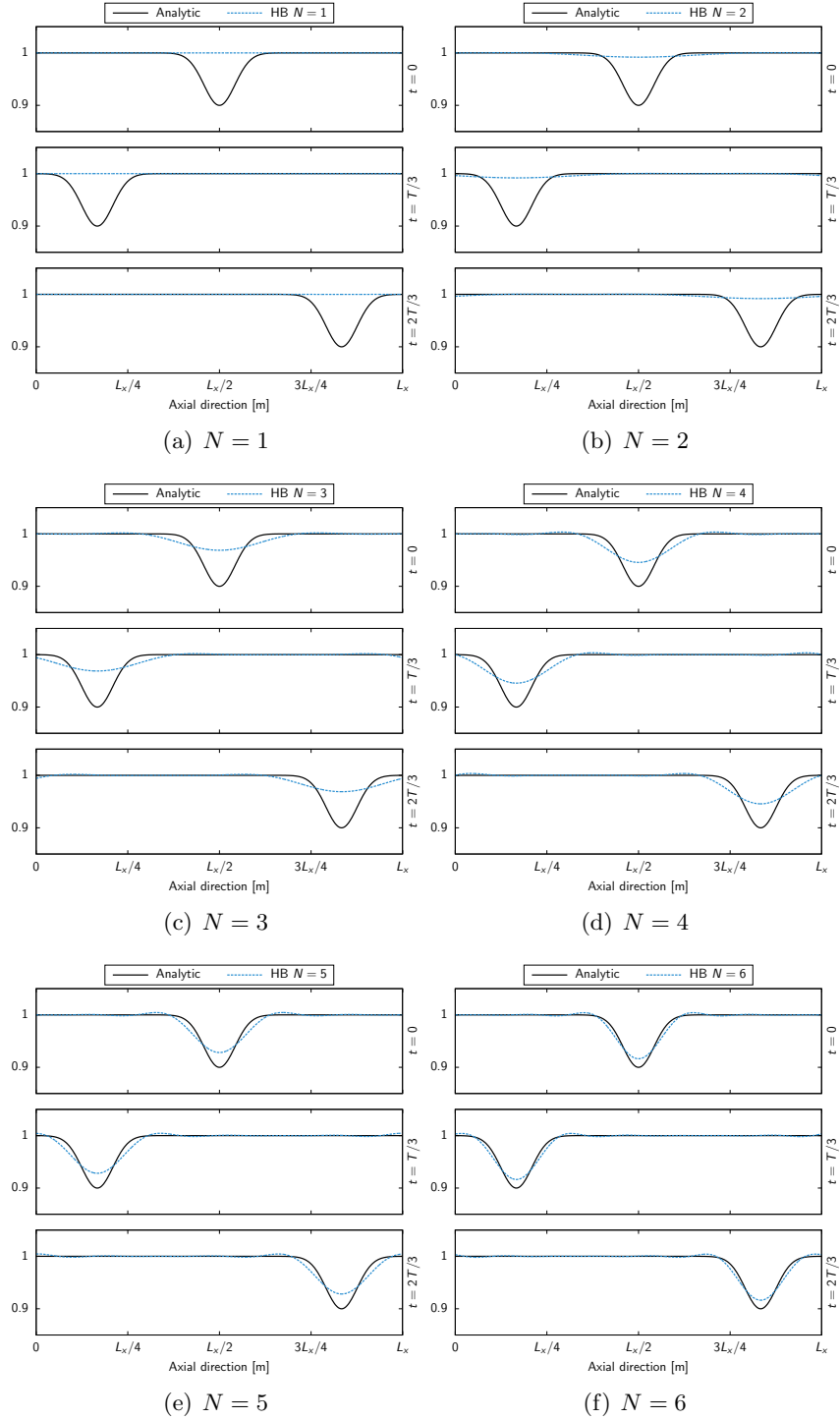


Figure 6.5: Linear advection of a Gaussian function representing a turbomachinery wake: numerical solutions at different time instances for different numbers of harmonics.

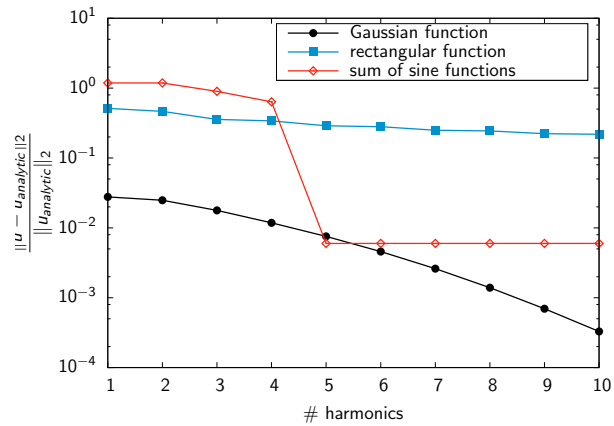


Figure 6.6: Linear advection of a Gaussian function representing a turbomachinery wake: convergence of the HB method error.

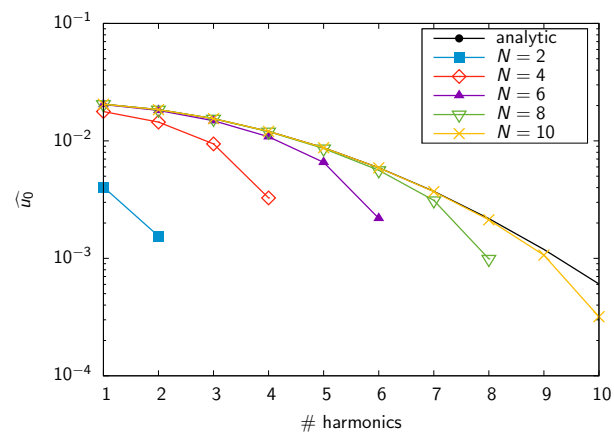


Figure 6.7: Linear advection of a Gaussian function representing a turbomachinery wake: discrete Fourier transform.

For a better understanding of the HB convergence behavior, we consider the spectral content of the Gaussian wake model. Precisely, the Fourier transform \hat{g} of a Gaussian function g defined as

$$g(x) = Ae^{-\alpha x^2}, \quad (6.3)$$

where A and α are constants, is

$$\hat{g}(f) = A'e^{-\alpha' f^2}, \quad (6.4)$$

where

$$\begin{cases} A' = A\sqrt{\frac{\pi}{\alpha}}, \\ \alpha' = \frac{\pi^2}{\alpha}. \end{cases} \quad (6.5)$$

For the similarity law of Lakshminarayana and Davino, α and α' can be identified as

$$\alpha = 0.693 \left(\frac{2}{L} \right)^2, \quad \alpha' = \frac{1}{0.693} \left(\frac{\pi L}{2} \right)^2. \quad (6.6)$$

The exponential factor of the wake law α is inversely proportional to its Fourier counterpart α' , meaning that their width will vary in opposite way: the thinner the wake, the wider its spectrum and *vice-versa*.

The convergence rate is inherently linked to the spectrum of the considered unsteady signal. As for the present case we know the analytical wake spectrum, we define the theoretical truncation error as the ratio of the energy contained in the unresolved part of the spectrum to the overall energy content of the full spectrum

$$\varepsilon_{th}(f) = \sqrt{\frac{\int_f^\infty |\hat{g}(\zeta)|^2 d\zeta}{\int_0^\infty |\hat{g}(\zeta)|^2 d\zeta}}. \quad (6.7)$$

Introducing the error function defined as

$$\text{erf}(x) = \frac{2}{\sqrt{\pi}} \int_0^x e^{-t^2} dt, \quad (6.8)$$

and the complementary error function defined as

$$\text{erfc}(x) = 1 - \text{erf}(x), \quad (6.9)$$

then

$$\int_0^\infty |\hat{g}(\zeta)|^2 d\zeta = \frac{1}{2} \int_{-\infty}^\infty |\hat{g}(\zeta)|^2 d\zeta \quad (6.10)$$

$$= \frac{A'^2}{2} \sqrt{\frac{\pi}{2\alpha'}}, \quad (6.11)$$

and

$$\int_f^\infty |\hat{g}(\zeta)|^2 d\zeta = \frac{A'^2}{2} \sqrt{\frac{\pi}{2\alpha'}} \text{erfc}(\sqrt{2\alpha'} f). \quad (6.12)$$

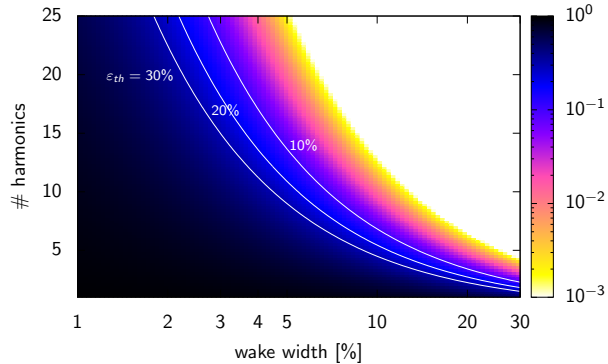


Figure 6.8: Theoretical truncation error of the Lakshminarayana and Davino wake law.

The theoretical truncation error can finally be written as

$$\varepsilon_{th}(f, L) = \sqrt{\operatorname{erfc}(\sqrt{2\alpha'(L)}f)}. \quad (6.13)$$

One can notice from Eq. (6.13) that the truncation error does not depend on the wake deficit Δu but only on the wake width L .

Eq. (6.13) is depicted in Figure 6.8 for varying numbers of harmonics and wake widths. It can be seen that the wider the spectrum, the higher the number of harmonics needed to reach a certain level of error. Moreover, for a thin wake width (*e.g.* 2% of the pitch) the number of harmonics required to capture it with a truncation error of 10% is up to 25 harmonics. In the limit of $L \rightarrow 0$, the wake becomes a Dirac function which represents the worst possible case, as the rectangular function was. In the preceding example, the Gaussian function had a width of 10% which, according to Eq. (6.13), is captured by using $N = 7$ harmonics for a target of 10% error.

This section provided analytical results of the convergence of Fourier-based time methods in the case of wake passing. To confirm these results, a turbomachinery like model problem is set up and solved using the Euler equations in the following section.

6.3 Application to a model turbomachinery configuration

6.3.1 Presentation of the case

We consider a simplified configuration modeling a turbomachinery stage. It consists of a periodic azimuthal perturbation propagated downstream of the inlet boundary of the computational domain. The domain is made of two grid blocks in relative motion, so that the perturbation, which is steady in the upstream block, is seen as unsteady by the downstream one. It is thus representative of turbomachinery wakes propagated across an inter-wheel interface. Figure 6.9 shows a sketch of the considered model turbomachinery problem.

The blocks are generated in cylindrical coordinates such that the presented configuration can be assimilated to a slice of a turbomachinery stage. Without loss of generality, we set the rotation velocity of the upstream block to zero (stator). The stator is composed of $B_{stator} = 10$ "virtual" blades and the rotor of $B_{rotor} = 12$ ones. The stator's pitch is therefore larger than the rotor's. These are termed "virtual" blades as no blade is actually meshed. The pitch ratio is representative of contra-rotating open rotor applications in which the first row contains more

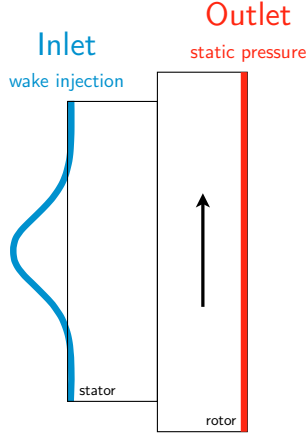


Figure 6.9: Sketch of the model turbomachinery flow problem.

blades than the second one. Indeed, in contra-rotating open rotor applications, the number of blades is typically smaller than classical turbomachinery configurations.

A wake is axially injected at the inlet of the turbomachinery model problem following the Lakshminarayana and Davino [64] similarity law.

6.3.2 Numerical Setup

The flow is modeled using the Euler equations in order to avoid wake thickening and vanishing associated with viscous effects. The velocity is not imposed at the inlet directly but rather through the total pressure and the total enthalpy distributions

$$p_{i0}(\theta) = p_{i_{ref}} \left[1 - \Delta p_i \cdot e^{-0.693(2\frac{\theta}{L})^2} \right], \quad (6.14)$$

$$h_{i0}(\theta) = h_{i_{ref}} \left[1 - \Delta h_i \cdot e^{-0.693(2\frac{\theta}{L})^2} \right], \quad (6.15)$$

where $p_{i_{ref}}$ is the inlet reference total pressure, Δp_i the total pressure deficit in the wake, $h_{i_{ref}}$ the reference total enthalpy, Δh_i the total enthalpy deficit in the wake and L the wake width. To impose a realistic distortion, the total pressure and enthalpy deficits are estimated from a separate turbomachinery simulation. This leads to $\Delta p_i = 0.025$ and $\Delta h_i = -0.007$. The negative sign is due to overturning in the wake, which is due to velocity composition, and therefore specific to rotors. The static pressure p_{s1} is imposed at the outlet

$$p_{s1} = \frac{p_{i_{ref}}}{\left(1 + \frac{\gamma-1}{2} M_0^2\right)^{\frac{\gamma}{\gamma-1}}}, \quad (6.16)$$

the mean velocity is thus set by imposing the target mean Mach number value M_0 . At the azimuthal boundaries, phase-lag conditions [31] are used to take into account the space-time periodicity.

The *elsA* [12] CFD code is used. Roe's scheme [82] along with a second-order MUSCL extrapolation is used for the spatial discretization of the convective fluxes and an implicit backward Euler scheme is used to march the HB equations in pseudo-time.

Each grid block has a radial extent of five grid points, *i.e.* four cells. The azimuthal grid density is similar in the stator and in the rotor blocks to guarantee a consistent capture of the wake on each side of the interface. To do so, if $\Delta\theta_{cell}$ denotes the azimuthal length of a cell at the interface, then

$$\Delta\theta_{cell} = \frac{2\pi}{B_{stator}} \frac{1}{N_{stator}} = \frac{2\pi}{B_{rotor}} \frac{1}{N_{rotor}}, \quad (6.17)$$

where N_{stator} and N_{rotor} are the number of cells in the stator and the rotor, respectively. Several wake thicknesses will be tested below from 30% down to 1% of the pitch. For this thinnest wake, mesh convergence is obtained with 500 cells in the azimuthal direction of the stator, which gives 600 cells for the rotor block. 30 grid points are put in the axial direction. Moreover, a constant aspect ratio of 5 with respect to the azimuthal length of the cells is kept, which sets the axial length of the case. This leads to a total number of grid points of approximately 170,000.

Convergence of the iterative procedure used to solve the HB equations is achieved after 3,000 iterations for all the simulations.

6.3.3 Spectral convergence study

The primary interest in this section is the wake capturing capabilities of the Fourier-based time methods in the rotating part. To analyze this, two error measures are defined and evaluated.

Spatial-spectrum based error measure Initially, we propose an error measure (ε_1) based on the loss of signal energy induced by the HB method at the interface. In fact, in the stator part, the wake is steady and is thus not filtered by the HB operator. Conversely, in the rotor part, the wake becomes unsteady due to the relative speed difference between the stator and the rotor. However, only a finite number of harmonics N is used to describe the unsteady field, hence the filtering.

The first error quantification is set up to quantify this filtering by using only spatial information and is defined as the L_2 -norm applied on the difference between the rotor and the stator spectra. It is equivalent to the analytical truncation error defined in Eq. (6.7). Indeed, the error is described as the ratio of the unresolved energy in the rotor block to the energy of the full spectrum, *e.g.* that of the stator block

$$\varepsilon_1(N) = \sqrt{\frac{\sum_{f=1}^{f_{max}} |\hat{s}_N^\theta(f) - \hat{r}_N^\theta(f)|^2}{\sum_{f=1}^{f_{max}} |\hat{s}_N^\theta(f)|^2}}, \quad (6.18)$$

where \hat{s}_N^θ denotes the spatial Fourier transform (indicated by the $\hat{\cdot}$ operator) of the azimuthal extraction (shown by superscript θ) of the result of a HB simulation using N harmonics, in the stator; \hat{r} denotes the spectrum of the signal transferred to the rotor. The highest frequency present in the spectrum is dictated by the spatial discretization. Thus, $f_{max} = 1/2\Delta\theta_{cells}$, using the notations of Eq. (6.17). As the azimuthal cell size is similar in both blocks, the same sampling is used leading to the same frequencies in both stator and rotor spectra. Details of the algorithm used to compute ε_1 are given in Appendix A.1.

The azimuthal velocity distributions (left hand-side) and the corresponding spatial spectra (right hand-side) are presented in Figure 6.10 for a relative wake thickness of 5% with respect

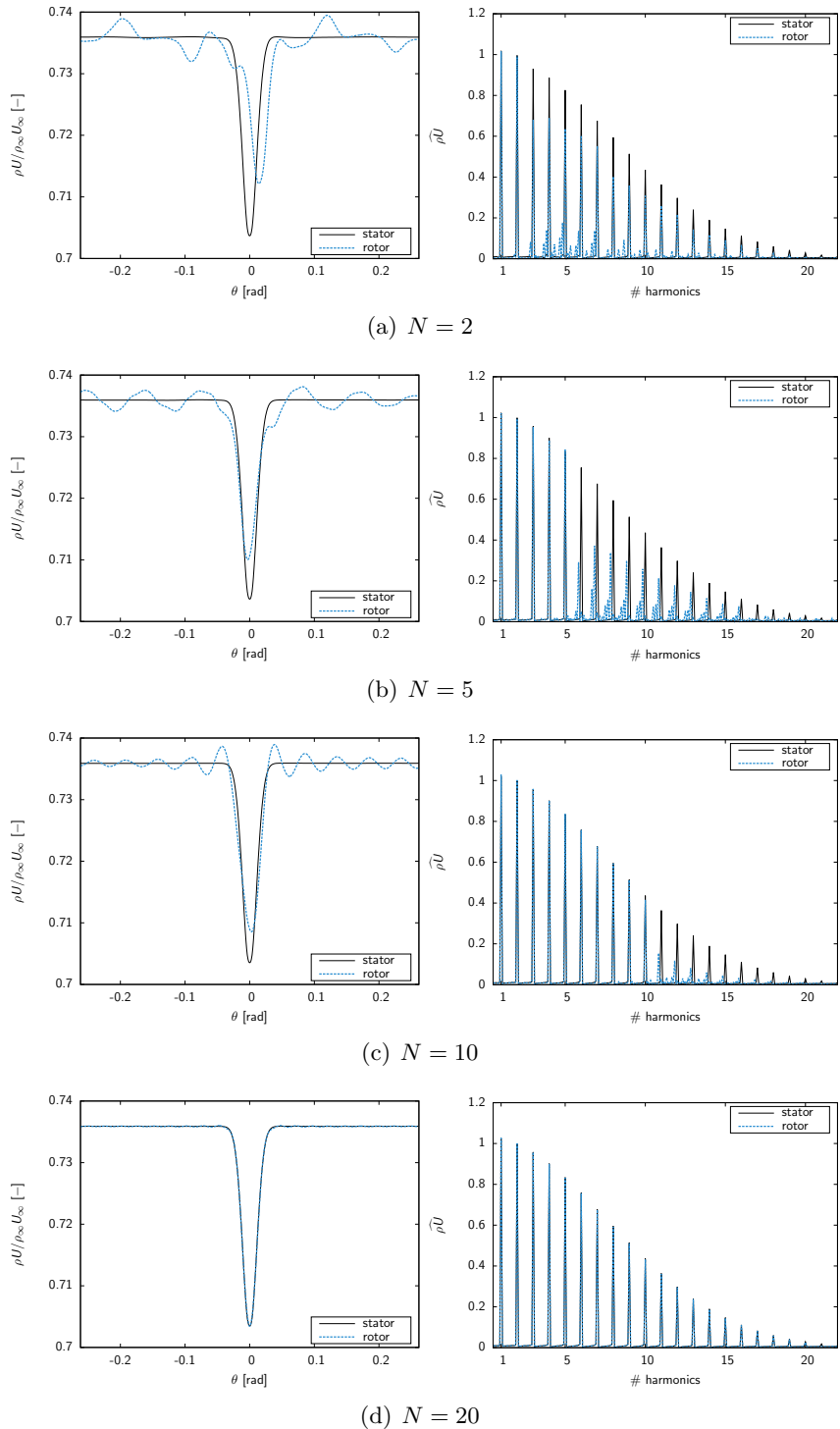


Figure 6.10: Wake of $L = 5\%$ width extracted in stator and rotor blocks. Signal and spatial Fourier analysis for different computations.

to the pitch and for HB computations using $N = 2, 5, 10$ and 18 . For the stator, the azimuthal distribution follows a Gaussian function as expected. On the contrary, the rotor distribution is aliased by the HB discretization and exhibits spurious oscillations that tend to disappear when the number of harmonics used in the computation increases. For $N = 10$, some oscillations are still present, but the wake captured in the moving block begins to converge to that leaving the upstream block.

Inspection of the spectra suggests the same conclusions. The amplitude of $\widehat{\rho U}$ improves when increasing the number of harmonics. For $N = 20$, the spectrum of the rotor block matches that of the stator block. This is consistent with the theoretical analysis, in which more than $N = 10$ harmonics are needed to capture the wake with less than 20% of error for this particular wake width (see Figure 6.8).

The filtering introduced by the HB approach acts primarily on the time resolution. For under-resolved HB computations, a dissipation error is observed. This dissipation is not spatially uniform and gives rise to dispersion errors on the spatial spectrum and to spurious high-frequencies as shown in Figure 6.10 for HB computations $N = 2$ to $N = 10$. These effects vanish when the HB computations converge, *i.e.* for $N \geq 10$. Therefore, the spectrum of the unresolved spurious frequencies is imposed to have a zero amplitude value to compute ε_1 .

In summary, for this wake thickness, the temporal filtering on a simulation involving less than ten harmonics is too harsh and leads to a significant amount of unresolved energy, which deteriorates the numerical representation of the wake.

For a more quantitative analysis, we compute the error measure ε_1 for each computation ranging over different wake thicknesses and numbers of harmonics. Results are summarized in Figure 6.11. Because it quantifies the unresolved energy in comparison to the resolved energy,

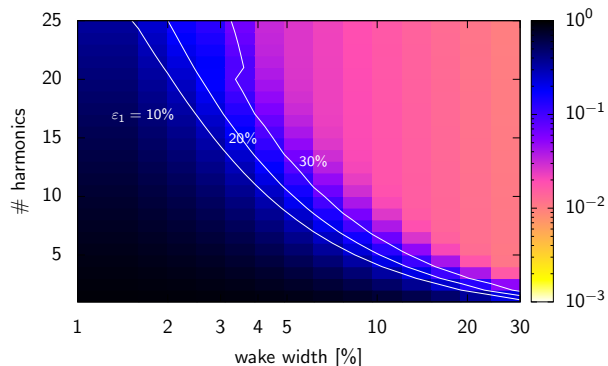


Figure 6.11: Evaluation of the error due to the wake capturing using the first error quantification ε_1 .

ε_1 exhibits a behavior similar to that of the theoretical error ε_{th} for a Gaussian function (Figure 6.8). The iso-error contours have a similar shape compared to the analytical ones. The conclusions are equivalent: the truncation error decreases with the wake thickness and with the number of harmonics used to capture the wake. Nevertheless, for thicker wakes and higher numbers of harmonics, the error measure ε_1 is over-estimated. For instance, around $N = 15$ and for $L = 25\%$, $\varepsilon_1 \approx 10^{-2}$ whereas the theoretical error ε_{th} is less than 10^{-4} . As discussed in the following, the error measure ε_1 does not represent a realistic measure, because of the spatial Fourier transform performed to compute the error.

As can be seen in Figure 6.12, the Fourier transform of the spatial signal in the stator

block tends to a plateau. The thicker the wake, the lower the frequency for which the plateau appears: approximately 15 harmonics for $L = 10\%$ (see Figure 6.12(a)) and 6 harmonics for $L = 25\%$ (see Figure 6.12(b)). Actually, for a N -harmonic HB computation, the spectrum is explicitly filtered in the moving block leading to an amplitude equal to zero above the N^{th} harmonic. Therefore, when the HB computations are converged, the difference between the spatial spectra in the stator and in the rotor block is driven by the plateau present in the spatial spectrum of the stator block.

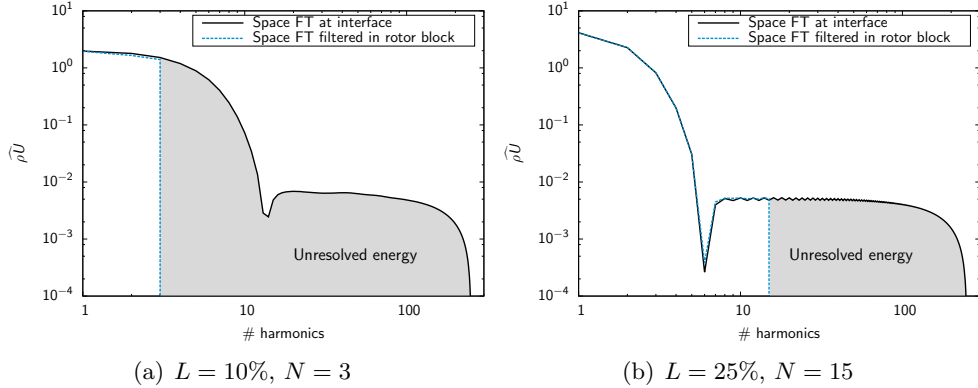


Figure 6.12: Discrepancies between spatial and temporal spectra.

This behavior is linked to the windowing of the signal on a bounded interval, namely the pitch. To highlight that, the influence of a modification on the inlet boundary condition is analyzed. The inlet wake distortion used in the model turbomachinery configuration is originally based on the analytical Lakshminarayana and Davino Gaussian law (see Eq. (6.2)). However, this law is discretized and imposed on a bounded interval that spans the angular pitch. As the relative thickness increases, the inlet condition diverges from the analytical Gaussian law for which the angular pitch is theoretically infinite. This is shown in Figure 6.13 through the spectra of three Gaussian laws. The relative thickness of the laws are modified through the size of the pitch $\Delta\theta$. The multiplication by a factor 100 of the pitch leads to a disappearance of the plateau in the spectrum, which accurately matches with the Fourier transform of a Gaussian function.

To sum up, a plateau appears in the spatial spectrum of the stator block. This plateau is explicitly filtered in the rotor block above the N^{th} harmonic, leading to an over-estimation of the first error measure. This over-estimation drives the error value for higher number of harmonics and thicker wakes. However, for lower number of harmonics and thinnest wakes, the computed error measure is superimposed with the analytical one.

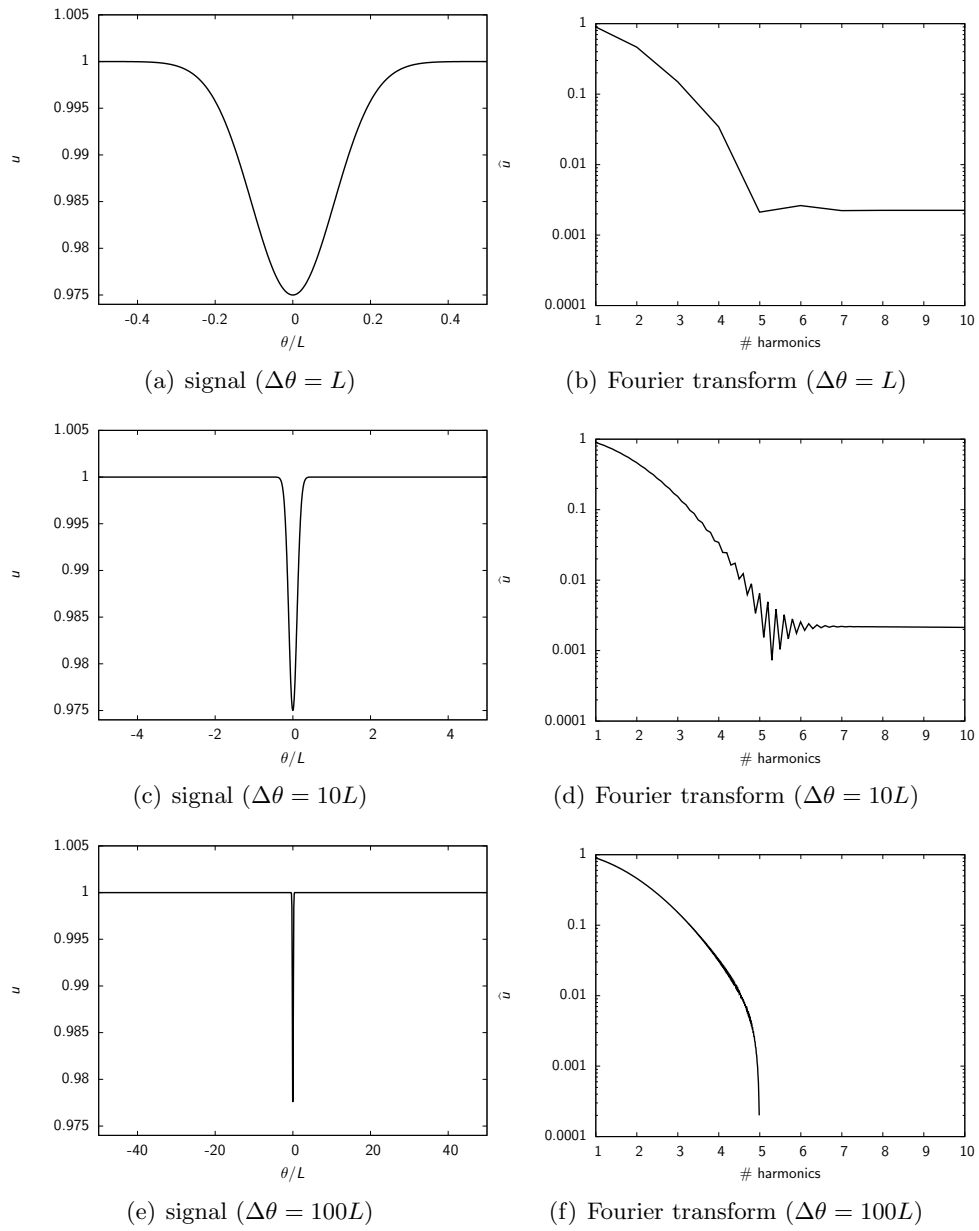


Figure 6.13: Evolution of the spectrum of the inlet boundary condition for different angular pitches.

Spatial/Time duality error measure To get a more realistic error measure, we take again into account the energy loss through the interface, but based on a spatial/time duality. As this loss of energy is precisely related to the filtering introduced on the temporal signal by the HB approach, the second error quantification ε_2 addresses the result on the temporal information.

Near the interface of the blocks, consider a fixed observer in the rotor frame of reference. This observer sees an unsteady wake passing as the blocks have a relative speed difference. The first error quantification has shown the influence of the number of harmonics on the spatial signal in the rotor block. The spatial/time duality error quantification will now point that this spatial influence is due to a temporal filtering done by the HB approach.

Following the same notation as in Eq. (6.18), the second error measure is written as

$$\varepsilon_2(N) = \sqrt{\frac{\sum_{f=1}^{f_{max}} |\hat{s}_N^\theta(f) - \hat{r}_N^t(f)|^2}{\sum_{f=1}^{f_{max}} |\hat{s}_N^\theta(f)|^2}}, \quad (6.19)$$

where superscript t denotes the temporal version of the Fourier transform. By definition, ε_2 quantifies the matching between a spatial signal and a temporal information. Again, the error is described as the unresolved energy in the rotor block, divided by the energy of the full spectrum, *e.g.* that of the stator block. For ε_1 , the amplitude of the harmonics above the N^{th} one was imposed to zero. On the contrary, for ε_2 , the temporal spectrum in the rotor block is, by essence null above the N^{th} harmonic, as the filtering acts on temporal values. Details of the algorithm used to compute ε_2 are given in Appendix A.2.

Figure 6.14 shows time signals extracted at two different azimuthal positions at the interface of the rotor block, named loc 1 and loc 2. The small phase shift between the two signals is due to the space lag between the two points, and is the same for any choice of the number of harmonics used in the computation. On the contrary, differences in terms of amplitude are only due to the use of an insufficient number of harmonics: as the number of modes used for the time approximation is increased from $N = 5$ to $N = 15$, the amplitude of the space-shifted signals tends to converge to the same value, and spurious oscillations tend to disappear. Therefore, in the following, only loc 1 will be considered.

Figure 6.15 describes the space and time spectra of the axial momentum $\widehat{\rho U}$ at loc 1, for computations using $N = 2, 5, 10$ and 20 harmonics and for a wake width of $L = 5\%$. The spatial spectrum contains the whole wavelength content associated to the incoming wake; on the contrary, due to the filtering introduced by the HB approach, the time spectrum is composed of only N harmonics.

For computations using less than 10 time harmonics, time spectra are truncated, and the amplitude of $\widehat{\rho U}$ differs from that of the corresponding mode in the spatial spectrum.

As the number of time harmonics is increased, the amplitude of lower harmonics becomes closer and closer to that of the corresponding harmonic in the reference signal, and errors move toward the higher resolved harmonics. For $N = 20$, the amplitudes of the 20 resolved harmonics are similar for both the time and space spectra.

In summary, the preceding analysis shows that, for under-resolved HB computations, the time signal is affected by both amplitude and phase errors, since the energy content is redistributed incorrectly among the resolved harmonics.

To quantify this error, we apply the error measure (6.19) to HB computations of the model turbomachinery problem corresponding to different choices of the wake thickness and different numbers of harmonics. Results are presented in Figure 6.16. The ε_2 error map is qualitatively

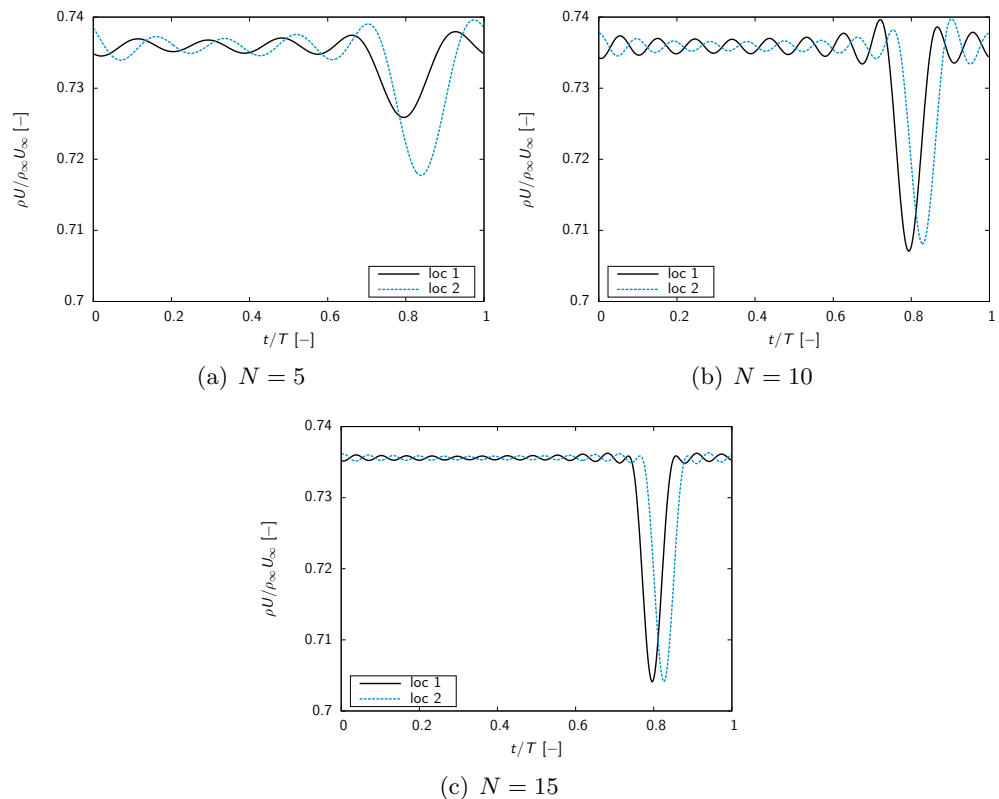


Figure 6.14: Temporal signal seen at loc 1 and loc 2 for a $L = 5\%$ wake width.

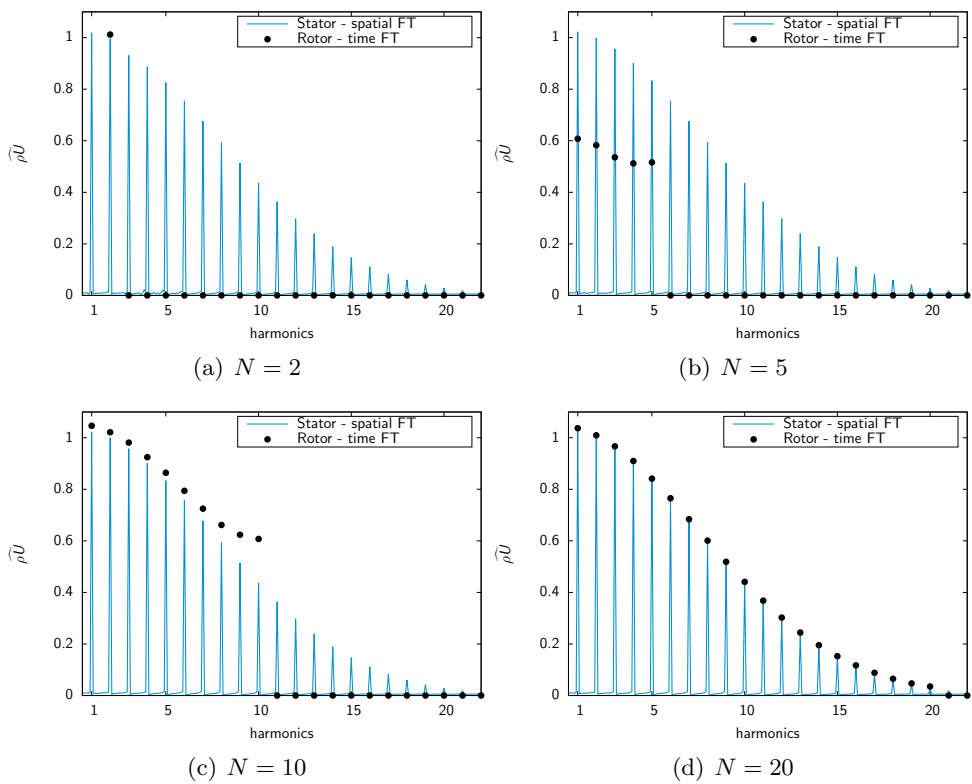


Figure 6.15: Spatial/time duality for a $L = 5\%$ wake width.

and quantitatively similar to the ε_1 discussed in the previous section. Again, the truncation error measured using ε_2 for thick wakes and high numbers of harmonics does not follow the trend observed with the theoretical error ε_{th} , due to the spatial filtering introduced at the interface by the phase-lag condition.

The preceding analysis shows that, for HB computations that are well converged in terms in harmonics, the spatial spectrum in the stator and the time spectrum in the rotor block tend to match, except for additional spatial errors introduced by the use of an azimuthal Fourier transform on a bounded interval, which confirms the validity of the error measure defined in Eq. (6.19).

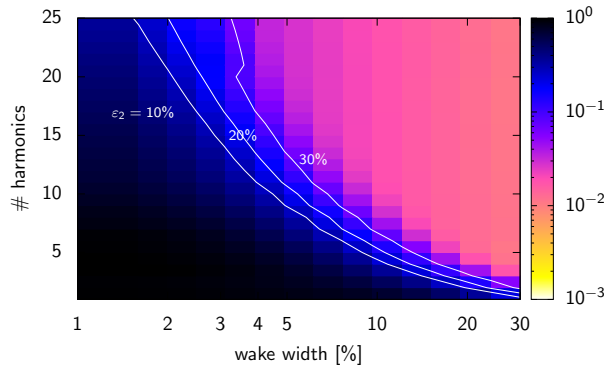


Figure 6.16: Evaluation of the error due to the wake capturing using the second error quantification (ε_2).

6.3.4 Comparison with the theoretical error measure

The preceding results show that approximated truncation error measures computed for the model turbomachinery problem using the non-linear Euler equations exhibit trends, with respect to the wake thickness and number of HB harmonics, in close agreement with the theoretical error measure derived in Section 6.2 for a Gaussian function. Figure 6.17 compares the different error measures for HB simulations of advected wakes of varying thickness versus the number of harmonics used for the time discretization. This corresponds to horizontal cuts of Figures 6.8, 6.11 and 6.16. For a wide range of harmonics the three error measures are seen to give results in very close agreement. For higher harmonics values, both the ε_1 and ε_2 error measures applied to the model turbomachinery problem exhibit a plateau. The preceding remarks suggest the idea that, since all error measure provide similar results, at least up to numbers of harmonics of interest for practical applicative problems, an *a priori* estimate of the number of harmonics required to achieve a given error level could be obtained by using the theoretical error measure Eq. (6.13), if a quick estimate of the wake thickness characteristic of a given turbomachinery problem is available. In the next Section, we show that a reasonable and more general estimate can be obtained from a preliminary steady computation based on the mixing plane interface condition.

6.3.5 Toward an *a priori* error estimate

In order to define an *a priori* error measure that can be used to estimate the number of harmonics required to achieve a reasonable convergence of the HB method, we suggest to evaluate the

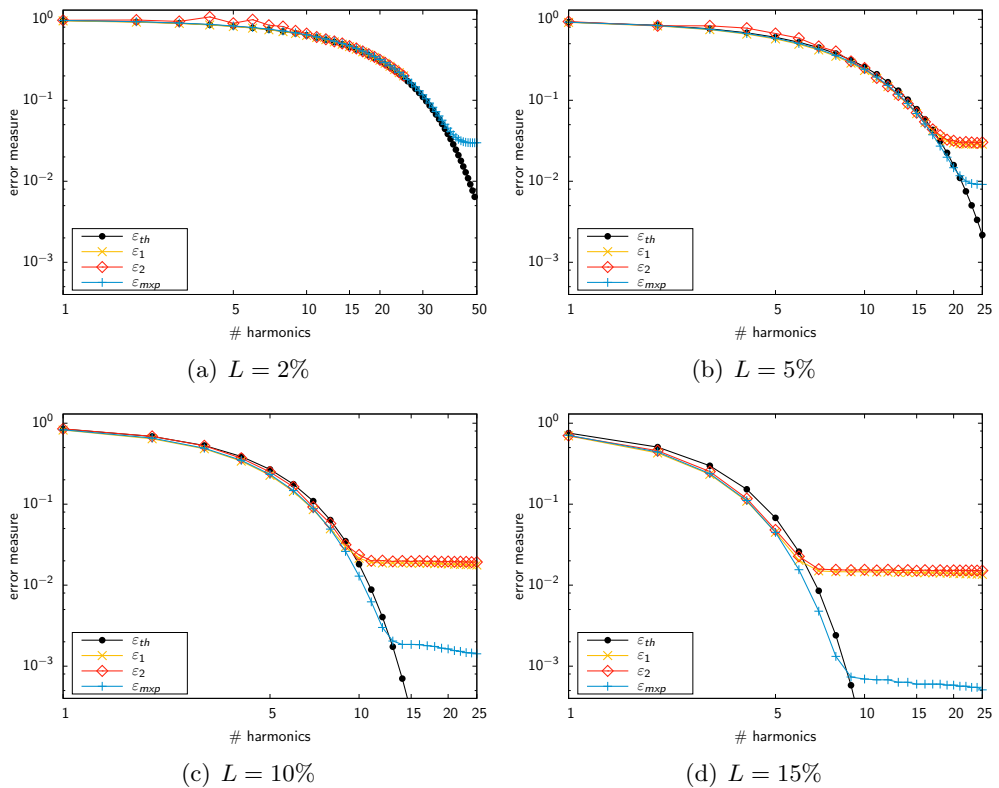


Figure 6.17: Truncation, computed and analytical errors for four wake widths.

wake thickness by using a preliminary mixing plane steady computation. Indeed, if potential effects due to the downstream row can be neglected, the spatial information at the interface in the stator block, essentially due to the incoming wakes, can be captured without taking into account the relative motion between the wheels, *i.e.* by means of a mixing plane computation. Given the approximated azimuthal distribution at the stator interface, we consider the cumulative energy content of the signal up to a given frequency f (or, equivalently, to a given harmonic $N = f/f_1$ where f_1 is the base frequency value of the considered unsteadiness, here the opposite blade passing frequency). The cumulative energy is defined as

$$E(f) = \frac{\int_0^f |\hat{g}(\zeta)|^2 d\zeta}{\int_0^\infty |\hat{g}(\zeta)|^2 d\zeta}, \quad (6.20)$$

where \hat{g} is the spectrum of the quantity of interest. By comparison with Eq. (6.7), the relation between the relative accumulated energy E and the truncation error ε_{mfp} is given by

$$E(f) = 1 - \varepsilon_{mfp}^2(f). \quad (6.21)$$

Note that this last error measure is based only on the amount of unresolved energy that is left in a computation if the spatial signal is truncated at a given cutoff frequency f , and does not require any information from the rotor block, but it depends only on the characteristics of the incoming wake.

To check if the new error measure represents an accurate estimate of the truncation error of an HB simulation, we carry out again a parametric study of the error versus different wake thicknesses and numbers of harmonics (equivalently, cutoff frequencies), and compare the results to those of the *a posteriori* error measures obtained for the model turbomachinery problem and for the theoretical error ε_{th} . Results corresponding to ε_{mfp} are superposed to the corresponding curves in Figure 6.17. The *a priori* error measure (ε_{mfp}) matches the theoretical estimate (ε_{th}) and the *a posteriori* measures ($\varepsilon_1, \varepsilon_2$) over a wide range of harmonics. Similarly to the *a posteriori* errors ε_1 and ε_2 , the *a priori* error exhibits a plateau for high N and high wake thicknesses, due to the application of the Fourier transform on a bounded interval. We also stress the close agreement between ε_{mfp} and ε_{th} : specifically, estimates of the number of harmonics needed to capture 99% of the cumulative energy (equivalently, to get a truncation error equal to 10%) are identical for all error measures.

This is indeed very attractive as a preliminary steady mixing plane simulation is cheaper than a harmonic balance computation. This tool will be assessed on two CROR configurations in Chapter 8 and applied in Chapter 9.

Summary

In this chapter, we showed that the main impulsive source of unsteadiness in turbomachinery flows is due to the relative motion of wakes generated by a given blade row with respect to the downstream row. Lakshminarayana and Davino [64] showed that the wake shed behind turbomachinery blades follows a similarity law for the velocity. It can be empirically approximated by a Gaussian function. The Fourier transform of a Gaussian function being analytical, a truncation error has been defined, which showed that the narrower the wake, the larger the Fourier spectrum resulting in a slower convergence of Fourier-based time methods. Based on these observations, we showed on a model turbomachinery computation, that the analytical truncation error can be *a priori* estimated using a mixing-plane steady

computation. Applying the *a priori* error estimate to the steady computation of any turbomachinery configuration provides a lower bound of the number of harmonics required to achieve a given level of convergence.

Part III

Applications

11th standard aeroelastic configuration

Abstract

The harmonic balance method along with an aeroelastic weak-coupling approach, is applied to the well-known 11th standard aeroelastic configuration of Fransson et al. [35]. It is shown that by using only one harmonic ($N = 1$), the damping curve of both the subsonic and the transonic operating points are superimposed with the reference unsteady computation. The agreement with both the experimental and the numerical data available is good, justifying the proposed approach. Moreover, a speed-up of seven is found compared to a classical time-marching scheme. This work has been published in

F. Sicot, A. Gomar, G. Dufour and A. Dugeai. Time-Domain Harmonic Balance Method for Turbomachinery Aeroelasticity. *AIAA Journal*, 52(1):62–71, January 2014

7.1 Presentation of the case

For external-flow aeroelasticity, the HB approach has been thoroughly validated by Gopinath and Jameson [39], Woodgate and Badcock [109] and Dufour et al. [23], mostly for the AGARD test cases of Davis [22]. Experimental data for turbomachinery aeroelasticity are more scarce: the STandard aeroelastic ConFigurations (STCF) experiments of Fransson et al. [35] are the reference in this respect, and have been widely used to validate different numerical approaches by Campobasso and Giles [13], Cinnella et al. [18], Duta et al. [26], Sbardella and Imregun [85] and Huang and Ekici [55] whose uses a similar harmonic balance approach as the one proposed in this work. The experiments are composed of 11 turbomachinery configurations that have been thoroughly investigated experimentally in an annular test rig at École Polytechnique Fédérale de Lausanne.

In particular, the 11th standard configuration is a turbine stator composed of 20 blades, and tested in the late 1990's by Fransson et al. [35]. The experimental results have been found to be highly reproducible and therefore suitable for code validation. Moreover, two flow regimes are considered, one subsonic and one transonic. In this respect, the transonic case allows to distinguish solvers able to capture non-linear unsteady effects. This is why this particular case is used here, since HB methods are meant to capture non-linear unsteady features. However, it must be pointed out that LUR approaches have been validated using the transonic case and show fair agreement with experimental data [13, 26, 85].

The geometry profile and the results are available over the internet [2]. To characterize the two flow regimes, measurements of static and total pressures as well as flow angles are done in two planes e_0 located 0.3 axial chord upstream of the turbine blade and e_1 located 0.6 axial chord downstream as shown in Figure 7.1. The results are given in terms of inlet Mach

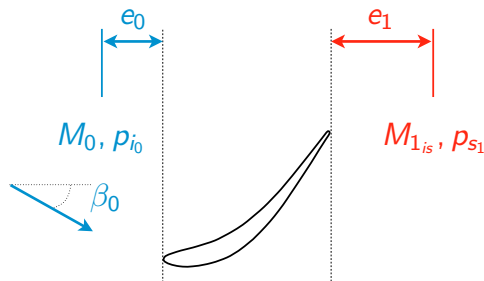


Figure 7.1: Position of the measurement planes in the STCF 11 configuration.

number M_0 , inlet total pressure p_{i0} , inlet flow angle β_0 , outlet isentropic Mach number $M_{1_{is}}$ and outlet static pressure p_{s1} . The isentropic Mach number is the Mach number computed if the stagnation pressure was taken constant (without loss)

$$M_{is} = \sqrt{\frac{2}{\gamma - 1} \left[\left(\frac{p_{i0}}{p_s} \right)^{\frac{\gamma-1}{\gamma}} - 1 \right]}, \quad (7.1)$$

where p_{i0} is the inlet total pressure and p_s the local static pressure. It is actually one way to interpret the static pressure as a velocity. The experimental results measured at plane e_0 and e_1 are given in Tab. 7.1. These will be used later on to set the boundary conditions of the CFD computations. To allow local validation of the steady flow, the experimental results of isentropic Mach number are given at blade wall.

	M_0 [-]	p_{i_0} [Pa]	β_0 [$^\circ$]	$M_{1_{is}}$ [-]	p_{s_1} [Pa]
Subsonic	0.31	124,600	15.2	0.69	90,700
Transonic	0.4	229,800	34	0.99	122,400

Table 7.1: Steady experimental results for the STCF 11 configuration.

For aeroelastic investigations, the blades oscillate harmonically in the first bending mode at a frequency $f = 209$ Hz for the subsonic case and $211.6 \text{ Hz} \leq f \leq 212.1 \text{ Hz}$ for the transonic case. Aeroelastic results are available such as the first harmonic of the unsteady pressure coefficient at blade walls (amplitude and phase), for several nodal diameters. These are measured using piezo-resistive pressure transducers.

The damping is evaluated at blade walls through the expression given by Fransson et al. [35]

$$\text{Damping} [-] = - \sum_{k=0}^{\# pts} \frac{c}{h} \frac{|\hat{p}_k|}{(p_{i_0} - p_{s_0})} S_k \arg(\hat{p}_k), \quad (7.2)$$

where c is the chord length, h the bending amplitude, $|\hat{p}|$ and $\arg(\hat{p})$ are the modulus and the phase of the complex first harmonic of static pressure, respectively, S the surface and k the k^{th} grid point at blade walls. The damping strongly varies under small changes in the local distribution. It is therefore recommended to look at the local distributions. No experimental damping curves are given. In fact, there is too few measurement points to integrate the results with confidence. However, Fransson et al. [35] provide numerical results of the damping curve obtained with a potential code.

7.2 Numerical setup

The blade passage is meshed using an O4H topology as shown in Figure 7.2. The number of grid points along the blade chord is 160 and the computed y^+ at the walls is $\mathcal{O}(1)$. 81 points are used to discretize the azimuthal direction. The blade has the same profile along the spanwise direction and no twist. Therefore, a 2.5D mesh is used with five points in the radial direction. The spanwise extent represents 1% of the chord. The total size of the mesh is 70,330.

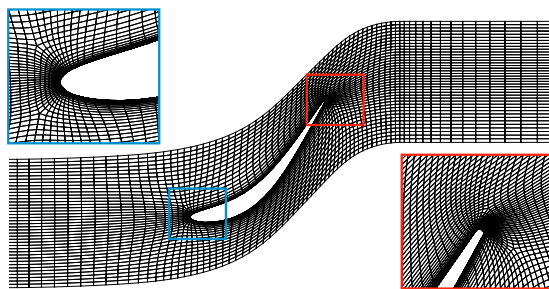


Figure 7.2: STCF 11 mesh.

The *elsA* [12] CFD code along with its aeroelastic module [24] is used to solve this configuration. The boundary conditions used for this case are: (i) an injection condition for the inlet

(with the relative flow angle, the Mach number and the total pressure set to the experimental values using Tab. 7.1), (ii) a constant static pressure condition for the outlet using also the value p_{s_1} given in Tab. 7.1, (iii) an adiabatic no-slip condition on blade walls, and (iv) periodic or phase-lagged conditions for azimuthal boundaries depending on the prescribed IBPA.

Turbulence is modeled using the one-equation model of Spalart and Allmaras [94]. Roe's scheme [82] along with a third-order MUSCL extrapolation is used to compute the convective fluxes. The classical Dual Time-Stepping [59] (DTS) time-integration scheme is taken for comparison to the proposed harmonic balance approach. The maximum CFL number is set to 20 for the steady computations, the inner loop of the DTS scheme and the HB simulations. For the DTS scheme, convergence in time discretization is obtained after 20 periods using 128 time steps per period. Iterative convergence for the inner loop is considered achieved when the normalized residuals drop by 5×10^{-2} (within a maximum of 50 sub-iterations).

Influence of the mesh discretization The mesh quality is assessed through a mesh convergence. To ensure the latter, three meshes are tested, the referenced one described above, and two meshes, coarse 2 and coarse 4, coarsened in the axial and azimuthal directions by a factor of two and four, respectively. The five grid points in the radial direction are kept unchanged.

The steady results for the two operating points are shown in Figure 7.3. The three meshes

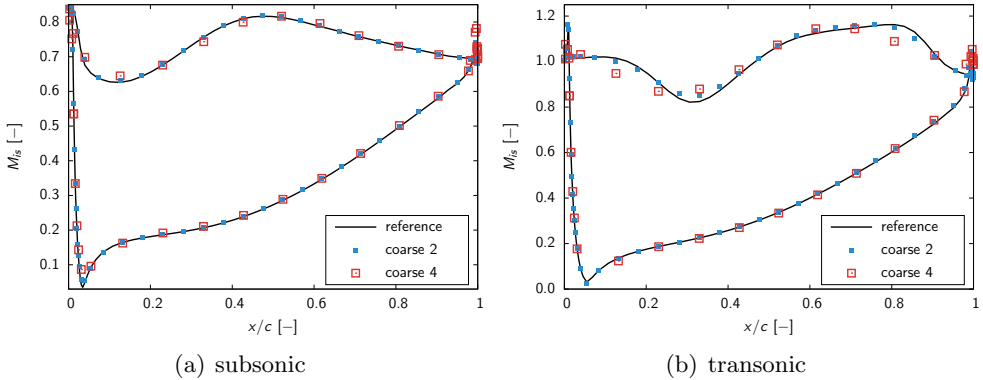


Figure 7.3: Influence of mesh discretization for the STCF 11 configuration.

give the same results for the subsonic case. On the pressure side (bottom curve), the three results are superimposed. On the suction side (top curve), some minor differences are observed in particular near the leading edge ($x/c \leq 0.2$). Nevertheless, the agreement between the three meshes is very good for the subsonic operating point. The results are more scattered for the transonic operating point. In fact, the coarse 4 mesh does not accurately predict the region where $x/c \leq 0.3$ and where $0.7 \leq x/c \leq 0.9$. This last zone seems smeared out. However, the results obtained with the coarse 2 mesh are in good agreement with the referenced mesh. Therefore, the reference mesh is retained for the following study.

Influence of the spatial discretization Four space schemes are used to compute both the subsonic and transonic steady fields. These schemes are the Jameson et al. [59] scheme (JST) with artificial viscosities $\kappa_4 = 0.016$ and κ_2 equal to 0.5 and 1.0 for the subsonic and the transonic inflow conditions, respectively. In addition to this scheme, three upwind Roe's

scheme [82] along with no extrapolation (Roe 1), a second-order (Roe 2) and a third-order (Roe 3) MUSCL extrapolations are used. The steady results for the two operating points are shown in Figure 7.4. For the subsonic case, the results are all superimposed except Roe 1.

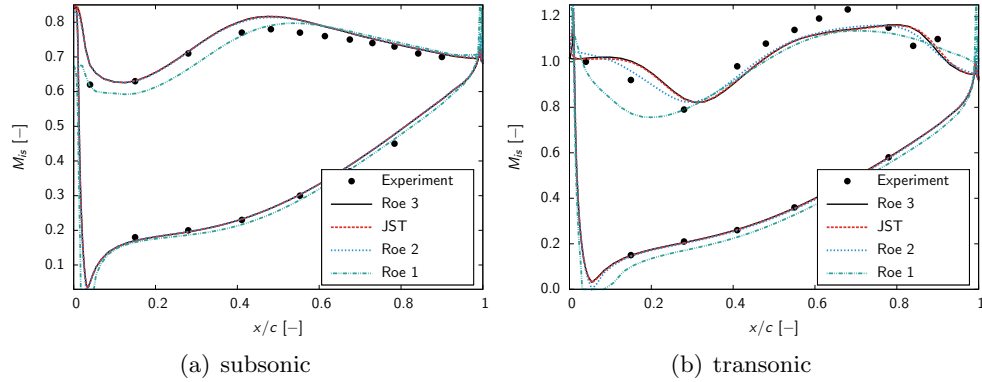


Figure 7.4: Influence of mesh discretization for the STCF 11 configuration.

This was expected as first-order schemes are not precise enough to accurately capture turbomachinery flow fields. For the transonic operating point, which is a numerically stiffer case, the Jameson et al. [59] and the Roe 3 scheme are superimposed. As for coarse meshes, the Roe 2 and Roe 1 schemes lack in predicting the suction side evolution indicated by two non-linear flow features: a recirculation bubble and a shock. In the following, the Roe 3 scheme is chosen to be the reference spatial scheme.

7.3 Subsonic case

Steady results For the subsonic case, the experimental inlet Mach number is 0.31 and the isentropic outlet Mach number is 0.69. Steady results for the isentropic Mach number at blade walls are compared to the experimental data in Figure 7.5. For this flow regime, the fluid remains subsonic. On the pressure side, the flow accelerates all the way to the trailing edge of the blade. The stagnation point is located at $x/c \approx 0.05$. On the suction side, the flow accelerates until a maximum speed at $\approx 40\%$ of the chord and finally decelerates toward the trailing edge. The agreement with the experimental data is fair. However, an over-prediction of the isentropic Mach number is observed on the suction side. This discrepancy is also reported in the literature (see Fransson et al. [35] for instance).

Aeroelastic results The aeroelastic experimental data are compared to the present results obtained with both the DTS and the HB approach. To explore the range of nodal diameters with the HB method, an incremental approach is used where each nodal diameter simulation is used to initialize the next one. Considering the opposite phase vibration case (the 10th nodal diameter), the amplitude and the phase of the pressure coefficient are presented in Figure 7.6. With only one harmonic (*i.e.* three instants), the HB results are superimposed with the DTS ones. Moreover, the numerical results are in fair agreement with the experimental data for the amplitude. However, for the phase, the sign change on the suction side is predicted at about 60 % of the chord, whereas the experimental location is about 25 %.

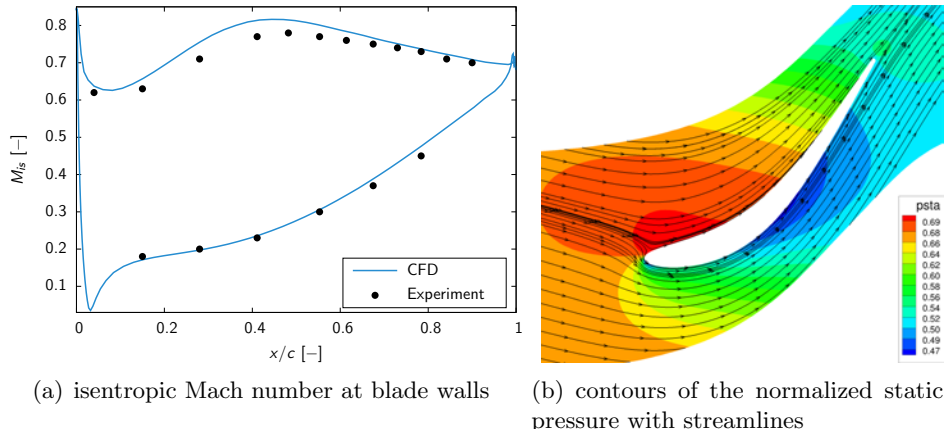


Figure 7.5: Steady results for the STCF 11 configuration, subsonic case.

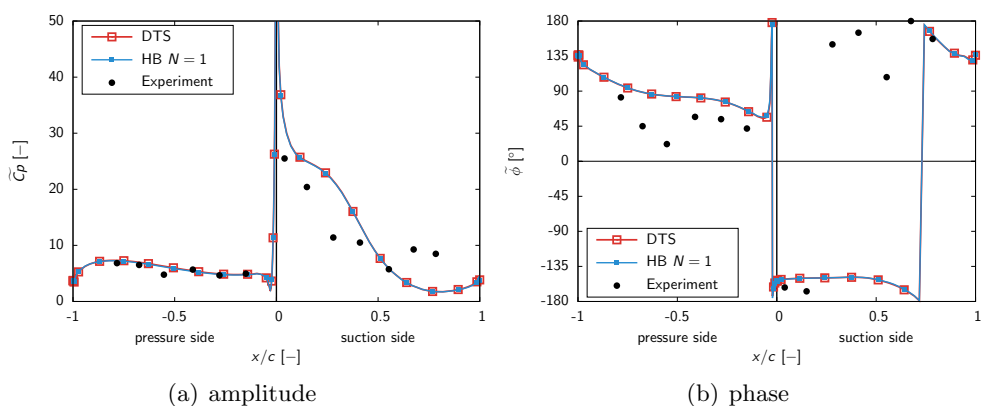


Figure 7.6: Wall pressure harmonic analysis for an opposite phase vibration, subsonic case.

The results for the -2 nodal diameter, corresponding to $\text{IBPA} = -36^\circ$, namely the mostly damped as will be seen later on, are shown in Figure 7.7. The HB and DTS data are superimposed, and are in fair agreement with the experiments. The amplitude levels are well captured and the phase prediction is slightly improved over the opposite phase case.

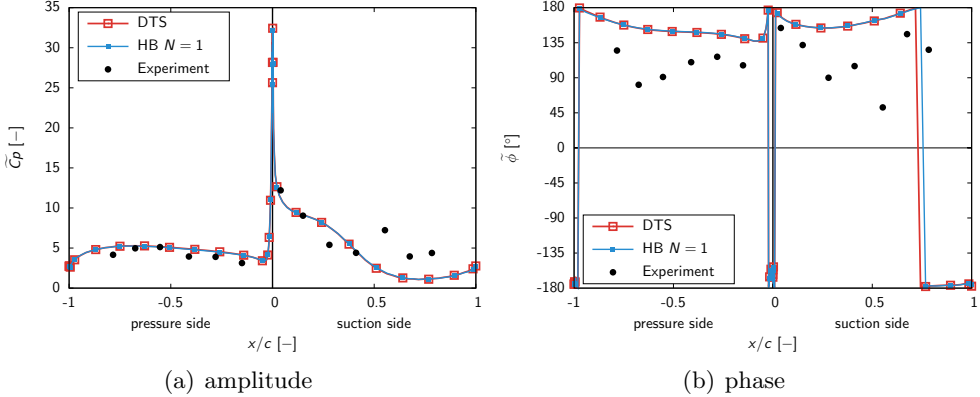


Figure 7.7: Wall pressure harmonic analysis for a $n_d = -2$, subsonic case.

The damping obtained from the previous calculations is depicted in Figure 7.8. Also plotted are the results from Fransson et al. [35], obtained with a potential code. These are the only damping results for the subsonic case known by the authors. Since the local variations are superimposed for the DTS and the HB approaches, so are the damping. The present results show similar trends and levels to those of Fransson et al. [35].

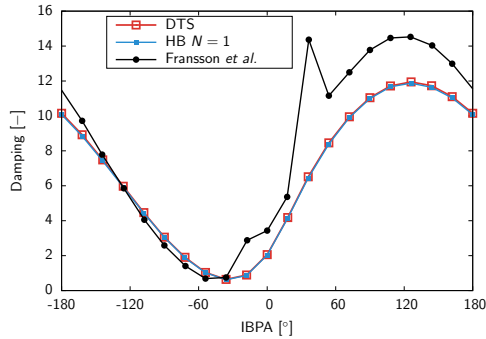


Figure 7.8: Aerodynamic damping coefficient versus IBPA, subsonic case.

7.4 Transonic case

The outlet isentropic Mach number is 0.99 for an inlet Mach number of 0.4. This case, for which experimental uncertainties are available, has been largely addressed in the literature by Campobasso and Giles [13], Cinnella et al. [18], Duta et al. [26], Sbardella and Imregun [85] and Huang and Ekici [55]. This test case is challenging in terms of non-linearities as a separation bubble and a shock are present.

Steady results Steady results of the isentropic Mach number are shown in Figure 7.9. For this flow regime, a small separation bubble develops on the suction side at the leading edge. The flow then accelerates, followed by a shock. The experimental data suggests that the shock appears sooner on the suction side than in the computations; all the results reported in the literature exhibit similar discrepancies (see Refs. [13, 18, 26, 35, 55, 85]). Otherwise, the present results are in fair agreement with experimental data.

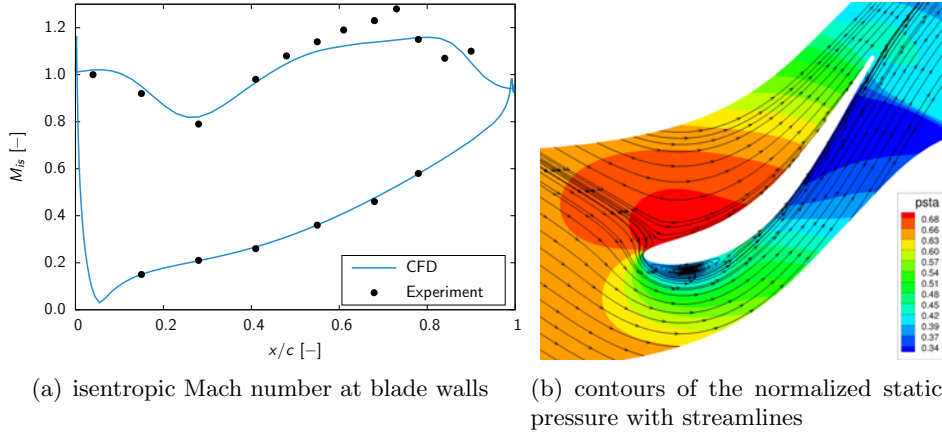


Figure 7.9: Steady results for the STCF 11 configuration, transonic case.

Aeroelastic results The aeroelastic experimental data are compared to the present results obtained with both the DTS and the HB approach. Considering the opposite phase vibration case (the 10th nodal diameter), the amplitude and the phase of the pressure coefficient are presented in Figure 7.10. Also plotted are the results of Cinnella et al. [18], computed with a non-linear viscous approach using also the Spalart-Allmaras turbulence model. The present HB and the DTS results are superimposed, which indicates that the one harmonic HB solution is able to reproduce the unsteady non-linear effects without increasing the number of harmonics. The results are in good agreement with the experimental data and display the same trends as that of Cinnella et al. [18]. A slight discrepancy can be observed within the shock region, where the amplitude and the phase phenomena are predicted further than the experiments indicate. This can be attributed to the poor prediction of the shock position (indicated in Figure 7.9) and thus the poor prediction of its interaction with the motion of the blade.

The results for the -2 nodal diameter are also shown in Figure 7.11. Again, the HB results are superimposed with the DTS ones. Moreover, these are in good agreement with the experiments, considering the uncertainties of the experimental data.

Let us clarify one important thing here: the convergence of the harmonic balance approach depends on the smoothness of the temporal phenomenon. This effect can be emphasized by two aeroelastic computations that have been performed using a harmonic balance approach. The first one is the case of an airfoil with an oscillating flap [23]. In this simulation, the flap is oscillating under transonic inflow conditions, resulting in a shock swinging temporally back and forth from the pressure side to the suction side. As the discontinuity is both spatial (a shock is seen on the field) and temporal (this shock is moving with respect to time), the number of harmonics needed to capture this phenomenon was high ($N = 3$). This is consistent with the

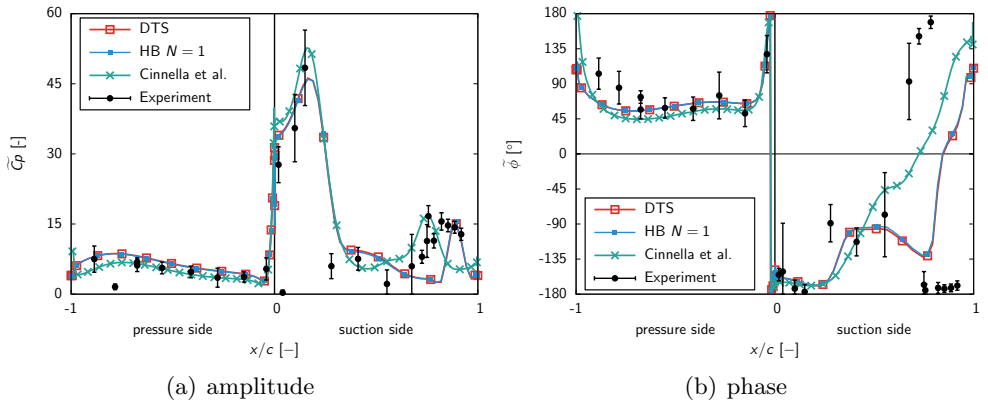


Figure 7.10: Wall pressure harmonic analysis for an opposite phase vibration, transonic case.

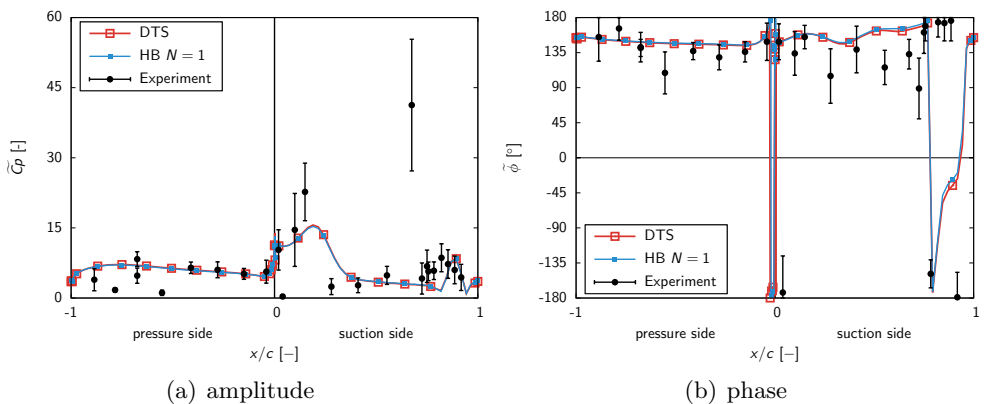


Figure 7.11: Wall pressure harmonic analysis for $n_d = -2$, transonic case.

capturing of a rectangular function as shown in Sec. 6. Contrarily, a recent publication [55] and the current results on the validation of the use of harmonic balance approach to predict aeroelasticity damping within turbomachinery, have highlighted different conclusions. Under the first bending mode of the blade, the shock remains steady in the relative bending frame of reference. As the shock is only spatial, both authors show a convergence of the harmonic balance approach with only $N = 1$ harmonic. Thus, if the shock structure is only spatial, Fourier-based time methods will not need extra harmonics to converge, while for a temporally moving discontinuity (which is not our case here), the number of harmonics to converge will be higher.

The damping is shown in Figure 7.12 for the transonic case. Also plotted are the results from Fransson et al. [35] (potential code), and from Cinnella et al. [18] (RANS code). The scattering is much more severe than for the subsonic case. The trends obtained with the RANS approaches are similar, but the discrepancies in terms of levels are significant. Recently, Vogt and Fransson [108] reported similar discrepancies for damping predictions of subsonic and transonic cascades, showing that the damping can be significantly affected by small local changes in the amplitude or the phase.

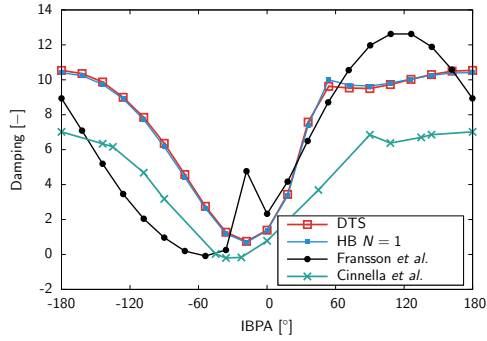


Figure 7.12: Aerodynamic damping coefficient versus IBPA, transonic case.

In terms of computational efficiency, the HB method is 7 times faster than the DTS for all the IBPAs which is very good considering that the DTS computations were done using chorochronic boundary conditions which already provides computational savings compared to a full 360° simulation. Actually the $N = 1$ harmonic balance computation is 3 times more expensive than a steady RANS simulation, which is consistent with the theoretical cost estimation (see Sec. 3.5.4).

Summary

The use of the harmonic balance approach to compute turbomachinery aeroelasticity has been validated against a well documented test case. The results are in good agreement with the experimental data and with the numerical results obtained by using different approaches. The harmonic balance approach has shown that with only one harmonic, the damping curve is retrieved compared to a classical time-marching scheme. The speed-up obtained is seven compared to a phase-lag approach with a classical time-marching scheme. This give us faith to apply the current approach to more demanding aeroelastic computations, namely contra-rotating open rotor aeroelasticity.

Isolated low-speed CROR configuration

Abstract

The studies performed in the previous chapters are finally used together to simulate the aeroelasticity of a low-speed CROR configuration. First, the steady results are analyzed to provide insight into the flow physics and give confidence in the results. The prediction tool defined in Chap. 6 is then used to estimate the number of harmonics required to simulate the unsteady rigid-motion response of the CROR using the harmonic balance approach. Aeroelastic simulations are then carried-out using the weak-coupling approach that has been validated in the previous chapter. The OPT algorithm develop in Chap. 5 is used to ensure the stability of the computations. Local excitation contours and the integrated damping are finally analyzed.

8.1 Presentation of the case

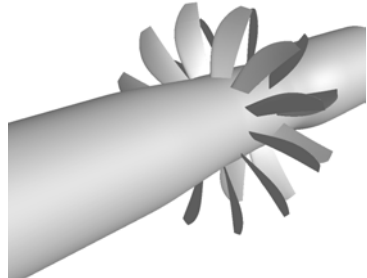


Figure 8.1: Low-speed isolated contra-rotating open rotor geometry.

The studied configuration is a pusher contra-rotating open rotor that comes from the know-how of Snecma (Safran). It is shown in Figure 8.1 for the Low-speed (LS) flight condition, representative of the take-off and landing. The simulated configuration does not include the spinner as the experimental setup does not take into account this part of the geometry. The experimental results were not available for comparison at the time this study was written.

M_0	J	M_{tip}
0.2	1.06	0.63

Table 8.1: Low-speed isolated contra-rotating open rotor flight condition parameters.

Table 8.1 recalls the main parameters of the case: the inflow Mach number M_0 , the advance ratio J (see Chap. 1) and the Mach number at the tip of the front rotor blades M_{tip} based on the inflow velocity and the advance ratio

$$M_{tip} = \sqrt{\frac{V_0^2 + (\Omega R)^2}{\gamma R t_0}} = \frac{V_0}{\sqrt{\gamma R t_0}} \sqrt{1 + \left(\frac{\Omega R}{V_0}\right)^2} = \frac{V_0}{\sqrt{\gamma R t_0}} \sqrt{1 + \left(\frac{\pi n D}{V_0}\right)^2} \\ = M_0 \sqrt{1 + \left(\frac{\pi}{J}\right)^2} \quad (8.1)$$

At this flight condition, the inflow Mach number M_0 is within the incompressible range ($M_0 < 0.3$). As the CFD flow solver used here is the *elsA* [12] CFD code which is a compressible code, a preconditionner might be needed for the computations to converge. Hopefully, the fluid is accelerated by the two rotors and the tip Mach number is high enough not to use any preconditionning. However, let us bare in mind that this range of Mach number might be tedious for a compressible flow solver. The advance ratio J is around 1 which is a classical value for low-speed propellers [7].

Two structural modes are considered for the aeroelastic study of this configuration: the second bending/flection mode (2F) and the first torsion mode (1T) of the front rotor. These were inputs of the current work. The shape of the modes is shown in Figure 8.2 with an arbitrary amplitude, large enough to ease the visualization. Two inflection lines are seen for

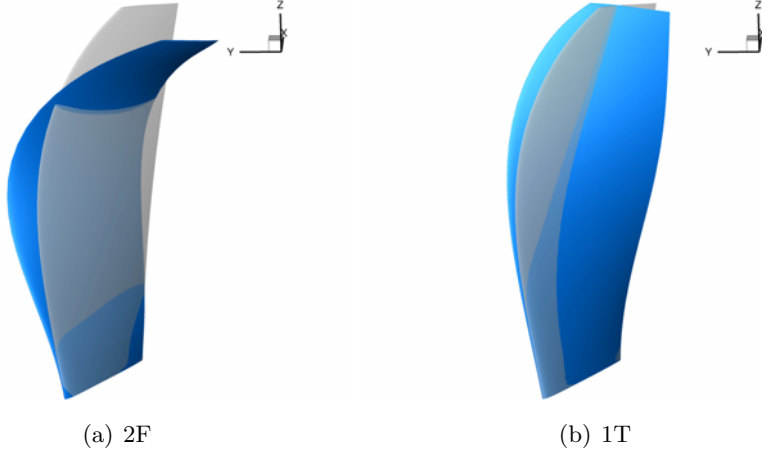


Figure 8.2: Low-speed isolated configuration: structural modes considered.

the 2F mode, while only one is seen for the 1T, hence their designation. The frequency, mass and stiffness of the modes are given with the corresponding modes. The ratio of the frequency of the blade passing frequency of the opposite row, namely the rear rotor, over the aeroelastic frequency of each mode varies between $3.19 \leq f_{BPF}/f_{AEL} \leq 3.87$. However, this last frequency governs the unsteady rigid-motion flow physics and will have to be computed along with the aeroelastic frequency. Therefore, the multi-frequential formulation of the harmonic balance approach will be used to simulate the aeroelastic response of the blades in Sec. 8.6.

8.2 Numerical setup

The CROR configuration is computed using a single-blade passage meshed with an O4H topology as shown in Figure 8.3(a). The number of grid points is reported in Figure 8.3(b) for a blade-to-blade section. 129 points discretize the blade, 45 the pitch and 181 the radial extent, among which 101 for the blade height. The same number of grid points is used for the front and the rear rotor blades. Finally, the total number of grid points is almost 5 million, which is in the mid-range of the literature values [5, 34, 81, 96, 111].

As a CROR is not shrouded, a sufficiently large far-field domain is taken to ensure a minimum influence of the far-field boundary conditions on the results. The computational domain is schematically reproduced in Figure 8.4. The radial extent is $3D$ while the axial one is $3.5D$, with D being the diameter of the front rotor. In the literature, Peters and Spakovszky [81] consider an axial extent of $7.5D$ with a radial extent of $4D$ while Zachariadis and Hall [111] consider $2.5D$ and $3.6D$, respectively. We are thus in the mid-range of the values taken in the literature. As highlighted by the underlined text in Figure 8.4, the boundary conditions used here are: (i) adiabatic walls for the blades and the hub (or spinner), (ii) constant stagnation values for the far-field, (iii) periodic or phase-lagged boundary conditions for the azimuthal boundaries of the channel and (iv) mixing-plane or sliding mesh interface for the rotors interface depending on the type of computation (steady or unsteady). In this case, the mesh stems from literature and industrial best practices and will not be assessed.

Turbulence is modeled using the one-equation model of Spalart and Allmaras [94]. Roe's

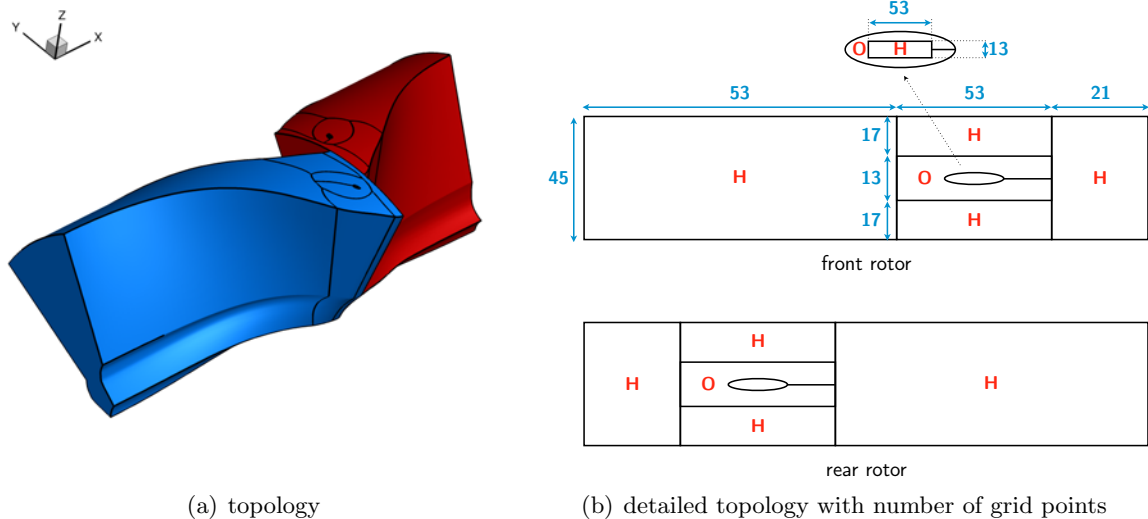


Figure 8.3: Low-speed isolated configuration mesh topology.

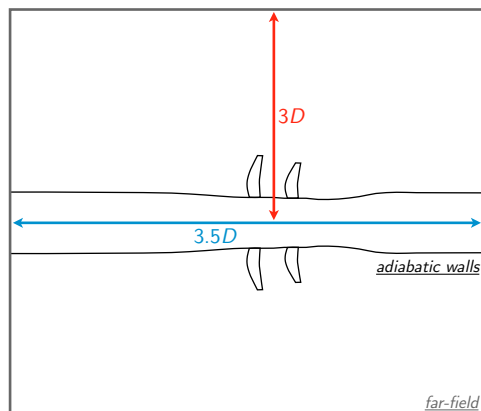


Figure 8.4: Low-speed isolated configuration far-field domain and boundary conditions.

scheme [82] along with a second-order MUSCL extrapolation is used to compute the convective fluxes. The maximum CFL number is set to 10 for the steady computations and to 5 for the unsteady simulations.

For the aeroelastic computations shown in Sec. 8.6, the aeroelastic module [24] of the *elsA* [12] CFD code is used. Again, only a one-blade passage domain is meshed. Phase-lag boundary conditions are therefore used and each computed frequency is associated to one phase-lag as shown by Guédene [42]. For the aeroelastic modes, four nodal diameters are considered, corresponding to Inter-Blade Phase Angles (IBPA) of: $[-60^\circ, -30^\circ, 30^\circ, 60^\circ]$. The aeroelastic coupling is considered to be linear (weak-coupling approach), therefore a very small amplitude of the mode is applied and the fluid response is analyzed. In this work, the two frequencies have a different physical meaning. In fact, while the blade passing frequency has been shown to convey the main flow physics (potential effects, wakes, tip vortices, to name but a few), the aeroelastic frequency is more likely to influence the near blade wall flow field. In fact, as recalled previously, the amplitude of vibration is kept very small, yielding a local influence of the blade vibration. Therefore, it seems reasonable to use the "cross grid" truncation pattern (see Sec. 3.5.3). Thus, the harmonic balance computations are run with five frequencies in total. In the rear rotor, the harmonics of the front rotor blade passing frequency are chosen. In the front rotor, the first frequency is the frequency associated to the vibration of the blade and the remaining ones are the harmonics of the rear rotor blade passing frequency. The time instances are automatically chosen using the OPT algorithm (see Sec. 5.3.2) which leads to a condition number always lower than 1.1 which ensure the stability of the computations.

Influence of the spatial discretization To assess the influence of spatial discretization, two space discretization schemes are used to simulate this low-speed CROR configuration. These schemes are the Jameson et al. [59] scheme (JST) with artificial viscosities $\kappa_4 = 0.016$, $\kappa_4 = 0.032$, $\kappa_4 = 0.064$ and κ_2 equal to 0.5. In addition to this scheme, we consider Roe's scheme [82] without MUSCL extrapolation (Roe 1), and with second-order (Roe 2) or third-order (Roe 3) MUSCL extrapolations.

Convergence histories of the different computations are shown in Figure 8.5 for the four schemes. The convergence is not very good. Only the Roe 1 and Roe 2 spatial schemes give a convergence that has an acceptable slope. On the contrary, the JST with $\kappa_4 = 0.016$ diverges and hardly converges when using different values of the artificial viscosity parameters. The higher the viscosity parameter κ_4 of the JST scheme, the better the convergence. Exceeding $\kappa_4 = 0.064$ should warn us that something might be wrong with the computation. As stated previously, this can be attributed to the range of Mach number in which this low-speed configuration operates or to any stiff flow features as for instance flow separation.

To further differentiate the spatial schemes, the steady results for the similarity coefficients are reported in Figure 8.6 for all spatial scheme, except the diverging JST $\kappa_4 = 0.016$ computation. Arbitrarily, the results are normalized by the Roe 2 values. The Roe 2, Roe 3, and the JST scheme with different choices of the dissipation coefficients give equivalent similarity coefficients as the difference is smaller than 1 %. In opposite, the first-order upwind scheme (Roe 1) gives a 5 % difference for both the traction coefficient C_T and the efficiency η . Cross-comparing these results with the convergence of the computations reported in Figure 8.5, the Roe 2 scheme is kept for the following as it gives both a good convergence of the residuals and consistent similarity coefficients.

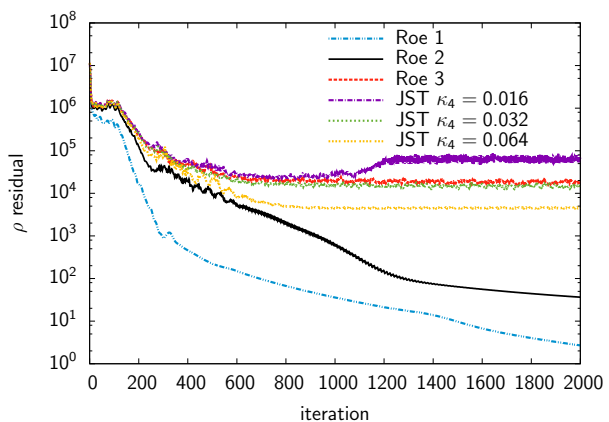


Figure 8.5: Low-speed isolated configuration: convergence of the steady computations using different spatial schemes.

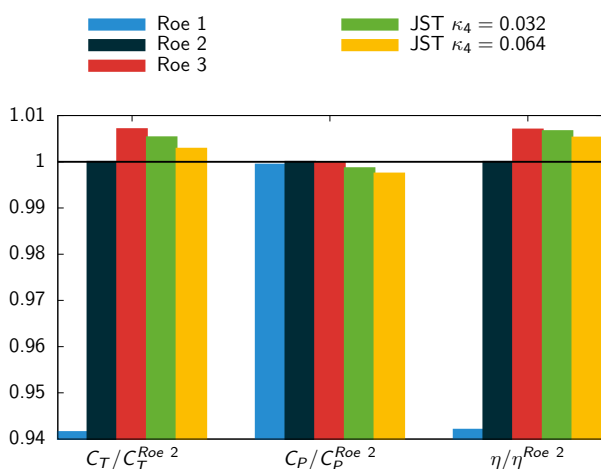


Figure 8.6: Low-speed isolated configuration: convergence of the similarity coefficients using different spatial schemes.

8.3 Steady results

8.3.1 Convergence analysis

Convergence of the steady computation using the Roe 2 space scheme is reported in Figure 8.7. The residuals show a four orders of magnitude decrease and the similarity coefficients are stable starting at 500 iterations. Therefore, according to Casey and Wintergerste [16], the solution is considered to be converged.

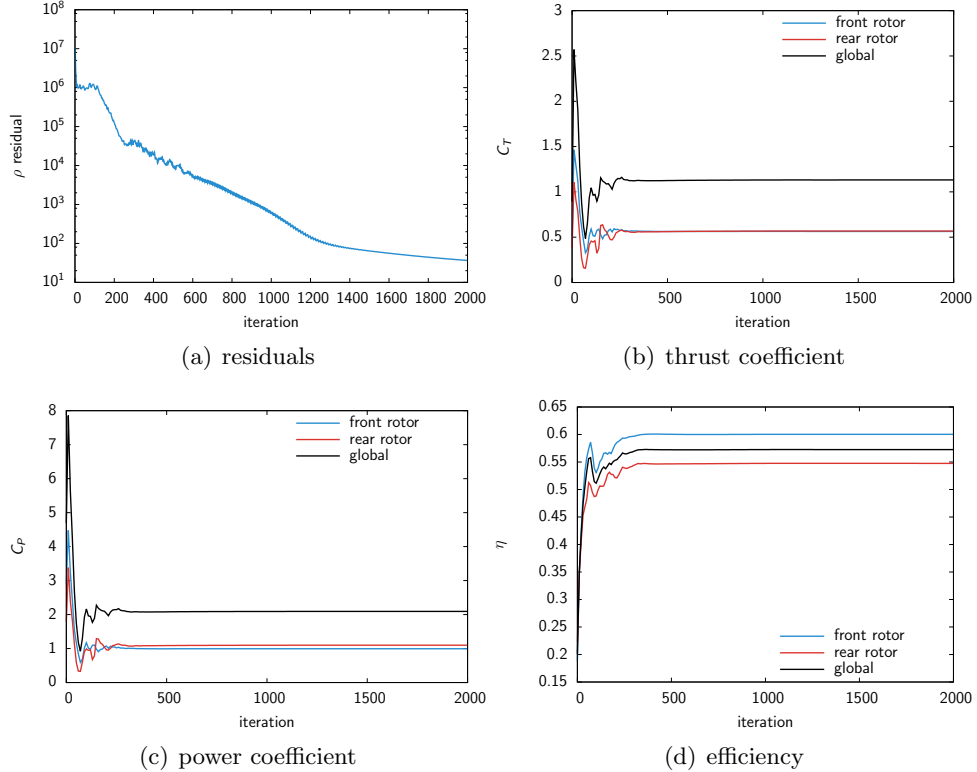


Figure 8.7: Low-speed isolated configuration: convergence of the Roe 2 steady computation.

8.3.2 Similarity coefficients

The similarity coefficients (defined in Sec. 1.3.3) are post-processed and reported in Tab. 8.2. The results are consistent with the efficiency estimation given in Eq. (1.17) for a propeller at

global			front			rear		
C_T	C_P	η	C_{T_f}	C_{P_f}	η_f	C_{T_r}	C_{P_r}	η_r
1.132	2.093	0.573	0.564	0.994	0.600	0.568	1.099	0.548

Table 8.2: Low-speed isolated configuration: similarity coefficients.

take-off flight conditions. In fact, each rotor of the CROR has an efficiency that is between 0.5

and 0.6. The advantage of the CROR is demonstrated here as the rear rotor is able to retrieve an additional thrust coefficient of 0.568 yielding a total of 1.132, while the front rotor alone would only give 0.564. The presence of a second rotor allows to more than double the total thrust of the engine. Nevertheless, the efficiency is affected compared to a single row propeller, as it goes from 0.600 for the front rotor alone to 0.573 for the CROR. However, achieving such a level of thrust coefficient ($C_T = 1.132$) with an isolated propeller would require a higher loading of the blades which is not consistent with an increase of the efficiency, necessary to meet the ACARE goals. Actually, this is the main advantage of the CROR engine: two rotors are used to create the thrust which allows to reduce the loading of each rotor compare to an isolated propeller, allowing thus higher inflow Mach numbers. In fact, the rotation of the rotors is reduced to maintain a subsonic Mach number optimizing thus the efficiency for a given level of thrust. Moreover, by maintaining a subsonic Mach number, the noise emissions are retained.

8.3.3 One-dimensional results: radial profiles

Radial profiles positioned at six locations upstream and downstream the rotors are extracted and shown in Figure 8.8(a). The absolute Mach number, absolute flow angle, static pressure, stagnation temperature and stagnation pressure are shown in Figure 8.8 against the radial position expressed relative to the radius of the front rotor blade R_f .

The absolute Mach number, shown in Figure 8.8(b), is increased by the two rotors as it goes from the inflow condition value $M = 0.2$ up to $M = 0.4$. Note that above $R/R_f = 1$, namely at the tip of the front rotor blade, the Mach number almost recovers the inflow condition. Moreover, it can be inferred from the absolute Mach number radial evolution, that the stream tube is contracting which is consistent with the observed acceleration of the fluid.

The pitch angle of the absolute velocity vector is shown in Figure 8.8(c). The front rotor deviates the flow of almost 20° , justifying the need for a second rotor. Between the fourth and the fifth extraction planes, namely passing through the rear rotor, the flow is straighten up. Remember that the very first motivation for adding a second rotor to a propeller was to recover the energy lost by the swirling flow (recall Sec. 1.3.2). This is observed in our simulations as the deflection angle is now close to 0° for $0.3 \leq R/R_f \leq 0.7$ in plane $P6$. Below that, the deflection angle remains negative. In the tip vortex region of the rear rotor, one can see the effect of the two tip vortices: between $0.8 \leq R/R_f \leq 0.9$, the front rotor tip vortex is seen as the deflection angle is positive while between $0.7 \leq R/R_f \leq 0.8$ the rear rotor is observed, which is consistent with the positive peak observe near the blade tip region in planes $P3$ and $P4$.

The goal of a CROR is to create thrust through an acceleration of the flow rather than to produce static pressure as in a compressor stage. This is highlighted in Figure 8.8(d) where the static pressure increases by at-most 2% which has to be compared with an almost 100% increase of the absolute Mach number. This is consistent with the low inflow Mach number that is within the incompressible range. A small increase is observed at each rotor crossing. Upstream the rotors, the potential effects can be seen. Actually, the flow is accelerated by the rotors, this acceleration yields a decrease of the static pressure (roughly through the Bernoulli theorem) and this pressure deficit is observed in planes $P1$, $P2$ and $P4$.

Figure 8.8(e) shows the stagnation temperature. An increase is observed at each rotor crossing. This is consistent as a propeller row gives work to the fluid. As such, the first principle of thermodynamics states that the enthalpy will raise resulting in an increasing stagnation temperature observed in our results. One can notice that the enthalpy increase is greater on

the rear rotor compared to the front rotor.

The stagnation pressure evolution is shown in Figure 8.8(f). As the static pressure and the absolute Mach number increases along with the crossing of the rotors, it is logical to have an increase of the stagnation pressure.

These 1D results provide us confidence in our simulation. In fact, the flow physic that was expected is observed in the results. To further analyze the simulation, 2D results are presented in the following section.

8.3.4 Two dimensional results: radial and axial cuts

Contours of the relative Mach number are shown in Figure 8.9 along with the pressure coefficient k_p , for both the front and the rear rotor, defined as

$$k_p = \frac{p_s - p_{s0}}{\rho n^2 D^2}, \quad (8.2)$$

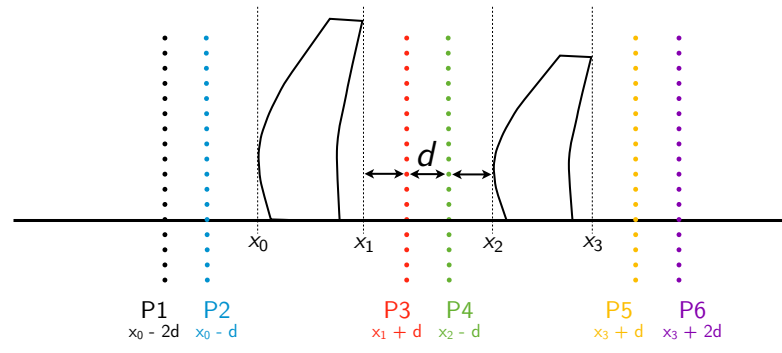
where the n and D parameters are the one of the front rotor to ease the comparison.

The negative k_p range is attributed to the suction side and the positive to the pressure side. The k_p should be interpreted as follow, a decreasing k_p means that the pressure gradient is negative, namely the flow is accelerating. Classically, the k_p axis is reversed so that the suction side is on top of the figure and the pressure side on bottom. The stagnation point is highlighted by the maximum of the pressure coefficient. On the pressure side ($k_p > 0$), the flow accelerates toward the trailing edge with a favorable pressure gradient. On the suction side, a rapid acceleration of the fluid is observed near the leading edge ($\partial k_p / \partial x \ll 0$) followed by a deceleration of the fluid along with an adverse pressure gradient. On the front rotor, the integrated pressure coefficient is increasing along with the relative span, at least when comparing the 50 % and the 75 % relative spans. After that, the pressure coefficient is almost constant on the front rotor. The loading is thus almost constant for relative spans greater than 50 %.

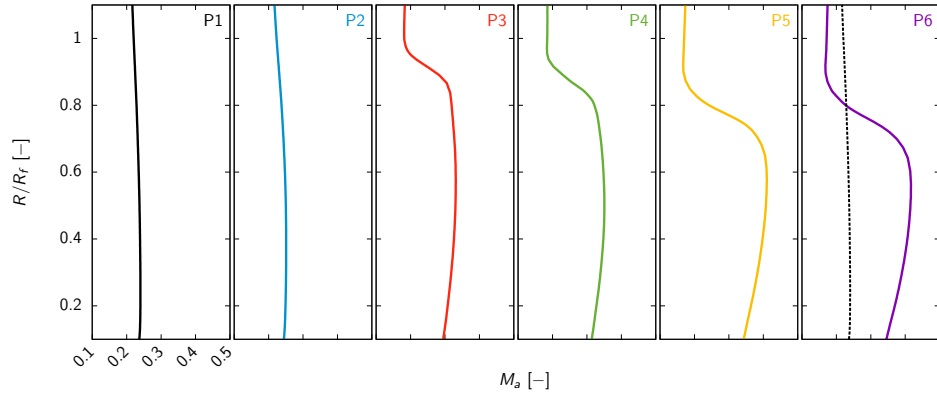
The pressure coefficients on the rear rotor have a similar shape compared to the one of the front rotor. However, the loading is larger on the rear rotor and near the tip of the blades $R/R_f > 75\%$, the integrated value of the pressure coefficient increases drastically. This is highlighted by the thrust coefficient of the rear rotor C_{Tr} which is reported in Tab. 8.2 and that is higher than the front rotor one. This is observed even though the diameter of the front rotor is chosen to normalize the pressure coefficient which lessened the thrust coefficient of the rear rotor.

Relative Mach number contours are also shown in Figure 8.9. As inferred by the tip Mach number value M_{tip} of the blade given in Tab. 8.1, the relative Mach number does not cross the sonic boundary $M_{rel} = 1$. The flow remains subsonic which is, aerodynamically speaking, a good feature for the performances since shocks create losses. Near the tip region of the rear rotor blades, the leaving of the tip vortex can be seen. In fact, for relative span $R/R_f \geq 90\%$, a low velocity region is seen on the rear rotor blades oriented from the pressure side to the suction side, hence the consistence with a tip vortex.

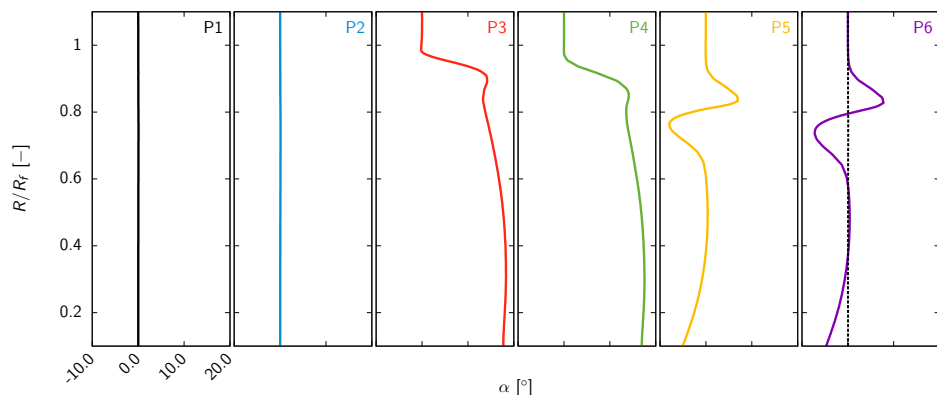
Axial cuts of the entropy are shown in Figure 8.10. The axial positions are the four planes $P3$, $P4$, $P5$ and $P6$ as defined in Figure 8.8(a). The tip vortices generated by the front rotor are seen in the $P3$ axial plane. The mixing plane approach is used for the steady computations presented here. This is emphasized by the $P4$ axial cut of entropy. A smooth, spatially-averaged field of entropy is seen with a ring of losses attributed to the front rotor tip



(a) position of the extraction planes



(b) absolute Mach number



(c) absolute flow angle

Figure 8.8: Low-speed isolated configuration: radial profiles.

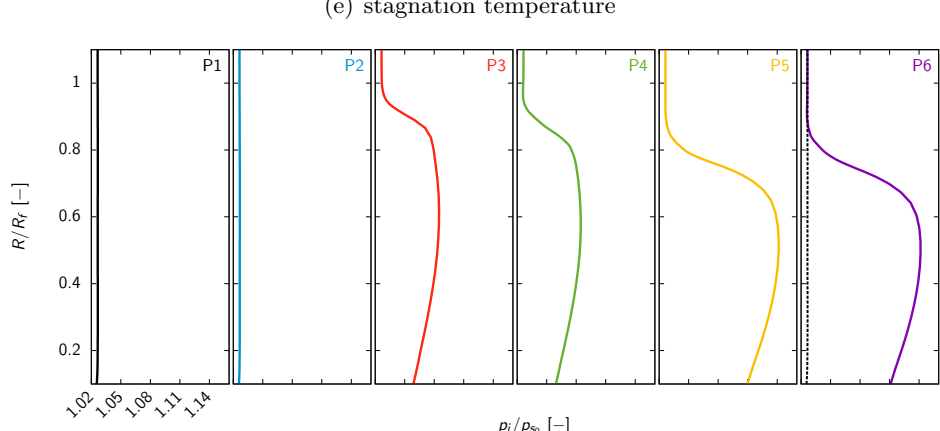
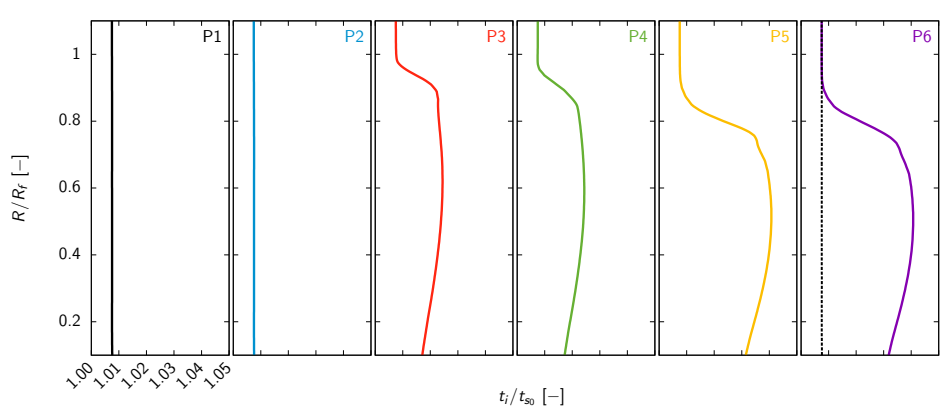
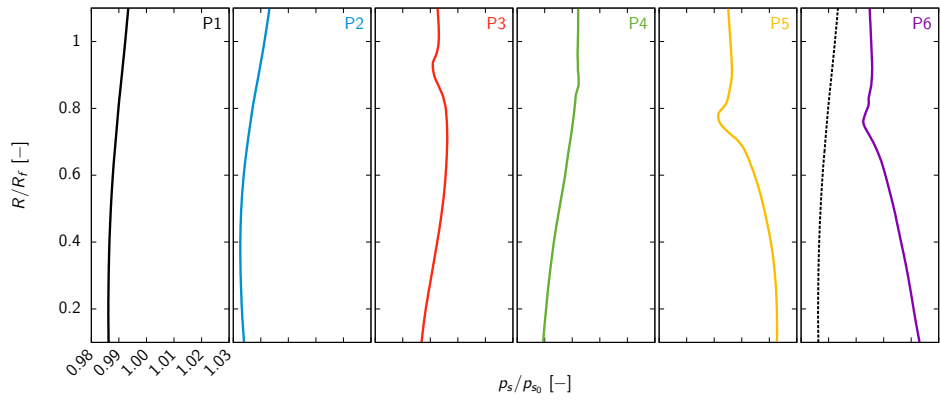


Figure 8.8: Low-speed isolated configuration: radial profiles (contd.).

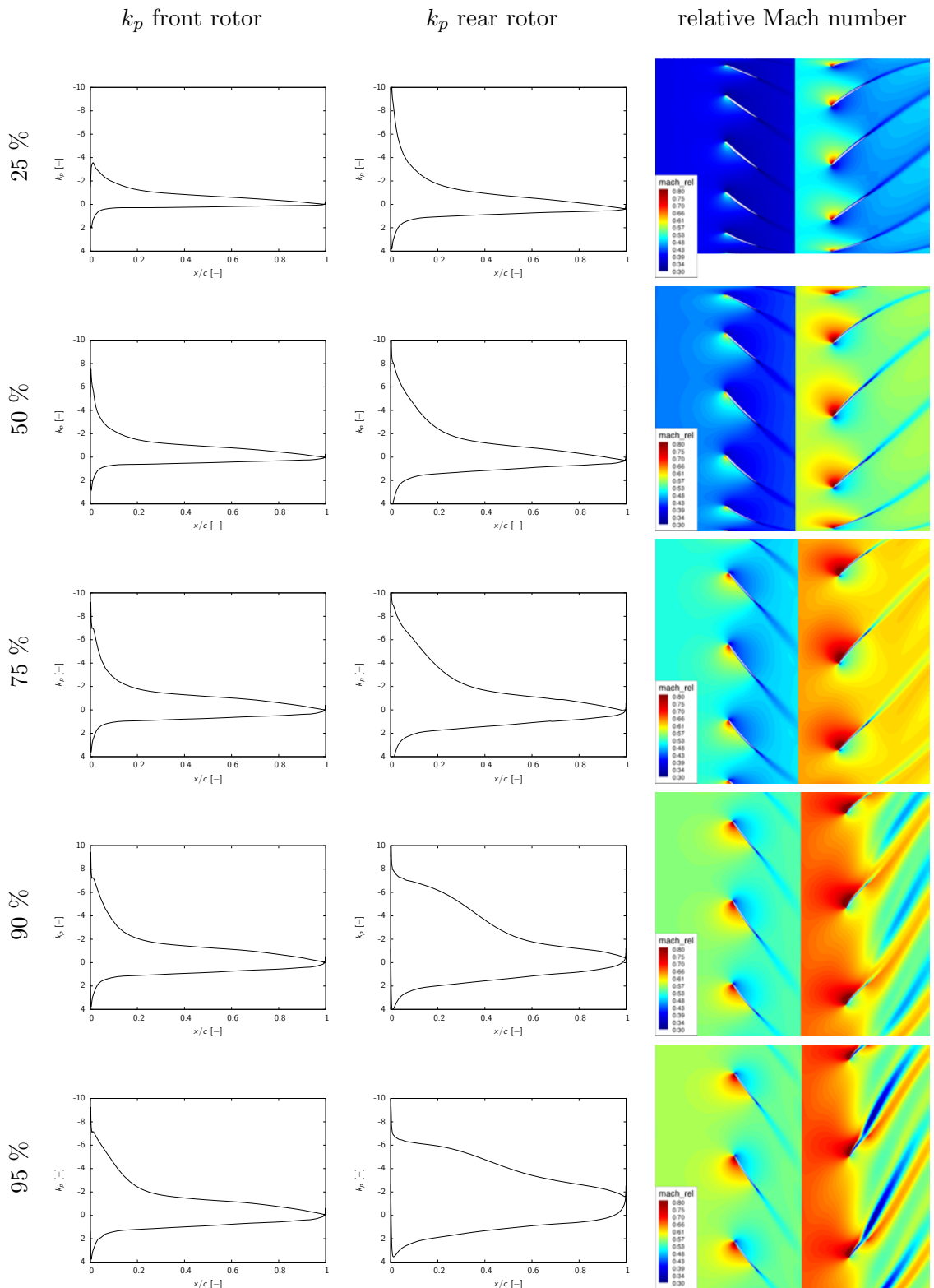


Figure 8.9: Low-speed isolated configuration: pressure coefficient and relative Mach number contours at different radial position.

vortices. This is of course the main weakness of the steady approach used here to compute the CROR configuration. In fact, as recalled in Chap. 1, the tip vortices and the wakes shed by the front rotor blades can impact the rear rotor blades and thus generate exceeding level of unsteadiness, responsible for noise and vibration. As the influence of the front rotor tip vortices is azimuthally-averaged, its influence is lessened. Therefore unsteady computations will be needed to predict the unsteady interactions of the front rotor with the rear one. This is the aim of the forthcoming Section 8.5. The remaining axial planes extracted at P_5 and P_6 depict the strong loading of the rear rotor blades. In fact, baring in mind that the axial planes are equidistant from the blades, the larger the loss traces, the stronger the loading of the blades. According to the Euler theorem applied on the two rotors, the enthalpy variation is equal to the variation of the dot product of the rotational velocity $U = \Omega R$ to the tangential absolute velocity V_θ . If the inflow is similar on both rotors, the work exchange should be the same. However, the flow has been accelerated by the front rotor resulting in a higher work exchange to obtain the same deviation on the rear rotor. This higher work exchange implies a greater loading of the rear rotor blades and thus higher pressure gradients. Therefore, the flow field will be more prone to boundary layer separation, which is observed in practice in Figure 8.10 by larger entropy values downstream the rear rotor blades. Moreover, even though the tip vortices shed by the front rotor blades are azimuthally-averaged, their trace is still seen and seems to indicate that they will interact with the rear rotor tip vortices.

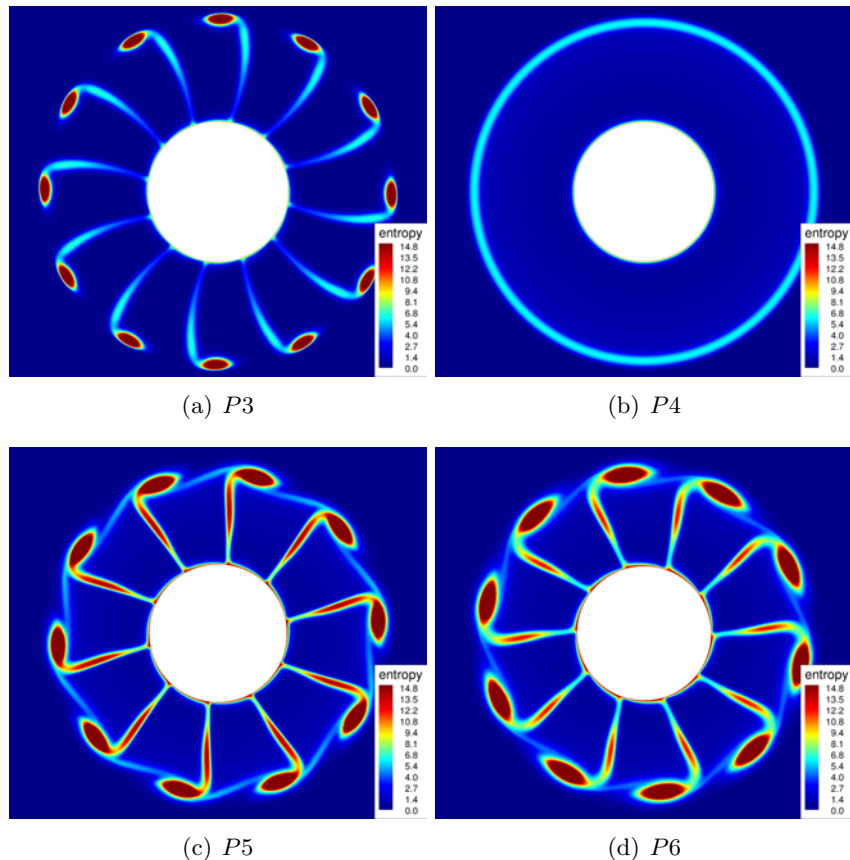


Figure 8.10: Low-speed isolated configuration: axial cuts of entropy.

8.4 Spectral convergence of the harmonic balance computations

8.4.1 Using the prediction tool

The prediction tool based on a mixing plane computation described in Sec. 6.3.5 is applied to the studied configuration to evaluate the required number of harmonics needed for the harmonic balance approach to be converged. The algorithm to compute the accumulation of energy is detail in Sec. A.3.

To have a global insight of the energy contained in the tangential distortion across the whole span, the energy accumulation is plotted using a color map in Figure 8.11. Three contour lines are added to ease the interpretation: 90%, 95% and 99% of accumulated energy, corresponding to a truncation error of respectively 30%, 20% and 10%.

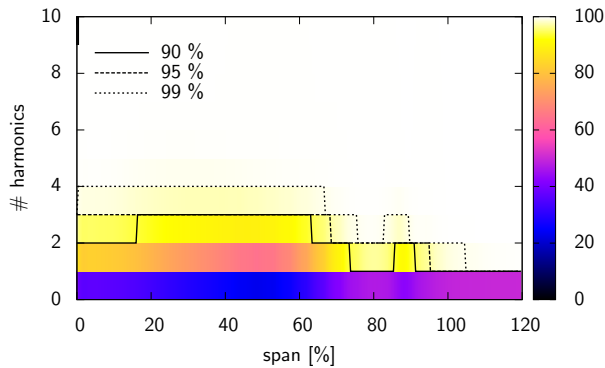


Figure 8.11: Low-speed isolated configuration: prediction of the number of harmonics needed to simulate the configuration.

The level of accumulated energy required for a computation to be rigorously converged is difficult to estimate. It seems reasonable, from an engineering standpoint, to consider that a 99% accumulation of energy should be a good criterion. To emphasize that, the reconstruction of a wake as a function of four levels of cumulative energy E is depicted in Figure 8.12. One

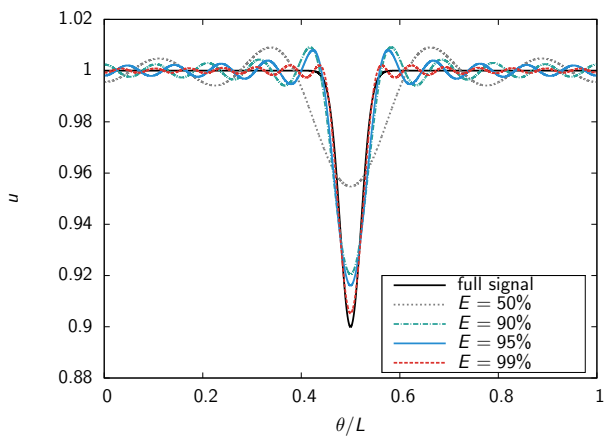


Figure 8.12: Reconstructions of a wake depending on the energy content kept in the signal.

can see that a reconstruction using only 50% of the energy leads to a signal that has neither the right wake deficit nor the correct width. Using 90% and 95% of the energy improve the resulting shape but large secondary oscillations remain, with a bad capture of the wake deficit. In opposite, by using 99% of the energy to reconstruct the signal, only minor oscillations are seen and the wake width and deficit are recovered with more than 95% accuracy. Thus, the 99% energy threshold ensures that the wake will be correctly transmitted to the opposite row, which is the prior concern of this Section.

Four harmonics are needed to capture 99% of the energy, even though at a relative span superior to 60%, only three harmonics would be needed. However, as the implementation of the harmonic balance used in this work does not allow a varying number of harmonics through the configuration, four harmonics is supposed to be sufficient to efficiently represent the unsteady flow field.

8.4.2 Analyzing the similarity coefficients

To confirm the number of harmonics needed to ensure the convergence of harmonic balance computations, simulations are run from one to four harmonics. The strategy used to launch the computation is as follow: the steady computation is used as an initial guess for the $N = 1$ HB computation. Then each new HB computation is launched with the previous one as initial solution.

Two harmonics are actually necessary to converge the temporal mean of the similarity coefficients as shown in Tab. 8.3. After that, a slight evolution of the coefficients is still seen but represents a change lower than 0.01% of the $N = 4$ results, hence the convergence. Note

steady		HB $N = 1$	HB $N = 2$	HB $N = 3$	HB $N = 4$
		(time average)			
C_T	1.1319	1.1334	1.1330	1.1330	1.1329
C_P	2.0927	2.0951	2.0944	2.0945	2.0946
η	0.5726	0.5727	0.5726	0.5726	0.5725

Table 8.3: Low-speed isolated configuration: analysis of the number of harmonics required to capture the time average similarity coefficients.

that a steady computation is sufficient to retrieve the temporal mean value of the similarity coefficients for this low-speed configuration. In fact, on this variables, a maximum of 0.1% difference is observed by comparing the mixing plane and harmonic balance results.

8.4.3 Analyzing the blade response

Of course, analyzing integrated results to assess the convergence of a computation is a primarily step that should be complemented with a local analysis. In this way, a discrete Fourier transform is performed to analyze the first harmonic of the static pressure on the rear rotor blades. Due to the passing of the front rotor wakes, these blades will experience a high level of unsteadiness. It is therefore considered as a bottleneck in the convergence of the HB computations, hence its analysis. The results are shown in Figure 8.13.

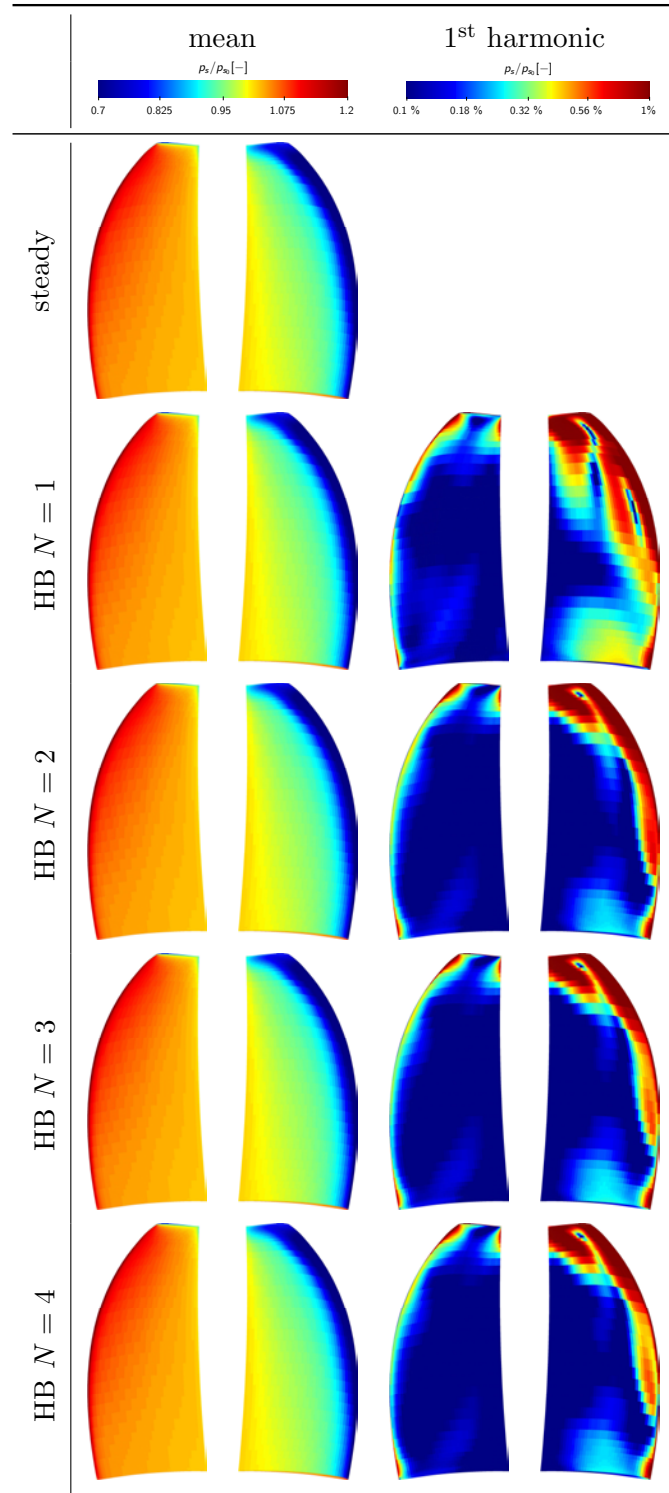


Figure 8.13: Low-speed isolated configuration: analysis of the number of harmonics required to capture the harmonic response of the rear rotor blades.

Only one harmonic is needed to converge the time-average value on the rear rotor blades. Actually, the steady computation already gave a good prediction of this time-averaged value. This is due to the range on which this low-speed CROR configuration operates. The Mach number is almost within the incompressible range. As such, the non-linearities of the Navier–Stokes equations remains small and steady approaches give good results.

Two to three harmonics are needed to converge the first harmonic pressure response on the rear rotor blade. This is a rough estimation as a small convergence of the harmonic pressure rise on the suction side of the blade between HB $N = 2$, $N = 3$ and $N = 4$ computations can be seen.

8.4.4 Analyzing the radial cuts

The final assessment of the convergence is done on radial cuts of entropy made at 75% of the height of the rear rotor blades. This is the region where the blades are most likely to be highly loaded, hence the choice of this span. The entropy spurious waves vanishes when computing the HB $N = 4$ even though the HB $N = 3$ computation give a relatively smooth entropy field. Nevertheless, the prediction tool, the similarity coefficients, the harmonic blade response and

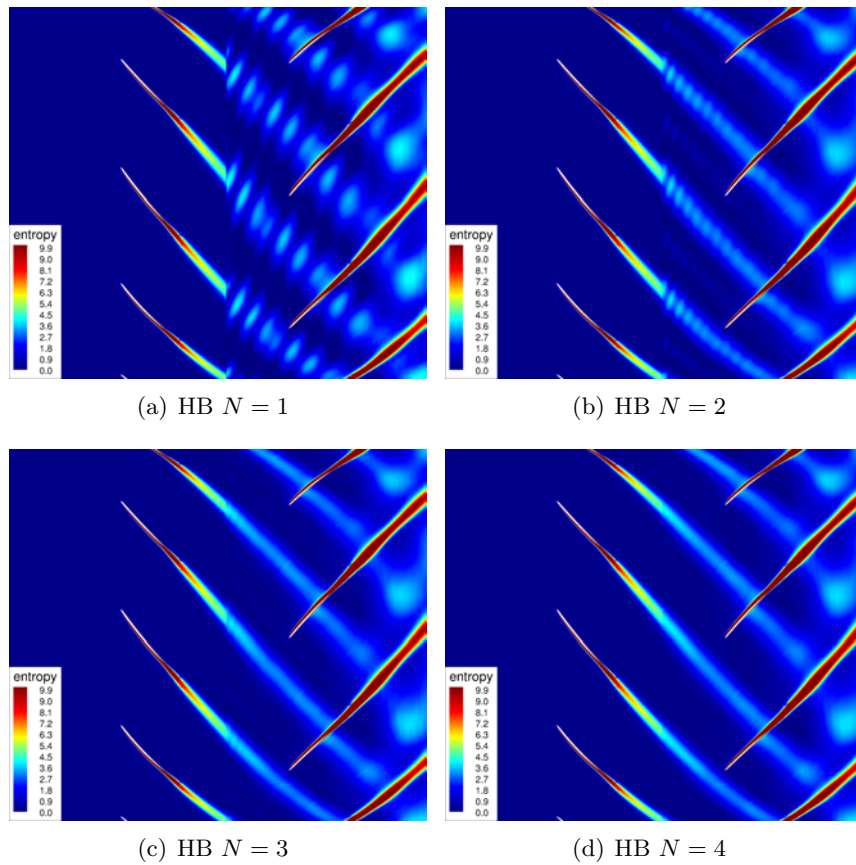


Figure 8.14: Low-speed isolated configuration: analysis of the number of harmonics required to capture the wake at a 75% height radial cut.

the radial cuts give us confidence in the HB $N = 4$ computation. It is therefore chosen to

further analyze the unsteady results on this HB $N = 4$ computation.

8.5 Unsteady rigid-motion results

8.5.1 Similarity coefficients

Figure 8.15 depicts the unsteady variation of the thrust coefficient C_T on both the front and the rear rotor. The time is normalized by the reference period of the current rotor (the rotation frequency n) and the thrust coefficient is normalized by its temporal mean value. This allows to assess the unsteady variations over one reference period.

The level of unsteadiness is rather the same on both rotors. It represents an envelope of approximately $\pm 3\%$ of the temporal mean value. This level is not negligible and justifies the use of unsteady methods on CROR configurations. Moreover, even though wakes are shed behind the front rotor that impinge the rear rotor blades, the level of unsteadiness perceived by the rear rotor is close to the front rotor ones. Actually, the rear rotor sees more unsteady flow phenomena but on a smaller area. This can be one of the reasons explaining the equal level of unsteadiness observed on the front and rear rotor blades.

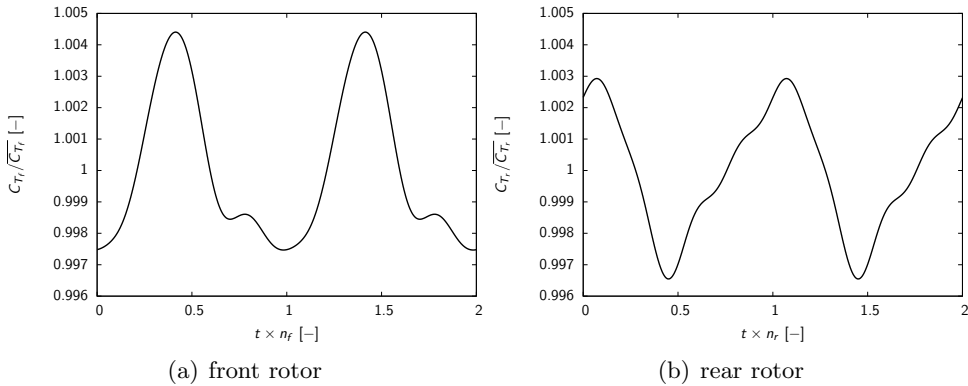


Figure 8.15: Low-speed isolated configuration: unsteadiness seen by the rotors.

To assess in more detail the unsteady flow field seen by the blade, a harmonic analysis on the blades is performed in the following section.

8.5.2 Two-dimensional results: harmonic blade response

A discrete Fourier transform is computed on the blades for the unsteady static pressure variable. This gives an idea of the level of unsteadiness seen locally by the blades. The amplitude of the first harmonic of the blade passing frequency of the opposite rotor is shown in Figure 8.16 for both blades. The legend is in logarithmic scale and it is different for the front and rear rotor blades. In fact, even though the integrated level of unsteadiness is relatively the same, this fails when looking at local results. Roughly, the harmonic amplitude of the static pressure on the rear rotor blade is ten times larger.

On the front rotor blade, the level is large as it is close to 0.1% of the inflow static pressure. Moreover, the pressure side exhibits a larger level of unsteadiness compared to the suction side. This is due to the relative position of the blades which makes the pressure side more vulnerable

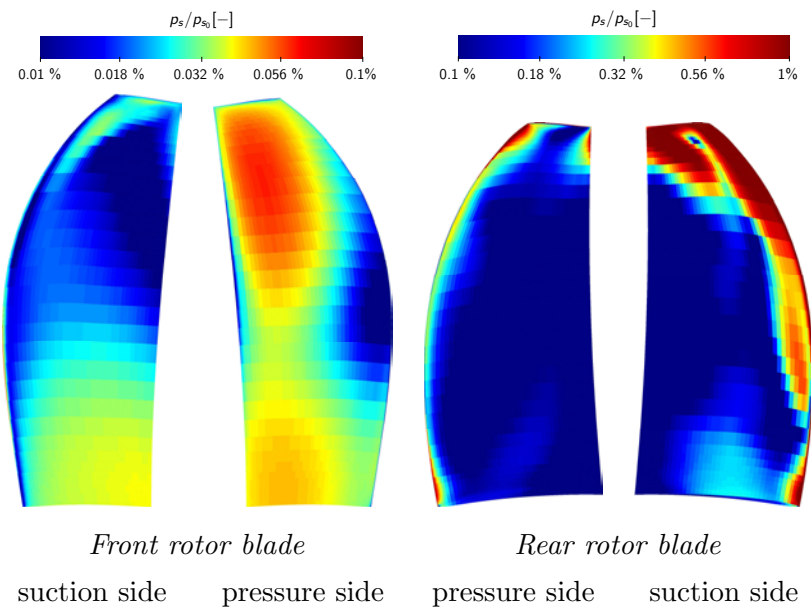


Figure 8.16: Low-speed isolated configuration: harmonic response of the front rotor blades.

to potential effects. In fact, as can be seen on radial cuts (as for instance in Figure 8.14) the suction side is shield from the flow field coming from downstream. The intensity is not uniform along span with a relatively higher amplitude of unsteadiness at the tip of the blade and near the hub on the pressure side. On the suction side, the largest level of unsteadiness is observed near the hub.

On the rear rotor blade, the level of unsteadiness is much larger than the one observed on the front rotor blade. Here, the level of unsteadiness goes up to 1% of the inflow static pressure. This is mostly due to the wake passing shed by the front rotor blades. In fact, on the leading edge of the suction side of the rear rotor blade, a strong harmonic response is observed, while it is much smaller on the pressure side. Baring in mind that the suction side sees the wake passing, one can deduce that this strong harmonic response is attributed to wake passing. In addition to that, in the tip region of the rear rotor blade, a stronger level of unsteadiness is observed. As mentioned previously, tip vortices are shed by the front rotor blades. Even though the rear rotor blades are clipped, as the stream tube contracts, there is a chance that the front rotor blades tip vortices interact with the rear rotor blades. This is investigated by analyzing axial cuts of entropy.

8.5.3 Two-dimensional results: axial cuts

Axial cuts of entropy at four planes (P_3 , P_4 , P_5 and P_6) are shown in Figure 8.17. The steady results are also reported for comparison. Compared to a steady computation, the harmonic balance approach allows to capture the impact of the front rotor tip vortices on the rear rotor. Between plane P_3 and P_4 , they have been diffused thanks to the viscosity effects. The interaction of the front and the rear rotor tip vortices is highlighted in the P_5 plane. At the end, in plane P_6 the vortices have almost merged and a large entropy trace remains. This confirms the impact of the front rotor tip vortices on the rear rotor blades, which explains the large static pressure fluctuations observed in the tip of the rear rotor blades. Nevertheless, for

this configuration, the steady mixing plane approach provides good results when comparing the axial cuts downstream the rear rotor ($P6$).

8.5.4 Two-dimensional results: radial cut of harmonic pressure

To further analyze the unsteadinesses that are seen in a CROR configuration, a radial cut at 75% of the rear rotor height of the first harmonic of the static pressure is shown in Figure 8.18. The two rotors rotating in opposite direction, a steady field for the former is seen as unsteady by the latter and *vice-versa*. Therefore the flow field is, by nature, discontinuous at the rows interface.

On the front rotor side of the interface, a high amplitude azimuthal pattern of static pressure is seen. It is representative of the potential effects: the blades deviates the stream lines and as the two rotors rotate in opposite directions, these deviations are finally seen as unsteady flow features by the front rotor.

On the rear rotor side of the interface, no azimuthal pattern of static pressure is observed near the interface. Conversely, the pressure unsteadinesses are mostly observed near the rear rotor blades. These pressure unsteadinesses come actually from the unsteady wake passing. In fact, the absolute velocity deficit in the wakes shed by the front rotor is seen as unsteady by the rear rotor. However, at the blade walls, the velocity is necessarily null. These velocity fluctuations are actually seen as pressure fluctuations since the presence of the blades transforms velocity into pressure at blade walls. Figure 8.19 supports this argument as the amplitude of the Mach number fluctuations vanishes in regions where the pressure fluctuations grows near the rear rotor blades.

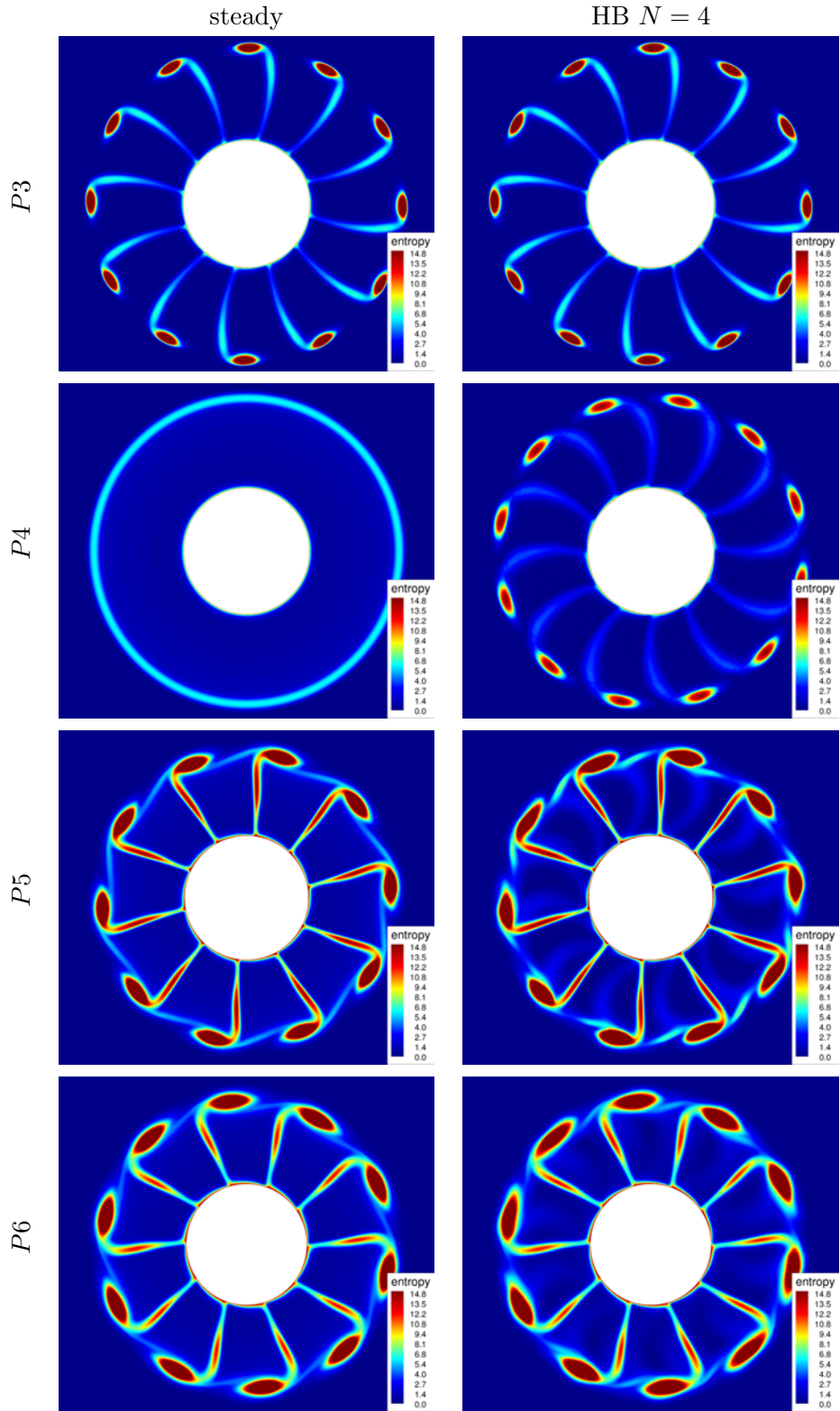


Figure 8.17: Low-speed isolated configuration: axial cuts of entropy.

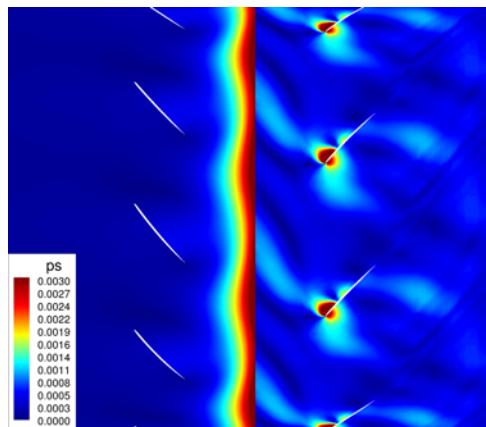


Figure 8.18: Low-speed isolated configuration: radial cut of the first harmonic of the static pressure normalized by the inflow static pressure.

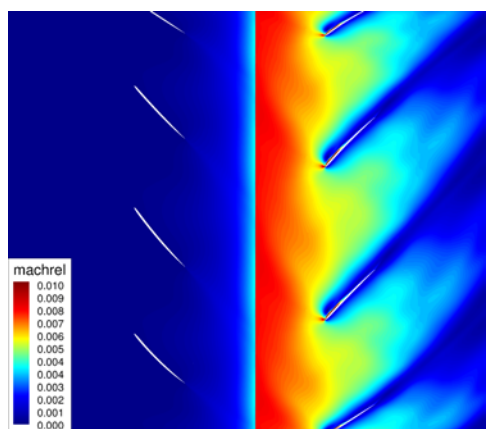


Figure 8.19: Low-speed isolated configuration: radial cut of the first harmonic of the relative Mach number.

8.6 Aeroelastic results

8.6.1 Stability curve

The damping as a function of the inter-blade phase angle, namely the stability curve, is reported in Figure 8.20 for the two modes considered. All the modes have a positive damping which clear this low-speed CROR configuration from flutter. The minimum damping is at $\text{IBPA}=30^\circ$ for the second flection mode and at $\text{IBPA}=-30^\circ$ for the first torsion mode. The variation of the damping against the inter-blade phase angle is limited for the 2F mode while a much larger interval of variation is observed for the 1T mode. To further analyze the aeroelastic behavior of the front rotor blades, the local excitation is computed and shown in the following section.

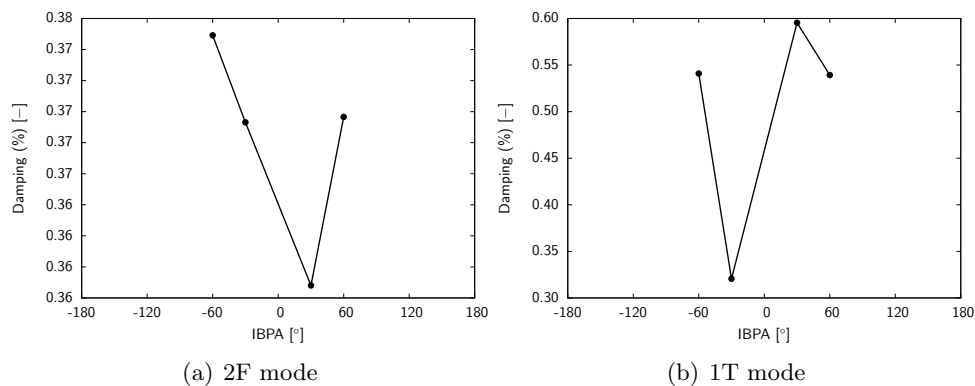


Figure 8.20: Low-speed isolated configuration: integrated damping for modes 2F and 1T.

8.6.2 Local excitation

The local excitation is shown on the pressure side and the suction side of the front rotor blades in Figure 8.21. It is the local damping given in each cell divided by the surface of the cell. It is therefore expressed in m^{-2} .

Firstly, the amplitude of variation of the damping is confirmed by the local results. In fact, higher excitation peaks are observed on the 1T mode results. This can be explained by the physical behavior of the 1T mode. The shape of this last has the tendency to change the angle of attack of the blade, which governs at first order the performance of the blade. Therefore, changing the angle of attack of the blades can have a strong impact on the flow field that develops around the blades. This can explain why the first torsion mode damping has a larger variation interval compared to the second flection mode.

Secondly, the variation of the excitation against IBPA is barely seen for the 2F mode. The shape of the results does not change. This is not true for the 1T mode. In fact, at the leading edge of the pressure side, a positive excitation structure is seen for all IBPA except $\text{IBPA} = -30^\circ$. Moreover, for this last, the two biggest excitation structures on the pressure and suction sides of the blade seem to propagate toward the hub.

Thirdly, inflection lines for the modes are also inflection lines for the local excitation values. Moreover, inflection lines for the flow physics as the strong adverse pressure gradient near the leading edge of the blade on the pressure side that lessened at approximately 25% of the chord is a region where the local excitation changes in terms of sign. This effect is not seen on the

pressure side where the flow physics is smoother compared to that of the suction side. Even though the local excitation values on the 1T mode are higher in terms of intensity, this is not observed in the damping value that has the same order of magnitude than the one of the 2F mode. Only the variation of damping between different inter-blade phase angles is affected.

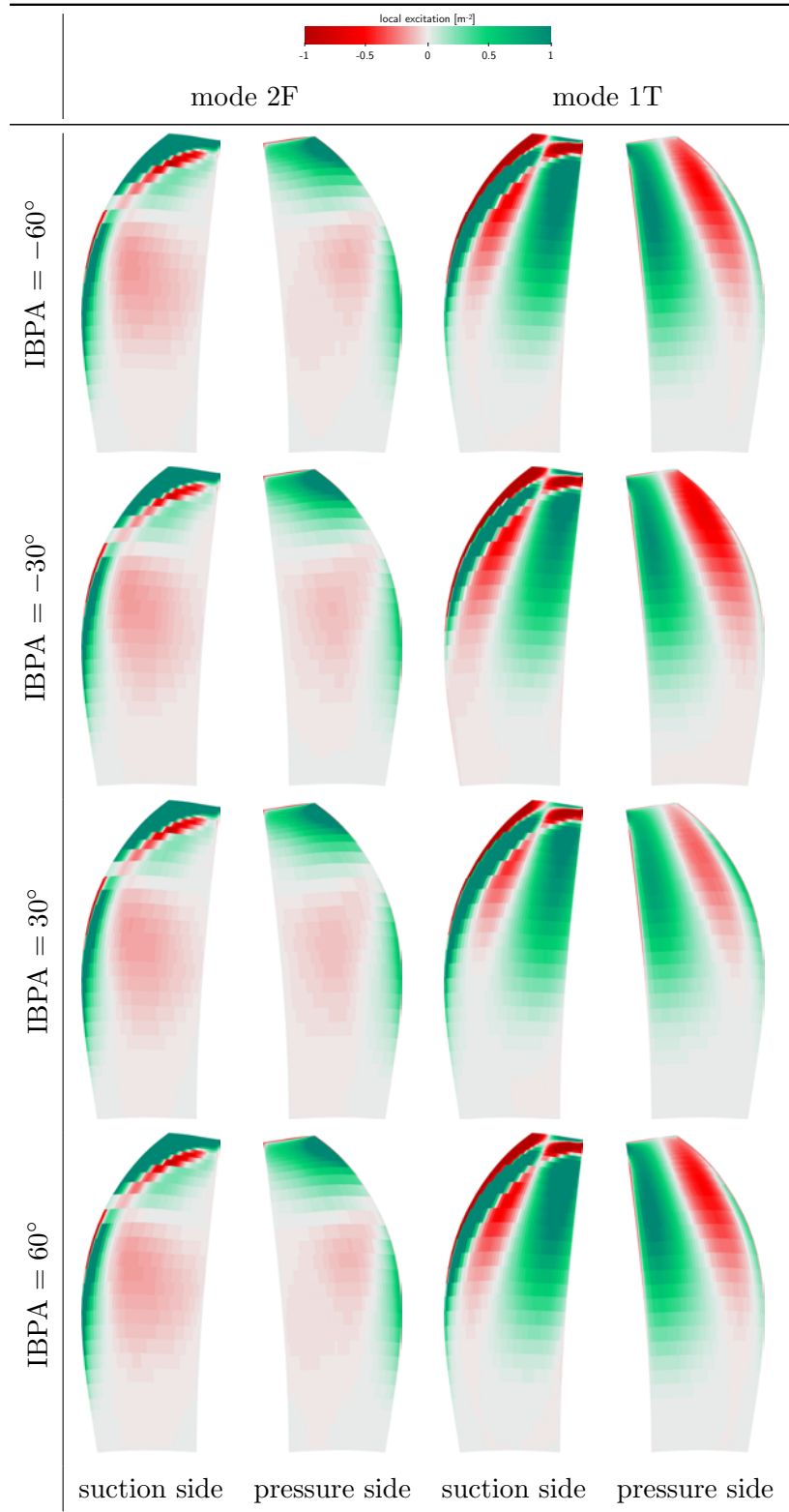


Figure 8.21: Low-speed isolated configuration: local excitation for modes 2F and 1T.

Summary

The multi-frequential harmonic balance approach along with the weak-coupling approach has been used in this chapter to simulate the flutter behavior of a low-speed CROR computation. It is shown that the local excitation varies in correlation with the inflection lines of the modes and with a change in aerodynamic behavior. This configuration is shown to be cleared from flutter as the damping is positive for all modes and all inter-blade phase angles. To further assess the approach, a more demanding configuration is studied, namely a high-speed CROR.

Isolated high-speed CROR configuration

Abstract

To further assess the proposed multi-frequential harmonic balance method along with a weak-coupling approach, a more demanding case is studied, namely a high-speed CROR configuration. The number of harmonics required to compute such a configuration is shown to be higher than the low-speed configuration. The unsteady rigid-motion computations are analyzed and aeroelastic simulations are then carried out, showing that the proposed approach is robust enough to assess such configurations.

9.1 Presentation of the case

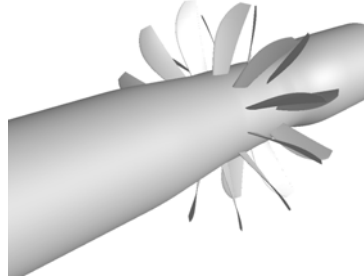


Figure 9.1: High-speed isolated contra-rotating open rotor geometry.

The configuration studied in this Chapter is the same as the previous one but with a different angle of attack of the blades as the inflow Mach number is larger. The geometry is shown in Figure 9.1. This geometry is the High-Speed (HS) version of the previous one, representative of the cruise flight condition. The rotation speed is kept almost constant between the two configurations, meaning that the only way to ensure a proper adaptation of the velocity field is to change the angle of attack of the blades.

The main input parameters of the case are recalled in Tab. 9.1. The inflow Mach number

M_0	J	M_{tip}
0.73	3.7	0.96

Table 9.1: High-speed isolated contra-rotating open rotor flight condition parameters.

is within the transonic range. Its high value can suggest the appearance of shocks in the flow field. This is emphasized by the M_{tip} which is near from being supersonic.

The same two structural modes are considered for the aeroelastic study of this configuration: the second bending/flection mode (2F) and the first torsion mode (1T) of the front rotor. These were inputs of the current work.

The frequency, mass and stiffness of the modes are given with the corresponding modes. The ratio of the frequency of the blade passing frequency of the opposite row, namely the rear rotor, over the aeroelastic frequency of each mode varies between $3.35 \leq f_{BPF}/f_{AEL} \leq 4.11$. Again, this last frequency governs the unsteady rigid-motion flow physics and will have to be computed alongside with the aeroleastic frequency. Therefore, the multi-frequential formulation of the harmonic balance approach will be used to simulate the aeroelastic response of the blades (see Sec. 9.6).

9.2 Numerical setup

The same topology and number of grid points is used to mesh this high-speed configuration. If nothing particular is said, the same numerical parameters are kept for the study of this high-speed configuration. The reader is referred to Sec. 8.2 for detailed information.

The same numerical approach as the low-speed configuration is chosen for the aeroelastic computations that will be presented in Sec. 9.6. For practical reasons, the harmonic balance computations are run with the same number of frequencies as the low-speed configuration, namely five frequencies in total. This might be not sufficient as suggested by the prediction tool shown below in Sec. 9.4. A partial convergence study is therefore conducted afterwards in Sec. 9.6.3. In the rear rotor, the harmonics of the front rotor blade passing frequency are chosen. In the front rotor, the first frequency is the frequency associated to the vibration of the blade and the remaining ones are the harmonics of the rear rotor blade passing frequency. The time instances are automatically chosen using the OPT algorithm which leads to a condition number always lower than 1.1, ensuring thus the stability of the computations.

Influence of the spatial discretization The same exercise as done in Sec. 8.2 is made below. Four schemes are evaluated based on the convergence of the computations and of the integrated results (similarity coefficients). For the Jameson et al. [59] scheme, the artificial viscosities are chosen as follow: $\kappa_2 = 1.0$ and $\kappa_4 = 0.016$. We will see that the computation converges with this low κ_4 coefficient. Therefore, only this coefficient will be tested.

The convergence of the computations using the four spatial schemes is reported in Figure 9.2. The convergence is good for all the spatial schemes. In fact, more than five orders of magnitude are lost on the residuals.

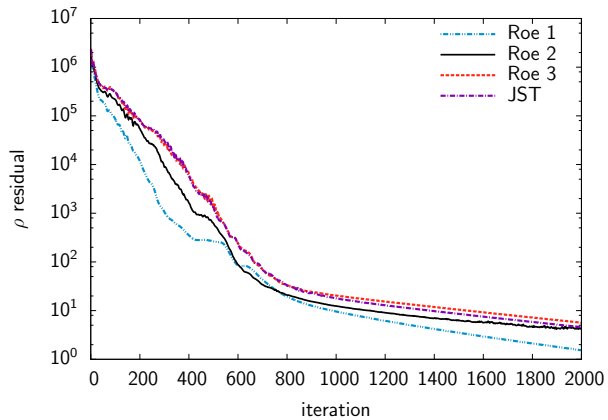


Figure 9.2: High-speed isolated configuration: convergence of steady computations using different spatial schemes.

The values of the similarity coefficients obtained with all the spatial schemes is reported in Figure 9.3. Arbitrarily, the values are given as a ratio over the Roe 2 values. The first-order upwind scheme (Roe 1) give similarity coefficients that are several percent lower than the Roe 2 value. The other schemes give results that are less than 1% close, therefore and for consistency with the approach retained for the low-speed configuration the Roe 2 scheme is chosen for the following computations.

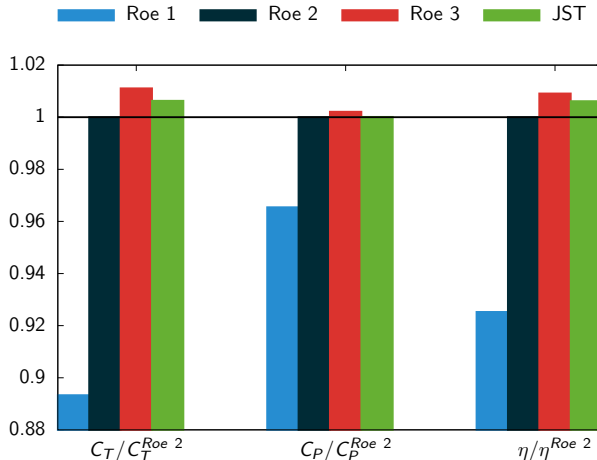


Figure 9.3: High-speed isolated configuration: convergence of similarity coefficients using different spatial schemes.

9.3 Steady results

9.3.1 Analysis of the convergence

The convergence of the simulation is obtained after 500 iterations for both the residuals and the similarity coefficients (Figure 9.4). More than five orders of magnitude are obtained for the residuals and the similarity coefficients are stabilized starting below 500 iterations. According to Casey and Wintergerste [16], this means that the steady simulation is converged.

9.3.2 Similarity coefficients

The similarity coefficients are reported in Tab. 9.2. They are representative of a cruise propeller (see Eq. (1.17)). Firstly, the thrust is higher on the rear rotor than on the front rotor, even though it is relatively well distributed. Bare in mind that the rear rotor similarity coefficient is normalized by the front rotor diameter. Therefore, the thrust produced by the rear rotor is larger than the one of the front rotor, relatively to its diameter. Secondly, the power coefficient is similar for both the front and the rear rotor. As the power coefficient represents the mechanical input given to flow, this means that the mechanical distribution is well repartitioned, which is a design wish for the integrity of the drive shaft. In fact a non-uniform power coefficient might give an additional momentum on the drive shaft which can deteriorates its mechanical properties.

global			front			rear		
C_T	C_P	η	C_{T_f}	C_{P_f}	η_f	C_{T_r}	C_{P_r}	η_r
0.902	3.849	0.858	0.411	1.926	0.780	0.491	1.922	0.935

Table 9.2: High-speed isolated configuration: similarity coefficients.

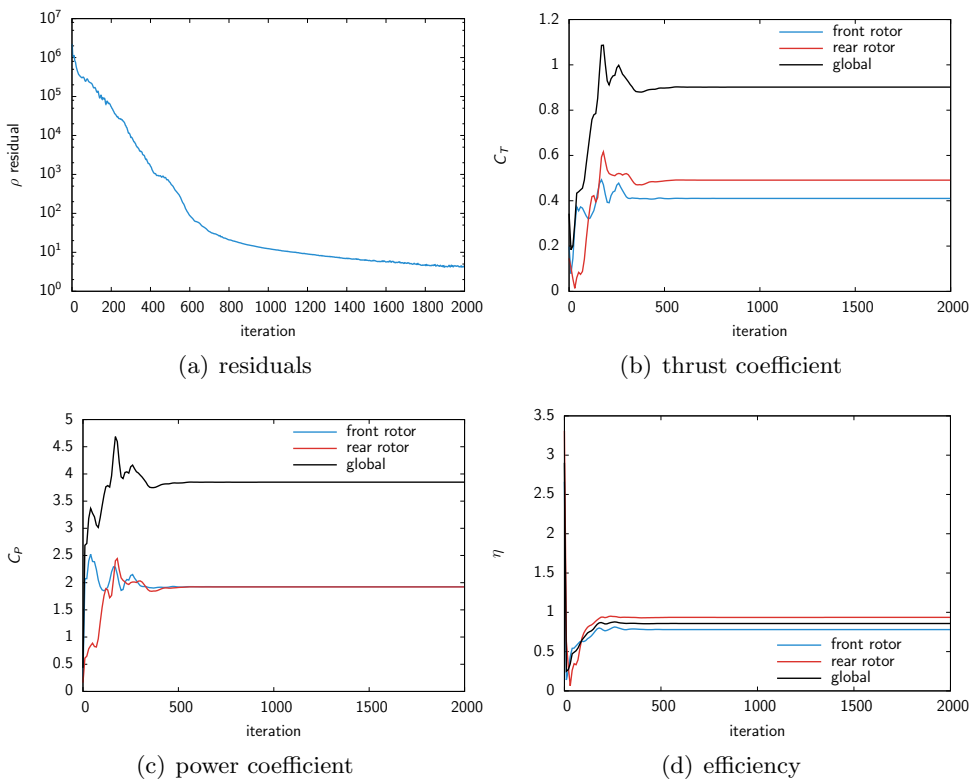


Figure 9.4: High-speed isolated configuration: convergence of the steady computation.

9.3.3 Radial profiles

Radial profiles are computed on the steady results and reported in Figure 9.5.

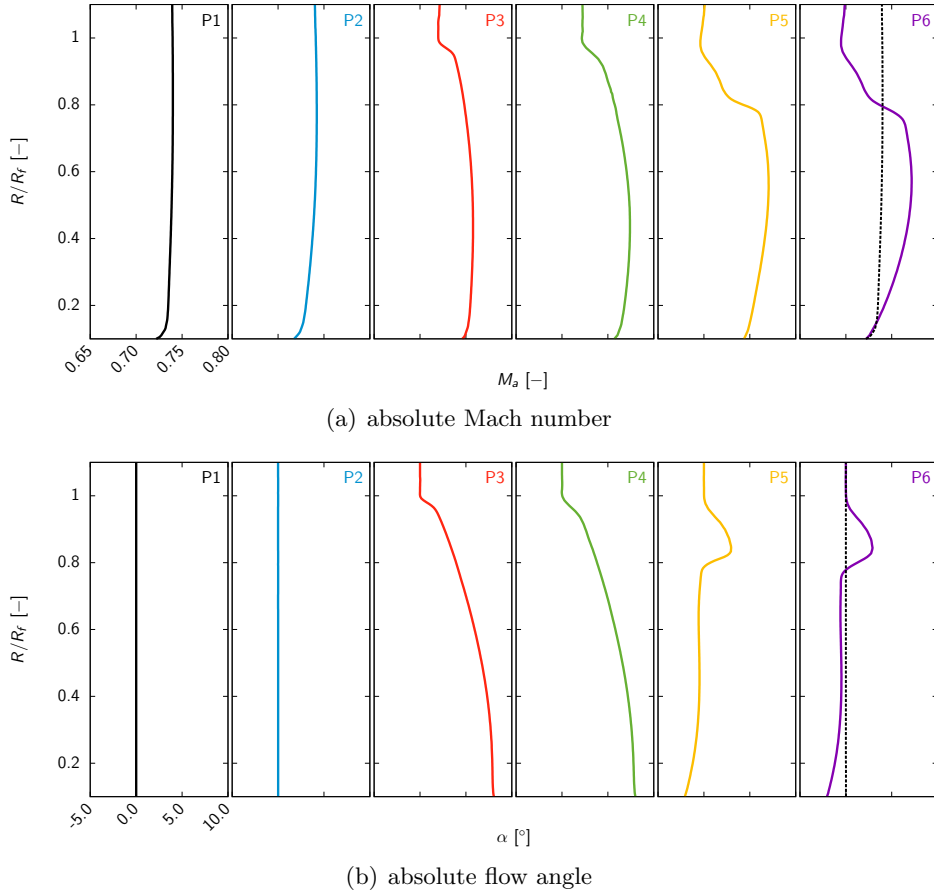
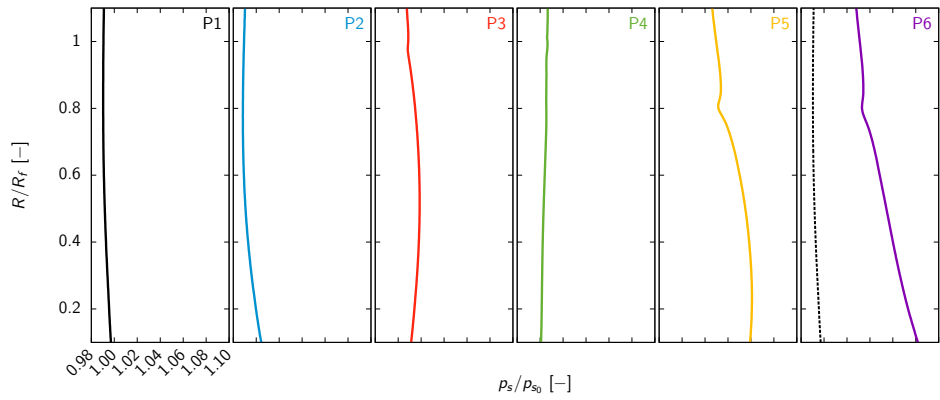


Figure 9.5: High-speed isolated configuration: radial profiles.

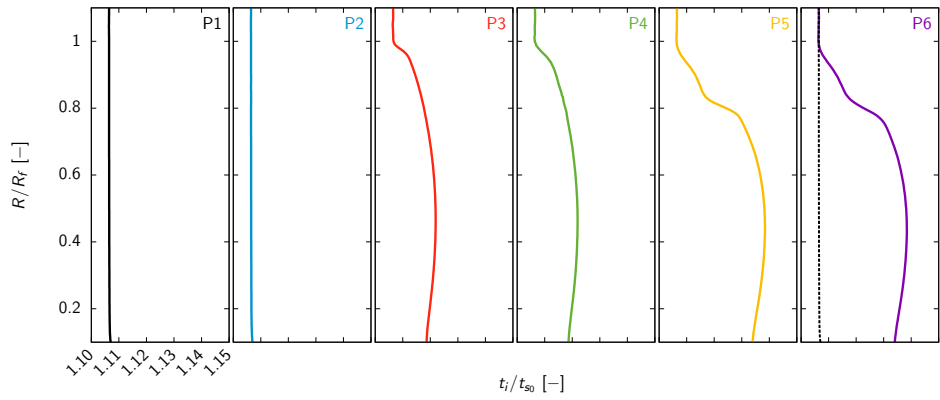
The absolute Mach number (Figure 9.5(a)) increases from its inflow value ($M_a = 0.73$) up to around $M_a = 0.76$. This represents a 4% increase that has to be compared to the 100% increase for the low-speed configuration. Nevertheless, this represents an absolute $\Delta M_a = 0.03$ increase for this high-speed configuration where it was $\Delta M_a = 0.2$ for the low-speed configuration. The stream tube contraction is smaller than the low-speed configuration as the increase in velocity remains bounded. It seems that the front rotor tip vortices do not interact with the rear rotor blades as the small increase near 90% of the span, which is attributed to the core of the front rotor tip vortex, is not contracted by the stream tube.

The absolute pitch angle (Figure 9.5(b)) of the velocity highlights, again, the advantage of using a CROR compared to a single row propeller system. In fact, the flow is deviated by the front rotor from its axial direction to a mean 5° velocity vector. The rear rotor then deviates back the flow field to make it almost purely axial with exceptions near the hub and near the front tip vortex region ($0.75 \leq R/R_f \leq 0.95$). This explains the efficiency of a CROR propeller system also for high-speed inflow conditions, which is the design priority.

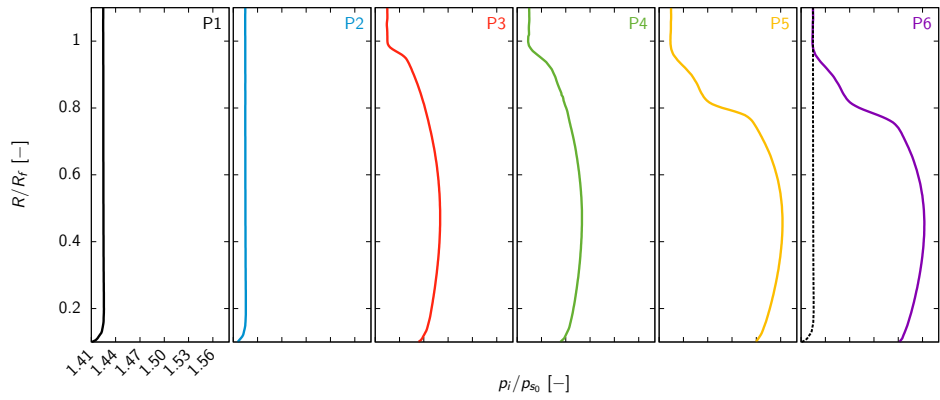
The static pressure (Figure 9.5(d)) increases by at-most 10% which is larger than it was for the low-speed inflow condition. These are clearly compressibility effects due to the high inflow



(d) static pressure



(e) stagnation temperature



(f) stagnation pressure

Figure 9.5: High-speed isolated configuration: radial profiles (contd.).

Mach number. As the goal of a CROR is to create thrust through a large mass-flow and a velocity increment, this static pressure rise helps increasing the mass-flow and thus participates to thrust. In fact, using roughly the perfect gas state-equation, a static pressure increase is seen as a density increase that participates to a high mass-flow, hence the contribution to the thrust. The potential effects can be seen in the $P2$ and $P4$ planes. In fact, the pressure decreases before crossing the rotor blades. This is due to the acceleration of the fluid that is done at each rotor crossing. This increase of velocity creates a decrease in static pressure that is seen upstream the rotors.

With the stagnation temperature rise shown in Figure 9.5(e), one can say that the rotors provide energy to the fluid to create the thrust. The stagnation pressure is shown in Figure 9.5(f). At each rotor crossing it increases since both the absolute velocity and the static pressure increase. Moreover, the stream tube contraction seems to be smaller compared to the low-speed flight condition. It will have to be confirmed by the forthcoming unsteady results.

9.3.4 Flow field around the blades

Relative Mach number contours and the pressure coefficient k_p are shown in Figure 9.6 for both the front and the rear rotors.

On the front rotor, for relative span $R/R_f = 25\%$, a compression is observed near the leading edge ($x/c \leq 0.2$) of the suction side. The pressure coefficient is then almost constant up to the trailing edge. For all relative spans, a small negative incidence is indicated by a crossing in k_p values of the front rotor, near the leading edge. This might indicate that either the incidence of the blades or the rotation speed is not well adapted for this inflow condition. The shock that was seen near the leading edge seems to change to a weak shock wave for higher relative spans ($R/R_f \geq 50\%$). On the suction side of the blade, the pressure coefficient k_p increases such that for $R/R_f \geq 75\%$, a shock is observed on the suction side of the blade at $x/c \approx 0.7$.

On the rear rotor, the flow field seems to be better adapted to the inflow conditions. In fact, no negative incidence is seen. A shock is observed at $x/c \approx 0.5$ for all relative spans that moves toward the trailing edge as for $R/R_f = 90\%$, it is located at $x/c \approx 0.6$. In fact, as the relative span increases, the relative Mach number grows which explains the movement of the shock toward the trailing edge. For $R/R_f = 95\%$, no shock is seen but rather a smooth compression of the flow. This is due to the leaving of rear rotor tip vortices that splits the pressure gradient responsible for the shock. In fact a low velocity trace seems to indicate a tip vortex. Globally, the pressure coefficients on the rear rotor have a higher integral, explaining the higher thrust coefficients observed in Sec. 9.3.2.

To investigate the structure of the tip vortices, axial cuts of entropy made at planes $P3$, $P4$, $P5$ and $P6$ are shown in Figure 9.7. One can notice that the vortices look much thinner compared to the low-speed inflow condition ones. This is due to the staggering angle of the blades. In fact, as the inflow Mach number is greater, the staggering angle should be decreased so that an almost constant rotation speed can be kept. Therefore, projecting the tip vortices on axial cuts will make the high-speed ones look thinner. Contrary to the low-speed inflow condition, the trace of the front rotor tip vortices seen in plane $P4$ seems to pass above the rear rotor tip vortices. This was also observed when looking at the radial profiles. This will be deeply investigated with unsteady simulations in Sec. 9.5.

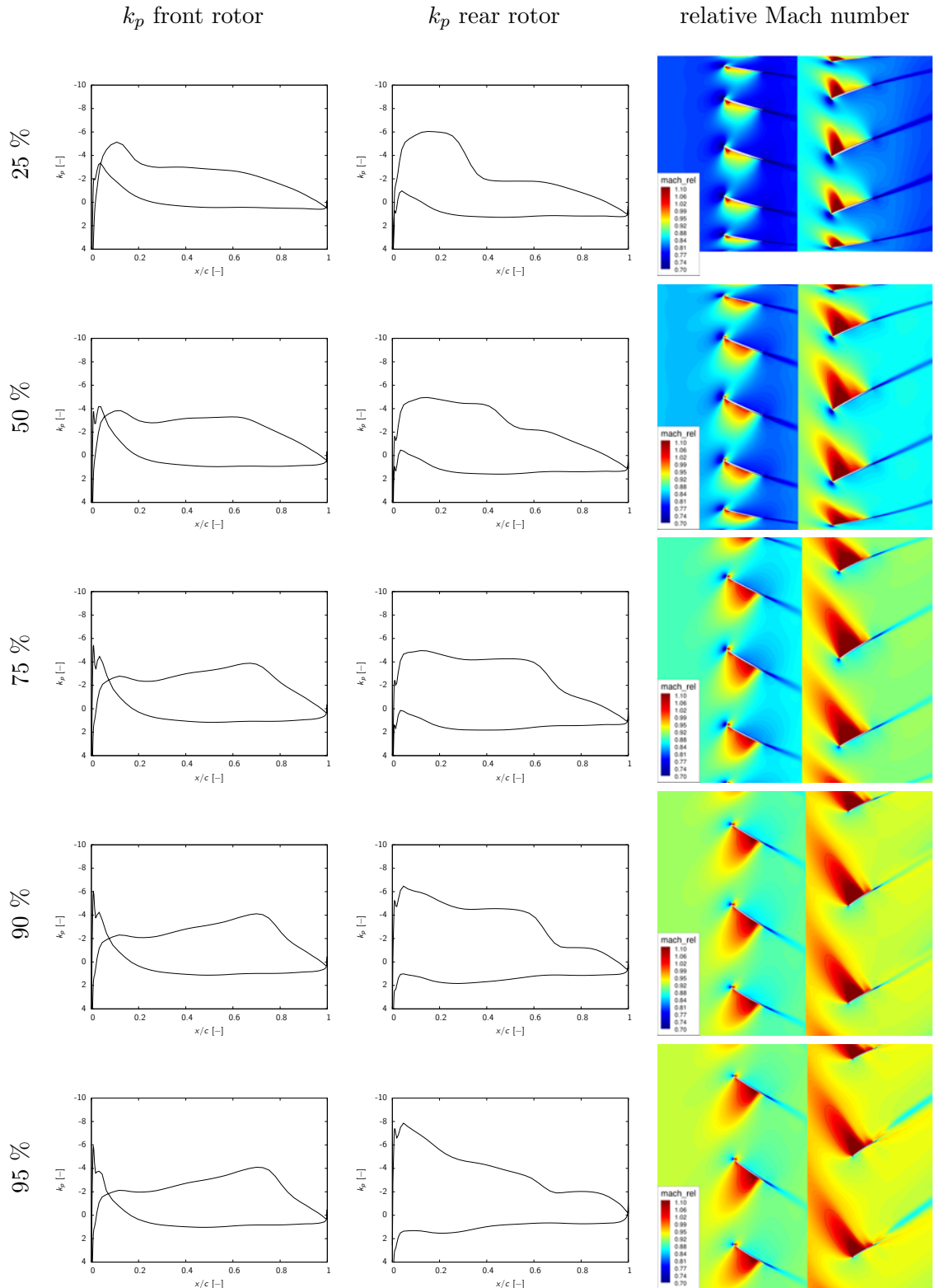


Figure 9.6: High-speed isolated configuration: pressure coefficient and relative Mach number contours at different radial position.

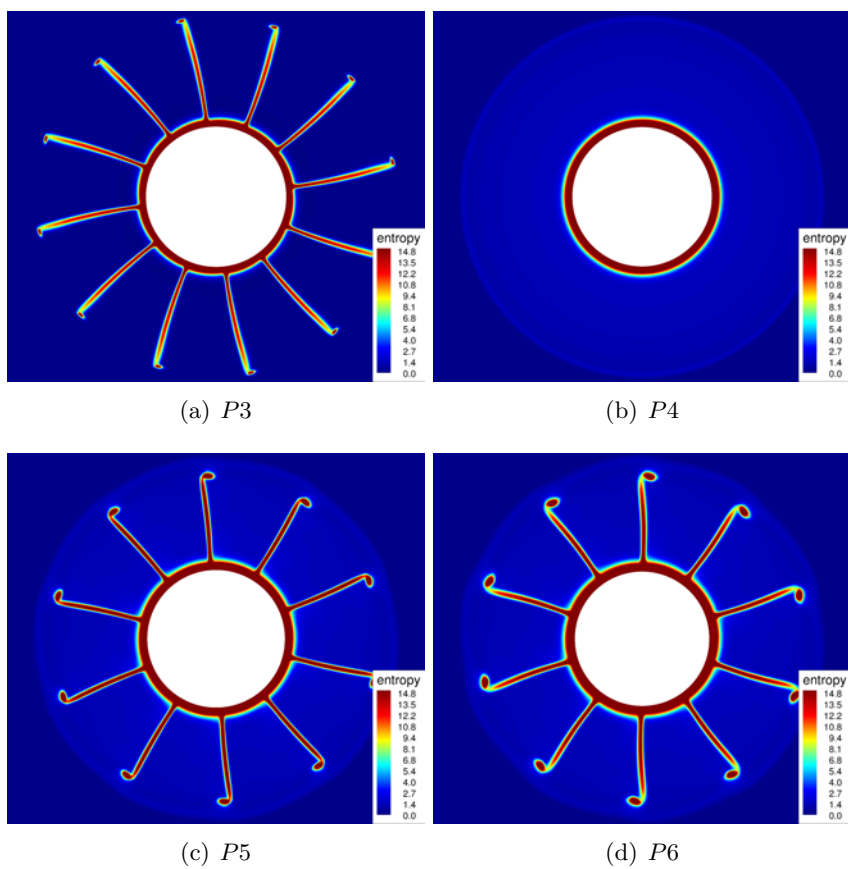


Figure 9.7: High-speed isolated configuration: axial cut of entropy.

9.4 *A priori* estimate of the required number of harmonics

9.4.1 Using the prediction tool

The prediction tool developed in Chap. 6 is used to estimate the number of harmonics needed to compute this high-speed configuration. Seven harmonics are required to capture 99% of the energy (Figure 9.8).

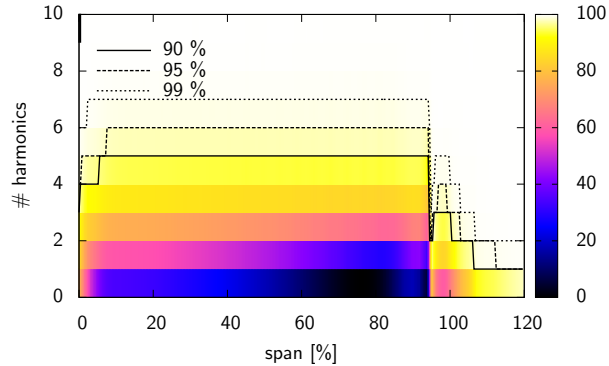


Figure 9.8: High-speed isolated configuration: prediction of the number of harmonics needed to simulate the configuration.

In the following, the HB $N = 7$ computation will be considered to be converged and therefore used to analyze the unsteady flow physics that develops on this CROR configuration.

9.4.2 Analyzing the radial cut

The assessment of the convergence is done on radial cuts of entropy made at 75% of the height of the rear rotor blade. No spurious entropy waves are seen in Figure 9.9, validating the estimation of the number of harmonics needed, provided by the prediction tool. This gives us confidence in the forthcoming results.

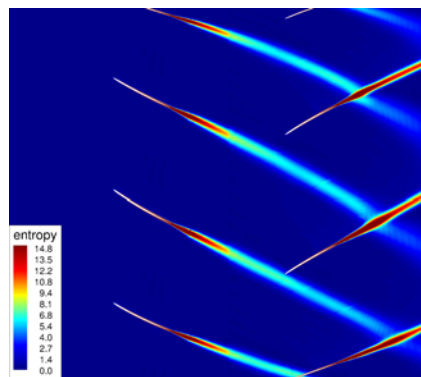


Figure 9.9: High-speed isolated configuration: analysis of the number of harmonics required to capture the wake at a 75% height radial cut.

9.5 Unsteady rigid-motion results

9.5.1 Similarity coefficients

The level of unsteadiness perceived by both rotors is reported in Figure 9.10 for the thrust coefficient. The envelop of the unsteadiness is $\pm 1\%$ on the front rotor and $\pm 2\%$ on the rear rotor.

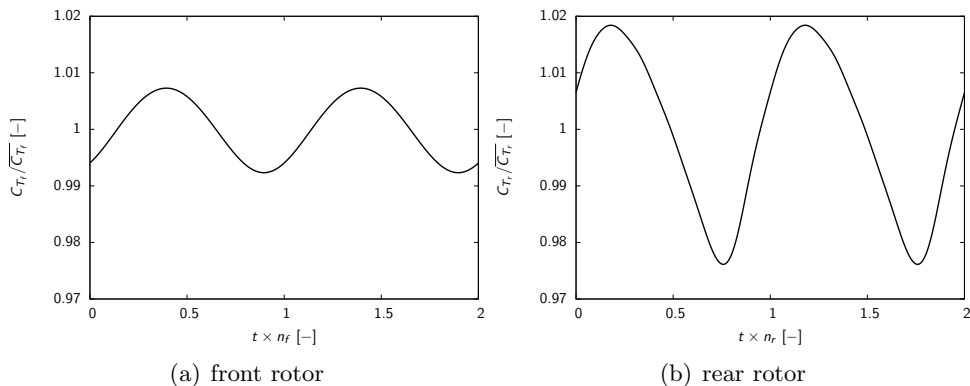


Figure 9.10: High-speed isolated configuration: unsteadiness seen by the rotors.

This has to be compared to the $\pm 3\%$ observed for both rotors on the low-speed configuration. The amplitude of unsteadiness is doubled on the rear rotor, compared to the front rotor one, meaning that the wake effects are much stronger than the potential ones when considering the high-speed inflow condition. The analysis of the shape of the unsteady thrust coefficient reveals that it is close to a sine shape function for the front rotor.

9.5.2 Two-dimensional results: harmonic blade response

To further analyze the unsteadinesses perceived by both rotors, a discrete Fourier transform of the first harmonic of the static pressure of the opposite blade passing frequency is shown in Figure 9.11. Note that the scale is different for the front and the rear rotors.

On the front rotor, the maximum amplitude is observed at the tip of the pressure side. This is consistent with the observation made on the low-speed configuration, where the pressure side was more exposed to pressure variations. In fact, the suction side is shielded from the downstream disturbances by the blade angle of attack. The suction side is not only shielded by the blade angle of attack but also by the shock that forms around $x/c \approx 0.7$ for relative span greater than 40%, as mentioned in Sec. 9.3.4. For relative span smaller than 40%, the shock is closer the leading edge, hence the pressure unsteadiness going upstream. On the tip of the front rotor blade, a vortex is formed that leaves the blades from the pressure side to the suction side. It helps increasing the pressure on the suction side, alleviating the formation of a shock. Therefore, at the tip of the blade, the pressure variations are observed all the way to the leading edge.

On the rear rotor, the suction side of the blade shows a large structure of high unsteadiness near the leading edge. This is attributed to the wake passing. In opposite, a large low amplitude region is observed in the middle of the suction side of the blade. This is attributed to the shielding effect of the shock. In fact, the shock is a discontinuity that prevents unsteady effects to affect the blade. On the pressure side, the level of unsteadiness is much larger than the

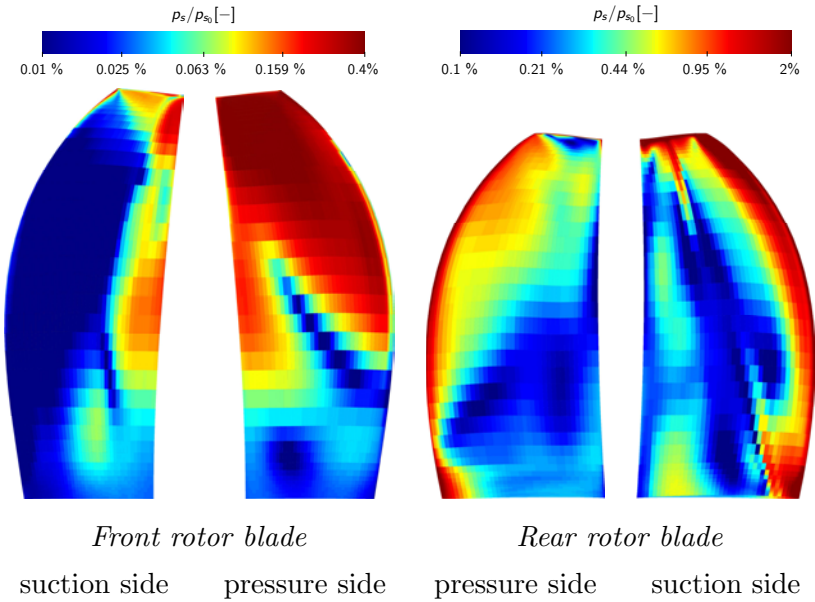


Figure 9.11: High-speed isolated configuration: harmonic response of the front rotor blades.

one observed on the low-speed configuration, relatively to the suction side level. Actually, the smaller angle of attack of the blades might explain this high level. Similar as the suction side of the front rotor blade that are shielded from potential effects coming from the rear rotor blades, the pressure side is relatively less affected by the wake passing than the suction side is. However, for the high-speed configuration, the angle of attack is smaller as said in Sec. 9.1. Therefore, the unsteady effects hitting the suction side of the rear rotor blades are more prone to affect the pressure side too. Moreover, as no shock is present on the pressure side, these unsteadinesses affects the whole chord.

9.5.3 Two-dimensional results: axial cuts

Axial cuts of entropy are shown in Figure 9.12 for several axis positions and compared to steady computation results. Clearly, the harmonic balance approach is able to transfer the tangential distortions between the rows, allowing thus to capture the interaction of the front tip vortices with the rear rotor blades. In this high-speed configuration, the front tip vortex does not hit the rear rotor blades. The difference with the mixing plane approach is tremendous and justifies the use of an unsteady approach over a steady one.

One can see that the prediction tool has provided the number of harmonics needed to ensure the continuity of the tangential information at the rows interface. In fact, at the $P4$ plane, no spurious entropy waves are seen, giving us confidence in the unsteady results.

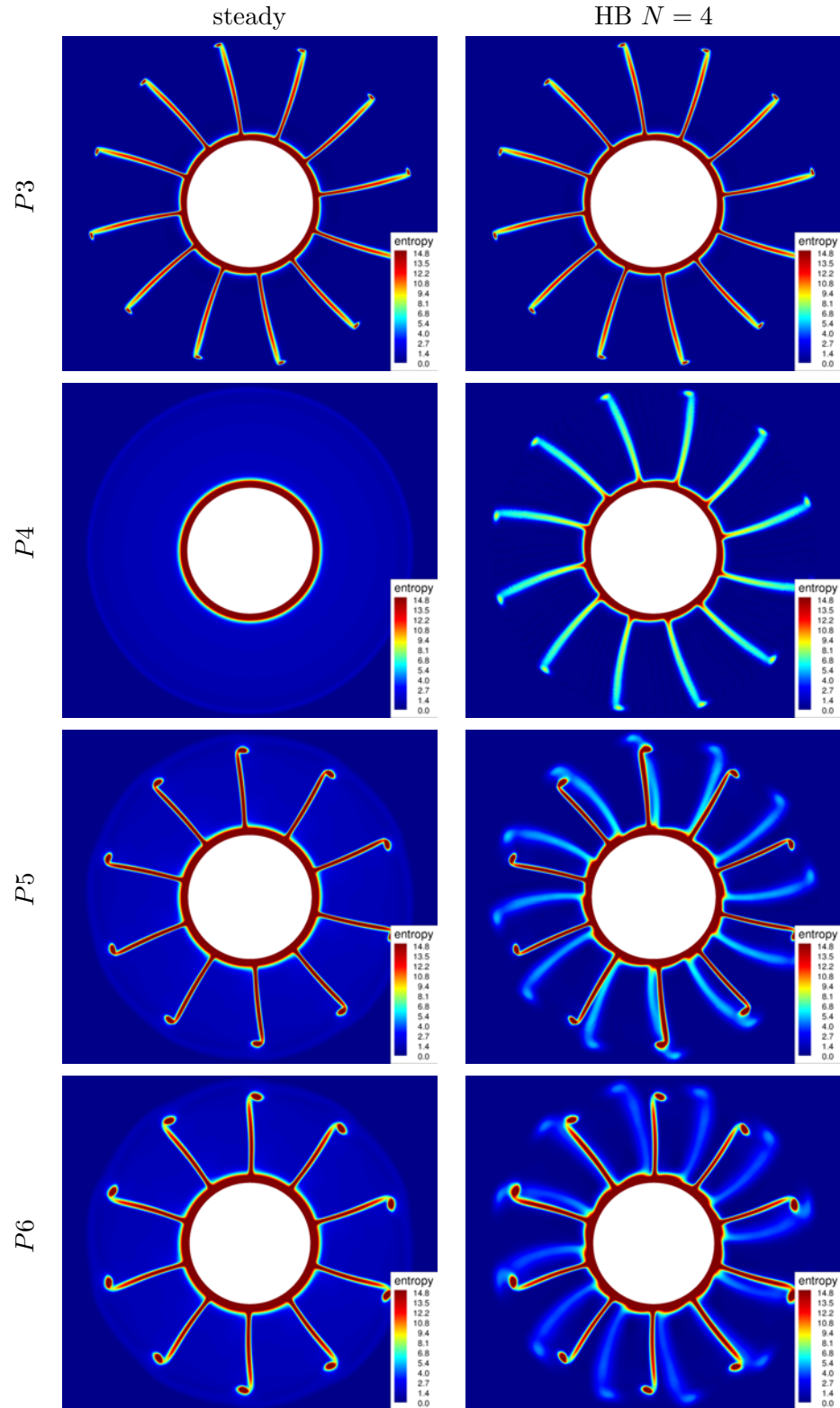


Figure 9.12: High-speed isolated configuration: axial cuts of entropy.

9.6 Aeroelastic results

9.6.1 Stability curve

The damping curves for the two modes of this high-speed configuration are shown in Figure 9.13. The damping is positive for all the inter-blade phase angles and modes, which clears this configuration for flutter. In fact, the damping is around 2.1 and 0.35 for the torsional mode and the flection mode, respectively. The torsional mode is much more damped than the flection one. In opposite to the low-speed configuration, the variation range is similar for both modes. The minimum damping is obtained for $\text{IBPA}=30^\circ$ for the 2F mode and $\text{IBPA}=-30^\circ$ for the 1T mode. To further analyze the aeroelastic behavior of the front rotor blades, the local excitation is computed and analyzed in the section below.

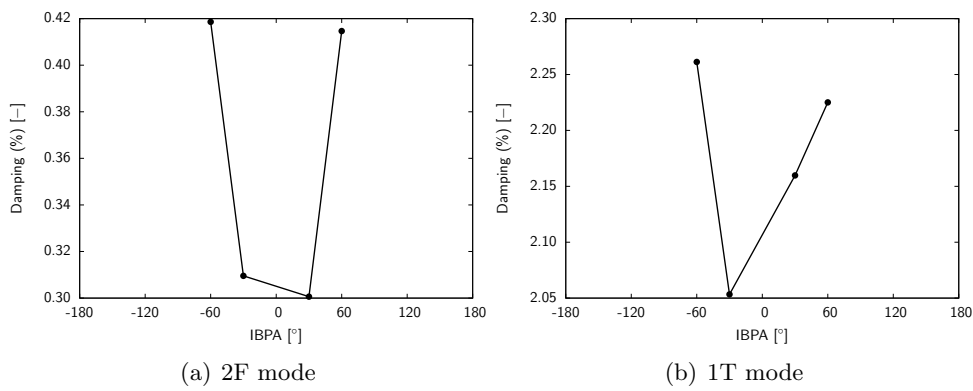


Figure 9.13: High-speed isolated configuration: integrated damping for modes 2F and 1T.

9.6.2 Local excitation

The local excitation is shown on the pressure side and the suction side of the front rotor blades in Figure 9.14. It is the local damping given in each cell divided by the surface of the cell. It is therefore expressed in m^{-2} .

Firstly, the level of local excitation is larger for the 1T mode than it is for the 2F mode. This is one explication for the difference in damping amplitude observed above. This can be attributed again to the displacement related to the 1T mode. In fact, this mode has the tendency to change the local angle of attack of the blade, yielding an unadapted inflow velocity. This angle of attack drives, for the most part, the aerodynamic behavior around the blade. Therefore, a small change in angle of attack can have a strong impact on the loading and the local excitation might be emphasized. Compared to the low-speed configuration, the local excitation is always positive on the leading edge of the blade, meaning that the change in angle of attack and in dihedral angle for the torsional and the flection mode, respectively, is a positive feature for the damping.

Secondly, the influence of the IBPA remains limited for the two modes. The global phenomenology is kept unchanged even though the amplitude varies. For the torsional mode, the local excitation of the tip of the blade seems to be sensitive to the IBPA. This is the tip vortex region, and advanced post-processing procedures might be required to fully understand the behavior of local excitation near the tip of the blades.

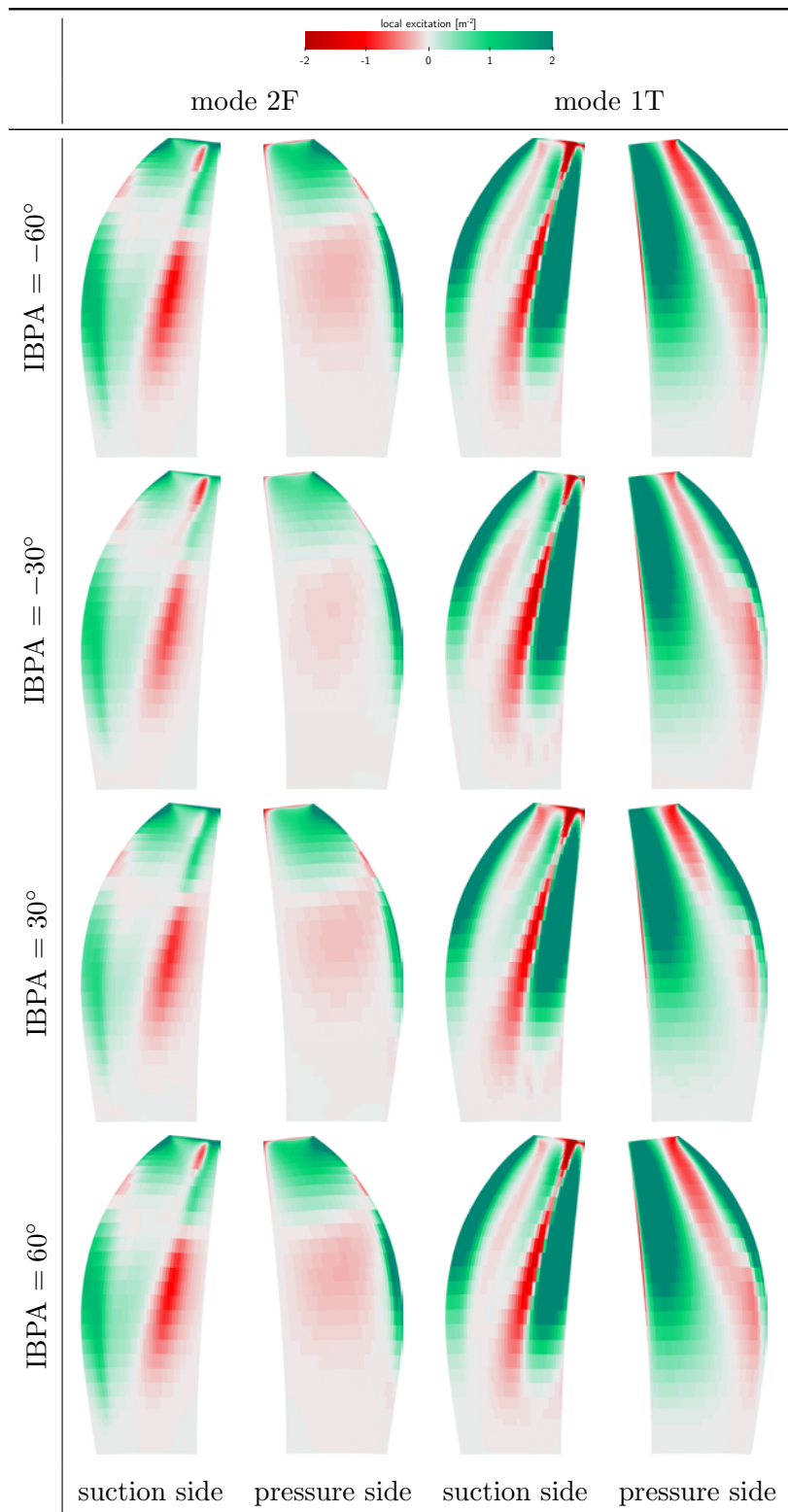


Figure 9.14: High-speed isolated configuration: local excitation for modes 2F and 1T.

Globally the shape of the local excitation contours is much more complicated on the high-speed configuration compared to the low-speed one. In fact, not only the modes inflection lines become inflection lines for the local excitation, but also the shock and the flow that develops in the tip region are important.

9.6.3 Influence of the number of harmonics on the aeroelastic results

All aeroelastic simulations so far have been carried out by using five harmonics. To assess the convergence of the capture of the damping by the multi-frequentiel HB approach, four set of frequencies are studied to run the HB computations on the second flection mode of the high-speed CROR configuration. For each computation, the vibration frequency is considered with one to several harmonics of the blade passing frequency of the rear rotor. As indicated in Sec. 3.5.3, several approaches exist to truncate the frequency sets. Here, only the "cross grid" truncation pattern is used with only one aeroelastic frequency. The local excitation and damping results are shown in Figure 9.15. Raising the number of harmonics of the rear rotor blade passing frequency changes the damping by at-most 10% but the contours of the local excitation are kept nearly unchanged. Only small differences are observed, that integrated produces the 10% observed on the damping value. Further investigation of the convergence for the choice of frequencies are needed, but this has not been done in this work.

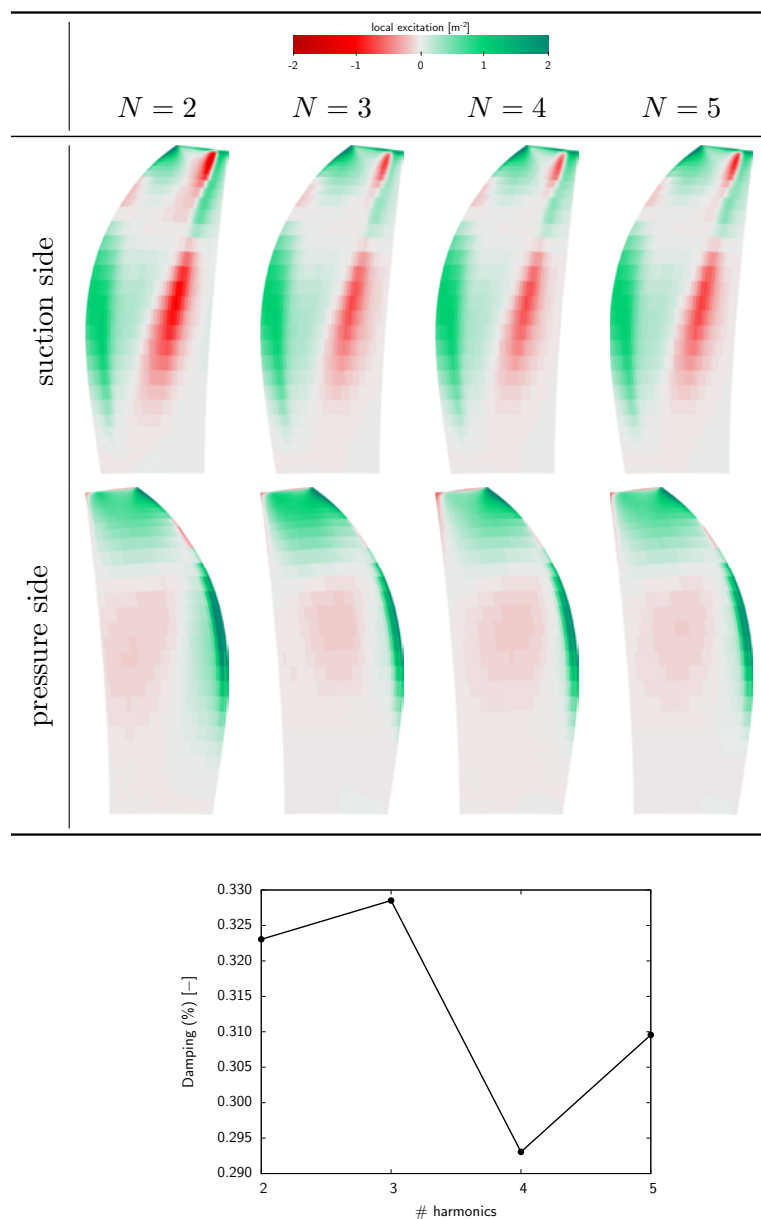


Figure 9.15: High-speed isolated configuration: convergence of local excitation and damping.

Summary

The multi-frequential harmonic balance method along with a weak-coupling approach has been assessed on a high-speed CROR configuration. The steady computations reveal highly non-linear features, namely shocks. The prediction tool defined in Chap. 6 is then used to estimate the number of harmonics required to simulate the configuration. Seven harmonics are needed for the high-speed configuration whereas only four were required for the low-speed one for the same accuracy. With no need for trial and error simulations to select the number of harmonics, results are shown to be consistent, namely tip vortices and wake interactions are well captured. Aeroelastic simulations are then undertaken. The results are scrutinized with focus on the integrated damping and the local excitation of the blades. This configuration is shown to be flutter free, similarly to the low-speed one. The proposed methodology is thus demonstrated to be able to tackle demanding industrial configurations.

Conclusion

In the present PhD work, the Harmonic Balance (HB) approach is applied to aeroelastic simulations of a new type of aircraft engine: the Contra-Rotating Open Rotor (CROR). The proposed methodology is first validated on analytical, linear and non-linear numerical test problems in *Chapter 4*. Two numerical issues are raised, which prevent the use of such an approach on arbitrary aeroelastic configurations: the conditioning of the multi-frequential HB source term and the convergence of the method. Original methodologies are developed to improve the condition number of the simulations (*Chapter 5*) and to provide a priori estimates of the number of harmonics required to achieve a given convergence level (*Chapter 6*). The HB method along with a weak-coupling approach is then validated for a standard configuration for turbomachinery aeroelasticity in *Chapter 7*. The results are shown to be in good agreement with the experimental data. The applicability of the method is finally demonstrated for aeroelastic simulations of CROR configurations in *Chapter 8* and *Chapter 9*.

Summary of the results

On the conditioning of multi-frequential harmonic balance methods

When the considered unsteadiness is related to a single frequency and its harmonics (*i.e.* periodic signal), Fourier analysis leads to a natural choice for the time instances needed to compute the source term: they are evenly spaced over the period. In this case, the mathematical problem is numerically well-defined, meaning that the conditioning of the operators ensures the stability of the approach. In opposite, when several arbitrary frequencies are considered (*i.e.* almost-periodic signal) the multi-frequential HB approach is required and its source term can be ill-conditioned.

As shown in *Chapter 5*, the time sampling has a major effect on the stability of the multi-frequential HB method, due to the condition number of the discrete Fourier transform matrix. One way to tackle this issue, is to consider a non-uniform time sampling along with an algorithm to properly choose the time instances as proposed by Guédene [42]. The Almost-Periodic Fourier Transform algorithm (APFT), originally developed by Kundert et al. [62] and implemented by Guédene [42], is shown to improve the discrete Fourier transform matrix condition number. However, for segregated frequencies, this condition number is shown to remain too large to be used within an industrial context.

As the aeroelasticity of CROR configurations is by essence composed of segregated frequencies, improved algorithms are needed to circumvent this difficulty. This is why, a gradient-based OPTimization algorithm (OPT) has been developed in the current work. It directly minimizes the condition number thanks to a gradient-based optimization method. This approach has

been proven to give a condition number that is always close to unity (*i.e.* the theoretical lower bound) for any input frequencies, thus alleviating the stability issues encountered for arbitrary multi-frequential HB computations. This is a pre-processing procedure that takes less than a minute. Therefore, the non-uniform time sampling proposed by Guédene [42] used together with the OPT algorithm developed in the present contribution enables to tackle problems with large frequency separation or large unsteadinesses, namely CROR aeroelasticity simulations can be considered. This work has been published in

T. Guédene, A. Gomar, F. Gallard, F. Sicot, G. Dufour, and G. Puigt. Non-Uniform Time Sampling for Multiple-Frequency Harmonic Balance Computations. *Journal of Computational Physics*, 236:317–345, March 2013

On the convergence of Fourier-based time methods

Efficiency of Fourier-based time methods results from a trade-off between accuracy and costs requirements. On one hand, the accuracy depends on the number of harmonics used to represent the frequency content of the time signal; on the other hand, computational costs and memory consumption of the computations also scale with the number of harmonics. The problem is that this number is configuration-dependent. Studies on the convergence of Fourier-based time methods for turbomachinery simulations have been previously reported in the literature, but with scattered results. For instance, using a frequency-domain approach, Vilmin et al. [104] obtain accurate solutions using 5 harmonics for a compressor stage and 3 harmonics for a centripetal turbine stage. For a transonic compressor stage with forced blade vibration, Ekici [27] use up to 7 harmonics with a time-domain harmonic balance approach. Finally, for a subsonic compressor stage, Sicot et al. [90] report that 4 harmonics is the minimal requirement to properly capture wake interactions. Moreover, a high number of harmonics ($\gg 10$) can prevent the use of such an approach, as it might be more expensive than a classical time-marching approach. This is particularly true on CROR configurations where the number of harmonics needed to reach convergence has been shown to be greater than ten on some configurations, as shown by François [33].

In *Chapter 6* we investigated the accuracy and convergence properties of Fourier-based time methods. It is highlighted that the convergence rate of these methods, in terms of harmonics required to describe the solution with a given level of accuracy, depends on the spectral content of the solution itself: Fourier-based time methods are particularly efficient for flow problems characterized by a narrow Fourier spectrum.

We showed that the most impulsive source of unsteadiness in turbomachinery flows is due to the generation of wakes in a relative motion. Lakshminarayana and Davino [64] showed that a wake can be empirically approximated by a Gaussian function. The Fourier transform of a Gaussian function being analytical, a truncation error has been defined. Based on this last, we showed that the narrower the wake, the larger the Fourier spectrum, which finally results in a slower convergence of Fourier-based time methods.

In addition to that, we showed on a turbomachinery model problem, that the analytical truncation error can be *a priori* estimated using a mixing-plane steady computation. Applying the *a priori* error estimate to the steady computation of any turbomachinery configuration provides the number of harmonics required to achieve a given level of convergence. It encompasses both the wake distortions and also any tangential disturbances, as for instance the tip vortices or the viscosity effects near the hub. We finally stressed that a 99% accumulation

of energy is a good threshold that ensures the continuity of the tangential distortions at the rows interfaces. Finally, this allows to *a priori* estimate the number of harmonics required to simulate a given turbomachinery configuration. This work has been submitted for publication in

A. Gomar, Q. Bouvy, F. Sicot, G. Dufour, P. Cinnella, and B. François. Convergence of Fourier-based time methods for turbomachinery wake passing problems. *Journal of Computational Physics*, submitted in December 2013

This preliminary step has a negligible cost compared to the overall HB simulation, since the steady computation is classically used to initialize the unsteady run, and extraction of energy accumulation across span takes less than a minute on a single processor. The capability of the tool to estimate the number of harmonics needed to converge an HB computation is verified on the industrial low-speed CROR configuration studied in *Chapter 8* and used to predict the required number of harmonics on the high-speed CROR configuration studied in *Chapter 9*.

On the validation of the harmonic balance approach for aeroelastic simulations

In *Chapter 7*, the proposed weak-coupling approach along with an HB approach has been validated on the 11th standard aeroelastic turbomachinery configuration. The results show that the HB approach provides local and global results close to the reference time-marching scheme with only $N = 1$ harmonic in the time period. Moreover, the results are in good agreement with the experimental data and with the results found in the literature, validating the current approach. At the cost of a memory increase (roughly equal to the number of instances used in the HB simulations), the computational saving is seven for this particular case compared to a phase-lag approach combined with a time-marching scheme. This work has been published in

F. Sicot, A. Gomar, G. Dufour and A. Dugeai. Time-Domain Harmonic Balance Method for Turbomachinery Aeroelasticity. *AIAA Journal*, 52(1):62–71, January 2014

Merging conclusions: the aeroelasticity of contra-rotating open rotors

The three elementary studies summarized above are finally used together to simulate the aeroelasticity of CROR configurations. A low-speed (*Chapter 8*) and a high-speed (*Chapter 9*) CROR configurations are assessed. First, the steady results are analyzed to provide insight into the flow physics and give confidence in the results. The prediction tool defined in *Chapter 6* is then used to estimate the number of harmonics required to simulate the unsteady rigid-motion response of the CROR using the HB approach. The results are analyzed to give the reader a global overview of the unsteady phenomena that will participate to the aeroelastic response of the CROR. Aeroelastic simulations are then launched using the weak-coupling approach that has been validated in *Chapter 7*. As the aeroelastic frequencies of the modes and the blade passing frequencies are not harmonically related, the OPT algorithm developed in *Chapter 5* is used to ensure a good conditioning of the multi-frequential HB source term. The results are finally assessed by post-processing the integrated damping and the local excitation of the blades.

Future work

On the applicability of Fourier-based time methods to contra-rotating open rotors

The multi-frequential HB approach enables new kinds of applications. In particular, the configuration of pusher CROR with a pylon becomes possible. In fact, a mono-frequential HB approach can not be used on such a configuration as the sandwiched row will see upstream and downstream blade passing frequencies that are not multiple integers, hence the need for the multi-frequential HB approach. This might be a very efficient approach as full annulus strategies that are commonly used in the literature to simulate such configurations (see for instance Stuermer [96]) are very expensive.

A pylon/rotor/rotor configuration shown in Figure 9.16(a) has been studied during this work, but is not reported. In fact, a preliminary steady mixing-plane simulation has been launched and the prediction tool developed in *Chapter 6* has been used to estimate the number of harmonics needed to capture the distortions shed by the pylon. The result is indisputable: on this particular configuration, up to 300 harmonics are required to capture 99% of the energy on the whole span (Figure 9.16(b)). This is due to the thin relative thickness of the wake shed by the pylon. The span being given relative to the front rotor height, one can argue that "only" 150 harmonics are needed to capture the pylon wake in the front rotor region.

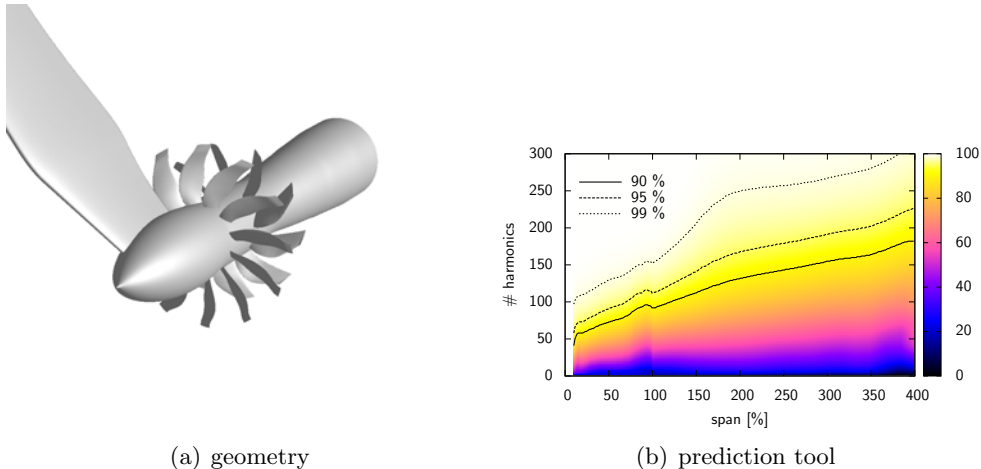


Figure 9.16: Number of harmonics required to compute an installed contra-rotating open rotor configuration.

For such impulsive unsteady signals, the Fourier basis is not optimal as shown in *Chapter 6*. Li et al. [66] propose a wavelet-balance approach to solve this type of large spectrum signals. This solution sounds promising and should be tested on wake signals to see if these can be captured using a low number of wavelet functions.

Ferrante et al. [32] used a multi-frequential Fourier-based time method to investigate incidence effects on the noise emission of a CROR. This sort of application is a good candidate for the multi-frequential HB approach as the full annulus distortion is more likely to be close to a sine function which requires few harmonics to be captured. The advantage of the prediction tool developed in the current work is that it can be used on any steady computation to *a priori*

estimate the number of harmonics required to simulate the configuration. As such, it helps choosing whether or not a Fourier-based time method might be more efficient than a classical time-marching approach.

On the aeroelasticity of contra-rotating open rotors

In this work, a numerical approach has been developed to simulate the aeroelasticity of CROR configurations. Only the flutter of the front rotor blades has been investigated. The rear rotor flutter remains to be studied. In particular, the wakes that are shed from the front rotor might lead to exceeding level of local excitation on the rear rotor, hence its importance.

In addition to that, forced response simulations are needed to evaluate the vibration level of the rear rotor blades as it might lead to structural fatigue. The problem is that the proposed approach relies on a weak-coupling meaning that the forced response can not be computed as the change in amplitude due to the fluid response is of prior importance. Therefore, a strong-coupling approach is required. However, using a classical time-marching approach can be tedious as time scales of the physical and the mechanical problems are scattered. One elegant approach might be to consider the multi-frequential HB approach for both the fluid and the structure [84]. As the method is based on Fourier coefficients, exchanging them for different time scales is compatible. This work is currently conducted by Cadel [11].

Appendices

Detailed algorithm to compute the convergence criteria

A.1 Detailed algorithm to compute ε_1

A sketch of the steps used to evaluate ε_1 from a computation is shown in Figure A.1. Two azimuthal lines are extracted in the stator and in the rotor respectively (step ①). These are duplicated using the phase-lag condition to retrieve the full 2π signal in both blocks. The axial momentum ρU variable is analyzed. The main advantages of this variable are that it is a representative variable for the wake, it is a conservative variable of the considered governing equations and finally, it is invariant under a change of reference frame, unlike the relative velocities for instance. Then, an azimuthal Fourier transform, denoted \mathcal{F}_θ , is carried out on each azimuthal 2π signals and gives the frequency content of the wake in both the stator and the rotor (step ②).

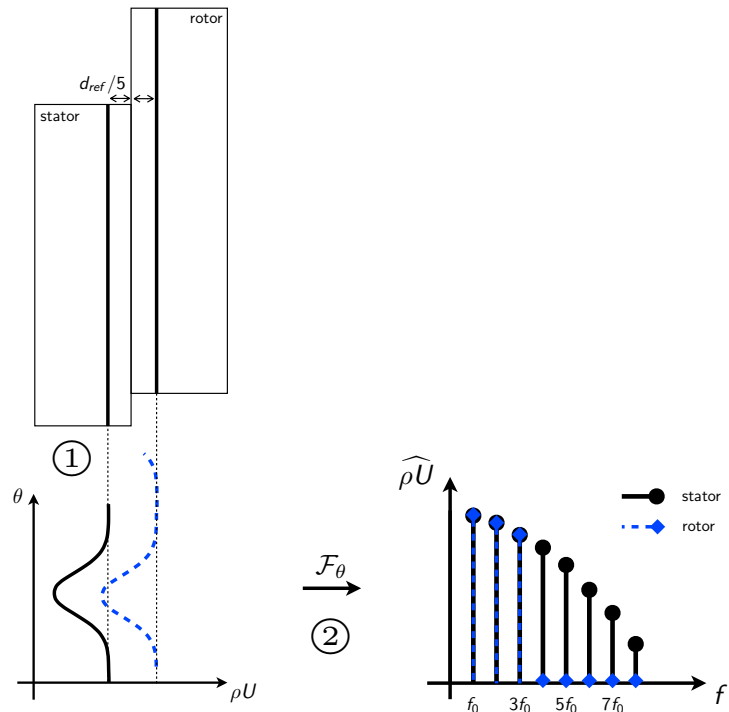


Figure A.1: Sketch of the steps needed to compute the first error quantification ε_1 .

However, due to the time interpolation between the two rows achieved at the interface,

spurious effects can appear upstream the interface as shown in Figure A.2. The effects of the rotor block are significant on the closest cells to the interface for the $N = 5$ computation and still appear on the very last cells before the interface for the $N = 10$ computation. They have disappeared when using $N = 15$ harmonics. To lessen the influence of this interpolation, and thus the spurious effects, the extraction of the axial momentum is not performed at the closest cell to the interface. If d_{ref} is the axial length of a block, the extraction is achieved at $d_{ref}/5$ of the interface upstream and downstream the stator and rotor block, respectively. It represents six time the length of a cell in the axial direction. As the governing equations are the Euler ones, there is no significant variation of the wake thickness within six cells, supporting this approach. Moreover, preliminary studies have shown that $d_{ref}/5$ is sufficient to lower the spurious effects while keeping the results consistent.

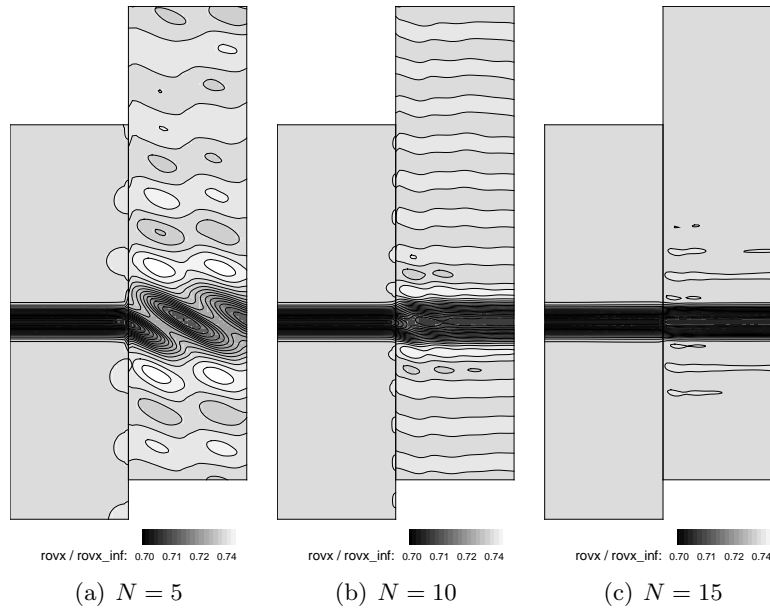


Figure A.2: Occurrence of spurious effects upstream the interface between stator and rotor blocks for a $L = 5\%$ wake width.

A.2 Detailed algorithm to compute ε_2

The steps to compute the second error quantification for each of the 375 computations, are schematically shown in Figure A.3. An azimuthal line is extracted in the stator domain, nearby the interface (step ①), like for the first error quantification. Contrary to this last, in the rotor block, a time probing is done at one point giving an unsteady time signal of $\rho U(t)$ (step ①'). The azimuthal signal is duplicated using the phase-lag condition to retrieve the full 2π signal. The temporal and spatial signals are then Fourier transformed so that their spectrum can be compared (step ②). The wake extraction is performed at the same axial distance of the interface as for the first error quantification. In this case, the location of the point in the rotor block has a direct impact on the results especially when the wake is under-resolved. To highlight this impact, the temporal Fourier transform is evaluated at two different locations

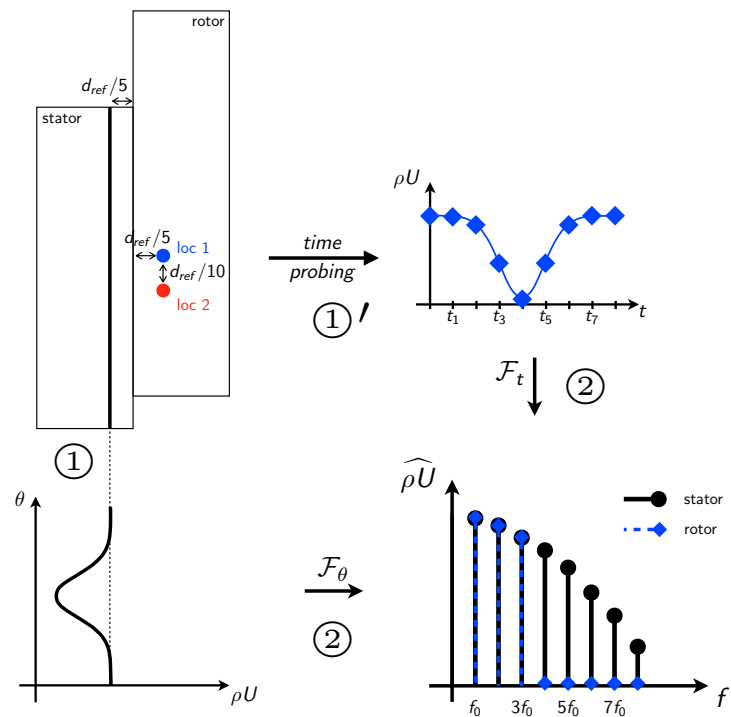


Figure A.3: Sketch of the steps needed to compute the second error quantification.

called loc 1 and loc 2. The two points are separated by a distance $\Delta\theta_{loc_1-loc_2} = d_{ref}/10$ in the azimuthal direction, as shown in Figure A.3.

A.3 Detailed algorithm to the tangential accumulated energy from a mixing plane computation

Figure A.4 shows the different steps: firstly, the row interface is extracted from a mixing-plane computation. Secondly, using this interface, the axial momentum is extracted for several spanwise positions in the region of interest (step ①). In a CROR configuration this is the region with a relative span ranging between 0% and 120%. In fact, beyond the 120% threshold, the influence of the blades on fluid unsteadiness decreases rapidly such that the fluid has a narrow spectrum as the whole spectrum energy lies in, at most, the first three harmonics. Then, for each radius, an azimuthal Fourier transform is performed to obtain the tangential spectrum of the axial momentum (step ②). The relative cumulative energy for a given number of harmonic

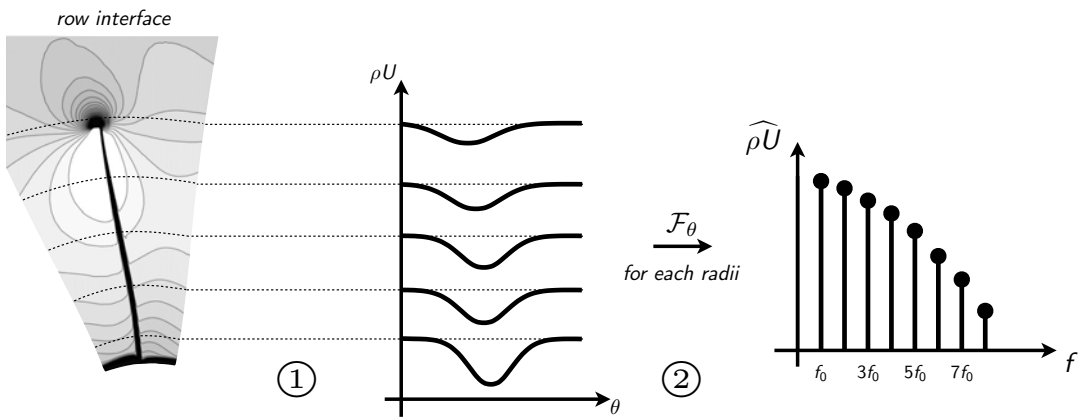


Figure A.4: Steps for the prediction tool based on an azimuthal Fourier transform of the axial momentum at the rotor/rotor interface.

N is then defined as:

$$E(N) = \frac{\sum_{k=1}^N [\widehat{\rho U}^\theta(k)]^2}{\sum_{k=1}^{\infty} [\widehat{\rho U}^\theta(k)]^2}, \quad (\text{A.1})$$

where $\widehat{\rho U}^\theta$ denotes the axial momentum spectrum extracted from the rows interface plane. In Eq. (A.1), the cumulative energy up to harmonic N is compared to the total energy.

Bibliography

- [1] <http://www.bp.com/en/global/corporate/about-bp/statistical-review-of-world-energy-2013/statistical-review-downloads.html>. *Cited in page ix*
- [2] <http://www.energy.kth.se/proj/projects/Markus%20Joecker/STCF/STCF11/stcf11.htm>. *Cited in page 100*
- [3] Global Market Forecast, Future Journeys 2013. Technical report, Airbus, 2013. URL <http://www.airbus.com/company/market/forecast/>. *Cited in page ix*
- [4] R. E. Bartels and A. I. Sayma. Computational Aeroelastic Modeling of Airframes and TurboMachinery: Progress and Challenges. *Physical Transactions of the Royal Society A*, 365:2469–2499, May 2007. *Cited in page 20*
- [5] S. Béchet, C. Negulescu, V. Chapin, and F. Simon. Integration of CFD Tools in Aerodynamic Design of Contra-Rotating Propellers Blades. In *3rd CEAS Conference*, Venice, Italy, October 2011. Council of European Aerospace Societies. *Cited in pages 11, 13, and 111*
- [6] A. S. Besicovitch. *Almost Periodic Functions*. Cambridge University Press, 1932. *Cited in pages 30 and 38*
- [7] J-M. Bousquet. *Introduction à l'aérodynamique des hélices*. 2012. *Cited in pages 8 and 110*
- [8] A. Brambilla. Multitone Signal Harmonic Balance Method. *Electronics Letters*, 35(21):1809–1810, October 1999. doi: 10.1049/el:19991241. *Cited in page 73*
- [9] M. Burnazzi. Assessment of Advanced Time Integration Approaches for Contra-Rotating Open Rotor Simulations. Final year project, Politecnico Di Milano, 2010. *Cited in page x*
- [10] R. H. Byrd, P. Lu, J. Nocedal, and C. Zhu. A Limited Memory Algorithm for Bound Constrained Optimization. *SIAM Journal on Scientific Computing*, 16(5):1190–1208, September 1995. doi: 10.1137/0916069. *Cited in page 69*
- [11] A. Cadel. *Développement d'un couplage aéroélastique dans un contexte d'approche spectrale non linéaire*. PhD thesis, Ecole Centrale de Lyon, 2017 (expected). *Cited in page 159*
- [12] L. Cambier, S. Heib, and S. Plot. The Onera Elsa CFD Software: Input from Research and Feedback from Industry. *Mechanics & Industry*, 14(03):159–174, January 2013. doi: 10.1051/meca/2013056. *Cited in pages xi, 36, 41, 49, 57, 58, 84, 101, 110, and 113*
- [13] M.S. Campobasso and M.B. Giles. Effects of Flow Instabilities on the Linear Analysis of Turbomachinery Aeroelasticity. *Journal of Propulsion and Power*, 19(2):250–259, March 2003. *Cited in pages 100, 105, and 106*
- [14] C. Canuto, M.Y. Hussaini, A. Quarteroni, and Th.A. Zang. *Spectral methods: Fundamentals in single domains*. Springer, 2006. *Cited in pages 43 and 76*
- [15] F. O. Carta. Coupled Blade-Disk-Shroud Flutter Instabilities in Turbojet Engine Rotors. *Journal of Engineering for Power*, 89(3):419–426, July 1967. *Cited in page 22*

Bibliography

- [16] M. Casey and T. Wintergerste. *ERCOFTAC Special Interest Group on "Quality and Trust in Industrial CFD" – Best Practice Guidelines*. European Research Community on Flow, Turbulence and Combustion, January 2000. *Cited in pages 115 and 138*
- [17] T. Chen, P. Vasanthakumar, and L. He. Analysis of Unsteady Blade Row Interaction Using Nonlinear Harmonic Approach. *Journal of Propulsion and Power*, 17(3):651–658, May 2001. doi: 10.2514/2.5792. *Cited in page 31*
- [18] P. Cinnella, P. De Palma, G. Pascazio, and M. Napolitano. A Numerical Method for Turbomachinery Aeroelasticity. *Journal of Turbomachinery*, 126:310–316, April 2004. *Cited in pages 100, 105, 106, and 108*
- [19] W. S. Clark and K. C. Hall. A Time-Linearized Navier-Stokes Analysis of Stall Flutter. *Journal of Turbomachinery*, 122(3):467–476, July 2000. doi: 10.1115/1.1303073. *Cited in pages 26 and 27*
- [20] AR Collar. The expanding domain of aeroelasticity. *Journal of the Royal Aeronautical Society*, 50(428):613–636, 1946. *Cited in page 18*
- [21] A. Datta and W. Johnson. An Assessment of the State-of-the-art in Multidisciplinary Aeromechanical Analyses. *American Helicopter Society Specialists' Conference on Aeromechanics*, January 2008. *Cited in page 20*
- [22] S. S. Davis. NACA 64A010 (NASA Ames Model) Oscillatory Pitching. Technical Report 702, AGARD, 1982. Data Set 2. *Cited in pages 42 and 100*
- [23] G. Dufour, F. Sicot, G. Puigt, C. Liauzun, and A. Dugeai. Contrasting the Harmonic Balance and Linearized Methods for Oscillating-Flap Simulations. *AIAA Journal*, 48(4):788–797, April 2010. doi: 10.2514/1.43401. *Cited in pages 42, 100, and 106*
- [24] A. Dugeai, Y. Mauffrey, A. Placzek, and F. Sicot. Aeroelastic capabilities of the elsA solver for rotating machines applications. In *International Forum on Aeroelasticity and Structural Dynamics*, Paris, France, June 2011. *Cited in pages 101 and 113*
- [25] J. Dugundji. Personal Perspective of Aeroelasticity During the Years 1953-1993. *Journal of Aircraft*, 40(5):809–812, September 2003. *Cited in page 18*
- [26] M. C. Duta, M. B. Giles, and M. S. Campobasso. The Harmonic Adjoint Approach to Unsteady Turbomachinery Design. *International Journal for Numerical Methods in Fluids*, 40(3-4):323–332, September 2002. doi: 10.1002/fld.289. *Cited in pages 100, 105, and 106*
- [27] K. Ekici. Harmonic Balance Analysis of Limit Cycle Oscillations in Turbomachinery. In *46st AIAA Aerospace Sciences Meeting including the New Horizons Forum and Aerospace Exposition*, Nashville, TN, USA, July 2010. doi: 10.2514/6.2010-6710. *Cited in pages 75 and 156*
- [28] K. Ekici and K. C. Hall. Nonlinear Analysis of Unsteady Flows in Multistage Turbomachines Using Harmonic Balance. *AIAA Journal*, 45(5):1047–1057, 2007. doi: 10.2514/1.22888. *Cited in pages 39, 40, 41, 43, 67, 70, and 72*
- [29] K. Ekici and K. C. Hall. Nonlinear Frequency-Domain Analysis of Unsteady Flows in Turbomachinery with Multiple Excitation Frequencies. *AIAA Journal*, 46(8):1912–1920, 2008. doi: 10.2514/1.26006. *Cited in pages 41 and 43*
- [30] K. Ekici, K. C. Hall, and E. Dowell. Computationally Fast Harmonic Balance Methods for Unsteady Aerodynamic Predictions of Helicopter Rotors. In *46th AIAA Aerospace Sciences Meeting and Exhibit*, Reno, NV, USA, January 2008. doi: 10.2514/6.2008-1439. *Cited in page 70*
- [31] J. I. Erdos, E. Alznert, and W. McNally. Numerical Solution of Periodic Transonic Flow through a Fan Stage. *AIAA Journal*, 15(11):1559–1568, November 1977. doi: 10.2514/3.60823. *Cited in page 84*

Bibliography

- [32] P. Ferrante, S. Vilmin, C. Hirsch, J.-C. Bonaccorsi, and P. Francescantonio. Integrated CFD-Acoustic Computational Approach to the Simulation of a Contra Rotating Open Rotor at Angle of Attack. In *Aeroacoustics Conferences*, Berlin, Germany, May 2013. doi: 10.2514/6.2013-2242. *Cited in pages 13 and 158*
- [33] B. François. *Unsteady Aerodynamic Simulations of Contra-Rotating Open-Rotors: Investigation of Efficient CFD Methods, Prediction and Understanding of In-Plane Forces*. PhD thesis, Université Pierre et Marie Curie, 2013. *Cited in pages xi, 9, 75, and 156*
- [34] B. François, M. Laban, M. Costes, G. Dufour, and J.-F. Boussuge. In-Plane Forces Prediction and Analysis in High-Speed Conditions on a Contra-Rotating Open-Rotor. *Journal of Turbomachinery*, 136(8):081002, August 2014. doi: 10.1115/1.4026311. *Cited in pages 13 and 111*
- [35] T.H. Fransson, M. Jöcker, A. Bölc, and P. Ott. Viscous and Inviscid Linear/Nonlinear Calculations Versus Quasi 3D Experimental Cascade Data for a New Aeroelastic Turbine Standard Configuration. *Journal of Turbomachinery*, 121(1):717–725, October 1999. *Cited in pages 42, 99, 100, 101, 103, 105, 106, and 108*
- [36] G. A. Gerolymos and V. Chapin. Generalized Expression of Chorochronic Periodicity in Turbomachinery Blade-Row Interaction. *La Recherche Aérospatiale*, 5:69–73, 1991. *Cited in page 41*
- [37] J. W. Gibbs. Fourier's Series. *Nature*, 59(1539):606, April 1899. doi: 10.1038/059606a0. *Cited in page 76*
- [38] A. Gomar, Q. Bouvy, F. Sicot, G. Dufour, P. Cinnella, and B. François. Convergence of Fourier-based time methods for turbomachinery wake passing problems. *Journal of Computational Physics*, submitted in December 2013. *Cited in pages 75 and 157*
- [39] A. Gopinath and A. Jameson. Time Spectral Method for Periodic Unsteady Computations over Two- and Three- Dimensional Bodies. In *43rd AIAA Aerospace Sciences Meeting and Exhibit*, Reno, NV, USA, January 2005. doi: 10.2514/6.2005-1220. *Cited in pages 38, 42, and 100*
- [40] A. Gopinath and A. Jameson. Application of the Time Spectral Method to Periodic Unsteady Vortex Shedding. In *44th AIAA Aerospace Sciences Meeting and Exhibit*, Reno, NV, USA, January 2006. doi: 10.2514/6.2006-449. *Cited in pages 42, 45, and 46*
- [41] A. Gopinath, E. van der Weide, J. J. Alonso, A. Jameson, K. Ekici, and K. C. Hall. Three-Dimensional Unsteady Multi-Stage Turbomachinery Simulations using the Harmonic Balance Technique. In *45th AIAA Fluid Dynamics Conference and Exhibit*, Reno, NV, USA, 2007. doi: 10.2514/6.2007-892. *Cited in pages 39, 40, 41, 67, 70, and 72*
- [42] T. Guédene. *Modélisation des interactions rotor-stator par une méthode d'équilibrage harmonique*. PhD thesis, Ecole Centrale de Lyon, 2012. *Cited in pages xi, 25, 36, 41, 57, 63, 68, 72, 74, 113, 155, and 156*
- [43] T. Guédene, A. Gomar, F. Gallard, F. Sicot, G. Dufour, and G. Puigt. Non-Uniform Time Sampling for Multiple-Frequency Harmonic Balance Computations. *Journal of Computational Physics*, 236:317–345, March 2013. ISSN 0021-9991. doi: 10.1016/j.jcp.2012.11.010. *Cited in pages 58, 63, and 156*
- [44] R.D. Hager and D. Vrabel. Advanced Turboprop Project. Technical report, National Aeronautics and Space Administration, Cleveland, OH (USA). Lewis Research Center, 1988. *Cited in pages ix, x, 9, 10, 13, and 14*
- [45] K. C. Hall. A linearized Euler analysis of unsteady flows in turbomachinery (GTL report No.190). Technical report, Massachussets Institute of Technology, Cambridge, MA, USA, 1987. *Cited in page 26*
- [46] K. C. Hall and E. F. Crawley. Calculation of unsteady flows in turbomachinery using the linearized Euler equations. *AIAA Journal*, 27:777–787, June 1989. doi: 10.2514/3.10178. *Cited in page 26*

Bibliography

- [47] K. C. Hall, J. P. Thomas, and W. S Clark. Computation of Unsteady Nonlinear Flows in Cascades Using a Harmonic Balance Technique. *AIAA Journal*, 40(5):879–886, May 2002. doi: 10.2514/2.1754. *Cited in pages x, 36, 38, and 39*
- [48] L. He. Fourier Methods for Turbomachinery Applications. *Progress in Aerospace Sciences*, 46(8):329–341, November 2010. doi: 10.1016/j.paerosci.2010.04.001. *Cited in page x*
- [49] L. He and W. Ning. Efficient Approach for Analysis of Unsteady Viscous Flows in Turbomachines. *AIAA Journal*, 36(11):2005–2012, November 1998. doi: 10.2514/2.328. *Cited in pages x, 27, and 31*
- [50] L. He, R. G. Wells, Y. S. Li, T. Chen, and W. Ning. Analysis of Rotor-Rotor and Stator-Stator Interferences in Multi-Stage Turbomachines. *Journal of Turbomachinery*, 124(4):564–571, November 2002. doi: 10.1115/1.1508382. *Cited in pages 29, 30, 31, and 32*
- [51] E. S. Hendricks. Development of an Open Rotor Cycle Model in NPSS Using a Multi-Design Point Approach. In *ASME Turbo Expo: Power for Land, Sea and Air (GT)*, volume 1, pages 441–450, Vancouver, BC, Canada, June 2011. doi: 10.1115/GT2009-59583. *Cited in page 13*
- [52] HP Hodson. Blade Row Interactions In Low Pressure Turbines. In Von Karman Institute, editor, *Blade Row Interference Effects Axial Turbomachinery Stages*, number 1998-02, February 1998. *Cited in page 45*
- [53] P.-A. Hoffer, T. Deconinck, Ch. Hirsch, B. Ortun, S. Canard-Caruana, G. Rahier, S. Pascal, and B. Caruelle. Aeroacoustic Computations of Contra-Rotating Open Rotors Using the Nonlinear Harmonic Method and a Chorochronic Approach. In *ASME Turbo Expo: Power for Land, Sea and Air (GT)*, volume 1: Aircraft Engine; Ceramics; Coal, Biomass and Alternative Fuels; Controls, Diagnostics and Instrumentation, pages 217–227, Copenhagen, Denmark, June 2012. doi: 10.1115/GT2012-68982. *Cited in page 13*
- [54] H. Huang and K. Ekici. Stabilization of High-Dimensional Harmonic Balance Solvers Using a Temporal Spectral Viscosity Operator. In *51st AIAA Aerospace Sciences Meeting including the New Horizons Forum and Aerospace Exposition*, Grapevine, TX, USA, January 2013. doi: 10.2514/6.2013-354. *Cited in page 42*
- [55] H. Huang and K. Ekici. An efficient harmonic balance method for unsteady flows in cascades. *Aerospace Science and Technology*, 29(1):144–154, August 2013. ISSN 1270-9638. doi: 10.1016/j.ast.2013.02.004. *Cited in pages 100, 105, 106, and 108*
- [56] F. W. Huber, O. P. Sharma, S. W. Gaddis, J. B. Staubach, and P. D. Johnson. Performance Improvement Through Indexing of Turbine Airfoils: Part 1-Experimental Investigation. *Journal of Turbomachinery*, 118(4):630–635, October 1996. *Cited in page 32*
- [57] C. Hughes and J. Gazzaniga. Low-speed wind tunnel performance of high-speed counterrotation propellers at angle-of-attack. In *25th AIAA/ASME/SAE/ASEE Joint Propulsion Conference*, Monterey, CT, USA, July 1989. *Cited in page 9*
- [58] IPCC. *Summary for Policymakers*. Climate Change 2013: The Physical Science Basis. Contribution of Working Group I to the Fifth Assessment Report of the Intergovernmental Panel on Climate Change, Cambridge, United Kingdom and New York, NY, USA, cambridge university press edition, 2013. *Cited in page ix*
- [59] A. Jameson, W. Schmidt, and E. Turkel. Numerical Solutions of the Euler Equations by Finite Volume Methods Using Runge-Kutta Time-Stepping Schemes. In *14th AIAA Fluid and Plasma Dynamic Conference*, Palo Alto, CA, USA, 1981. doi: 10.2514/6.1981-1259. *Cited in pages 50, 58, 102, 103, 113, and 137*
- [60] F. Kachra and S. Nadarajah. Aeroelastic Solutions Using the Nonlinear Frequency-Domain Method. *AIAA Journal*, 46(9):2202–2210, September 2008. ISSN 0001-1452. doi: 10.2514/1.27602. *Cited in pages 35 and 36*

Bibliography

- [61] C. Kato and M. Ikegawa. Large eddy simulation of unsteady turbulent wake of a circular cylinder using the finite element method. In *Advances in Numerical Simulation of Turbulent Flows*, volume 1, pages 49–56, 1991. *Cited in page 35*
- [62] K. Kundert, G. Sorkin, and A. Sangiovanni-Vincentelli. Applying Harmonic Balance to Almost-Periodic Circuits. *IEEE Transactions on microwaves Theory and Techniques*, 36(2):366–378, February 1988. doi: 10.1109/22.3525. *Cited in pages 41, 64, 68, 74, and 155*
- [63] M. Laban, J.C. Kok, and B.B. Pranant. Numerical Tools for Contra-Rotating Open-Rotor Performance, Noise and Vibration Assessment. In *27th Congress of the International Council of the Aeronautical Sciences*, Nice, France, September 2010. *Cited in pages 14 and 20*
- [64] B. Lakshminarayana and R. Davino. Mean Velocity and Decay Characteristics of the Guidevane and Stator Blade Wake of an Axial Flow Compressor. *Journal of Engineering for Power*, 102(1):50–60, 1980. doi: 10.1115/1.3230231. *Cited in pages 31, 75, 79, 84, 95, and 156*
- [65] F. Lane. System Mode Shapes in the Flutter of Compressor Blade Rows. *Journal of the aeronautical sciences*, 23(1):54–66, 1956. *Cited in pages 21 and 31*
- [66] Xin Li, Bo Hu, Xieting Ling, and Xuan Zeng. A wavelet-balance approach for steady-state analysis of nonlinear circuits. *Circuits and Systems I: Fundamental Theory and Applications, IEEE Transactions on*, 49(5):689–694, May 2002. ISSN 1057-7122. *Cited in page 158*
- [67] R. C. Maple, P. I. King, P. D. Orkwis, and J. M. Wolff. Adaptive Harmonic Balance Method for Nonlinear Time-Periodic Flows. *Journal of Computational Physics*, 193(2):620–641, January 2004. doi: 10.1016/j.jcp.2003.08.013. *Cited in page 42*
- [68] J. G. Marshall and M. Imregun. A Review of Aeroelasticity Methods with Emphasis on Turbomachinery Applications. *Journal of Fluids and Structures*, 10:237–267, April 1996. doi: 10.1006/jfls.1996.0015. *Cited in pages 18 and 20*
- [69] D. Mavriplis, Z. Yang, and N. Mundis. Extensions of Time Spectral Methods for Practical Rotorcraft Problems. In *50th AIAA Aerospace Sciences Meeting including the New Horizons Forum and Aerospace Exposition*, Nashville, TN, USA, January 2012. doi: 10.2514/6.2012-423. *Cited in pages 42 and 45*
- [70] M. McMullen and A. Jameson. The Computational Efficiency of Non-Linear Frequency Domain Methods. *Journal of Computational Physics*, 212(2):637–661, March 2006. doi: 10.1016/j.jcp.2005.07.021. *Cited in page 36*
- [71] M. McMullen, A. Jameson, and J. Alonso. Acceleration of Convergence to a Periodic Steady State in Turbomachinery Flows. In *39th Aerospace Sciences Meeting and Exhibit*, Reno, NV, USA, January 2001. doi: 10.2514/6.2001-152. *Cited in pages 33, 34, and 35*
- [72] M. McMullen, A. Jameson, and J. AlAlonso. Application of a Non-Linear Frequency Domain Solver to the Euler and Navier-Stokes Equations. In *40th AIAA Aerospace Sciences Meeting and Exhibit*, Reno, NV, USA, January 2002. doi: 10.2514/6.2002-120. *Cited in pages 35, 36, 42, 45, and 46*
- [73] M. McMullen, A. Jameson, and J. J. Alonso. Demonstration of Nonlinear Frequency Domain Methods. *AIAA Journal*, 44(7):1428–1435, July 2006. ISSN 0001-1452. doi: 10.2514/1.15127. *Cited in page 35*
- [74] C. L. Merkle and M. Athavale. Time-accurate unsteady incompressible flow algorithms based on artificial compressibility. In *8th Computational Fluid Dynamics Conference*, University Park, PA, USA, June 1987. *Cited in page 57*
- [75] A. A. Mikolajczak, R. A. Arnoldi, L. E. Snyder, and H. Stargardter. Advances in Fan and Compressor Blade Flutter Analysis and Predictions. *Journal of Aircraft*, 12(4):325–332, 1975. *Cited in page 22*
- [76] A. Mosahebi and S. Nadarajah. An Adaptive Non-Linear Frequency Domain Method for Viscous Flows. *Computers & Fluids*, 75:140–154, April 2013. ISSN 0045-7930. doi: 10.1016/j.compfluid.2012.12.016. *Cited in pages 36 and 42*

Bibliography

- [77] S. Nadarajah and A. Jameson. Optimum Shape Design for Unsteady Three-Dimensional Viscous Flows Using a Nonlinear Frequency-Domain Method. *Journal of Aircraft*, 44(5):1513–1527, September 2007. ISSN 0021-8669. doi: 10.2514/1.27601. *Cited in page 35*
- [78] S. Nadarajah, M. McMullen, and A. Jameson. Optimal Control of Unsteady Flows Using Time Accurate and Non-Linear Frequency Domain Methods. In *33rd AIAA Fluid Dynamics Conference and Exhibit*, Orlando, FL, USA, June 2003. doi: 10.2514/6.2003-3875. *Cited in page 35*
- [79] W. Ning and L. He. Computation of Unsteady Flows Around Oscillating Blades Using Linear and Nonlinear Harmonic Euler Methods. *Journal of Turbomachinery*, 120(3):508–514, 1998. doi: 10.1115/1.2841747. *Cited in pages 27 and 31*
- [80] J. Nocedal. Updating Quasi-Newton Matrices with Limited Storage. *Mathematics of computation*, 35(151):773–782, 1980. *Cited in page 69*
- [81] A. Peters and Z. S. Spakovszky. Rotor Interaction Noise in Counter-Rotating Propfan Propulsion Systems. *Journal of Turbomachinery*, 134:1–12, January 2012. *Cited in pages 13 and 111*
- [82] P. L. Roe. Approximate Riemann Solvers, Parameter Vectors and Difference Schemes. *Journal of Computational Physics*, 43(2):357–372, October 1981. doi: 10.1016/0021-9991(81)90128-5. *Cited in pages 58, 84, 102, 103, and 113*
- [83] L. P. Ruiz-Calavera and D. Perdones-Diaz. CFD Based Aeroelastic Calculation of Propeller Loads. In *28th Congress of the International Council of the Aeronautical Sciences*, Brisbane, Australia, September 2012. *Cited in pages 14 and 20*
- [84] L. Salles, L. Blanc, F. Thouverez, and A. M. Gouskov. Dynamic analysis of fretting-wear in friction contact interfaces. *International Journal of Solids and Structures*, 48(10):1513–1524, 2011. doi: 10.1016/j.ijsolstr.2011.01.035. *Cited in page 159*
- [85] L. Sbardella and M. Imregun. Linearized Unsteady Viscous Turbomachinery Flows Using Hybrid Grids. *Journal of Turbomachinery*, 123(3):568–582, July 2001. *Cited in pages 100, 105, and 106*
- [86] C. E. Shannon. Communication in the Presence of Noise. *Proceeding of the Institute of Radio Engineers*, 37(1):10–21, January 1949. doi: 10.1109/JPROC.1998.659497. *Cited in page 37*
- [87] F. Sicot. *Simulation Efficace des Ecolements Instationnaires Périodiques en Turbomachines*. PhD thesis, Ecole Centrale de Lyon, 2009. *Cited in pages xi, 25, and 36*
- [88] F. Sicot and A. Dugeai. Numerical Investigation of Propellers Whirl Flutter using elsA. In *International Forum on Aeroelasticity and Structural Dynamics*, Paris, France, June 2011. *Cited in page 14*
- [89] F. Sicot, G. Puigt, and M. Montagnac. Block-Jacobi Implicit Algorithms for the Time Spectral Method. *AIAA Journal*, 46(12):3080–3089, December 2008. doi: 10.2514/1.36792. *Cited in pages 42 and 58*
- [90] F. Sicot, G. Dufour, and N. Gourdain. A Time-Domain Harmonic Balance Method for Rotor/Stator Interactions. *Journal of Turbomachinery*, 134(1):011001, January 2012. doi: 10.1115/1.4003210. *Cited in pages 41, 42, 75, and 156*
- [91] F. Sicot, T. Guedeney, and G. Dufour. Time-Domain Harmonic Balance Method for Aerodynamics and Aeroelastic Simulations of Turbomachinery Flows. *International Journal of Computational Fluid Dynamics*, 27(2):68–78, February 2013. doi: 10.1080/10618562.2012.740021. *Cited in page 42*
- [92] F. Sicot, A. Gomar, G. Dufour, and A. Dugeai. Time-Domain Harmonic Balance Method for Turbomachinery Aeroelasticity. *AIAA Journal*, 52(1):62–71, January 2014. doi: 10.2514/1.J051848. *Cited in pages 99 and 157*
- [93] Doug Smith. A case study and analysis of the Tacoma Narrows Bridge failure. Technical report, Department of Mechanical Engineering, Carleton University, Ottawa, Canada, March 1974. *Cited in page 19*

Bibliography

- [94] P. R. Spalart and S. R. Allmaras. A One-Equation Turbulence Transport Model for Aerodynamic Flows. In *30th AIAA Aerospace Sciences Meeting and Exhibit*, Reno, NV, USA, January 1992. AIAA Paper 92-0439. doi: 10.2514/6.1992-439. *Cited in pages 33, 58, 102, and 111*
- [95] W.C. Strack, G. Knip, A.L. Weisbrich, J. Godston, and Bradley E. Technology and benefits of aircraft counter rotation propellers. Technical report, National Aeronautics and Space Administration, Cleveland, OH (USA). Lewis Research Center, 1981. *Cited in page 10*
- [96] A. Stuermer. Unsteady CFD Simulations of Contra-Rotating Propeller Propulsion Systems. In *44th AIAA/ASME/SAE/ASEE Joint Propulsion Conference & Exhibit*, Hartford, CT, USA, July 2008. *Cited in pages 11, 13, 111, and 158*
- [97] C.A. Tatossian, S.K. Nadarajah, and P. Castonguay. Aerodynamic Shape Optimization of Hovering Rotor Blades using a Non-Linear Frequency Domain Approach. *Computers & Fluids*, 51(1):1–15, December 2011. *Cited in page 35*
- [98] J. P. Thomas, E. H. Dowell, and K. C. Hall. Nonlinear Inviscid Aerodynamic Effects on Transonic Divergence, Flutter, and Limit-Cycle Oscillations. *AIAA Journal*, 40(4):638–646, April 2002. doi: 10.2514/2.1720. *Cited in page 42*
- [99] J. P. Thomas, E. H. Dowell, and K. C. Hall. Modeling Viscous Transonic Limit Cycle Oscillation Behavior Using a Harmonic Balance Approach. *Journal of Aircraft*, 41(6):1266–1274, April 2004. doi: 10.2514/1.9839. *Cited in page 42*
- [100] J. P. Thomas, K. C. Hall, and E. H. Dowell. Discrete Adjoint Approach for Modeling Unsteady Aerodynamic Design Sensitivities. *AIAA Journal*, 43(9):1931–1936, September 2005. doi: 10.2514/1.731. *Cited in page 42*
- [101] E. van der Weide, A. Gopinath, and A. Jameson. Turbomachinery Applications with the Time Spectral Method. In *35th AIAA Fluid Dynamics Conference and Exhibit*, Toronto, ON, Canada, June 2005. doi: 10.2514/6.2005-4905. *Cited in pages 37 and 40*
- [102] J. M. Verdon and J. R. Caspar. A linearized unsteady aerodynamic analysis for transonic cascades. *Journal of Fluid Mechanics*, 149:403–429, December 1984. doi: 10.1017/S002211208400272X. *Cited in page 26*
- [103] S. Verley and A. Dugeai. Counter-rotating open rotor whirl flutter phenomenon investigations using elsA solver. In *13th ONERA-DLR Aerospace Symposium*, Palaiseau, France, May 2013. *Cited in page 14*
- [104] S. Vilmin, C. Hirsch, E. Lorrain, and M. Swoboda. Unsteady Flow Modeling across the Rotor/Stator Interface using the Nonlinear Harmonic Method. In *ASME Turbo Expo: Power for Land, Sea and Air (GT)*, volume 6: Turbomachinery, Parts A and B, pages 1227–1237, Barcelona, Spain, May 2006. doi: 10.1115/GT2006-90210. *Cited in pages 30, 31, 32, 33, 75, and 156*
- [105] S. Vilmin, E. Lorrain, and C. Hirsch. Application of a Nonlinear Harmonic Method to the Simulation of Clocking Effects. In *ASME Turbo Expo: Power for Land, Sea and Air (GT)*, volume 7: Turbomachinery, Parts A and B, pages 1601–1609, Orlando, FL, USA, June 2009. doi: 10.1115/GT2009-59475. *Cited in page 32*
- [106] S. Vilmin, É. Lorrain, F. Debrabandere, B. Tartinville, A. Capron, and C. Hirsch. The Nonlinear Harmonic Method Applied to the Combined Effects of Multi-row Unsteady Flows. In *ASME Turbo Expo: Power for Land, Sea and Air (GT)*, number GT2013-94847, San Antonio, TX, USA, June 2013. *Cited in page 33*
- [107] L. Vion, G. Dellatre, F. Fallisard, and L. Jacquin. Counter-Rotating Open Rotor (CROR): flow physics and simulation. In *20^{ieme} Congrès Français de Mécanique*, August 2011. *Cited in page 13*
- [108] D. Vogt and T. H. Fransson. Turbomachinery Aeroelasticity Analyses – Everyday Business or Exceptional Challenge? In *9th European Turbomachinery Conference, invited lecture*, Istanbul, Turkey, March 2011. *Cited in page 108*

Bibliography

- [109] M. A. Woodgate and K. J. Badcock. Implicit Harmonic Balance Solver for Transonic Flow with Forced Motions. *AIAA Journal*, 47(4):893–901, April 2009. doi: 10.2514/1.36311. *Cited in pages 42 and 100*
- [110] S. Yabili. Evaluation of Turbomachinery Methods fo the Simulation of Counter Rotating Open Rotor. Final year project, Institut Supérieur de l’Aéronautique et de l’Espace (ISAE), September 2010. *Cited in page xi*
- [111] A. Zachariadis and C. A. Hall. Application of a Navier–Stokes Solver to the Study of Open Rotor Aerodynamics. *Journal of Turbomachinery*, 133(3):31025–031025–11, July 2011. *Cited in pages 11, 13, and 111*

METHODE D'ÉQUILIBRAGE HARMONIQUE MULTI-FRÉQUENTIELLE POUR LA SIMULATION DES DOUBLETS D'HÉLICES CONTRA-ROTAIVES : APPLICATION À L'AÉROÉLASTICITÉ

RESUME : La mécanique des fluides numérique a permis d'optimiser de nombreux systèmes dont, notamment, les moteurs d'avions. Dans l'industrie aéronautique, les calculs numériques d'écoulements sont principalement limités à des approches stationnaires de par le coût prohibitif des simulations instationnaires. Néanmoins, les écoulements qui se développent dans les machines tournantes, à savoir les principaux composants d'un moteur d'avion, sont majoritairement périodiques en temps. En partant de cette hypothèse de périodicité temporelle, des approches dites spectrales en temps ont vu le jour il y a plus de quinze ans. Elles restent principalement limitées à des écoulements mono-fréquentiels, à savoir composés d'une seule fréquence de base et de ses harmoniques. Récemment, une méthode d'équilibrage harmonique multi-fréquentielle a été développée et implémentée dans le code de calcul *e/sA*, élargissant le champ des applications possibles. En particulier, l'étude de l'aéroélasticité des machines tournantes multi-étages devient alors envisageable.

Cette thèse se propose d'appliquer la méthode d'équilibrage harmonique multi-fréquentielle pour étudier l'aéroélasticité d'une configuration nouvelle de moteur d'avion: les doublets d'hélices contra-rotatives. La méthode est tout d'abord validée analytiquement et numériquement sur des cas tests linéaires et non-linéaires avec succès. Deux problèmes sont soulevés pour l'utilisation d'une telle méthode sur des configurations aéroélastiques arbitraires: le conditionnement du terme source et la convergence de la méthode. Des approches originales ont été développées afin d'améliorer le conditionnement et de fournir une estimation *a priori* du nombre d'harmoniques nécessaire pour obtenir un certain niveau de convergence. La méthode d'équilibrage harmonique est ensuite validée sur un cas standard d'aéroélasticité des machines tournantes et montre des résultats très proches de ceux expérimentaux. L'applicabilité de la méthode est finalement démontrée pour la simulation de l'aéroélasticité des doublets d'hélices contra-rotatives.

Mots clés : Approche spectrale en temps, Doublet d'hélices contra-rotatives, Aéroélasticité, Équilibrage harmonique, Multi-fréquentiel

MULTI-FREQUENCY HARMONIC BALANCE APPROACH FOR THE SIMULATION OF CONTRA-ROTATING OPEN ROTORS : APPLICATION TO AEROELASTICITY

ABSTRACT: Computational Fluid Dynamics (CFD) has allowed the optimization of many configurations among which aircraft engines. In the aeronautical industry, CFD is mostly restricted to steady approaches due to the high computational cost of unsteady simulations. Nevertheless, the flow field across the rotating parts of aircraft engines, namely turbomachinery blades, is essentially periodic in time. Years ago, Fourier-based time methods have been developed to take advantage of this time periodicity. However, they are, for the most part, restricted to mono-frequent flow fields. This means that only a single base-frequency and its harmonics can be considered. Recently, a multi-frequent Fourier-based time method, namely the multi-frequent Harmonic Balance (HB), has been developed and implemented into the *e/sA* CFD code, enabling new kinds of applications as, for instance, the aeroelasticity of multi-stage turbomachinery.

The present PhD thesis aims at applying the HB approach to the aeroelasticity of a new type of aircraft engine: the contra-rotating open rotor. The method is first validated on analytical, linear and non-linear numerical test problems. Two issues are raised, which prevent the use of such an approach on arbitrary aeroelastic configurations: the conditioning of the multi-frequent HB source term and the convergence of the method. Original methodologies are developed to improve the condition number of the simulations and to provide *a priori* estimates of the number of harmonics required to achieve a given convergence level. The HB method is then validated on a standard configuration for turbomachinery aeroelasticity. The results are shown to be in fair agreement with the experimental data. The applicability of the method is finally demonstrated for aeroelastic simulations of contra-rotating open rotors.

Keywords: Fourier-based time method, Contra-rotating open rotor, Aeroelasticity, Harmonic balance, Multi-frequentiel

